

VOLUME 78

APRIL 25, 1974

NUMBER 9

JPCHAx

THE JOURNAL OF
PHYSICAL
CHEMISTRY

PUBLISHED BIWEEKLY BY THE AMERICAN CHEMICAL SOCIETY

THE JOURNAL OF PHYSICAL CHEMISTRY

BRYCE CRAWFORD, Jr., *Editor*

WILMER G. MILLER, *Associate Editor*

ROBERT W. CARR, Jr., **FREDERIC A. VAN-CATLEDGE**, *Assistant Editors*

EDITORIAL BOARD: A. O. ALLEN (1970-1974), C. A. ANGELL (1973-1977), F. C. ANSON (1974-1978), V. A. BLOOMFIELD (1974-1978), J. R. BOLTON (1971-1975), L. M. DORFMAN (1974-1978), M. FIXMAN (1970-1974), H. S. FRANK (1970-1974), R. R. HENTZ (1972-1976), W. J. KAUZMANN (1974-1978), R. L. KAY (1972-1976), D. W. McCLURE (1974-1978), R. M. NOYES (1973-1977), J. A. POPLE (1971-1975), B. S. RABINOVITCH (1971-1975), H. REISS (1970-1974), S. A. RICE (1969-1975), F. S. ROWLAND (1973-1977), R. L. SCOTT (1973-1977), A. SILBERBERG (1971-1975), J. B. STOTHERS (1974-1978), W. A. ZISMAN (1972-1976)

AMERICAN CHEMICAL SOCIETY, 1155 Sixteenth St., N.W., Washington, D. C. 20036

Books and Journals Division

JOHN K CRUM *Director*

RUTH REYNARD *Assistant to the Director*

CHARLES R. BERTSCH *Head, Editorial Processing Department*

D. H. MICHAEL BOWEN *Head, Journals Department*

BACIL GUILLEY *Head, Graphics and Production Department*

SELDON W. TERRANT *Head, Research and Development Department*

©Copyright, 1974, by the American Chemical Society. Published biweekly by the American Chemical Society at 20th and Northampton Sts., Easton, Pa. 18042. Second-class postage paid at Washington, D. C., and at additional mailing offices.

All manuscripts should be sent to *The Journal of Physical Chemistry*, Department of Chemistry, University of Minnesota, Minneapolis, Minn. 55455.

Additions and Corrections are published once yearly in the final issue. See Volume 77, Number 26 for the proper form.

Extensive or unusual alterations in an article after it has been set in type are made at the author's expense, and it is understood that by requesting such alterations the author agrees to defray the cost thereof.

The American Chemical Society and the Editor of *The Journal of Physical Chemistry* assume no responsibility for the statements and opinions advanced by contributors.

Correspondence regarding accepted copy, proofs, and reprints should be directed to Editorial Processing Department, American Chemical Society, 20th and Northampton Sts., Easton, Pa. 18042. Head: **CHARLES R. BERTSCH**. Editorial Assistant: **JOSEPH E. YURVATI**.

Advertising Office: Centcom, Ltd., 50 W. State St., Westport, Conn. 06880.

Business and Subscription Information

Send all new and renewal subscriptions *with payment to* Office of the Controller, 1155 16th Street, N.W., Washington, D. C. 20036. Subscriptions should be renewed promptly to avoid a break in your series. All correspondence and telephone calls regarding changes of

address, claims for missing issues, subscription service, the status of records, and accounts should be directed to Manager, Membership and Subscription Services, American Chemical Society, P.O. Box 3337, Columbus, Ohio 43210. Telephone (614) 421-7230.

On changes of address, include both old and new addresses with ZIP code numbers, accompanied by mailing label from a recent issue. Allow four weeks for change to become effective.

Claims for missing numbers will not be allowed (1) if loss was due to failure of notice of change in address to be received before the date specified, (2) if received more than sixty days from date of issue plus time normally required for postal delivery of journal and claim, or (3) if the reason for the claim is "issue missing from files."

Subscription rates (1974): members of the American Chemical Society, \$20.00 for 1 year; to nonmembers, \$60.00 for 1 year. Those interested in becoming members should write to the Admissions Department, American Chemical Society, 1155 Sixteenth St., N.W., Washington, D. C. 20036. Postage to Canada and countries in the Pan-American Union, \$5.00; all other countries, \$6.00. Air freight rates available on request. Single copies for current year: \$3.00. Rates for back issues from Volume 56 to date are available from the Special Issues Sales Department, 1155 Sixteenth St., N.W., Washington, D. C. 20036.

Subscriptions to this and the other ACS periodical publications are available on microfilm. Supplementary material not printed in this journal is now available in microfiche form on a current subscription basis. For information on microfilm or microfiche subscriptions, write Special Issues Sales Department at the address above.

THE JOURNAL OF
PHYSICAL CHEMISTRY

Volume 78, Number 9 April 25, 1974

JPCHAx 78 (9) 857-950 (1974)
ISSN 0022-3654

| | | |
|---|--|-----|
| Relative Reaction Rates Involving Thermal Fluorine-18 Atoms and Thermal Fluoromethyl Radicals with Oxygen, Nitric Oxide, Sulfur Dioxide, Nitrogen, Carbon Monoxide, and Hydrogen Iodide | Richard Milstein, Ronald L. Williams, and F. S. Rowland* | 857 |
| Fall-Off Behavior of a Thermal Unimolecular System in the Presence of a Weak Collider Inert Bath Gas | F. M. Wang and B. S. Rabinovitch* | 863 |
| On Electron Capture in γ -Irradiated Methylcyclohexane Glass | T. B. Truong, A. Bernas,* and J. Roncin | 857 |
| Reactions Involving Electron Transfer at Semiconductor Surfaces. V. Reactivity and Electron Paramagnetic Resonance of Electron Transfer Sites on Rutile | Joseph Cunningham* and Anthony L. Penny | 870 |
| Effect of Silylation upon the Hydrogenating Activity of Supported Platinum Catalysts | Harold H. Kung, Beverley I. Brookes, and Robert L. Burwell, Jr.* | 875 |
| Flash Photolysis and Time-Resolved Mass Spectrometry. III. Termolecular and Surface Recombinations of Ground State Iodine Atoms | Richard T. Meyer | 878 |
| Pulse Radiolytic Study of Ni^{2+} . Nickel-Carbon Bond Formation | M. Kelm, J. Lilie, A. Henglein,* and E. Janata | 882 |
| Radiolysis and Photolysis of the Hydrogen Peroxide- <i>p</i> -Nitrosodimethylaniline-Oxygen System | M. Hatada, I. Kraljic, A. El Samahy, and C. N. Trumbore* | 888 |
| Pulse Radiolysis Studies of Chloride Complexes of Thallium(II). Absorption Spectra and Stability Constants of TlCl^+ , TlCl_2 , and TlCl_3^- | R. W. Dodson and H. A. Schwarz* | 892 |
| Electron Spin Resonance of γ Irradiation Induced Free Radicals in Polyvinylpyridines | J. C. Ronfard Haret, A. Lablache Combier, and C. Chachaty* | 899 |
| The Influence of True Chemical Equilibrium on the Viscosity-Mobility Product of Electrolytes | Paul Hemmes | 907 |
| An Empirical Intermolecular Potential Energy Function for Water | Lester L. Shipman and Harold A. Scheraga* | 909 |
| Electrical Conductance and Ultrasonic Relaxation for Lithium Perchlorate in Tetrahydrofuran | Paul Jagodzinski and Sergio Petrucci* | 917 |
| Theory of Ion-Complexing Effects in Ion-Exchange Column Performance | Frederick M. Golden, Klara I. Shiloh, Gerhard Klein, and Theodore Vermeulen* | 926 |
| Analysis of Inertial Effects on Electron Spin Resonance Spectra in the Slow Tumbling Region | G. V. Bruno and J. H. Freed* | 935 |
| Infrared Attenuated Total Reflection Spectra of Adsorbed Layers at the Interface between a Germanium Electrode and an Aqueous Solution of Sodium Laurate | Tatsuo Higashiyama and Tohru Takenaka* | 941 |
| Skeletonized Films and Measurement of Their Optical Constants | M. S. Tomar | 947 |

There is no supplementary material for this issue.

* In papers with more than one author, the asterisk indicates the name of the author to whom inquiries about the paper should be addressed.

AUTHOR INDEX

- Bernas, A., 867
Brookes, B. I., 875
Bruno, G. V., 935
Burwell, R. L., Jr., 875
- Chachaty, C., 899
Combier, A. L., 899
Cunningham, J., 870
- Dodson, R. W., 892
- El Samahy, A., 888
- Freed, J. H., 935
- Golden, F. M., 926
- Haret, J. C. R., 899
Hatada, M., 888
Hemmes, P., 907
Henglein, A., 882
Higashiyama, T., 941
- Jagodzinski, P., 917
Janata, E., 882
- Kelm, M., 882
Klein, G., 926
- Kraljic, I., 888
Kung, H. H., 875
- Lilie, J., 882
- Meyer, R. T., 878
Milstein, R., 857
- Penny, A. L., 870
Petrucci, S., 917
- Rabinovitch, B. S., 863
Roncin, J., 867
Rowland, F. S., 857
- Scheraga, H. A., 909
Schwarz, H. A., 892
Shiloh, K. I., 926
Shipman, L. L., 909
- Takenaka, T., 941
Tomar, M. S., 947
Trumbore, C. N., 888
Truong, T. B., 867
- Vermeulen, T., 926
- Wang, F. M., 863
Williams, R. L., 857

THE JOURNAL OF PHYSICAL CHEMISTRY

Registered in U. S. Patent Office © Copyright, 1974, by the American Chemical Society

VOLUME 78, NUMBER 9 APRIL 25, 1974

Relative Reaction Rates Involving Thermal Fluorine-18 Atoms and Thermal Fluoroethyl Radicals with Oxygen, Nitric Oxide, Sulfur Dioxide, Nitrogen, Carbon Monoxide, and Hydrogen Iodide¹

Richard Milstein, Ronald L. Williams, and F. S. Rowland*

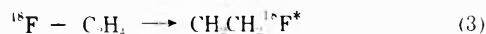
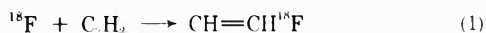
Department of Chemistry, University of California, Irvine, California 92664 (Received November 15, 1973)

Publication costs assisted by the Division of Research, U. S. Atomic Energy Commission

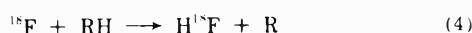
The reactions of thermal ¹⁸F atoms have been studied with O₂, NO, SO₂, N₂, and CO in competition with addition to C₂H₂ or C₂H₄. Addition to C₂H₄ is 0.83 ± 0.02 as rapid, and total reaction with SO₂ is 0.04 ± 0.02 as fast as addition to acetylene. The reaction rates with the molecules O₂, NO, N₂, and CO are all <0.01 *vs.* addition to acetylene, at about 4000 Torr. The relative rates of reaction of CH₂¹⁸FCH₂ radicals with various scavengers are HI, (1.0); NO, 5.0 ± 0.5; O₂, 1.05 ± 0.10; SO₂, 0.33 ± 0.10; CO, 0.005 ± 0.002. For CH¹⁸F=CH radicals, the relative rates are HI, (1.0); CO, 0.022 ± 0.007; N₂, <0.003.

Introduction

Thermal ¹⁸F atoms are readily produced through fast neutron irradiation of SF₆, by the ¹⁹F(n,2n)¹⁸F nuclear reaction, followed by nonreactive moderating collisions with other molecules of SF₆.²⁻⁷ When other components of a gaseous mixture with SF₆ are restricted to total mole fractions ≤0.05, essentially all (>97%) of the ¹⁸F atoms react with thermal kinetic energy.⁶ In the presence of C₂H₂ or C₂H₄, approximately 85⁷ and 60%,⁶ respectively, of such ¹⁸F atoms react by addition to the π bond, as in (1) and (3). The fluorovinyl ¹⁸F radical formed in (1) can be readily converted to CH₂=CH¹⁸F by reaction with HI as in (2);⁷ the assay of the radioactivity of CH₂=CH¹⁸F is straightforward by radio gas chromatography.



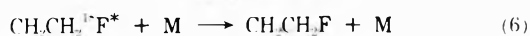
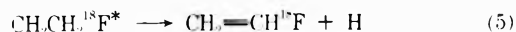
The competition between other possible thermal reactions of ¹⁸F and the addition reaction 1 can be studied by observing the diminution in the yield of CH₂=CH¹⁸F *vs.* the concentration ratio of the competing species and C₂H₂.^{4,5} The competition of hydrogen atom abstraction from a series of RH (and RD) molecules, as in (4), has



been studied in detail, using this indirect method of observation in which H¹⁸F is assayed by measuring the amount of "missing" CH₂=CH¹⁸F.

We have now extended these indirect measurements to five additional simple molecules: N₂, O₂, CO, NO, and SO₂. Some of these experiments contain an additional complication, and thereby furnish additional information. The determination of the yield of (4) by diminution of the yield from (2) implicitly accepts the premise that the molecule RH does *not* interfere with reaction (2) itself (*i.e.*, that RH competes with C₂H₂ for ¹⁸F, but not with HI for CH=CH¹⁸F). While some of these simple molecules (*e.g.*, N₂) might be anticipated also to be inert toward CH=CH¹⁸F, others (*e.g.*, O₂, NO) are well known as free radical scavengers and ought to compete readily with HI for any CH=CH¹⁸F radicals formed. Consequently, the C₂H₂ competition system is only applicable when the competing molecule is inert toward reactions with a free radical.

The addition of thermal ¹⁸F to C₂H₄ in (3) forms excited C₂H₄¹⁸F* radicals capable either of decomposition by H atom loss, as in (5), or stabilization plus reaction with HI, as in (6) or (7).^{6,8,9} These C₂H₄¹⁸F* radicals are





monoenergetically excited from the exothermicity of the addition reaction, broadened slightly by the Maxwellian distribution of thermal energies in the reacting species. At a fixed total pressure, collisional stabilization occurs at essentially a constant rate, since most of the collisions are with SF₆. The yield of CH₂=CH¹⁸F from decomposition should therefore also be constant. Most important, this yield of CH₂=CH¹⁸F is *not* affected by any competition between HI and some other species for an intermediate radical, but gives directly a measure of a yield which is proportional to that of the original CH₂CH₂¹⁸F*. Any direct competitive reaction with some added species which resulted in permanent removal of thermal ¹⁸F from the system would immediately decrease the observed yield of CH₂=CH¹⁸F from C₂H₄. In addition, if the added species is capable of reacting with thermalized CH₂CH₂¹⁸F radicals, the observed yield of CH₃CH₂¹⁸F will be diminished by this competition.

We have carried out separate competition reactions in excess SF₆ between HI, C₂H₄, and/or C₂H₂, and each of the species N₂, CO, O₂, NO, and SO₂. None of these five species proved to be competitive (slight reaction with SO₂) in reaction rate for thermal ¹⁸F atoms with addition to the π bond systems. The last three are all excellent scavengers for stabilized CH₂CH₂¹⁸F radicals, and relative reaction rates were obtained for each *vs.* the abstraction reaction 6 with HI. Carbon monoxide also exhibited a lesser scavenging ability for both CH₂CH₂¹⁸F and CH=CH¹⁸F radicals; N₂ did not react to any observable extent with CH=CH¹⁸F radicals.

Experimental Section

General Techniques. The basic experimental techniques for forming ¹⁸F atoms from the ¹⁹F(n,2n)¹⁸F reaction have been detailed earlier.²⁻⁷ The current experiments involve only minor changes from those given in these references.

Research grade C₂H₄ (Phillips), C₂H₂ (Matheson), and NO (Matheson) were used in these experiments. In addition, CP grade CO and SO₂ (both Matheson), Industrial Grade O₂ (Liquid Carbonic), and Hi Pure N₂ (Liquid Carbonic) were used. Except for NO, which was purified by distillation from a pentane slush bath, the gases were not further purified.

The ¹⁸F-labeled products were separated on a 50-ft dimethylsulfolane column operating at 25°.

Results and Discussion

Competition between Acetylene and Ethylene for Thermal ¹⁸F Atoms. The earlier experiments with thermal ¹⁸F atoms involved the competition between H abstraction from RH and addition to C₂H₂ as the π bond competitor, while CH₂=CH¹⁸F was the assayed radioactive product. Since both C₂H₂ and C₂H₄ were used as competitors in the present experiments, several samples containing both were irradiated and analyzed to establish a relative rate between these two molecules. The results of these experiments are given in Table I. Two experiments without C₂H₂ present are included to provide information about the distribution of C₂H₄¹⁸F* radicals between CH₂=CH¹⁸F and CH₃CH₂¹⁸F at a total pressure of 4000 Torr.

The yield of CH₂=CH¹⁸F arises predominantly from initial addition to C₂H₂, plus a small component from CH₂CH₂¹⁸F* decomposition. From the average of the two

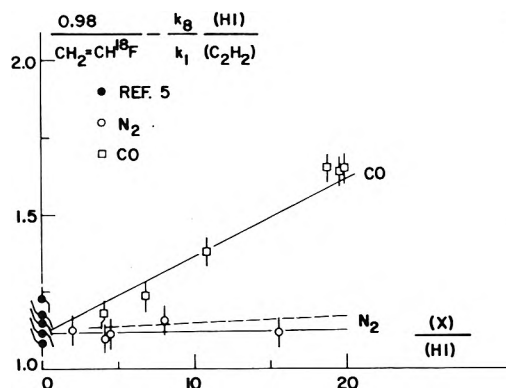


Figure 1. Competition of HI with CO and with N₂ for CH₂=CH¹⁸F radicals: O, N₂ vs. HI; □, CO vs. HI; ----, upper limit for fit to N₂ data.

C₂H₄ experiments, we estimate the CH₂=CH¹⁸F/CH₃CH₂¹⁸F ratio from CH₂CH₂¹⁸F* to be 0.027 at 4000 Torr. This ratio has been used to correct the raw mixture data by subtracting 0.027 × (CH₃CH₂¹⁸F) from the observed yield of CH₂=CH¹⁸F, and adding an equal amount to the observed CH₃CH₂¹⁸F yield. All four experiments consistently show that ¹⁸F reaction with C₂H₂ is slightly favored (1.20 ± 0.02) over reaction with C₂H₄. The mole fraction ratio was varied by a factor of 4 without effect on this competitive reaction ratio.

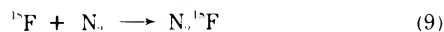
A small yield of C₂H₃¹⁸F (estimated as about 0.5% of the total yield)⁶ arises from the reaction of *hot* ¹⁸F with C₂H₄,¹⁰ followed by rapid decomposition of the highly excited C₂H₄¹⁸F* radical. A small yield of CH=C¹⁸F is also observed from hot reactions of ¹⁸F with C₂H₂.⁷ When the observed yield from C₂H₄ is corrected for hot reactions (the CH=C¹⁸F yield has not been included for C₂H₂), a minor upward correction is made in the ratio of thermal reactivities to 1.21 ± 0.02, favoring C₂H₂ over C₂H₄.

Competition between Molecular Nitrogen and C₂H₂. Several competitive experiments involving N₂ *vs.* C₂H₂ are summarized in Table II. These data are plotted in Figure 1, in the form [(0.98)/(CH₃CH₂¹⁸F)] - [k₈(HI)/k₁(C₂H₂)] *vs.* (N₂)/(C₂H₂). This method of graphing the data was discussed in detail earlier,⁵ and simply recognizes that the thermal reactions competing for ¹⁸F include reaction 8 with HI, as well as the addition to C₂H₂ and



possible addition to N₂. In all but one of the experiments in Table II, the ratio of HI/C₂H₂ is fixed and the correction factor k₈(HI)/k₁(C₂H₂) is therefore constant (k₈/k₁ = 0.37).⁵ It has been included only to be consistent for comparisons with ref 5.

The best fit to the data in Figure 1 is a horizontal line, indicating that k₉(N₂)/k₁(C₂H₂) is zero within the experimental error, *i.e.*



N₂ is an inert molecule in these experiments. In principle, the possible reactions of ¹⁸F with N₂ include the formation of both N¹⁸F and N₂¹⁸F. However, the former is highly endothermic because of the great bond strength of N₂, and cannot occur with thermal ¹⁸F atoms. The combination reaction 9 requires a third body for removal of the excitation energy released by formation of the N-¹⁸F bond; the failure to observe removal of ¹⁸F atoms by this competitive path could result either from initial failure to

E I: Competitive Reactions of ^{18}F Atoms with C_2H_4 and C_2H_2 in HI-Scavenged Excess SF_6

| SF_6 | Sample pressures, Torr | | | Observed yields, % | | Product yields ^a (%) from | | Specific yield ratio $\text{C}_2\text{H}_2/\text{C}_2\text{H}_4$ |
|---------------|------------------------|------------------------|------|-------------------------------------|-------------------------------------|--------------------------------------|------------------------|---|
| | C_2H_2 | C_2H_4 | HI | $\text{C}_2\text{H}_3^{18}\text{F}$ | $\text{C}_2\text{H}_5^{18}\text{F}$ | C_2H_2 | C_2H_4 | |
| 3800 | 0 | 166 | 33.4 | 1.65 | 57.3 | 0 | 59.0 | |
| 3810 | 0 | 167 | 33.3 | 1.52 | 60.1 | 0 | 61.6 | |
| 3800 | 55.2 | 111 | 33.4 | 25.2 | 39.7 | 24.1 | 40.8 | 1.19 |
| 3800 | 83.3 | 82.4 | 33.3 | 38.8 | 30.2 | 38.0 | 31.0 | 1.21 |
| 3820 | 83.3 | 83.3 | 33.4 | 38.9 | 31.4 | 38.0 | 32.3 | 1.18 |
| 3830 | 112 | 54.3 | 33.3 | 51.8 | 20.2 | 51.3 | 20.7 | 1.20 |

^a Yield C_2H_2 = $(\text{C}_2\text{H}_3^{18}\text{F}) - (0.027)(\text{C}_2\text{H}_5^{18}\text{F})$. Yield C_2H_4 = $(1.027)(\text{C}_2\text{H}_5^{18}\text{F})$. [1.65/57.3 = 0.029; 1.52/60.1 = 0.025; average = 0.027.]

TABLE II: Effect of N_2 on Absolute Yields of $\text{C}_2\text{H}_3^{18}\text{F}$ from ^{18}F Reactions with C_2H_2 in SF_6 - C_2H_2 -HI Mixtures

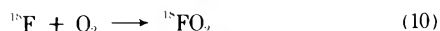
| SF_6 | Sample pressures, Torr | | | Observed yield, % $\text{C}_2\text{H}_3^{18}\text{F}$ |
|---------------|------------------------|------|--------------|--|
| | C_2H_2 | HI | N_2 | |
| 3790 | 80.2 | 40.4 | 81.3 | 74.5 |
| 3800 | 98.1 | 27.6 | 119 | 80.3 |
| 3800 | 56.9 | 28.5 | 117 | 76.3 |
| 3730 | 36.5 | 18.4 | 147 | 72.7 |
| 3800 | 20.8 | 10.8 | 168 | 75.0 |

form N_2^{18}F or from rapid decomposition of such a complex. Our experiments do not distinguish between these possibilities.

The dotted line on Figure 1 represents an upper limit on the reactivity of N_2 with ^{18}F , and corresponds to a value of k_9/k_1 of ≤ 0.002 .

The observation without difficulty of the expected amount of $\text{CH}_2=\text{CH}^{18}\text{F}$ also demonstrates that N_2 does not compete at all with HI in reactions with $\text{CH}=\text{CH}^{18}\text{F}$ radicals.

Competition between Molecular Oxygen and C_2H_4 . Several experiments involving competition between O_2 and C_2H_4 are summarized in Table III. The two competitions involved in these samples are (a) between reactions 3 and 10 for ^{18}F atoms; and (b) between O_2 and HI for $\text{C}_2\text{H}_4^{18}\text{F}$ radicals.



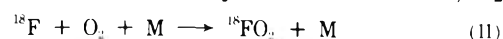
The data of 3800 Torr show a slow decrease in the yield of $\text{C}_2\text{H}_3^{18}\text{F}$ and a rapid decrease in the yield of $\text{C}_2\text{H}_5^{18}\text{F}$ with increasing concentration of O_2 (and decreasing C_2H_4 and HI). Consider the following hypothesis concerning the effect of an added molecule upon the reaction of ^{18}F with C_2H_4 : assume that the added molecule is completely inert toward reaction with ^{18}F . In this case, all ^{18}F atoms will react with C_2H_4 and HI whether or not the additive is present. However, if the additive is present and the mole fractions of C_2H_4 and HI have been correspondingly reduced, then the reacting ^{18}F atoms will have made on the average more inert collisions prior to reaction with C_2H_4 than in experiments without the additive. These extra collisions have no effect on thermal ^{18}F atom reactions, but they will reduce the probability of hot ^{18}F reactions with C_2H_4 . At an $(\text{SF}_6)/(\text{C}_2\text{H}_4 + \text{HI})$ ratio of 20, about 0.5%¹⁰ of the ^{18}F atoms react hot to form $\text{CH}_2=\text{CH}^{18}\text{F}$. With an inert moderator replacing 4/5 of the $(\text{C}_2\text{H}_4 + \text{HI})$, the ratio of $(\text{SF}_6)/(\text{C}_2\text{H}_4 + \text{HI})$ is now 100, and only about 0.1% of the ^{18}F atoms will form $\text{CH}_2=\text{CH}^{18}\text{F}$ by hot reaction. Consequently, if O_2 acts only as an inert moderator toward ^{18}F in the experiments of Table III, the yield of $\text{C}_2\text{H}_3^{18}\text{F}$ should diminish from about 1.6% with zero O_2 to 1.2% with $(\text{O}_2)/(\text{C}_2\text{H}_2) = 3$, in excellent agreement with the actual observations. An approximate cor-

rection for the hot yield of $\text{C}_2\text{H}_3^{18}\text{F}$ is made in the last two columns of Table III, and the final column indicates no effect of O_2 on the reaction of ^{18}F with C_2H_4 within the errors of measurement.

A similar analysis also holds for the experiments of Table III carried out at a lower pressure (1000 Torr). The correction for "hot" formation of $\text{CH}_2=\text{CH}^{18}\text{F}$ is dependent on the $(\text{SF}_6)/(\text{C}_2\text{H}_4)$ ratio, but not on total pressure, and the percentage yield of $\text{CH}_2=\text{CH}^{18}\text{F}$ is larger at lower pressure. The "hot" correction now represents a lesser fraction of the total $\text{CH}_2=\text{CH}^{18}\text{F}$ yield, and is similar for all four experiments. Again, there is no evidence for a decreasing yield of $\text{C}_2\text{H}_3^{18}\text{F}$ with increasing O_2 concentration.

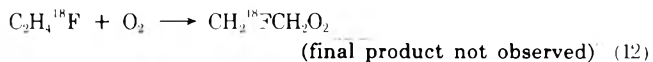
If, on the other hand, measurable quantities of ^{18}F atoms were permanently removed by reaction with O_2 to form $^{18}\text{FO}_2$, then the yield of $\text{C}_2\text{H}_4^{18}\text{F}^*$ (and therefore of $\text{C}_2\text{H}_3^{18}\text{F}$) would be correspondingly reduced. Since the final column of Table III shows no evidence for diminished yields of $\text{C}_2\text{H}_3^{18}\text{F}$ at high O_2 concentration, the conclusion must be drawn that the removal of ^{18}F by O_2 is negligible. From the 1000-Torr data of Table III, we estimate that the maximum ^{18}F removal can be no more than 0.10% (4.02-4.62% is actually -0.60%, and even +0.10% is a generous estimate) for a fourfold excess of O_2 vs. C_2H_4 , and therefore an upper limit on the relative rates of $k_{11}/k_3 \leq 0.006$ or $k_{11}/k_1 \leq 0.005$.

Since FO_2 is known to exist,¹¹ the third-order rate constant for reaction 11 is certainly not zero. However, O_2



will have an effect on the reactions of ^{18}F with C_2H_4 only if the ^{18}F atom becomes permanently bonded. The formation and reverse decomposition of $^{18}\text{FO}_2$ does not remove ^{18}F from the system, and any ^{18}F atoms released by $^{18}\text{FO}_2$ decomposition can still react with C_2H_4 to form $\text{C}_2\text{H}_4^{18}\text{F}^*$.

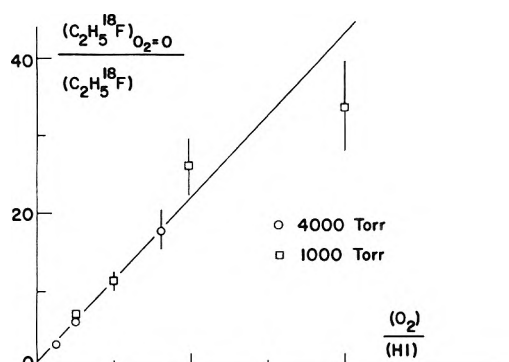
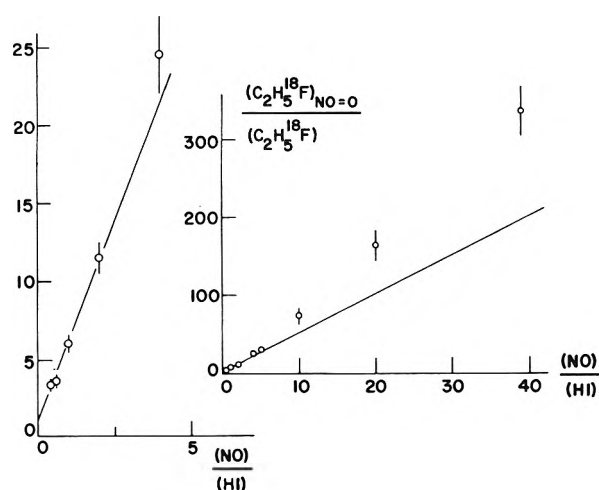
If O_2 is assumed to be effectively inert toward removing thermal ^{18}F , then the initial yield of $\text{C}_2\text{H}_4^{18}\text{F}^*$ is still about 60% and almost all of these radicals will be collisionally stabilized at 4000-Torr pressure. In this case, the second competition now must be considered: the stabilized $\text{C}_2\text{H}_4^{18}\text{F}$ radicals can now undergo either reaction 7 with HI to form $\text{C}_2\text{H}_5^{18}\text{F}$, or reaction 12 with O_2 to form



eventually some oxygenated species not detectable with our present chromatographic analysis. The sum of the yields of reactions 7 and 12 will be a constant, and the ratio of these yields will be given by equation 13, with the O_2 concentrations carried as subscripts. Equations 12 and 13 can also be written in general form for any scavenger molecule S. The data of Table III are graphed in Figure 2

TABLE III: Effect of O₂ upon Absolute Yields of C₂H₃¹⁸F and C₂H₅¹⁸F from ¹⁸F Reactions with C₂H₄ in SF₆-C₂H₄-O₂-HI Mixtures

| SF ₆ | Sample pressures, Torr | | | Observed yields, % | | Correction for hot yield of C ₂ H ₃ ¹⁸ F (est hot yield) | Thermal yield, corrected |
|-------------------|-------------------------------|------|----------------|---|---|---|--------------------------|
| | C ₂ H ₄ | HI | O ₂ | C ₂ H ₃ ¹⁸ F | C ₂ H ₅ ¹⁸ F | | |
| 3800 ^a | 166 | 33.4 | 0 | 1.65 | 57.3 | 0.54 ± 0.18 | 1.11 ± 0.18 |
| 3810 ^a | 167 | 33.3 | 0 | 1.52 | 60.1 | 0.54 ± 0.18 | 0.98 ± 0.18 |
| 3780 | 118 | 23.2 | 59.3 | 1.37 | 18.5 | 0.38 ± 0.13 | 0.99 ± 0.13 |
| 3750 | 90.3 | 17.9 | 91.1 | 1.20 | 9.5 | 0.30 ± 0.10 | 0.90 ± 0.10 |
| 3750 | 47.8 | 8.9 | 143 | 1.15 | 3.3 | 0.16 ± 0.05 | 0.99 ± 0.05 |
| 927 | 46.4 | 4.7 | 23.5 | 4.62 | 7.93 | 0.60 ± 0.20 | 4.02 ± 0.20 |
| 907 | 45.3 | 4.6 | 45.3 | 4.57 | 4.83 | 0.59 ± 0.20 | 3.98 ± 0.20 |
| 865 | 43.2 | 4.4 | 86.7 | 4.77 | 2.13 | 0.56 ± 0.19 | 4.21 ± 0.19 |
| 796 | 40.0 | 4.0 | 159 | 5.14 | 1.65 | 0.52 ± 0.17 | 4.62 ± 0.17 |

^a From Table I.**Figure 2.** Competition of HI with O₂ for CH₂¹⁸FCH₂ radicals: total pressures (Torr) O, 4000; □, 1000.**Figure 3.** Competition of HI with NO for CH₂¹⁸FCH₂ radicals.**TABLE IV: Absolute Yields of C₂H₃¹⁸F and C₂H₅¹⁸F from ¹⁸F Reactions in SF₆-C₂H₄-NO-HI Mixtures**

| SF ₆ | Sample pressures, Torr | | | Observed yields, % | |
|-----------------|-------------------------------|------|------|--|---|
| | C ₂ H ₄ | HI | NO | C ₂ H ₃ ¹⁸ F ^a | C ₂ H ₅ ¹⁸ F |
| 2760 | 151 | 15.3 | 75.6 | 1.87 | 2.05 |
| 2690 | 150 | 15.1 | 150 | 1.89 | 0.82 |
| 2530 | 150 | 15.1 | 300 | 1.99 | 0.37 |
| 2240 | 150 | 15.3 | 595 | 2.14 | 0.18 |
| 2830 | 151 | 15.2 | 7.5 | 1.96 | 17.7 |
| 2830 | 152 | 15.0 | 7.9 | 2.02 | 17.2 |
| 2820 | 150 | 15.0 | 15.0 | 2.03 | 10.1 |
| 2810 | 150 | 15.1 | 30.2 | 2.13 | 5.23 |
| 2780 | 151 | 15.1 | 60.1 | 2.06 | 2.46 |

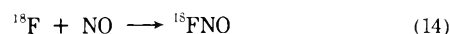
^a Estimated correction for hot C₂H₃¹⁸F: 0.65% in each case.

according to eq 13, and exhibit a reasonable straight line with a slope of 1.05 ± 0.10 . The two sets of data at 4000 and 1000 Torr are in excellent agreement. Therefore, the relative efficiencies of O₂ and HI for reacting with thermalized C₂H₄¹⁸F radicals are in the ratio 1.05 ± 0.10 .

$$\frac{(C_2H_5^{18}F)_{O_2=0}}{(C_2H_5^{18}F)_{O_2=x}} = \frac{\text{yield of (12)} + (C_2H_5^{18}F)_x}{(C_2H_5^{18}F)_x} = \frac{k_{12}(O_2) + k_7(HI)}{k_7(HI)} = 1 + \frac{k_{12}(O_2)}{k_7(HI)} \quad (13)$$

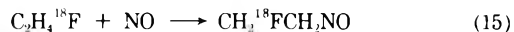
Competition between NO and C₂H₄. The absolute yields of C₂H₃¹⁸F and C₂H₅¹⁸F from a series of SF₆-C₂H₄-NO-HI mixtures are summarized in Table IV. In these experiments, the total pressure has been maintained essentially constant at 3000 Torr, and the C₂H₃¹⁸F yield is observed to be constant within the error limits. Correction for the

“hot” yield of C₂H₃¹⁸F can be made here, as with O₂ above, but the correction is the same for all nine samples and does not affect the basic conclusion: there is no evidence for removal of ¹⁸F atoms by reaction 14. From an



estimate of 0.10% for the maximum reduction in the yield of C₂H₃¹⁸F at high NO concentrations, we calculate that $k_{14}/k_1 \leq 0.01$. Again, FNO is well known,¹² but requires a third body for formation in the gas phase.

Even with (NO)/(HI) ratios < 1, the yield of C₂H₄¹⁸F has been substantially depleted through the reaction of the fluoroethyl radicals with NO, as in (15). The data are



expressed in the scavenger eq 13, with NO substituted for O₂, in Figure 3.¹³ The slope of the line in Figure 3 indicates that NO is five times as efficient a scavenger as HI for C₂H₄¹⁸F radicals. At high ratios of (NO)/(HI), the yields of C₂H₅¹⁸F fall below 1%, and are subject to substantial errors in measurement. The scavenger equation does not give a straight line for these concentrations, but shows progressive upward curvature in Figure 3. However, in the region in which appreciable yields of C₂H₅¹⁸F are still found (*i.e.*, (NO)/(HI) < 4), the data are satisfactorily fitted with the scavenger efficiency of NO as 5.0 ± 0.5 times that of HI.

Competition between SO₂ and C₂H₄. Experiments involving competition between SO₂ and C₂H₄ are less satis-

TABLE V: Absolute Yields of $\text{C}_2\text{H}_3^{18}\text{F}$ and $\text{C}_2\text{H}_5^{18}\text{F}$ from ^{18}F Reactions in $\text{SF}_6\text{-C}_2\text{H}_4\text{-SO}_2\text{-HI}$ Mixtures

| SF_6 | Sample pressures, Torr | | | Observed yields, % | | Correction for hot yield of $\text{C}_2\text{H}_3^{18}\text{F}$ (est hot yield) | Thermal yield, corrected |
|---------------|------------------------|------|---------------|-------------------------------------|-------------------------------------|---|--------------------------|
| | C_2H_4 | HI | SO_2 | $\text{C}_2\text{H}_3^{18}\text{F}$ | $\text{C}_2\text{H}_5^{18}\text{F}$ | | |
| 2780 | 140 | 14.2 | 69 | 2.02 | 19.2 | 0.61 | 1.41 |
| 2720 | 136 | 13.7 | 136 | 1.91 | 11.9 | 0.59 | 1.32 |
| 2600 | 130 | 13.1 | 260 | 1.91 | 6.97 | 0.56 | 1.35 |
| 2390 | 119 | 11.9 | 478 | 1.74 | 3.62 | 0.52 | 1.22 |

TABLE VI: Absolute Yields of $\text{C}_2\text{H}_3^{18}\text{F}$ and $\text{C}_2\text{H}_5^{18}\text{F}$ from ^{18}F Reactions in $\text{SF}_6\text{-C}_2\text{H}_4\text{-CO-HI}$ Mixtures

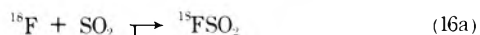
| SF_6 | Sample pressures, Torr | | | Observed yields, % | | Correction for hot yield of $\text{C}_2\text{H}_3^{18}\text{F}$ (est hot yield) | Thermal yield, corrected |
|---------------|------------------------|------|-------------|-------------------------------------|-------------------------------------|---|--------------------------|
| | C_2H_4 | HI | CO | $\text{C}_2\text{H}_3^{18}\text{F}$ | $\text{C}_2\text{H}_5^{18}\text{F}$ | | |
| 3300 | 166 | 34.1 | 519 | 1.69 | 55.1 | 0.54 | 1.15 |
| 2300 | 166 | 33.9 | 1580 | 1.76 | 48.3 | 0.53 | 1.23 |
| 3800 | 118 | 23.0 | 58.8 | 1.49 | 58.4 | 0.38 | 1.11 |
| 3800 | 118 | 23.2 | 59.6 | 1.43 | 62.5 | 0.38 | 1.05 |
| 3800 | 91.2 | 17.9 | 91.2 | 1.31 | 60.9 | 0.30 | 1.01 |
| 3810 | 90.3 | 17.9 | 91.2 | 1.39 | 59.5 | 0.30 | 1.09 |
| 3810 | 48.2 | 9.1 | 143 | 1.11 | 55.2 | 0.16 | 0.95 |
| 3790 | 47.3 | 9.1 | 142 | 1.21 | 57.4 | 0.15 | 1.06 |

factory than in all of the other systems for several reasons. First, SO_2 and HI react rapidly to form a complex $\text{SO}_2\cdot\text{HI}$. The concentration ratio for the formation of this complex has been measured as $(\text{SO}_2\cdot\text{HI})/(\text{HI}) = 0.37$ at 10° in excess SO_2 .¹⁴ Thus, in each of our samples, approximately 27% of all HI molecules are bound in the form of $\text{SO}_2\cdot\text{HI}$, and some assumptions must be made concerning the relative reactivity toward H abstraction of $\text{SO}_2\cdot\text{HI}$ and HI. In the calculations for Figure 4 we have assumed (without any experimental basis) that these two species furnish H atoms to radicals with equal efficiency. In the event that $\text{SO}_2\cdot\text{HI}$ will not furnish H atoms, this assumption would then entail a 27% error.

Second, the SO_2 samples are very sensitive to impurities (e.g., I_2) in the HI, and give poorer reproducibility from one series of runs to another, and sometimes within a series.

The yields of $\text{C}_2\text{H}_3^{18}\text{F}$ and $\text{C}_2\text{H}_5^{18}\text{F}$ from a series of $\text{SF}_6\text{-C}_2\text{H}_4\text{-SO}_2\text{-HI}$ mixtures are summarized in Table V. Other runs showed similar $\text{C}_2\text{H}_3^{18}\text{F}$ yields, but the $\text{C}_2\text{H}_5^{18}\text{F}$ yields were somewhat erratic, falling as much as a factor of 2 below the data of Table V.

The possible reactions of ^{18}F with SO_2 are given in eq 16. Although the reaction of macroscopic F atoms with



SO_2 (to form F_2SO_2 eventually) has been reported as "quite rapid,"¹⁵ the sum of the rate constants for all SO_2 reactions removing ^{18}F is much less than that for reaction of ^{18}F with C_2H_4 . The ratio of k_{16}/k_3 is estimated to be 0.04 ± 0.02 from the slight diminution of $\text{CH}_2=\text{CH}^{18}\text{F}$ yield with increasing SO_2 in Table V.

As with O_2 and NO , SO_2 markedly inhibits the reaction of $\text{C}_2\text{H}_4^{18}\text{F}$ radicals with HI. The corrected $\text{C}_2\text{H}_5^{18}\text{F}$ data are shown with open circles in Figure 4. A correction is applied for the diminished formation of $\text{C}_2\text{H}_4^{18}\text{F}^*$ through reaction 16, using the data on $\text{C}_2\text{H}_3^{18}\text{F}$, itself corrected for hot reaction. The relative rates of k_{17}/k_7 can be calculated from the corrected data as 0.35 ± 0.05 . If our assumption were incorrect that free HI and $\text{SO}_2\cdot\text{HI}$ have equal collision probabilities for furnishing an H atom to the $\text{CH}_2^{18}\text{FCH}_2$ radical, then this ratio would be incorrect by

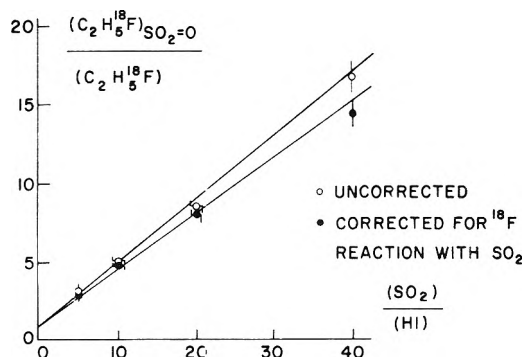


Figure 4. Competition of HI with SO_2 for $\text{CH}_2^{18}\text{FCH}_2$ radicals: \circ , uncorrected data; \bullet , data corrected for thermal ^{18}F reaction with SO_2 .

as much as 27%. For this reason, coupled with the scatter in other runs not listed in Table V, we estimate that $k_{17}/k_7 = 0.33 \pm 0.10$.



The scavenger efficiencies of SO_2 and O_2 have been shown to be more or less equivalent for CH_3 radicals,^{16,17} and for the radicals formed during recoil tritium reactions with cyclohexene.¹⁸ On the other hand, the relative reactivity of SO_2 for C_2H_5 radicals is indicated as only about 0.01 times that of O_2 for C_2H_5 . Our results with $\text{CH}_2^{18}\text{FCH}_2$ radicals give a value quite similar to the factor of 3 found for O_2 vs. SO_2 in reacting with CH_3 .¹⁹

Competition between CO and C_2H_4 or C_2H_2 . The yields of $\text{C}_2\text{H}_3^{18}\text{F}$ and $\text{C}_2\text{H}_5^{18}\text{F}$ from $\text{SF}_6\text{-C}_2\text{H}_4\text{-CO-HI}$ mixtures are summarized in Table VI. The possible reaction of ^{18}F with CO is given by eq 18, since abstraction of either O or



C would be highly endothermic. Again, the species FCO has been reported in spectroscopic experiments.²⁰ The yields of $\text{C}_2\text{H}_3^{18}\text{F}$, after correction for the hot yield, show no tendency to decrease with increasing CO concentration. The tendency toward slight increases in $\text{C}_2\text{H}_3^{18}\text{F}$ yield for very high CO concentrations presumably reflects a somewhat lower efficiency of CO vs. SF_6 for stabilization of $\text{C}_2\text{H}_4^{18}\text{F}^*$ radicals formed by addition of thermal

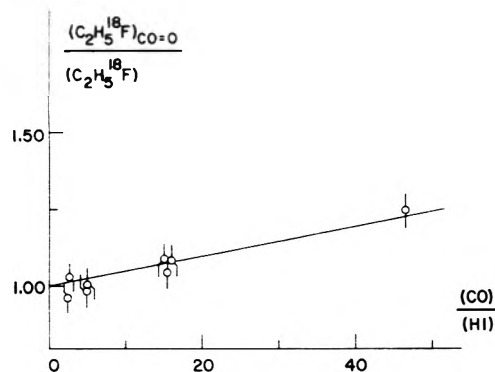


Figure 5. Competition of HI with CO for $\text{CH}_2^{18}\text{FCH}_2$ radicals.

TABLE VII: Absolute Yield of $\text{C}_2\text{H}_5^{18}\text{F}$ from ^{18}F Reactions with C_2H_2 in $\text{SF}_6\text{-C}_2\text{H}_2\text{-CO-HI}$

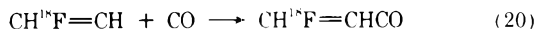
| SF ₆ | Sample pressures, Torr | | | Observed yields, % C ₂ H ₅ ¹⁸ F |
|-----------------|-------------------------------|------|-----|--|
| | C ₂ H ₂ | HI | CO | |
| 3440 | 15.2 | 7.6 | 150 | 53.5 |
| 1660 | 7.3 | 3.7 | 72 | 53.4 |
| 3000 | 40.7 | 20.3 | 82 | 71.9 |
| 2990 | 26.4 | 15.1 | 104 | 67.3 |
| 3000 | 18.8 | 10.5 | 115 | 61.6 |
| 2995 | 13.5 | 6.7 | 126 | 53.4 |

^{18}F . This lower efficiency would permit a fractional decomposition equivalent to a lower pressure of pure SF_6 . We estimate that the ratio of rate constants for $k_{18}/k_3 < 0.01$.

In this system, too, the observed yield of $\text{C}_2\text{H}_5^{18}\text{F}$ is diminished by increasing CO concentrations, although the effect is much less marked than with O_2 , NO , and SO_2 . The interfering reaction is presumably the simple addition to CO, as given in (19), and the data are shown in Figure 5. From the slope of the line in Figure 5, we estimate the relative rates of k_{19}/k_7 as 0.005 ± 0.002 .



The yields of $\text{C}_2\text{H}_5^{18}\text{F}$ from $\text{SF}_6\text{-C}_2\text{H}_2\text{-CO-HI}$ mixtures are less than from CO-free experiments, as shown in Table VII. Since ^{18}F has been shown not to react with CO in the C_2H_4 experiments of Table VI, the diminished yields of $\text{C}_2\text{H}_5^{18}\text{F}$ are attributed to the interception of $\text{CH}^{18}\text{F}=\text{CH}$ radicals by CO, as in (20). These data have



been shown in Figure 1, together with the N_2 data. The slope of the CO line in Figure 1 indicates that k_{20}/k_2 is approximately 0.022 ± 0.005 .

Carbon monoxide has not normally been thought of as a radical scavenger, and indeed it has a much lower efficiency for these radicals than HI, O_2 , NO , or SO_2 . However, our values for CO efficiency are considerably higher than the 10^{-5} calculated for CO vs. O_2 in scavenging CH_3 radicals.²¹ In the absence of more efficient scavenger molecules, CO can be expected to remove free radicals at an appreciable rate.

Fates of Scavenged Radicals. We have measured the disappearance of $\text{CH}_2^{18}\text{FCH}_2$ and $\text{CH}^{18}\text{F}=\text{CH}$ radicals through reaction with several different species, but have actually observed the products only in the reactions with HI to form the corresponding molecules $\text{C}_2\text{H}_5^{18}\text{F}$ and $\text{CH}_2=\text{CH}^{18}\text{F}$. None of the radical-scavenger adducts (e.g.,

TABLE VIII: Relative Scavenger Efficiencies for Removal of Radicals

| Radical | Scavenger | Relative efficiency |
|------------------------------------|---------------|---------------------|
| $\text{CH}_2^{18}\text{FCH}_2$ | HI | (1.0) |
| | NO | 5.0 ± 0.5 |
| | O_2 | 1.05 ± 0.10 |
| | SO_2 | 0.33 ± 0.10 |
| | CO | 0.005 ± 0.002 |
| $\text{CH}^{18}\text{F}=\text{CH}$ | HI | (1.0) |
| | CO | 0.022 ± 0.007 |
| | N_2 | < 0.003 |

Relative Rates of Removal of ^{18}F by Reaction at 4000 Torr

| | |
|------------------------|-----------------|
| C_2H_2 | (1.0) |
| C_2H_4 | 0.83 ± 0.02 |
| SO_2 | 0.04 ± 0.02 |
| O_2 | < 0.005 |
| NO | < 0.01 |
| CO | < 0.01 |
| N_2 | < 0.002 |

$\text{CH}_2^{18}\text{FCH}_2\text{O}_2$, $\text{CH}^{18}\text{F}=\text{CHCO}$, etc.) have been characterized in other systems, but all should have reasonable chemical stability once formed. In our analytical system, no volatile product would have been observed from the radio gas chromatographic columns in the available time period, even if the scavenged radical had done nothing more complex than react with HI, e.g., to form $\text{CH}_2\text{FCH}_2\text{OOH}$ or $\text{CH}^{18}\text{F}=\text{CHCHO}$.

We, of course, have no information about the structure of any of these radical-scavenger species, and do not know if the radicals are bonded to the O atoms of NO or SO_2 , or to the N or S atoms, respectively. In the cases of O_2 , NO , and SO_2 the fraction of ^{18}F radioactivity being diverted into these complex radical species is quite substantial, frequently accounting for more than 50% of all of the ^{18}F atoms. Under these circumstances, other kinds of tracer analyses have an excellent chance of success in searching for the missing ^{18}F products.

Summary

The relative rates of reaction of ^{18}F , $\text{CH}_2^{18}\text{FCH}_2$, and $\text{CH}^{18}\text{F}=\text{CH}$ with the various species are summarized in Table VIII.

References and Notes

- (1) This research was supported by AEC Contract No. AT(04-3)-34, Agreement No. 126.
- (2) T. Smail and F. S. Rowland, *J. Phys. Chem.*, **74**, 1866 (1970).
- (3) T. Smail, G. Miller, and F. S. Rowland, *J. Phys. Chem.*, **74**, 3464 (1970).
- (4) R. L. Williams and F. S. Rowland, *J. Phys. Chem.*, **75**, 2709 (1971).
- (5) R. L. Williams and F. S. Rowland, *J. Phys. Chem.*, **77**, 301 (1973).
- (6) R. L. Williams and F. S. Rowland, *J. Phys. Chem.*, **76**, 3509 (1972).
- (7) R. L. Williams and F. S. Rowland, *J. Amer. Chem. Soc.*, **95**, 1047 (1972).
- (8) N. Colebourne, J. F. J. Todd, and R. Wolfgang, "Chemical Effects of Nuclear Transformations," Vol. 1, International Atomic Energy Agency, Vienna, 1965, p. 149.
- (9) J. F. J. Todd, N. Colebourne, and R. Wolfgang, *J. Phys. Chem.*, **71**, 2875 (1967).
- (10) Straight-line graphs of D/S (i.e., $\text{C}_2\text{H}_5^{18}\text{F}/\text{C}_2\text{H}_5^{18}\text{F}$) vs. $1/P$ for C_2H_4 in 95% SF_6 show a nonzero intercept of about 0.009 ± 0.003 , indicating that, of the approximately 60% yields (59.0 and 61.6% in the two experiments of Table I) attributed to π bond reaction of ^{18}F with C_2H_4 , about 0.5% was formed in reactions initiated by hot ^{18}F atoms.
- (11) V. I. Vedeneev, Yu. M. Gershenson, A. P. Dement'ev, A. B. Nalbandyan, and O. M. Sarkisov, *Izv. Akad. Nauk. SSSR, Ser. Khim.*, 1438 (1970).
- (12) R. Schmutzler, *Angew. Chem., Int. Ed. Engl.*, **7**, 440, 455 (1968).
- (13) These NO-scavenged experiments were carried out with (HI)/(C_2H_4) ratio of 0.1, rather than the 0.2 used with O_2 . From the relative rates of reaction of ^{18}F with C_2H_4 , C_2H_2 , and HI, we estimate that a yield of 60.4% at (HI)/(C_2H_4) = 0.1 is equivalent to 58.7% at a ratio of 0.2.

- (14) S. Witekowa and T. Witek, *Rocz. Chem.*, **31**, 437 (1957).
 (15) G. Schatz and M. Kaufman, *J. Phys. Chem.*, **76**, 3586 (1972).
 (16) A. Good and J. C. J. Thynne, *Trans. Faraday Soc.*, **63**, 2708 (1967).
 (17) F. C. James, J. A. Kerr, and J. P. Simons, 11th International Symposium on Free Radicals, Berchtesgaden-Konigsee, Germany, Sept 1973.
 (18) D. C. Fee, S. S. Markowitz, and J. K. Garland, *Radiochim. Acta*, **17**, 135 (1972).
 (19) A. Good and J. C. J. Thynne, *Trans. Faraday Soc.*, **63**, 2720 (1967).
 (20) D. E. Milligan, M. E. Jacox, A. M. Bass, J. J. Cornford, and D. E. Mann, *J. Chem. Phys.*, **42**, 3187 (1965).
 (21) J. A. Kerr and J. G. Calvert, *J. Phys. Chem.*, **69**, 1022 (1965).

Fall-Off Behavior of a Thermal Unimolecular System in the Presence of a Weak Collider Inert Bath Gas¹

F. M. Wang and B. S. Rabinovitch*

Department of Chemistry, University of Washington, Seattle, Washington 98195 (Received December 17, 1973)

Publication costs assisted by the National Science Foundation

The behavior of the thermal unimolecular methyl isocyanide isomerization system has been examined at 245° over the whole range of fall-off from the low to high pressure regions at infinite dilution by the weak collider, helium, and by the strong collider, butane. The pressure displacement factor for the helium fall-off curve relative to the behavior of the pure substrate increases with decreasing order of reaction, as predicted. A comparison with theoretical calculations indicates that the collisional behavior of helium is intermediate between exponential and step ladder models for the collisional transition probability distribution function although the behavior seems closer to the latter, in disagreement with earlier work. The average amount of energy transferred per collision is $\langle \Delta E \rangle_{ST} = 350 \text{ cm}^{-1}$ for helium in this system.

Introduction

The collisional efficiency of an inert bath gas in a given thermal unimolecular gas-phase system is a function of the temperature, the degree of dilution of substrate by bath gas, and the region of fall-off in question.² For the methyl isocyanide isomerization system, the effect of dilution of inert gases has been examined experimentally in the limiting low-pressure region.³ The dependence of efficiency on temperature has also been investigated with helium bath gas.⁴ No systematic study has ever been made of the variation of the collisional efficiency with the order of reaction, *i.e.*, with the degree of fall-off. That is to say, no comprehensive example exists of unimolecular fall-off in the presence of an inert gas.

Buff and Wilson⁵ have given a general discussion of fall-off behavior for weak colliders; they employed a highly simplified collisional transition probability model in a practical example. Tardy and Rabinovitch⁶ have made a stochastic treatment of the inert bath collisional efficiency for various assumed forms of the transition probability distribution function and for various average energy transfer amounts or step sizes. They have predicted quantitatively the extent to which a weak collider shifts the fall-off behavior to higher collision rates and broadens the range of collision rates over which the reaction order changes; the displacement factor increases with increasing collision rate and with decreasing average step size. This comparison has been documented semiquantitatively in an earlier note,⁷ for the case of several medium-efficiency inert bath gases; the agreement with the theoretical prediction was

qualitatively correct for the limited data over a narrow range of fall-off ($k/k_\infty = 0.3-1$).

In the present paper, a systematic examination of the variation of relative collisional efficiency with fall-off region has been made for helium as the inert gas in the thermal methyl isocyanide isomerization system. It was anticipated that helium, being the weakest collider, would provide the most accessible and strongest test of the variation. Because it was desired to cover a very wide range of fall-off, the present study was carried out at 245° rather than at 280°, at which temperature most studies of the vibrational energy transfer in the low-pressure regime of this system have previously been made.⁸ Since the strong collider fall-off of the parent substrate had been studied at temperatures other than 245°, and most completely at 230°,⁹ it was necessary to convert the fall-off behavior from that temperature to 245° with use of the known pressure-dependent Arrhenius parameters. In order to strengthen the comparison of the helium behavior with the strong collider reference, the fall-off behavior in the presence of butane, which has previously been shown to display unit collisional efficiency,^{10,11} was also examined over a fairly wide range of fall-off at 245°.

Experimental Section

The preparation and purification of methyl isocyanide have been described.^{7,12} After purification, no impurity was detectable by gas chromatography. Matheson butane contained a small amount of methane and was purified by the freeze-pump-melt method. Assayed reagent grade of

helium from the Air Reduction Co. was used without further purification. All condensible reactants were degassed prior to each run.

A static method was employed for the kinetic runs. The reaction vessel was immersed in a molten $\text{KNO}_3\text{-NaNO}_2$ salt bath maintained close to 245° with a proportional controller. The temperature gradient over the bath was $\pm 0.2^\circ$ and invariant during a run. Over the entire series of runs, temperature between 244.5 and 246° were used. All rate constants were corrected to a temperature of 245° with use of the known activation energies at the pressure of the run, as given in ref 9.

A series of spherical Pyrex reaction vessels which ranged in volume from 8 ml to 12 l were used.

Each reactor was initially seasoned with methyl isocyanide and acetonitrile and reseasoned whenever the vessel had been opened to air. A conventional vacuum apparatus served for gas handling, storage, and measurements. Inert gases were measured in a standard volume and were then expanded into the reactor together with a known amount of isocyanide.

Runs made in different vessels were checked for consistency by coverage of overlapping pressure regions. In the lower pressure region, approximately 4.0×10^{-6} mol of methyl isocyanide (~ 0.01 Torr) was used in each run; an amount of $\sim 1.0 \times 10^{-6}$ mol of substrate ($\sim 0.30\text{-}8$ Torr) was used in higher pressure runs. In all cases, 12% of propionitrile was added to the isocyanide as an internal analytical standard. Dilution ratios of helium/methyl isocyanide varied from 60- to 2000-fold excess over the parent substrate, except in two cases where the ratio was no less than 30-fold. Isomerization was carried to 5-65% conversion. Products of reaction were passed through a silver cyanide column to remove the residual methyl isocyanide. The helium and the bulk of the butane were pumped away prior analysis. A 15 ft \times $\frac{3}{16}$ in. column of tricresylphosphate on Chromosorb W was used for analysis. "Simple" calibrations with standard mixtures which were admitted directly to the chromatograph were made from run to run. For butane and higher pressure helium runs, "pragmatic" calibrations with standard mixtures were made which imitated the run procedures. Product analysis based on the internal propionitrile standard agreed within a few per cent with values computed on an absolute basis; averaged values from these two methods were used in rate constant calculations.

Results

Several correction factors were considered in the treatment of the data. A dead space correction ranged from 0.5 to 2%, depending on the vessel. Heterogeneity was negligible at all pressures in the present study. A time correction for the pumping down of helium runs in the lower pressure fall-off region was less than 4%. Self-heating is negligible at all pressures. A dilution ratio of 60:1 or over may be considered to correspond to infinite dilution for helium, according to the earlier work of Lin.^{3,8}

In the helium study, at higher pressures pragmatic calibrations were used to evaluate the rate constants; simple calibrations could be employed in the lower pressure region, where both calibration methods gave the same results. For butane runs, pragmatic calibrations were found to be essential.

The fall-off of the isomerization of methyl isocyanide in the presence of helium at 245° is illustrated in Figure 1. Also shown is the fall-off curve for parent substrate; these

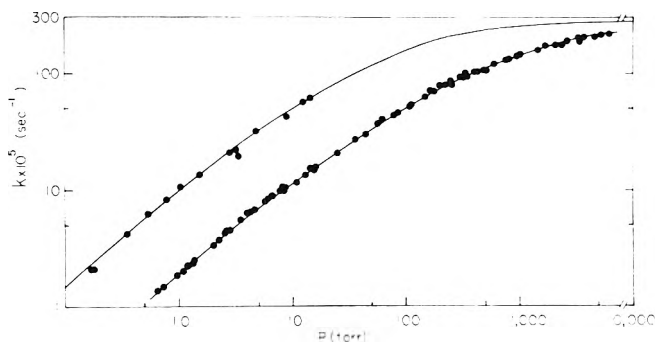


Figure 1. Pressure dependence of unimolecular rate constants at 245° for CH_3NC with (a) C_4H_8 at infinite dilution (circles) and pure substrate (upper solid curve); (b) He at infinite dilution; the lower solid curve connects the experimental points. The pure substrate curve is transposed from SR work at 230° .

data were read directly from the Schneider and Rabinovitch 230° curve (Figure 1, ref 9), and were then brought to 245° by applying the appropriate energy of activation⁹ at each pressure.

A few runs were carried out with the pure parent substrate at 245° in the limiting low-pressure region ($\sim 10^{-2}$ Torr). The data points (not shown) fell right on the transposed SR curve. Experiments were also done with butane as the inert bath collider. To facilitate the comparison in Figure 1a, butane pressures were converted to equivalent pressures of CH_3NC with use of the parameters given in Table I. Detailed rate constants are given in the Ph.D. thesis of Wang (ref 1).

Relative collision efficiencies on a collision-per-collision basis, β_ω , and on a pressure basis, β_p , are correlated through the equation

$$\beta_\omega = \beta_p (\mu_{AM}/\mu_{AA})^{1/2} (s_{AA}/s_{AM})^2$$

where μ_{AM} and s_{AM} are the reduced mass and the effective collision diameter of the collision pair. The excellent agreement between butane and substrate curves allows use of the transposed SR substrate curve with good confidence.

The relative collisional efficiency of an inert gas, at infinite dilution of substrate by inert, is defined⁶ as the ratio of the collision rate in the pure parent substrate (A) system relative to the collision rate due to an inert gas (M) required to produce the same specific reaction rate constant

$$\bar{\beta}_\omega(\infty) = \omega(A)/\omega(M) \quad k(A) = k(M)$$

where the ω subscript refers to a particular collision rate in the pure substrate system, and (∞) refers to infinite dilution of substrate by weak collider M; the bar refers to the "integral" quantities defined in ref 2 and obtained by comparison of k values rather than of differential changes, Δk . Since the comparison is made for $k(A) = k(M)$, obviously $\bar{\beta}_\omega(\infty)$ is a comparison at a fixed measure of fall-off, expressed as k/k_∞ . The pressure p and specific collision rate ω are interchangeable through the correlation factors cited in Table I. The pressure displacement factor is just the reciprocal of the integral quantity $\bar{\beta}_\omega(\infty)$. The relative collisional efficiencies of helium at different positions of fall-off were readily obtained from the smoothed data of Figure 1. Results are tabulated in Table II. A value of $\bar{\beta}_\omega(\infty)$ was not measured above $k/k_\infty = 0.775$ because experimental error rises rapidly in comparing the pressure displacement between curves which asymptoti-

TABLE I: Some Parameters for Correlation of β_p and β_ω at 245°

| | $\sigma_M, \text{Å}$ | $\epsilon_M/k, \text{°K}$ | $\Omega_{AM}^{(2,2)*}$ | $s_{AM}, \text{Å}$ | $(\mu_{AM}/\mu_{AA})^{1/2}$ | $(s_{AA}/s_{AM})^2$ | β_p/β_ω |
|----------------------------------|----------------------|---------------------------|------------------------|--------------------|-----------------------------|---------------------|------------------------|
| CH ₃ NC | 4.47 | 380 | 1.80 | 5.99 | 1.00 | 1.00 | 1.00 |
| n-C ₄ H ₁₀ | 5.23 | 325 | 1.32 | 5.57 | 1.08 | 1.16 | 0.80 |
| He | 2.58 | 10.2 | 0.85 | 3.24 | 0.422 | 3.42 | 0.69 |

^a Values as used earlier in ref 8.

cally approach $k/k_\infty = 1$. The estimated error in this comparison at the highest fall-off value was 4%.

The pressure displacement method for determining $\bar{\beta}_\omega(\infty)$ should give the same result in the low-pressure region ($\omega \rightarrow 0$) as the conventional slopes method used in the earlier work.¹² Indeed, when slopes of rate constants plotted against pressure in the second-order region (not shown) were intercompared between helium and pure substrate, an almost identical value of $\beta_0(\infty)$ (within 0.8%) was obtained. The low-pressure value ($k/k_\infty = 0.005$) of $\beta_p = 0.14$ obtained from Figure 1 corresponds to a value of $\bar{\beta}_0(\infty) = 0.203$. The value reported earlier⁸ was $\bar{\beta}_0(\infty) = 0.25$, after conversion to 245° from 280.5° by the appropriate factor.⁴ The main contribution to the discrepancy, such as it is, comes from the different values of the substrate activation rate constants k_a^A used in evaluating β_p . If the low-pressure values of Chan, *et al.*,⁸ are used here, instead of the transposed SR curve, the present work with helium gives $\bar{\beta}_0(\infty) = 0.23$, which is in excellent agreement with the earlier result. In this paper the complete fall-off data of SR have been adopted, rather than those of Chan, *et al.*, which apply only to the low-pressure region, since it is the whole fall-off range in which we are interested.

Discussion

It has been shown by Tardy and Rabinovitch that the thermal unimolecular collisional efficiency in the second-order region at infinite dilution, $\bar{\beta}_0(\infty)$, is uniquely determined by a reduced energy parameter, E' , for a specific collisional transition probability model. The parameter E' is defined as $E' = \langle \Delta E \rangle / \langle E^+ \rangle$, where $\langle \Delta E \rangle$ is the average size of the energy amount removed from the hot molecule in down steps, and $\langle E^+ \rangle$ is the average excess energy above threshold at thermodynamic equilibrium.

The extremes of collision transition probability models examined were an exponential (EXP) and a step ladder δ function (SL) distribution of down jumps.

On referring to the universal curve, Figure 7(I) of ref 2, the value of $\bar{\beta}_0(\infty) = 0.20$ is found to correspond to a value of $E' = 0.90$ for an EXP model, and $E' = 0.80$ for an SL model. The value of $\langle E^+ \rangle$ for methyl isocyanide at 245° has been calculated^{4,6} to be 440 cm⁻¹. Hence, the energy removed by helium per collision is, in round numbers, 400 and 350 cm⁻¹ for the EXP and SL models, respectively.

As k/k_∞ increases toward unity, the pressure displacement factor increases as $\bar{\beta}_\omega(\infty)$ decreases. This is due to the fact that the average energy of the reacting species at high pressures is greater than that at low pressures. For a given substrate system, Tardy and Rabinovitch have predicted the shape of the fall-off, and thus the theoretical variation of $\bar{\beta}_\omega(\infty)$ with pressure, for various transition probability distribution models, and given mean step size, degree of dilution, and temperature. Thus, from the possible experimental values of $\langle \Delta E \rangle$ and from the observed fall-off behavior for helium under the specified experimental conditions, the particular model of collision tran-

sition probabilities that affords the best agreement between theory and experiment can be deduced, in principle.

The general expression for the rate of reaction in a thermally activated system can be expressed as a sum over energy states

$$\text{rate} = \sum_i (KN_2^s)_i$$

where the superscript *s* stands for the steady-state population, and

$$\mathbf{N}^s = \begin{bmatrix} N_1^s \\ N_2^s \end{bmatrix}$$

the population vector \mathbf{N}^s is partitioned at the reaction threshold energy, E_0 . The rate constant matrix is diagonal

$$\mathbf{K} = \begin{bmatrix} 0 & 0 \\ 0 & k \end{bmatrix}$$

The general expression assumes two limiting forms. First, in the second-order region, $k_i \gg \omega$, for all, *i*; the reaction rate is determined essentially by the activation rate

$$\text{rate} = \sum_i (P_3 N_1^s)_i; \quad \omega \rightarrow 0$$

where the transition probability matrix \mathbf{P} is partitioned at E_0 as

$$\mathbf{P} = \begin{bmatrix} P_1 & P_2 \\ P_3 & P_4 \end{bmatrix}$$

here P_3 represents up-transitions from below, to levels above E_0 .

The second limiting form is assumed in the high-pressure limit. The steady-state population vector \mathbf{N}_1^s below E_0 takes the equilibrium value \mathbf{N}_1^e for a strong collider at any pressure; both \mathbf{N}_1^s and \mathbf{N}_2^s take on the equilibrium form for weak, as well as strong colliders as $\omega \rightarrow \infty$. At the high-pressure limit, the operational test is that $\omega \gg k_i$, for all *i*. Then

$$\text{rate} = \sum_i (KN_2^e)_i; \quad \omega \rightarrow \infty$$

The relative collisional efficiency $\bar{\beta}_\omega(\infty)$ defined earlier can now be expressed as

$$\bar{\beta}_\omega(\infty) = \omega(A)/\omega(M); \quad \sum_i [K(N_2^s)^{sc}]_i = \sum_i [K(N_2^s)^{wc}]_i$$

where the strong collider (sc) superscript refers to the parent substrate A, and the weak collider (wc) designation refers to the inert gas M. In view of the fact that the steady-state populations for a strong collider are larger than those for a weak collider, the relative collisional efficiency is interpreted operationally as the relative increase in collision number necessary to compensate for the less efficient transitions induced by weak colliders, so as to maintain the overall rate constant for the weak collider equal to that for the strong collider.

TABLE II: Measured and Theoretical Values of Collisional Efficiency for He at Various k/k_∞ (245°)

| k/k_∞ | $\bar{\beta}_\omega(\infty)$ | | | | | | | | $\bar{\beta}_{0.005}/\bar{\beta}_{0.775}$ | $\bar{\beta}_0/\bar{\beta}_{1.0}$ |
|------------------|------------------------------|-------|-------|-------|-------|-------|-------|-------|---|-----------------------------------|
| | 0 | 0.005 | 0.01 | 0.05 | 0.10 | 0.50 | 0.775 | 1.0 | | |
| Exptl | (0.203) ^a | 0.199 | 0.194 | 0.170 | 0.154 | 0.112 | 0.096 | | 2.08 | |
| EXP ^b | 0.198 | 0.196 | 0.195 | 0.178 | 0.168 | 0.141 | 0.133 | 0.128 | 1.47 | 1.55 |
| SL ^c | 0.2000 | 0.196 | 0.190 | 0.163 | 0.149 | 0.108 | 0.092 | 0.084 | 2.13 | 2.38 |

^a Extrapolated value. ^b $\langle \Delta E \rangle = 400 \text{ cm}^{-1}$; $E' = 0.90$. ^c $\langle \Delta E \rangle = 350 \text{ cm}^{-1}$; $E' = 0.80$.

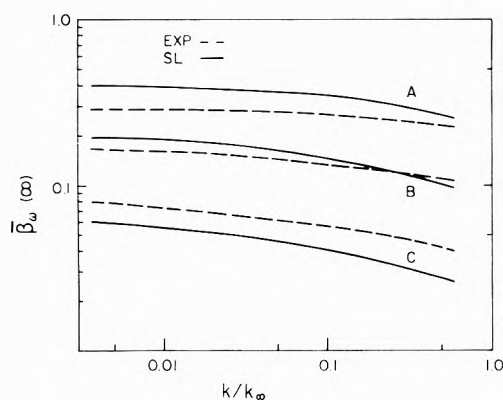


Figure 2. Plots of $\bar{\beta}_\omega(\infty)$ vs. k/k_∞ for CH_3NC at 245° with mean step sizes of (a) 560, (b) 340, and (c) 170 cm^{-1} on EXP (cashed line) and SL (solid) models.

The calculated behavior of $\bar{\beta}_\omega(\infty)$ as a function of the degree of fall-off is exhibited in Figure 2 for both the SL and EXP models at three different step sizes. The calculations were made for the CH_3NC system at 518°K .

For high values of $\langle \Delta E \rangle$, *i.e.*, for $E' > 1$, it has been established⁶ that in the second-order region the number of molecules transported above the critical threshold E_0 on the basis of an SL model of collisional transition probabilities is greater than the transport provided by an EXP model. At sufficiently large values of $\langle \Delta E \rangle$, the steady-state population vector \mathbf{N}_1^e below E_0 approaches the equilibrium \mathbf{N}_1^e for both models, and all the more as k/k_∞ increases toward unity.^{2,6} But the EXP model is less efficient in pumping molecules above E_0 due to the fact that the exponential distribution has a head which corresponds to high probability for small jumps of size much less than $\langle \Delta E \rangle$. On the other hand, for a given initial value of E' , the long tail of the EXP distribution, which gives finite probability for long jumps of size greater than $\langle \Delta E \rangle$, becomes more important as the average energy of reacting molecules $\langle E_r^+ \rangle$ increases ($\langle E_r^+ \rangle_{\omega=0} = 1.27 \text{ kcal mol}^{-1}$ and $\langle E_r^+ \rangle_{\omega=\infty} = 3.09 \text{ kcal mol}^{-1}$) with increasing collision rate ($k/k_\infty \rightarrow 1$). Thus, the relative efficiency of the EXP model increases as $k/k_\infty \rightarrow 1$, and this results in the efficiency curves for the two models converging with increase of pressure (Figure 2, curves A).

For small values of $\langle \Delta E \rangle$ for which $E' < 0.5$, it has been shown that in the low-pressure region the steady-state concentration of reactant molecules below E_0 is greater for the EXP than for the SL distribution, due to the tail of the EXP distribution which permits some fraction of the more-efficient large steps. As the collisional rate increases, the average energy possessed by reacting molecules again increases toward the high-pressure value and further accentuates the role of the tail of EXP distribution in reaching further. Hence, as k/k_∞ approaches unity, the relative efficiency of the EXP model is enhanced and the EXP and SL curves spread apart (Figure 2, curves C).

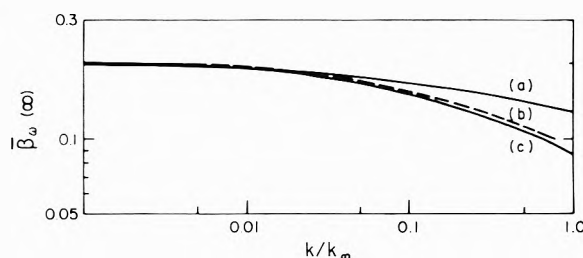


Figure 3. Variation of $\bar{\beta}_\omega(\infty)$ with fall off k/k_∞ based on (a) calculated 400-cm^{-1} EXP model, (b) experimental data, and (c) calculated 350-cm^{-1} SL model, at 245° for $\text{CH}_3\text{NC-He}$ system.

At intermediate step sizes, the behavior falls between the limits described above. The SL model starts off at $\omega = 0$ as the more efficient one of the two, but crosses over at higher values of k/k_∞ to become less effective in replenishing the energized molecules above the reaction threshold (Figure 2, curves B).

The variation of $\bar{\beta}_\omega(\infty)$ with the degree of fall-off, interpolated earlier for the calculated curves² for the step sizes determined earlier for helium, is shown in Figure 3 and summarized in Table II. The two curves are hardly distinguishable experimentally at the lower end of the fall-off regime, say, at $k/k_\infty < 0.05$. The measured behavior for $\text{CH}_3\text{NC-He}$ fall-off lies in between the two extreme models; at higher values of k/k_∞ it follows the SL model more closely. The ratio of $\bar{\beta}_{0.005}(\infty)/\bar{\beta}_{0.775}(\infty)$, which describes the accessible experimental range of variation of k/k_∞ , equals 1.47 for the EXP case, and 2.13 for the SL. The experimental observed value of 2.08 is intermediate in behavior but indicates that a SL model is closer for helium. This work has thus provided an experimental demonstration of the variation of fall-off shape in the presence of a weak bath gas, *i.e.*, of a decrease of collisional efficiency with increase in the k/k_∞ ratio, as predicted by the theory.

In earlier thermal work,^{3,13} the appropriate model of the collisional probability distribution was deduced for this same system from the study of dilution effects in the low-pressure region. The relative efficiency $\beta_0(D)$ increased with decreasing degree of dilution ($D \rightarrow 0$); however, the experimental error did not provide the requisite experimental precision required to distinguish clearly between the detailed predictions from the several models.

In addition to the earlier results from thermal dilution work, chemical activation studies^{14,15} in several systems involving helium bath gases have indicated a collisional probability model intermediate between, but closer to the EXP distribution than to the SL model. The present work has suggested a model which lies between the two extreme cases, but closer to the SL function. While the available experimental accuracy of the present study exceeds that attained in the thermal dilution work, one should be conservative in overriding the chemical activation results owing to the generally lower diagnostic sensitivity of ther-

mal activation systems. In any case, the conclusion that can be drawn is that helium is best represented by a transition probability model intermediate between the two extreme cases of SL and EXP distributions.

References and Notes

- (1) This work was supported by the National Science Foundation and is abstracted from the Ph.D. Thesis of F. M. W., 1974.
- (2) D. C. Tardy and B. S. Rabinovitch, *J. Chem. Phys.*, **48**, 1282 (1968).
- (3) Y. N. Lin and B. S. Rabinovitch, *J. Phys. Chem.*, **72**, 1726 (1968).
- (4) S. C. Chan, J. T. Bryant, and B. S. Rabinovitch, *J. Phys. Chem.*, **74**, 2055 (1970).
- (5) F. P. Buff and D. J. Wilson, *J. Chem. Phys.*, **32**, 677 (1960).
- (6) D. C. Tardy and B. S. Rabinovitch, *J. Chem. Phys.*, **45**, 3700 (1966).
- (7) T. Fujimoto, F. M. Wang, and B. S. Rabinovitch, *Can. J. Chem.*, **50**, 19 (1970).
- (8) S. C. Chan, B. S. Rabinovitch, J. T. Bryant, L. D. Spicer, T. Fujimoto, Y. N. Lin, and S. P. Pavlou, *J. Phys. Chem.*, **74**, 3160 (1970).
- (9) F. W. Schneider and B. S. Rabinovitch, *J. Amer. Chem. Soc.*, **84**, 4215 (1962); part I.
- (10) S. C. Chan, J. T. Bryant, L. D. Spicer, and B. S. Rabinovitch, *J. Phys. Chem.*, **74**, 2058 (1970).
- (11) B. S. Rabinovitch, Y. N. Lin, S. C. Chan, and K. W. Watkins, *J. Phys. Chem.*, **71**, 3715 (1967).
- (12) F. J. Fletcher, B. S. Rabinovitch, K. W. Watkins, and D. J. Locker, *J. Phys. Chem.*, **70**, 2823 (1966).
- (13) B. S. Rabinovitch, D. C. Tardy, and Y. N. Lin, *J. Phys. Chem.*, **71**, 1549 (1967).
- (14) G. Kohlmaier and B. S. Rabinovitch, *J. Chem. Phys.*, **38**, 1692 (1963).
- (15) B. S. Rabinovitch, H. F. Carroll, J. D. Rynbrandt, J. H. Georgakakos, B. A. Thrush, and R. Atkinson, *J. Phys. Chem.*, **75**, 3376 (1971).

On Electron Capture in γ -Irradiated Methylcyclohexane Glass

T. B. Truong, A. Bernas,*

Equipe de Recherches CNRS n°98, Université Paris VI, 91405 Orsay, France

and J. Roncin

Laboratoire Associé de Physico-Chimie des Rayonnements, Université Paris XI (Received August 6, 1973)

Publication costs assisted by CNRS

Recent and present stimulated luminescence experiments have shown (besides trapped electrons e_t^-) a solvent-derived negative species X^- in γ -irradiated methylcyclohexane (MCH) glass or in uv-excited TMPD-MCH system at 77 K. In the former case, an ir e_t^- bleaching is necessary for X^- formation. The following conclusions are made. (1) The small decrease $-\Delta[X]$ due to X^- formation has not been detected by epr but a comparison with the uv-excited TMPD-MCH case makes plausible that X is the methylcyclohexyl radical R_{MCH} . (2) X^- production efficiency examined as a function of e_t^- bleaching wavelength displays a sharp maximum and its resonance character resembles that of a typical resonance electron attachment cross-section curve. (3) An INDO calculation of the lowest electronic energy states of the π and σ structures of R_{MCH} and R_{MCH}^- has shown that electron attachment to R_{MCH} is not expected to occur in the gas phase and that the attachment observed in the solid phase necessitates a distortion from $R_{\text{MCH}}(\pi)$ to $R_{\text{MCH}}(\sigma)$. The energy (≈ 0.2 eV) corresponding to the maximum of X^- formation efficiency curve may correlate with the activation energy of this π to σ structural change. Implications on electron kinetic energy relaxation in γ -irradiated glasses and phase effects on electron attachment processes are evoked.

Electron-ion pairs are produced in γ -irradiated organic glasses and, in the absence of electron scavengers, most of the photoelectrons become matrix trapped. A subsequent optical excitation or "bleaching" of these electrons, under wavelength λ_b , induces a neutralization luminescence¹ and it has been noticed that the luminescence excitation spectrum closely parallels the trapped electrons (e_t^-) and anions absorption bands.²

Corroborating previous optical absorption observations,³ recent stimulated luminescence experiments⁴ have shown (besides e_t^-) the existence of a solvent-derived negative species X^- in γ -irradiated 3-methylpentane (3MP) and methylcyclohexane (MCH) glasses or in uv-excited TMPD, 3MP, or TMPD-MCH systems at 77 K (TMPD = tetramethyl-*p*-phenylenediamine).

An identification of X is now being attempted and the

necessary conditions for X^- formation and implications more precisely specified. γ -Irradiated pure MCH will exemplify present experimental findings.

Experimental Section

The experimental conditions for γ and uv irradiations and luminescence recordings have been described earlier.⁴ The γ -ray doses range from 8×10^{19} to 1.4×10^{21} eV g^{-1} .

Esr analysis are performed at 77 K with a JEOL Jesme 1 X spectrometer. A quartz iodine lamp with a silicium filter ($\lambda \geq 1100$ nm) was used for bleaching the irradiated sample when located in the epr spectrometer cavity.

Results

(a) As in the 3MP case,⁴ if the uv stimulation of the γ -irradiated MCH sample is performed directly after γ -irra-

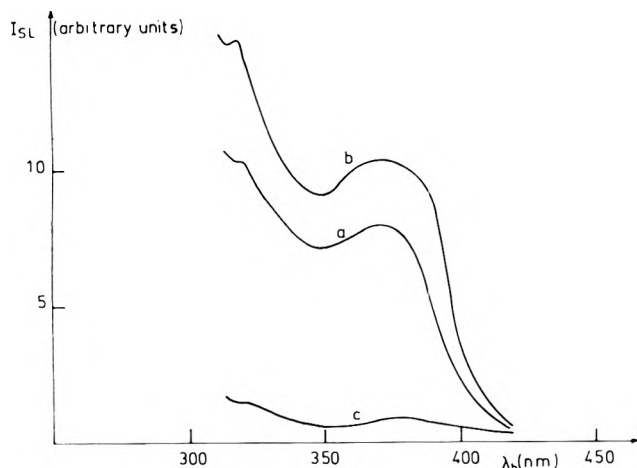


Figure 1. Intensity of stimulated luminescence (I_{SL}) in the uv region for γ -irradiated MCH glasses (analyzing wavelength, λ_{an} 445 nm): (a) γ dose = 1.1×10^{20} eV g^{-1} , bleaching at λ_b 1400 nm for 2 min; (b) γ dose = 1.1×10^{20} eV g^{-1} , bleaching at λ_b 1100 nm for 30 min; (c) γ dose = 4×10^{20} eV g^{-1} , bleaching at λ_b 1400 nm for 30 min. As shown in ref 10, e_t^- is maximum for a dose of 1.5×10^{20} eV g^{-1} and decreases at higher doses.

diation, the luminescence excitation spectrum or so-called stimulated spectrum attributable to X^- is absent. However, following a 1400-nm bleaching (which lies in the e_t^- absorption band) the X^- stimulated spectrum appears very similar to the one previously recorded for 3MP.⁴ The stimulated luminescence intensity is similarly found to increase with the 1400-nm bleaching time (Figure 1). On the other hand, when thermally released, the mobile electrons do not give rise to X^- . The observation that only the optically excited trapped electrons can be captured has also been made for dissociative attachment on acetonitrile,⁵ methyl vinyl ether,⁶ and dimethyl ether⁷ following γ -irradiations of mixed systems. Such a situation is, however, by no means general. Careful epr and optical spectroscopic studies have shown that a direct electron attachment under γ -irradiations does occur on MTHF radicals.⁸

(b) After γ -irradiation and before the trapped electron infrared bleaching, the epr spectrum consists of eight bands corresponding to the methylcyclohexyl radical⁹ (R_{MCH}) and in the trapped electron singlet.

After bleaching the samples under $\lambda_b \geq 1100$ nm, the e_t^- signal disappears completely. The remaining R_{MCH} signal shows no decrease in intensity. However, the neutralization luminescence recorded later on the same pre-bleached sample does exhibit a luminescence for $\lambda_b < 650$ nm, attesting to X^- formation. The same observations were made for various γ -ray doses giving rise to different ratios e_t^-/R_{MCH} .¹⁰

Following a γ -dose of 1.1×10^{20} eV g^{-1} corresponding to the maximum e_t^- concentration, the ratio e_t^-/R_{MCH} before bleaching has been estimated and effectively found smaller than 3%. Thus, if X represents the methylcyclohexyl radical, the decrease $-\Delta[X]$ due to X^- formation would be too small to be detected by epr.

Hence, with better defined bleaching conditions, our experiments have but confirmed previous negative epr results^{10,11} and do not permit a decisive direct identification of X . However, the fact that R_{MCH} is the only solvent-derived photoproduct observed from the uv-excited TMPD-MCH systems (in accordance with ref 12) makes plausible that $X = R_{MCH}$.

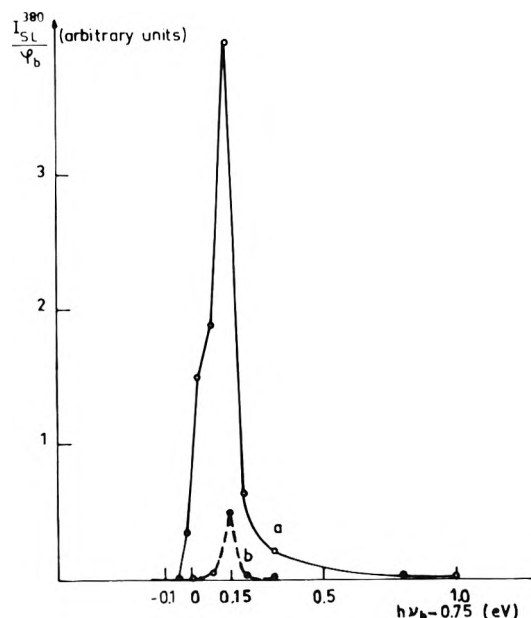


Figure 2. X^- formation efficiency vs. detrapped electron kinetic energy (I_{SL} is compared at 380 nm). The bleaching intensity I_b is kept constant at 1.4×10^{14} photons $sec^{-1} cm^{-2}$: (a) γ dose = 1.1×10^{20} eV g^{-1} ; (b) γ dose = 4×10^{20} eV g^{-1} .

(c) Whatever the nature of X^- , the relative bleaching efficiency for X^- formation at different wavelength λ_b has been checked. In a search for a possible analogy with an electron capture cross-section function, it has been considered that the bleaching photon energy is used first to extract the trapped electron and that the excess energy is imparted as kinetic energy of the freed electron. If the electron has to jump over a potential barrier it may possess some kinetic energy even at the photoextraction threshold; this would not, however, alter the arguments developed below.

From previously reported experiments,¹³ the electron detrapping threshold energy in a MCH matrix has been set at 0.75 ± 0.05 eV, hence the abscissa in Figure 2 are taken as $hc/\lambda_b - 0.75$ (eV) and the corresponding figures are considered to be equal to the kinetic energy of the attaching electron, except for a possible additive constant. The stimulated luminescence intensity I_{SL} at a definite wavelength (380 nm) in the X^- spectra region (Figure 1), being itself proportional to X^- concentration, has been corrected for the quantum electron detrapping efficiency φ_b ¹³ as given by curve b of Figure 2 in ref 13; hence, whatever λ_b , the intensity I_{SL} refers to a constant number of released electrons. The resulting curve (Figure 2) displays a sharp maximum at λ_b 1400 nm (~ 0.9 eV) and its resonant character resembles that of a typical resonance electron attachment cross-section curve. Its shape and the spectral position of its maximum are found not to depend on the γ -ray dose, that is, it does not vary with the mean e_t^-X distance. If such an analysis is correct, the highest probability for electron attachment to X would thus be met for electrons of about 0.2-eV kinetic energy.

Previous^{3,4} and present experiments agree that neither the γ -ray ejected "dry" nor the thermally detrapped electrons are capable to give rise to X^- , even though, as shown in Figure 2 of ref 4, these thermally released electrons constitute a high proportion of the initial total e_t^- population. On the other hand, the photoelectrons produced in the uv-excited (325 ± 50 nm) TMPD-MCH sys-

tems are able to form X^- directly, the intermediate step of the ir release appearing unnecessary. It has been verified further that, in these photoionization experiments, an e^- release under 325 ± 50 nm excitation, simultaneous to TMPD photoionization, does not form X^- either; in a control experiment where a 325-nm bleaching had followed MCH γ -irradiation (dose = 3×10^{19} eV g $^{-1}$), no X^- stimulated luminescence was recorded. It should be stressed further that, under such ionization conditions, the initial kinetic energy of the photoelectron is close to 1 eV,¹⁴ in striking contrast to the γ -irradiation case.

Discussion

Hence, as suggested by Williams and coworkers⁵ we believe that the bleached or optically "excited" electron is capable of attachment because it satisfies stringent energy requirements. A simultaneous CH vibrational excitation in X radical under 1400 nm (~ 0.9 eV) could possibly increase the electron capture cross section of X, as suggested in ref 4, in analogy to the reported temperature effect in the dissociative attachment cross section in N_2O .¹⁵ However the direct formation of X^- observed in the photoionization case disagrees with such an interpretation. Furthermore, bleachings with λ_b 1200 or 1750 nm (~ 1.0 and 0.7 eV, respectively) where CH stretching modes are also located were found inefficient.

Assuming now that X is the methylcyclohexyl radical $R\cdot$, an INDO calculation¹⁶ of the total electronic energy of isolated $R\cdot$ and $R^-\cdot$ leads to the following results.

(1) The π structure for $R\cdot$ is more stable by about 0.2 eV than the σ structure. (The σ structure retained in the calculation has a sp^3 hybridization at the radical site.)

(2) The attaching electron is accommodated in the unpaired electron orbital, that is, on the tertiary carbon atom. Hence, C-H vibrations are not expected to significantly interfere with the electron capture process.

(3) Contrary to the radical energies situation, the σ structure of $R^-\cdot$ turns out to be more stable than the π one by about 0.8 eV and is located about 0.5 eV above $R(\sigma)$.

Thus the following can be concluded. (a) An electron attachment on $R\cdot$ is not expected to occur in gaseous phase. (b) When environmental conditions lower (as expected¹⁷) the $R^-(\sigma)$ energy level to such an extent that the $R(\sigma)$ electron affinity becomes positive, the observable electron attachment requires a distortion of the R-structure. (c) Since the esr coupling constants previously observed for $R\cdot$ in solid MCH also correspond to a σ structure,⁹ it is clear that the transition from the σ structure of the MCH molecule to the π structure of the radical (and vice versa) is not inhibited by steric hindrance in a MCH glassy matrix at 77 K. The energy difference of 0.2 eV between the two $R\cdot$ structures is thus expected to be preserved in these solid conditions. Finally, the good correspondance noted between such a value and the energy position of the peak of our experimental attachment curve (Figure 2) may suggest a correlation between these two terms and substantiate the view that the latter reflects a resonance electron attachment process.

The present findings and their interpretation seem to contain two types of more general implications: one, bear-

ing on the γ -radiolysis of organic solids, the second, on phase effects on electron attachment requirements.

(a) The distinctive behavior of X with respect to electron capture, following either solute photoionization or solvent radiolysis, seems to imply that in the course of the slowing down collisions, the secondary electrons travelling in the γ -irradiated samples never reach an energy of 0.2 eV; the electron trapping would occur before their reaching thermal energies. In other words, matrix cavity trapping would constitute an energy relaxation mode in agreement with previous suggestion that thermalization and trapping may be synchronous.¹⁸⁻²⁰

(b) Extrapolation of gas-phase electron attachment data to condensed phase conditions may suffer from several restrictions. One of these, as already mentioned, is related to the increase of electron affinity values determined for gaseous species due to surrounding molecules polarization. Hence, a negative ion which would easily autoionize in the gas may be stabilized and detected in a liquid or solid environment.

On the other hand, presently reported experiments suggest that an electron scavenger, found efficient in gaseous phase, may appear as inefficient when used in solid matrix γ -irradiations if the maximum of its resonance attachment cross section is so located that matrix trapping has already occurred at a higher electron kinetic energy. Furthermore, if a change in geometry of the attaching species X is required for X^- formation, electron attachment may become proscribed in some solid environment due to steric hindrance.

Acknowledgments. We are particularly indebted to Professor L. G. Christophorou for numerous and pertinent reprints and remarks.

Our thanks are also due to Dr. F. Kieffer and his group for help with the γ -irradiations.

References and Notes

- W. M. Mc. Clain and A. C. Albrecht, *J. Chem. Phys.*, **43**, 465 (1965).
- A. Déroutède and F. Kieffer, *Nature (London)*, **215**, 1475 (1967); A. Déroutède, *J. Luminesc.*, **3**, 302 (1971).
- A. Eckstrom, S. Suenram, and J. E. Willard, *J. Phys. Chem.*, **74**, 18 (1970).
- T. B. Truong and A. Bernas, *J. Phys. Chem.*, **76**, 3894 (1972).
- M. A. Bonin, J. Lin, K. Tsuji, and F. Williams, *Advan. Chem. Ser.*, **No. 82**, 269 (1968).
- M. Irie, K. Hayashi, S. Okamura, and H. Yoshida, *J. Phys. Chem.*, **75**, 476 (1971).
- H. Yoshida, M. Irie, O. Shimada, and K. Hayashi, Conference on Elementary Processes in Radiation Chemistry, Notre Dame, April 7, 1972.
- J. Teply, I. Janovsky, F. Kiss, and K. Vacek, *Int. J. Radiat. Phys. Chem.*, **4**, 265 (1972).
- C. Chachaty, *J. Chim. Phys.*, **64**, 614 (1967).
- M. Shirrom and J. E. Willard, *J. Amer. Chem. Soc.*, **93**, 2184 (1968).
- D. P. Lin and L. Kevan, *J. Chem. Phys.*, **55**, 2629 (1971).
- S. Siegel and K. Eisenhal, *J. Chem. Phys.*, **42**, 2494 (1965).
- A. Bernas, D. Grand, and T. B. Truong, *J. Chem. Soc., Chem. Commun.*, **13**, 759 (1972).
- A. Bernas, M. Gauthier, and D. Grand, *J. Phys. Chem.*, **76**, 2236 (1972).
- E. L. Chaney and L. G. Christophorou, *J. Chem. Phys.*, **51**, 883 (1969).
- J. A. Pople, D. L. Beveridge, and P. A. Dobosh, *J. Amer. Chem. Soc.*, **90**, 4201 (1968).
- L. E. Lyons in "Physics and Chemistry of the Organic Solid State," D. Fox, M. Labes, and A. Weissberger, Ed., Interscience, New York, N.Y., 1963, p 746.
- P. H. Towari and G. R. Freeman, *J. Chem. Phys.*, **51**, 1276 (1969).
- N. Houser and R. C. Jarnagin, *J. Chem. Phys.*, **52**, 1069 (1970).
- S. S. Takeda, N. Houser, and R. C. Jarnagin, *J. Chem. Phys.*, **54**, 315 (1971).

Reactions Involving Electron Transfer at Semiconductor Surfaces.¹ V. Reactivity and Electron Paramagnetic Resonance of Electron Transfer Sites on Rutile

Joseph Cunningham* and Anthony L. Penny

Chemistry Department, University College, Cork, Ireland (Received July 10, 1974)

Publication costs assisted by the U.S. Air Force Office of Scientific Research

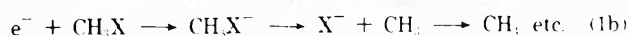
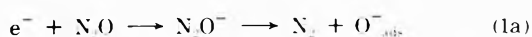
Extent and kinetics of dissociation are reported following contact at room temperature between gaseous nitrous oxide and powdered rutile samples thermally activated at 670°K. Parallel studies by electron paramagnetic resonance establish that contact with N₂O results in the loss of one paramagnetic center from the rutile sample per nitrous oxide molecule dissociated. Boundary layer theory accounts for the observed extent of N₂O dissociation, but it is shown that this could follow *either* from indirect dissociative electron transfer involving conduction band electrons *or* from direct electron transfer involving paramagnetic surface centers whose concentrations were established during thermal activation. Selectivity in electron transfer is demonstrated by failure of the activated rutile surfaces to dissociate methyl halides.

Introduction

Band theory represents pure stoichiometric zinc oxide or titanium dioxide as large band gap intrinsic semiconductors with valence-conduction band gaps respectively equal to 3.2 and 3.05 eV.² Deviations from stoichiometry in the direction of excess metal occur in all real samples but particularly in powdered samples thermally activated *in vacuo*,³ such as employed in the present study. Thermal promotion of electrons from metal-excess donor centers, such as Zn⁰_{int} or Zn⁻_{int} in ZnO or Ti³⁻_{int} in TiO₂, into the conduction band confers n-type extrinsic conductivity. Donor densities *ca.* 10¹⁶ cm⁻³ and electron mobilities 5–40 cm²/V sec have been reported⁴ for high-purity powdered ZnO. Comparable donor densities (10¹⁶–10²⁰ cm⁻³)^{5a} and smaller mobilities (0.15–1.25 cm²/V-sec)^{5b} have been reported⁵ for pure single crystals of TiO₂. Various workers have attempted to correlate electron paramagnetic resonance (epr) signals observed in vacuum-activated ZnO and TiO₂ with metal-excess donor centers,^{6–9} while others have argued that conduction band electrons are responsible¹⁰ for the singlet epr signal with *g* ~ 1.96 in ZnO. Conduction band electrons in TiO₂ have been correlated^{9a} with a broad optical absorption band with maximum at 1.5 μm.

In view of the referenced electrical and spectroscopic evidence for coexistence of metal excess centers and for electrons mobile in the conduction band, consideration of electron transfer at the surfaces of TiO₂ and ZnO should take into account both direct and indirect processes. In this paper, the single-step transfer of an electron from a surface donor center to an adsorbed species corresponds to *direct* transfer, whereas *indirect* electron transfer denotes a three-stage process with electrons being promoted from donors into the conduction band and migrating some distance *via* the conduction band before finally reacting with the adsorbed species. Although electron localization by the adsorbed species is achieved in each case, the adsorbed species may receive the electron from different surface environments in the direct and indirect processes. Consequently, differences may arise in rates of direct and indirect electron transfer and the electron adducts produced may form in different surface environments. Formation of O₂⁻_{ads} in three surface environments on ZnO

and three different environments on TiO₂ has been deduced from recent epr studies^{11,12} without, however, defining the role(s) of direct and/or indirect electron transfer in their formation. Information on these roles is sought in the present study by combining epr studies with the use of gaseous N₂O, CH₃I, and CH₃Cl as molecular probes for measuring the availability of electrons at the surface. Previous papers in this series^{13–15} demonstrated that all these gases underwent dissociative electron attachment at the surface of vacuum-activated zinc oxide and that a model based on indirect electron transfer could account for the observed results. In view of the similarities noted between ZnO and TiO₂, the present study examines TiO₂ surfaces by similar techniques to determine if dissociative electron attachment processes 1a and 1b also occur on rutile.



Experimental Section

Materials. One batch of high-purity TiO₂, kindly supplied by New Jersey Zinc Co. (sample MR-128) was utilized for all present experiments. The material was 98–99% rutile with surface area 5.4 m² g⁻¹, average particle size 0.22 μm, and low impurity levels (*e.g.*, Cl₂ ~0.07%, Al₂O₃ <0.1%). New samples of this material were preactivated *in vacuo* prior to each measurement. Activation of some preliminary samples at 670°K under 10⁻⁶ Torr on a conventional oil-pumped vacuum system protected by liquid nitrogen traps confirmed the notorious sensitivity of oxide materials toward reduction by trace hydrocarbons. Thin layers of ZnO or TiO₂ thus activated on quartz substrates showed anomalously high conductances which decreased by orders of magnitude when O₂, N₂O, or CH₃I were admitted at room temperature. Room temperature epr spectra of 20-mg samples of ZnO or TiO₂ activated in such reducing conditions at 670°K in Spectrosil tubes showed at room temperature strong signals with *g* values at 2.003 and 1.998, respectively. The *g* values were similar to signals attributed by Miller and Haneman to surface carbon impurities,¹⁶ but production of such large signals was avoided when samples were prepared on a greaseless.

ion-pumped vacuum system. Unless otherwise noted, all results relate to samples preactivated at 670°K at 10^{-7} Torr on this system. Subsequent introduction of gases to preactivated samples was also made using this vacuum system. Spectroscopically pure N_2O or O_2 (BOC grade X) were used as supplied. Methyl halides were purified before use by passage through P_2O_5 and by subsequent trap to trap distillation.

Reactions in TiO_2 -Gas Systems. Samples (0.1–5 g) of the high-purity rutile were activated at 670°K in contact with Spectrosil walls (to avoid the contamination by ions possible if contacted with Pyrex at this temperature). Stainless steel stopcocks served to isolate from the ion pump and from a quadrupole mass spectrometer a section of the vacuum system of small volume (133 cm^3), comprising the Spectrosil container, pirani gauge, and liquid nitrogen traps. These latter components served to monitor the buildup of noncondensable gas product following introduction of the condensable methyl halides or N_2O . Photo-assisted reaction was studied by focussing the output of a 200-W medium-pressure xenon arc lamp onto the sample surface, using filters to limit incident light to 350–380 nm. Product gases from dark or photo-assisted reactions were introduced into the mass spectrometer for analysis.

Spectroscopic Measurements. Samples (0.1 g) activated *in vacuo* between Spectrosil windows of a circular cell 1 mm thick \times 30 mm o.d. were fitted to the sample position of a Beckmann DK2 diffuse reflectance spectrometer yielding absorbance *vs.* wavelength 200–2000 nm against an MgO reference. Since measured absorbance was reproducible to ± 0.05 , gases contacted with the activated TiO_2 were regarded as having zero effect unless they produced larger changes than this. Smaller samples (20–50 mg) were activated in Spectrosil tubes of 5 mm o.d. for study at 77–300°K in a variable temperature insert fitted to the multipurpose cavity of a Decca XI epr spectrometer. The g values of signals were measured relative to a sealed powder reference of (Mn^{2+} -MgO) attached to the outside of the sample tube. One striking experimental difference between epr measurements on ZnO and TiO_2 samples of similar weight activated in similar manner was that the TiO_2 samples did not significantly reduce the Q of the cavity whereas ZnO seriously reduced it. The observation appeared consistent with the much lower mobility^{4,5} reported for conduction band electrons in TiO_2 and obviated the need to correct TiO_2 epr intensities for changes in cavity Q . In cases when it was desired to convert TiO_2 signal intensity observed at 77°K to spin concentration, the integrated area under the rather broad epr signals was measured and compared with the integrated area under a peak of comparable width measured in identical conditions on a reference sample of DPPH dispersed in MgO or alkali halide and held in identical configuration in the cavity at 77°K.

Break-seals were used to admit gases to samples *in situ* in the cavity but such contact was always made at room temperature to avoid condensation of gases onto the Spectrosil walls. Light from a 150-W medium pressure mercury arc lamp incident on the samples *in situ* in the cavity at 300 or 77°K served to test if new signals were produced or existing signals modified by uv illumination.

Results and Discussion

A. N_2O Decomposition over Rutile. Gaseous N_2 was produced when pure N_2O was brought into contact at

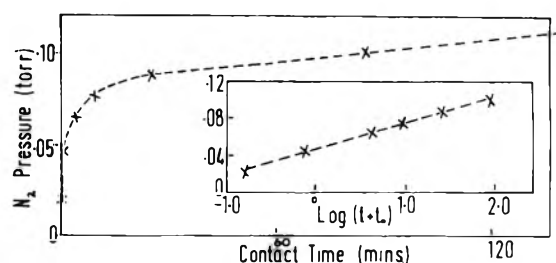


Figure 1. Growth of gaseous nitrogen product from room temperature contact of 400 Torr of N_2O with rutile preactivated *in vacuo* at 683°K. Pressure of noncondensable gas product (98% N_2) increasing with duration of room temperature contact with 0.1-g sample. Inset: data represented according to Elovich expression 1b.

room temperature with high-purity rutile samples preactivated by 16 hr heating to 683°K under 10^{-7} Torr residual pressure in a "clean" vacuum system. Figure 1 illustrates typical data showing the formation of N_2 product under 400 Torr N_2O pressure. The initially rapid rate of N_2 formation and its subsequent decline to very low values in the dark after 2 hr contact time suggested that these data on $V(N_2)$, the volume of nitrogen produced at time t , would conform to Elovich-type expressions

$$dV(N_2)/dT = A \exp(-BV(N_2)) \quad (1a)$$

and

$$V(N_2) = C \log(t + t_0) + D \quad (1b)$$

In these expressions, A , B , C , D , and t_0 are constants whose physical significance depends on the model chosen for the surface process and the value of t_0 is empirically chosen as that which best linearizes data on a plot of form (1b). The inset of Figure 1 confirms that the buildup of N_2 product in the N_2O - TiO_2 system could be fitted to this expression with choice of $t_0 = 0$; *i.e.*, $V(N_2)$ increased linearly with $\log t$. These new results on limited N_2O decomposition over high-purity rutile at room temperature greatly resemble those previously reported by us on N_2O dissociation over high purity zinc oxide.^{13,14} Those previous studies of the N_2O -ZnO system showed that it was possible, by preactivation of the ZnO in H_2 at 600°K, to raise the extent of N_2O decomposition above that achieved over vacuum-activated ZnO. Formation at the surface under reducing conditions, of additional electron-excess centers capable of donating electrons to adsorbed N_2O , provided an adequate explanation of enhanced dissociation in a pre-reduced N_2O -ZnO system, particularly in view of a recent claim by Roussel and Teichner¹⁷ that surface zinc atoms are effective in reducing N_2O . It was of interest to determine whether preactivation of rutile in reducing atmospheres would likewise increase the attainable N_2O decomposition. Prior activation in hydrogen or carbon monoxide did effect a significant increase, as may be seen by comparing data in Figure 2 for a TiO_2 sample preactivated in carbon monoxide with data in Figure 1 for a similar sample preactivated *in vacuo*. The inset in Figure 2 illustrates that, despite the probable surface nature of some of the electron-transferring sites on TiO_2 pre-reduced in CO, buildup of N_2 product still obeyed the Elovich expression (1b).

Although the above results established a strong similarity between the activity of high-purity TiO_2 and ZnO for limited decomposition of N_2O in the dark, one marked difference between the N_2O - TiO_2 and N_2O -ZnO systems emerged from our attempts to detect additional photo-

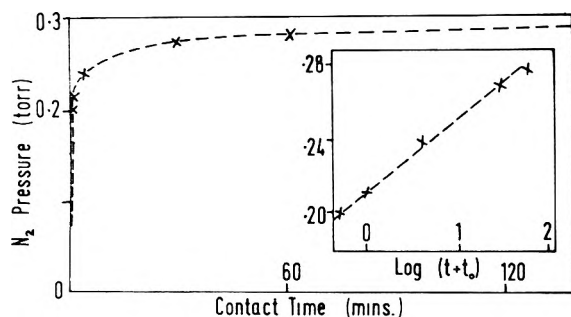
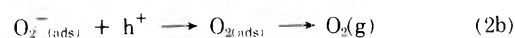
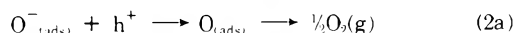


Figure 2. Growth of product nitrogen from room temperature contact between 400 Torr of N_2O and rutile preactivated at $673^\circ K$ in CO. Pressure of noncondensable gas product (98% N_2) increasing with duration of room temperature contact with 0.1-g sample. Inset: data represented according to Elovich expression 1b.

assisted decomposition when the N_2O - TiO_2 systems were exposed to uv illumination. Neither the light output of a 200-W xenon-mercury arc filtered to yield only wavelengths 350–390 nm nor the full light output of this lamp yielded during illumination any significant enhancement above the slow rate of N_2 formation measured before and after illumination. The contrast between this negative result for the uv-illuminated N_2O - TiO_2 system and previously reported large enhancement in the rate of N_2 formation in dark-equilibrated N_2O -ZnO systems similarly illuminated,¹⁴ is of interest for two reasons. First, it demonstrates, in conjunction with Figure 3, that mere comparability in the rates of energy deposition into ZnO and TiO_2 powders by light inside their band edges did not suffice to achieve comparable photoassisted dissociation (note that the comparison was made with closely similar photon fluxes at wavelengths 365 ± 15 nm incident on ZnO or TiO_2 and that Figure 3 shows absorbance values of the N_2O - TiO_2 and N_2O -ZnO systems at 365 nm to be very similar in their diffuse reflectance spectra). Requirements other than similarity in surface heating, or photo-generation in TiO_2 and ZnO of comparable numbers of electrons, holes and electron-hole pairs, must therefore be involved in achieving photoassisted dissociation of N_2O . Secondly, the absence of photoassisted reaction in the N_2O - TiO_2 system could be understood if that system were incapable of photodesorbing oxygen *via* (2a) or (2b).



Such photodesorption is generally accepted as necessary for continuing photo-stimulated processes on ZnO, including N_2O dissociation.^{11,14} It is shown below that processes 2a and 2b should not be possible at the dark-equilibrated N_2O - TiO_2 interface if one model of direct electron transfer dominates in this system.

B. Epr Measurements on TiO_2 and N_2O/TiO_2 Systems. An epr spectrum typical of the high-purity rutile sealed *in vacuo* after preactivation on the ion-pumped vacuum system at $670^\circ K$ is shown in Figure 4a. This spectrum was recorded with the sample at $77^\circ K$ and three features can be distinguished at magnetic field values corresponding to $g = 1.999$, $g = 1.965$, and $g = 1.948$. Spectra at different incident microwave power levels (from 100 to 1 mW) showed that the feature with $g = 1.999$ saturated readily whereas the features at $g = 1.965$ and $g = 1.948$ were not saturated even with 100-mW incident microwave power. These results essentially agree with prior reports^{8,9,11} of

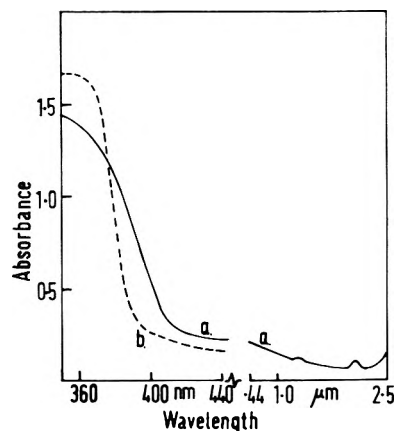


Figure 3. Diffuse reflectance spectra at room temperature of TiO_2 (curves a) and ZnO (curve b) powders after preactivation *in vacuo* and exposure to N_2O .

two types of center with different relaxation times in vacuum-activated TiO_2 . Some of these reports attribute the broad asymmetric signal with g values 1.965 and 1.949 in vacuum-activated rutile powders to Ti^{3+} ions at various sites, *i.e.*, Ti^{3+}_{int} or $Ti^{3+}_{(Ti^{4+})}$. Others suggested that more complex centers involving Ti^{3+} adjacent to an oxygen vacancy in the anatase structure, *e.g.*, $(Ti^{3+}-V_{ox}-Ti^{4+})$, can also give rise to an asymmetric signal with these g values.

The sharper and more symmetric signal with $g = 1.999$ has been attributed to impurities or to interstitial Ti^{3+} , *i.e.*, $Ti^{3+}_{(int)}$. Formation and intensity of this signal appears from published work to be more sensitive than the asymmetric signal to the nature of the TiO_2 (whether anatase or rutile) and to the gas environment during activation. Formation of the symmetric signal is reportedly favored¹⁸ by the anatase structure and by its prior reduction in CO. Since the TiO_2 used for the present study was 98–99% rutile before activation, the relatively large intensity of the symmetric, anatase-favored epr signal with $g = 1.999$ was surprising, and possibly indicative of considerable rearrangement of the TiO_2 crystal structure close to the surface after 16 hr activation at $670^\circ K$ *in vacuo*. Consequently, measurements of the concentration of paramagnetic centers were not attempted for the structure-sensitive epr singlet with $g = 1.999$.

Measurements of spin concentration were made on the centers responsible for the broad asymmetric signal with g values at *ca.* 1.965 and 1.948, because the literature indicated this to be less structure-sensitive than the signal at $g \sim 2.00$. Since the asymmetric signal with $g = 1.965$ and 1.948 was not saturated in our measurement conditions, its spin concentration was easily determined by comparison with integrated signal intensity from standards prepared by dispersing DPPH into MgO or alkali halides. Comparisons run in identical conditions at $77^\circ K$ yielded a value of 2.6×10^{18} paramagnetic centers with $g = 1.965$ and $1.948/cm^3$ of vacuum-activated TiO_2 . The well-established general difficulties involved in determining spin concentrations by comparison with standard samples mean that an uncertainty of up to $\pm 50\%$ should be associated with this spin concentration in TiO_2 . Signal intensity was not affected on warming the sample up to room temperature *in vacuo* and recooling to $77^\circ K$ for measurement. However, when samples were warmed to room temperature and N_2O at pressures up to 400 Torr was contacted

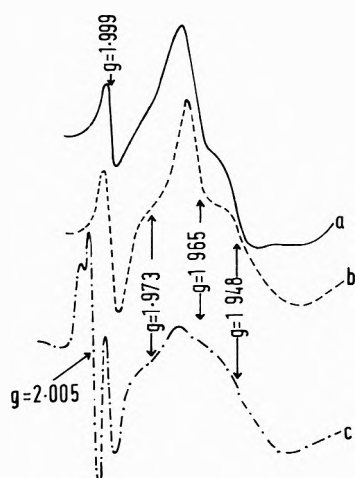
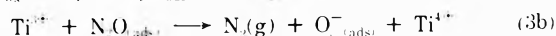
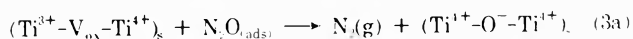


Figure 4. Electron paramagnetic resonance (epr) spectra taken at 77°K of rutile samples after various treatments: spectrum 4a, after activation *in vacuo* of 10^{-7} at 720°K; spectrum 4b, after reduction at 623°K by H_2 ; spectrum 4c, as in 4b with the addition of *in situ* uv illumination incident on the rutile sample.

with the sample for 5–60 min before reevacuation and recooling to 77°K, it was found that the intensity of the asymmetric signal with $g = 1.965$ and $g = 1.948$ was reduced to 10% of the value measured on the same sample prior to N_2O admission. The number of these paramagnetic centers removed by N_2O corresponded to $5.4 \pm 2.7 \times 10^{17}/g$ of rutile activated *in vacuo*. The measured dissociation of N_2O to N_2 over a rutile sample activated in identical conditions (*cf.* section A and Figure 1) corresponded to $8.5 \pm 1.0 \times 10^{17}$ N_2O molecules dissociated per gram of rutile for equal contact time. Within experimental error, these numbers could be consistent with removal of between 1 and 0.5 paramagnetic center for each nitrous oxide molecule dissociated at room temperature. The implications of this correspondence can be considered in terms of various models for dissociative electron transfer from the paramagnetic centers to adsorbed nitrous oxide.

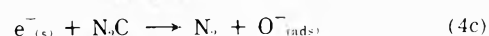
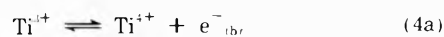
Models for direct dissociative electron transfer from rutile to N_2O can reasonably be based upon the identifications suggested by previous workers for the asymmetric epr signal with components at $g = 1.965$ and $g = 1.948$. These identifications fall into two categories: centers based on titanium interstitials $Ti^{3+}_{(int)}$ as the electron donor, and more complex centers based on oxygen vacancies, V_{ox} , in association with one or more adjacent cation, *e.g.*, $(Ti^{3+}-V_{ox}-Ti^{4+})$. Goodenough, in a recent review,^{2b} has suggested that in most reduced rutile it is necessary to think of both types of defects coexisting, the dominant defect depending upon sample preparation. Direct electron transfer processes based on these two classes may be represented as in (3a) and (3b).



The following features of our observations on the N_2O - TiO_2 system can be accounted for with (3a) as the dominant electron transfer site at the rutile surface. First, our observations that preactivation of the samples in the reducing gases H_2 or CO increased the concentration of paramagnetic centers (*cf.* Figure 4a and b) and the surface reactivity (*cf.* Figures 1 and 2) are consistent with the claims of many workers that activation in reducing

conditions favors centers involving oxygen vacancies.^{2,11} Secondly, since direct dissociative electron transfer *via* (3a) would necessarily imply that active centers were at the surface or close enough to it for electron tunnelling, the epr-measured concentration of *ca.* $6 \times 10^{17} g^{-1}$ should be distributed over *ca.* $5.4 m^2$ (the surface area per gram). Three per cent of the surface sites would then be paramagnetic with consequent high probability of line-broadening and this is consistent with the large line width of the asymmetric signal in vacuum-activated rutile (Figure 4a) and yet larger line width in samples preactivated in reducing conditions (Figure 4b). Thirdly, extent of room temperature N_2O dissociation here achieved over high-purity vacuum-activated rutile (16×10^{16} molecules m^{-2}) is much greater than previously achieved over high-purity ZnO vacuum-activated in similar conditions (1×10^{16} molecules m^{-2}). This is consistent with reported ease of formation of oxygen vacancies in rutile (such as required for process 3a) and evidence indicating that oxygen vacancies do not readily form¹⁹ in ZnO . Fourthly, since process 3a effectively destroys the oxygen vacancy by "filling" it with the oxygen fragment from N_2O dissociation, the process does not produce exposed O^-_{ads} or $O_2^-_{ads}$ species at the surface (no epr signals corresponding to these were seen in the present study). Consequently process 2a or 2b should not be possible and this is consistent with failure of uv illumination to cause photoassisted dissociation of N_2O in dark-equilibrated N_2O -rutile systems.

Process 3b lacks the ability to account for the first, second, and fourth feature of the results as just enumerated and, consequently, it appears less appropriate than (3a) as a model for direct electron transfer in the N_2O - TiO_2 system. However, since energy levels reported for Ti^{3+} lie very close to the conduction band, room temperature experiments with N_2O cannot distinguish between process 3a as an acceptable direct electron-transfer mechanism and an equivalent but indirect electron-transfer process comprising



Model 3a (above) delineated clearly the nature of a probable surface environment on rutile with which N_2O_{ads} could interact to achieve direct electron transfer. Comparable precision is, however, not yet possible in defining for process 4 the surface environment denoted by $e^-_{(s)}$, since some current theories²⁰ represent surface electrons as quantized with respect to movement into the solid but free to move over the surface, while others emphasise the importance of surface states ("dangling bonds") in localizing surface electrons²¹ and yet others treat surface electronic states as modifications of bulk lattice states.²² In these circumstances gross simplifications, which do not require the nature of the electron transfer site to be identified in detail, can be useful in discussing indirect electron transfer. One such simplification is the boundary layer theory of depletive chemisorption²³ in which electron transfer from an electron-rich substrate (such as n-type TiO_2 or ZnO) to electron accepting molecules (such as O_2 or N_2O) at the surface is treated in a manner similar to the accumulation of charge and potential across a dielectric condenser. From such treatments expression II can be derived for the maximum number of charged species which can accumulate per unit area of surface as a

result of indirect electron transfer from a concentration n_d of donor centers within the solid of dielectric constant ϵ .

$$N_0 \simeq 10^3 (\epsilon E_0' n_d)^{1/2} \quad (\text{II})$$

E_0' is the surface potential which develops across the boundary layer of depth D as a result of electron localization at the surface and can reasonably be assumed as ca. 1 V for semiconducting metal oxides. The measured density of paramagnetic centers at $g = 1.965$ and 1.948 in the rutile samples would correspond to $n_d = 2.6 \times 10^{18} \text{ cm}^{-3}$, if distributed *uniformly throughout the TiO₂ lattice*. Inserting these values of E_0' and n_d into (II) yields $N_0 = 7 \times 10^{12} / \text{cm}^2$ as the maximum allowed electron concentration at the TiO₂ surface. The measured maximum specific activity of the TiO₂ surface for the dissociation of N₂O corresponded to 1.6×10^{13} N₂O molecules dissociated/cm² of TiO₂. In view of the approximations involved in the application of expression II, there is adequate agreement between measured N₂O decomposition in the N₂O-TiO₂ system and that calculated in terms of indirect dissociative electron transfer *via* (4a), (4b), and (4c).

The foregoing numerical considerations are inconclusive since they indicate that the observed dark dissociation in the N₂O-TiO₂ system may be equally well accounted for by direct or indirect dissociative electron transfer. The ability of both models to account for observed dissociation may *not* be coincidental and may originate because the electron-transfer process to N₂O is direct but occurs from electron-excess surface species *whose surface concentration was established in accordance with boundary layer considerations* during vacuum activation. For example, it would appear that (II) should define the attainable surface concentration of electron transfer sites such as Ti³⁺_(int) on TiO₂ or Zn⁰_(int) on ZnO, which clearly carry an extra electron relative to the bulk lattice. The bulk concentration of donors is the value of n_d relevant for such calculations. Appropriate independent experimental values of n_d are available for zinc oxides but not for TiO₂ and it has previously been reported that insertion of these independent values of n_d into (II) predicts extent of electron transfer at activated ZnO surfaces which agree well with measured N₂O dissociation. This agreement was previously attributed to an indirect dissociative electron transfer mechanism but, in the light of the present discussion, it is seen to be also fully consistent with establishment of the boundary layer limited concentration of Zn⁰_(int) sites at the surface during vacuum activation, followed by direct electron transfer to N₂O when it was later admitted at room temperature.

The previously noted regeneration of reproducible activity for the N₂O-ZnO system by successive thermal activations of ZnO *in vacuo* may be understood on the basis of reestablishment of the boundary layer allowed surface concentration of excess zinc. Thermal regeneration of reproducible activity in the N₂O-TiO₂ system in the present study may likewise be understood in terms of boundary layer allowed surface concentration of Ti³⁺ centers, each bearing excess charge relative to the normal lattice. This hypothesis would lead to the expectation that expression II should define the number of (Ti³⁺-V_{ox}-Ti⁴⁺) centers present at 77°K upon a TiO₂ surface previously activated *in vacuo* at higher temperature. Direct dissociative electron transfer to N₂O *via* (3a) could then account for the adequate agreement noted above between expression II and observed N₂ formation.

The effect of preactivation in H₂ or CO in increasing dissociative electron transfer above that predicted by (II) is not necessarily inconsistent with the present hypothesis since surface reduction may lead to surface centers, *e.g.* (Ti³⁺-V_{ox}-Ti³⁺) which are not negatively charged relative to the perfect lattice. If, as suggested above, direct dissociative electron transfer *via* (3a) is the dominant factor in N₂O dissociation over TiO₂ preactivated in N₂ or CO, the justification given previously for Elovich kinetics, *viz.*, that they arose from electron transfer from bulk to negatively charged surface at increasing surface potential,^{13,23} would not suffice to explain the Elovich type kinetics in the inset in Figure 2. The question of whether electron redistribution within the surface may also lead to Elovich kinetics requires further study.

C. Effects of Other Gases on TiO₂. Admission of CH₃I or CH₃Cl to rutile samples, in the dark after their preactivation *in vacuo* at 670°K to obtain signals similar to Figure 4a, did not produce any significant change in intensity of the asymmetric signal with $g = 1.965$ and $g = 1.948$. This was unexpected since dissociative electron transfer processes analogous to (3a) and (3b) should be favored by the lower appearance potential for dissociative electron attachment to the methyl halides. Furthermore, previous studies revealed similarities in the effects of N₂O and of methyl halides in decreasing the intensity of an epr signal originating from electron excess centers in vacuum activated ZnO.^{14,15} In the present study the methyl halides also failed to affect the symmetric signal at $g \sim 2.00$ and this epr evidence for lack of chemical interaction between the methyl halides and TiO₂ was paralleled in our search for new chemical products from CH₃I-TiO₂ and CH₃Cl-TiO₂ systems. No product gases were observed upon contacting the methyl halide with vacuum activated rutile in the dark, nor did products appear when these samples were exposed to uv illumination. This contrast between ready electron transfer in the N₂O-TiO₂ system and total absence of corresponding effects in methyl halide-TiO₂ systems thus affords another direct illustration that successful electron transfer at these surfaces requires more than juxtaposition of an electron-rich surface and an electron attaching molecule. Present results do not unequivocally identify the selectivity factors which determine that electron transfer from rutile is possible to N₂O but not to methyl halides. Considerations of whether or not the adsorbed molecule (or fragments from it) can provide a stable irreversible electron trapping level must however play a role. Thus the strongly covalent nature of Ti-Cl or Ti-I bonds militate against dissociative electron transfer of type 1b to methyl halides on rutile. Conversely, the ease of formation of oxygen anions on TiO₂ surfaces favors dissociative electron transfer to N₂O, as in (1a). Effective non-dissociative electron attachment to molecular oxygen was also demonstrated in the present study by the fact that admission of O₂ completely removed all the epr signals shown in Figure 4a.

Conclusions

Both the epr studies and the observed dissociation of N₂O when contacted with TiO₂ confirm the occurrence of electron transfer at the N₂O(g)-rutile interface at room temperature. The apparent success of boundary layer theory in accounting for the extent of electron transfer to N₂O can be explained *either* in terms of indirect electron transfer *via* the conduction band, *or* in terms of direct

transfer from paramagnetic surface centers whose numbers were established during thermal activation. The electron transfer process at the rutile surface was more selective than electron transfer at ZnO surfaces or reported gas-phase dissociative electron attachment.

References and Notes

- (1) Work supported in part by the U. S. Air Force Office of Scientific Research through the European Office of Aerospace Research under Grant No. 71-2148.
- (2) (a) G. Heiland, E. Mollwo, and F. Stockman, *Solid State Phys.*, **8**, 191 (1959); (b) J. B. Goodenough, "Progress in Solid State Chemistry," H. Reiss, Ed., Vol. 5, Chapter 4, Pergamon Press, Oxford, 1971, p 344.
- (3) T. J. Gray, C. C. McCain, and N. G. Masse, *J. Phys. Chem.*, **63**, 472 (1959).
- (4) H. Chon and D. Prater, *Discuss. Faraday Soc.*, **41**, 380 (1966).
- (5) (a) O. W. Johnson, W. D. Ohlsen, and P. I. Kingsbury, Jr., *Phys. Rev.*, **175**, 1102 (1968); (b) J. H. Becker and W. R. Hosler, *ibid.*, **137**, A1872 (1965).
- (6) J. Schneider and A. Rauber, *Z. Naturforsch. A*, **16**, 712 (1961).
- (7) Y. Fujita and J. Turkevitch, *Discuss. Faraday Soc.*, **41**, 407 (1966).
- (8) R. D. Iyengar, M. Codell, J. Karra, and J. Turkevitch, *J. Amer. Chem. Soc.*, **88**, 5055 (1966).
- (9) M. Che, C. Naccache, B. Imelik, and M. Prettre, *C. R. Acad. Sci. Ser. C.*, **264**, 1901 (1967).
- (10) R. J. Kokes, *J. Phys. Chem.*, **66**, 99 (1962).
- (11) R. D. Iyengar and M. Codei, *Advan. Colloid Interface Sci.*, **3**, 365 (1972).
- (12) J. O. Cope and I. D. Campbell, *J. Chem. Soc., Faraday Trans. 1*, **69**, 1 (1973).
- (13) J. Cunningham, J. J. Kelly, and A. L. Penny, *J. Phys. Chem.*, **74**, 1992 (1970).
- (14) J. Cunningham, J. J. Kelly, and A. L. Penny, *J. Phys. Chem.*, **75**, 617 (1971).
- (15) J. Cunningham and A. L. Penny, *J. Phys. Chem.*, **76**, 2353 (1972).
- (16) D. J. Miller and D. Haneman, *Surface Sci.*, **24**, 639 (1971).
- (17) P. Roussel and S. J. Teichner, *Catal. Rev.*, **6**, 133 (1972).
- (18) M. Primet, M. Che, C. Naccache, M. F. Mathieu, and B. Imelik, *J. Chem. Phys. Physiochim. Biol.*, **67**, 1624 (1970).
- (19) J. M. Smith and W. E. Vehse, *Phys. Lett.*, **31A**, 147 (1970).
- (20) J. A. Pals, *Philips Res. Rep., Suppl.*, No. 7 (1972), and references therein.
- (21) (a) A. H. Beonstra and J. van Ruler, *Surface Sci.*, **4**, 141 (1966); (b) A. H. Beonstra, *Philips Res. Rep., Suppl.*, No. 3 (1968); (c) F. Meyer and J. M. Morabito, *J. Phys. Chem.*, **75**, 2922 (1971).
- (22) C. Ertl and H. Gerischer, in "Physical Chemistry," Vol. X, H. Eyring, D. Henderson, and W. Jost, Ed., Academic Press, London, 1970, Chapter 7.
- (23) P. B. Weisz, *J. Chem. Phys.*, **21**, 1531 (1953).

Effect of Silylation upon the Hydrogenating Activity of Supported Platinum Catalysts

Harold H. Kung, Beverley I. Brookes, and Robert L. Burwell, Jr.*

The Ipatieff Laboratory, Department of Chemistry, Northwestern University, Evanston, Illinois 60201 (Received October 23, 1973)

Publication costs assisted by the Petroleum Research Fund

Platinum/silica and platinum/alumina of low metal content and rather high dispersion have been silylated by treatment with hexamethyldisilazane in oxygen carrier or in hydrogen carrier at 100°. Hydrogenations on silylated and unsilylated catalysts have been studied in a liquid-phase batch reactor at 20° with cyclopentene and di-*tert*-butylacetylene and in a pulse reactor at -46.5° with ethylene. In the most straightforward case, the hydrogenation of cyclopentene, silylation in oxygen reduces the rate only about 20%. It is concluded that hydrogenation is predominantly confined to the surface of metallic platinum under our conditions, that is, that reaction of olefin with hydrogen atoms which have migrated from platinum to the surface of silica is of minor importance and that provision of a new channel of supply of olefin to the surface of platinum by initial adsorption of olefin on silica is similarly of low importance.

Introduction

Heterogeneous catalysts based on group VIII metals most often consist of tiny particles of metal, usually between 1.5 and 5 nm in diameter, dispersed upon the internal surface of a high area, porous support such as alumina or silica. As compared with metal powders, such supported catalysts exhibit a much lower rate of sintering and a much increased metallic surface area per unit weight of metal. In addition to providing such mechanical action, the support might affect the rates per unit area of metal surface and also selectivities of catalytic reactions. Some possible origins of such effects are (a) electronic interaction between metal particle and support; (b) effect of the support upon the morphology and exposure of crystal planes of the metal particles; (c) provision of channels of supply of reactant to the surface of the metal particles other than adsorption from the fluid phase, for example, in hydrogenation, by preliminary adsorption of olefin from

the fluid phase onto the support followed by migration of the olefin to the metal; (d) potentiation by the metal particles of reaction upon the support, for example, in hydrogenation, dissociative adsorption of hydrogen on the surface of the metal followed by diffusion of hydrogen atoms onto the support and addition there to molecules of olefin. Such a sequence has been called "spillover"¹⁻⁴ but few cases of spillover have been unequivocally demonstrated and the subject has engendered a number of controversies.

Indeed, the whole question of the effect of support has been a difficult one. It has not been possible to prepare catalysts containing sets of metal particles, identical in shape, size, etc., dispersed upon different supports. It will be noted that items a and b above involve the direct interaction between the metal particle and the support whereas c and d depend upon the free surface of the support. It would be interesting, then, to have two catalysts containing identical particles and differing only with re-

spect to the surface of the support, the bulk of the support being identical in both cases. We report here an approach to such a situation. We have compared Pt/SiO₂ and Pt/Al₂O₃ before and after silylation⁵ by hexamethyldisilazane [(CH₃)₃Si]₂NH which converts surface hydroxyl groups to trimethylsiloxy groups. Hydrogenations of cyclopentene and di-*tert*-butylacetylene in the liquid phase⁶ and of ethylene in the gas phase have been used to diagnose the effect of silylation.

Experimental Section

Catalysts. Davison Grade 59 silica gel, 270 to 400 mesh, was converted to Pt/SiO₂ by the ion exchange method of Dorling, Lynch, and Moss.⁷ In this, silica gel is ion exchanged with a "platinum ammine"⁸ prepared by reaction between aqueous ammonia and chloroplatinic acid, washed, dried in air at 68°, purged with hydrogen and heated slowly to 300°, held at 300° for 2 hr, and cooled in hydrogen.

Catapal SB (Continental Oil Co.) of 400+ mesh, calcined at 650° and rehydrated at 25°, was employed for Pt/Al₂O₃. It was impregnated with aqueous chloroplatinic acid, dried in air at 120°, calcined in oxygen at 500°, and reduced with hydrogen at 780°. After cooling in hydrogen, the catalyst was rehydrated by standing in a desiccator over water.

Pt/Filtros was prepared by impregnating 60–80 mesh Filtros FS-140 with aqueous chloroplatinic acid, drying at 120°, calcining in oxygen at 490°, reducing at 490°, and cooling in hydrogen. Filtros FS-140 (Filtros Corp., East Rochester, N. Y.) is a siliceous material of low area with micron-size pores and substantial pore volume. One would expect catalysts using it as a support to contain large crystallites of platinum.

Irreversible chemisorption of hydrogen at 25° was measured by a pulse technique on reduced catalyst treated with hydrogen at 25°, then heated to and cooled from 450° in helium. The technique was similar to that of Free⁹ but helium was used as the carrier gas and the hydrogen pulse was converted to one of water just before the catharometer by passage over hot copper oxide. Content in impurity in the gases was less than 0.1 ppm at the catalyst. The listed dispersions are 100 times the ratio of atoms of hydrogen chemisorbed to total atoms of platinum.

In silylation, the catalyst was first hydrated in an atmosphere of 100% relative humidity for 1 day. Oxygen was then passed over the catalyst at 150° for about 45 min. After cooling to 100°, hexamethyldisilazane was injected into the oxygen stream, 1 cc per gram of catalyst being employed. After all silazane had evaporated, the oxygen flow was continued for about 45 min, replaced briefly by a flow of nitrogen (helium in runs with ethylene) and that by one of hydrogen after which the catalyst was heated at 150° for 3–4 hr and then cooled in hydrogen. Some silylations were run using a flow of hydrogen throughout. Catalysts were analyzed for carbon content by combustion microanalysis.

Rates of Hydrogenation. Cyclopentene and di-*tert*-butylacetylene were hydrogenated in the liquid phase using a small reactor agitated in a rotary fashion at 1800 rpm.⁶ About 0.1 cc of cyclopentene or the acetylene, 10–40 mg of catalyst, 1.0 cc of solvent (cyclohexane), and a total pressure of 1 atm were employed. However, up to 200 mg of Pt/Filtros had to be used. The identity of rates from successive injections of reactant and in sandwiching runs with the acetylene between runs with cyclopentene estab-

TABLE I: Comparison of Rates of Hydrogenation on Silylated and Unsilylated Catalysts

| Silylated in | C % ^a | k _t ^b | k ₁₀ /k _t ^c |
|--|--------------------|-----------------------------|--|
| 0.5% Pt/SiO ₂ , Dispersion 54% | | | |
| None | 0.0 | 15.7 | 0.65 |
| O ₂ | 3.27 | 13 | 0.50 |
| O ₂ | 3.20 | 13 | 0.50 |
| H ₂ | 3.07 | 12 | 0.32 |
| H ₂ | 3.52 | 9.6 | 0.29 |
| 1.15% Pt/Al ₂ O ₃ , Dispersion 30% | | | |
| None | 0.0 | 6.7 | 0.89 |
| O ₂ | 1.08 | 4.6 | 0.40 |
| O ₂ | 0.73 | 4.6 | 0.40 |
| 4.1% Pt/Filtros, Dispersion 0.28% | | | |
| None | 0.0 | 11 | 0.54 |
| O ₂ | 0.031 ^d | 8.5 | 0.37 |

^a % carbon from combustion microanalysis. ^b Turnover number in molecules of cyclopentene hydrogenated per sec per surface Pt atom. Correction has been made for the increase in weight of the catalyst consequent to silylation. ^c Ratio of rate of hydrogenation of di-*tert*-butylacetylene to that of cyclopentene. The rate of hydrogenation of di-*tert*-butylacetylene is that of its consumption not that of the consumption of hydrogen which is larger because of the formation of alkane. Rates of consumption of hydrogen were corrected to the listed values by product composition data. In ref 6, rates of hydrogen consumption were employed. ^d Determined by gas chromatographic analysis of carbon dioxide formed by combustion *in situ*.

lished that the runs reported here were free from the effects of extrinsic poisons. We have previously shown that the rates are not influenced by the mass transport of hydrogen.⁶ All rates were strictly zero order in olefin to at least 99% conversion and rates were proportional to the quantity of catalyst. Rates are reported as turnover numbers, the number of molecules of olefin hydrogenated per second per surface platinum atom (more exactly, per hydrogen atom chemisorbed as described above). Results are presented in Table I.

Rates of hydrogenation of ethylene on 0.5% Pt/SiO₂ at -46.5° were determined in the gas phase by the pulse technique. Rehydrated Pt/SiO₂ was placed in a 3.4-mm i.d. tube (giving a bed length of a few mm between Pyrex glass wool plugs), heated in oxygen at 150°, silylated at 100°, purged with helium, reduced with hydrogen at 150°, and cooled to -46.5° in hydrogen. An injection valve purged with helium to avoid contamination was used to inject a pulse of ethylene plus hydrogen (1:2 mole ratio) at a selected total pressure into a stream of very pure hydrogen flowing at about 38 cc/min which then passed over the catalyst following which the pulse was analyzed chromatographically for ethane and ethylene. In the control experiments, the catalyst treatment was the same except that there was no treatment with disilazane. Ten successive pulses of ethylene were passed over the catalyst in each case. The quantity of ethylene in some pulses varied from that of the standard pulse. The total number of molecules of ethane formed was independent of the initial pressure of the pulse and of the serial number of the pulse. The observed pulse width was independent of the initial pressure of the pulse. No loss of hydrocarbon to the catalyst could be detected but a loss of one molecule of ethylene per 20 surface platinum atoms could probably not have been observed. Results of these experiments appear in Table II.

We have also silylated a Pt/SiO₂ catalyst before reduction. A 0.35% Pt/SiO₂ catalyst was prepared by ion ex-

TABLE II: Pulse Hydrogenation of Ethylene on Silylated and Unsilylated Pt/SiO₂ at -46.5°

| C % | Wt of catalyst, mg | Surface Pt atoms × 10 ¹⁸ | C ₂ H ₄ molecules per pulse × 10 ¹⁸ | Conversion to ethane % | Turnover no. ^d |
|-------------------|--------------------|-------------------------------------|--|------------------------|---------------------------|
| 0 ^a | 8.35 | 0.0685 | 3.24 | 12.5 | 1.2 |
| 3.34 ^b | 7.11 | 0.0585 | 3.25 | 9.9 | 1.1 |
| 0 ^a | 15.52 | 0.127 | 11.1 | 12.3 | 1.4 |
| 2.80 ^c | 15.52 | 0.127 | 11.1 | 6.6 | 0.77 |

^a Unsilylated reference catalyst. ^b A fresh sample of catalyst silylated *in situ*. ^c The catalyst of the previous run silylated *in situ* but without rehydration after the first runs. ^d See text.

change, dried, put in flowing oxygen at 100°, silylated, purged with nitrogen, and reduced with hydrogen at a temperature rising to 250°. The resulting material was rather inactive in the hydrogenation of cyclopentene.

In the general case, calculation of rate constants from conversions in a pulse reactor requires knowledge of the shape of the pulse and of the rate at which the pulse moves through the catalyst bed. In the present case, however, hydrogenation is zero order in ethylene² and all that need be known about pulse shape is the width of the pulse at its base.³ In separate experiments, pulse shapes were measured as close as possible to the end of the catalyst bed. We estimate that the width of the pulse in the gas phase just beyond the catalyst bed was 4.8 sec for the pulse containing 3.24×10^{18} molecules of ethylene and 7.5 sec for that containing 11.1×10^{18} , but these figures are of low precision. The geometries of the catalyst tube were different for the two pulse sizes.

In separate experiments, the transit time of nitrogen and ethylene pulses at -46.5° were measured in a system which contained a silica gel bed 35.2 mm long in a tubing of internal diameter 3.4 mm. The mass of the silica gel was 0.115 g. The transit time for a pulse of nitrogen was 60 sec. The transit time of a pulse of ethylene varied with its size. Extrapolation to zero molecules of ethylene gave a transit time about 3.4 times that of nitrogen. With 1.0×10^{18} molecules of ethylene, the factor was 2.1, with 3.3×10^{18} molecules it was 1.7, and with 10.0×10^{18} it was 1.4. The retention time in the Pt/SiO₂ bed was thus substantial. After silylation of the silica bed, the factor was about 1.15 extrapolated to zero ethylene and it was indistinguishable from unity above 1.0×10^{18} . The pulse widths beyond the silica gel bed for nitrogen on both silylated and unsilylated silica and for ethylene on silylated were all the same. However, the width of an ethylene pulse was larger on the unsilylated silica (about twice as large with 3.2×10^{18} molecules of ethylene). Thus, the pulse width in the unsilylated Pt/SiO₂ should have been a little larger than in the silylated but not very much since the bed length was but a few mm *vs.* 35.2 mm in the experiments just described.

Discussion

Tables I and II present comparisons of rates of hydrogenation of cyclopentene and di-*tert*-butylacetylene in the liquid phase and of ethylene in the gas phase on silylated and unsilylated catalysts. A carbon content of 3.3% on silylated Davison Grade 59 silica gel corresponds to 1.7 trimethylsilyl groups per nm² taking the specific area as 325 m² per g. Since the cross sectional area of neopentane is about 0.6 nm² in physical adsorption,¹⁰ silylation of Pt/SiO₂ produced an essentially complete monolayer of tri-

methylsilyl groups. Coverage on Pt/Al₂O₃ is lower. On the more extensively silylated sample there are 0.7 groups per nm² taking the specific area as 250 m²/g.¹¹ All catalysts were hydrophobic and the Pt/SiO₂ could not be made to sink in water.

Let us first consider the Pt/SiO₂ and the Pt/Filtros catalysts silylated in oxygen. It is striking that silylation results in reduction of the rate of hydrogenation of cyclopentene by only 20%. Such a small effect of exposure to hexamethyldisilazane at 100° is perhaps surprising. During this exposure the 99.9+% of the surface of the catalyst which is silica is converted from a highly hydrophilic to a strongly hydrophobic surface. We reject the idea of hydrogen spillover on the surface covered with methyl groups. This would require dissociative adsorption of hydrogen on a methylated surface to be thermodynamically favorable.

No surface platinum atom of a Pt/SiO₂ catalyst whose dispersion is 54% can be many platinum atoms removed from the nearest free surface of silica or silylated silica. On Pt/Filtros, however, the crystallites of platinum are much larger and the average surface atom of platinum is much farther removed from the exposed surface of the support. The nearly identical effect of silylation with the two catalysts would indicate that possibility c of the Introduction, a channel of supply of olefin to platinum proceeding on the surface of silica, does not contribute importantly to the rate.

Thus, it is unlikely that the 20% reduction in the rate of hydrogenation is the result of compensating effects: elimination of spillover serving to decrease the rate and provision of a new channel of supply of olefin serving to increase the rate. Under the conditions of our experiments, we conclude that the silica surface contributes insignificantly to the rate of hydrogenation and that hydrogenation involves only the surface of the platinum.

As shown in Table I, the rate of hydrogenation of di-*tert*-butylacetylene is decreased relatively more by silylation than is that of cyclopentene both on Pt/SiO₂ and on Pt/Filtros. This suggests that the reduction in rate of the hydrogenations of cyclopentene and the acetylene results mainly from a small degree of contamination of the surface of platinum by residues attached during silylation. One would expect that the degree of blocking by such residues would be greater for adsorption of the larger and more hindered acetylene than of cyclopentene.

In general, similar conclusions apply to Pt/Al₂O₃.

Silylation in hydrogen results in a somewhat greater degree of reduction in the rate of hydrogenation both of cyclopentene and of the acetylene. We have avoided silylation in an inert atmosphere on the view that such silylation would be more likely to contaminate an unprotected platinum surface. During silylation in either oxygen or hydrogen the platinum surface will be covered by adsorbed layers of oxygen or hydrogen. It appears that the adsorbed layer of oxygen is somewhat more effective in protecting the platinum surface. In particular, adsorbed oxygen may better protect edges of crystallites against blockage. The adsorbed layer of oxygen would project from the surface of platinum and would then be removed during subsequent treatment with hydrogen.

In addition one might expect some contribution to reduction in the rate of hydrogenation on Pt/SiO₂ and Pt/Al₂O₃ by pore blocking. Sufficiently narrow necks in the pore structures might be blocked by silylation and such blockage should more affect the bulkier di-*tert*-butylacetylene than cyclopentene. However, the near identity of

the degree of reduction of rates of hydrogenation on Pt/Filtros and Pt/SiO₂ suggests that this is not a major effect since Filtros has pores primarily in the micron range.

The strong binding of olefins and arenes to silanol groups is much reduced by silylation.¹² As described in the Experimental Section, we found that an ethylene pulse moves much more slowly through the unsilylated catalyst than through the silylated one. However, a pulse narrows as it enters an adsorbent bed and moves with a smaller linear velocity. These effects compensate so that, to a first approximation, a horizontal plane normal to the direction of flow is exposed to ethylene for the same length of time both in the gas just before the bed and in the bed itself. That is, the linear width changes on entering the catalyst bed but the "time" width does not. Thus any element perpendicular to the direction of flow is exposed to ethylene for the same time in the gas phase and in both the silylated and unsilylated catalyst. As the pulse leaves the catalyst bed, its linear velocity and width increase to the values obtaining just before the bed. In practice, of course, the pulse widens as it passes through a bed of adsorbent and we found the widening to be greater with the unsilylated than with the silylated catalyst as would be expected because of the greater residence time in the former. We believe that the effect of the difference in such widening is small because the high activity of the catalysts required us to use a catalyst bed only a few mm long. In summation, we consider the data from the pulse experiments to be subject to more uncertainties in interpretation than those with the liquid-phase reactor. Nevertheless, the pulse experiments do establish that the effect of silylation upon the hydrogenation of ethylene is rather small. They also suggest that the silylated catalyst might

be used advantageously where it is desired to minimize adsorption of olefin on the support.

From the near identity of rates of hydrogenation of ethylene on Pt/SiO₂ and on evaporated films of platinum, Schlatter and Boudart had also concluded that spillover of hydrogen contributed negligibly to the rate of hydrogenation.² This conclusion, of course, involves the conclusion that the hydrogenation of ethylene on platinum is structure insensitive. The technique of the present paper does not involve the question of structure sensitivity.

Acknowledgment. Acknowledgment is made to the donors of the Petroleum Research Fund, administered by the American Chemical Society, for the support of this work.

References and Notes

- (1) W. C. Neikam and M. A. Vannice, *Proc. Int. Congr. Catal.*, 5th, 609 (1973).
- (2) J. C. Schlatter and M. Boudart, *J. Catal.*, **24**, 482 (1972).
- (3) A. J. Moffat, *J. Catal.*, **27**, 456 (1972).
- (4) G. E. E. Gardes, G. Pajonk, and S. J. Teichner, *C. R. Acad. Sci., Ser. C*, **277**, 191 (1973).
- (5) J. Bohemen, S. H. Langer, R. H. Perrellt, and J. H. Purnell, *J. Chem. Soc.*, 2444 (1960).
- (6) R. L. Burwell, Jr., D. Barry, and H. H. Kurg, *J. Amer. Chem. Soc.*, **95**, 4466 (1973).
- (7) T. A. Dorling, B. W. J. Lynch, and R. L. Moss, *J. Catal.*, **20**, 190 (1971).
- (8) This is not a solution containing Pt(NH₃)₄²⁺ as implied in ref 7 but a mixture of Pt(NH₃)₅Cl³⁺ and Pt(NH₃)₆⁴⁺ as indicated in Gmelin, "Handbuch der Anorganischen Chemie," 8 Auflage, Platin, Teil D, 1957, pp 480 and 493, and confirmed by experimental work in this laboratory. At the pH of the ion exchange both ions are present primarily as the conjugate bases.
- (9) J. Freil, *J. Catal.*, **25**, 139 (1972).
- (10) A. L. McClellan and H. F. Harnsberger, *J. Colloid Interface Sci.*, **23**, 577 (1967).
- (11) "Catapal Aluminas," Continental Oil Company, 1971.
- (12) S. J. Gregg and K. S. W. Sing, "Adsorption, Surface Area, and Porosity," Academic Press, London, 1967, p 96.

Flash Photolysis and Time-Resolved Mass Spectrometry. III. Termolecular and Surface Recombinations of Ground State Iodine Atoms¹

Richard T. Meyer

Sandia Laboratories, Albuquerque, New Mexico 87115 (Received June 18, 1973; Revised Manuscript Received January 28, 1974)

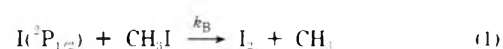
Publication costs assisted by Sandia Laboratories

The formation of molecular iodine after the flash photolysis of methyl iodide was studied under conditions for which termolecular recombination and surface recombination of iodine atoms separately dominated the reaction kinetics. Using NO as a deactivator of I(²P_{1/2}) atoms and as a third body for recombination, the rate constant for termolecular recombination was measured as 2.4 (±1.4) × 10¹³ M⁻² sec⁻¹. Surface recombination occurred when helium was used as a diluent and when the walls of the reaction vessel were not wetted with H₃PO₄. The surface recombination was first order and diffusion controlled. The measured diffusion coefficient was 0.23 cm² sec⁻¹, calculated for 300 K and 1 atm.

1.0. Introduction

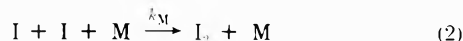
The flash photodecomposition of methyl iodide has been shown to yield methyl radicals² and excited state iodine atoms.³ We have previously reported studies of the

bimolecular reaction of excited iodine atoms with methyl iodide to yield molecular iodine^{4a}

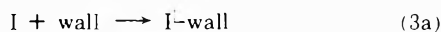


and also studies of the reactions of the methyl radicals to form methane, ethane, ethylene, and acetylene.^{4b}

The formation of gaseous molecular iodine by termolecular recombination



and by surface recombination



are two other processes which occur in the methyl iodide system. The source of the ground state iodine atoms are (i) the flash photodecomposition of methyl iodide to the extent of about 16% of the total yield of iodine atoms,⁵ (ii) the collisional deactivation of excited atoms by CH₃I, I₂, and other third bodies,⁶⁻¹¹ and (iii) the collisional deactivation at the walls of the reaction vessel.^{7,12,13}

In this paper, we report our studies of reactions 2 and 3. Experiments were performed in order to understand all I₂-forming processes in the methyl iodide system and to define under what conditions any one I₂-forming reaction would predominate over the other reactions. The rate constant for termolecular recombination with NO as the third body has been measured ($2.4 (\pm 1.4) \times 10^{13} M^{-2} \text{sec}^{-1}$) and compared to Porter's value ($3.0 \times 10^{13} M^{-2} \text{sec}^{-1}$).¹⁴ Surface recombination of iodine atoms has been found to follow a first-order, diffusion-controlled mechanism. Re-evaluations of the rate constants for the bimolecular chemical reaction 1 and collisional deactivation of I(²P_{1/2}) atoms are presented in another paper.¹⁵

2.0. Principles of Analysis

2.1. Termolecular Recombination. Porter, *et al.*,^{16,17} have shown that the homogeneous gas-phase recombination of iodine atoms occurs *via* the formation of intermediate complexes between the iodine atom and the third body.



In the case of NO as a third body, the NOI complex was actually observed in spectroscopic absorption for high temperatures of I and NO.¹⁴ However, at the low concentrations of (I) and (M) used in the experiments reported here, the equilibrium reaction 4 is sufficiently far to the left that the recombination can be reliably described by reaction 2 and the following rate equation

$$d(I_2)/dt = k_M(I)^2(M) \quad (6)$$

where $k_M(M)$ is a summation for all third bodies in a mixture. Measurement of the formation of I₂ as a function of time provides the means of evaluating $k_M(M)$, since

$$(I)_t = 2[(I_2)_t - (I_2)_i] \quad (7)$$

2.2. Surface Recombination. When helium was used as the inert third body and when the internal surface of the reaction vessel was not coated with a wetting agent, the present experiments revealed a very slow I₂-forming process which was inversely proportional to gas pressure. This process has been identified as a first-order, diffusion-controlled surface recombination of iodine atoms. Reasonable agreement between theory and experiment was obtained using a Chapman-Enskog model¹⁸ for xenon diffusing in helium. At 310 K, which is the estimated tempera-

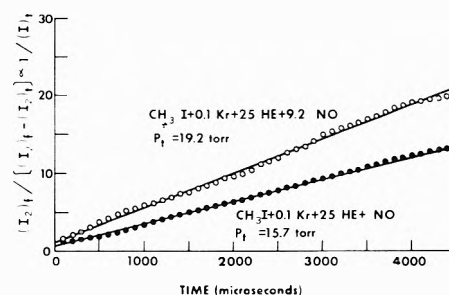


Figure 1. Second-order plot of I₂ formation due to termolecular atom recombination in presence of NO. H₃PO₄-wetted black glass reaction vessel.

TABLE I: Rate Constants Measured for Termolecular Recombination of I Atoms in Presence of NO as the Third Body^a

| Expt no. | P _T , Torr | (CH ₃ I) ₀ × 10 ⁵ , M | (NO) ₀ × 10 ⁵ , M | % decomposition of CH ₃ I | k _{NO} × 10 ⁻¹³ , M ⁻² sec ⁻¹ |
|----------|-----------------------|--|---|--------------------------------------|---|
| 2161 | 32.1 | 6.29 | 6.29 | 2.6 | 1.84 |
| 2162 | 31.4 | 6.15 | 6.15 | 2.7 | 0.80 |
| 2163 | 30.8 | 6.04 | 6.04 | (2.6) ^b | 0.88 |
| 2165 | 30.3 | 5.93 | 5.93 | (2.6) ^b | 1.35 |
| 2166 | 29.8 | 5.85 | 5.85 | (2.6) ^b | 1.14 |
| 2167 | 29.4 | 5.77 | 5.77 | (2.6) ^b | 1.38 |
| 2169 | 16.0 | 3.14 | 3.14 | 2.5 | 4.49 |
| 2170 | 15.7 | 3.08 | 3.08 | 2.4 | 6.33 |
| 2171 | 15.4 | 3.03 | 3.03 | 2.5 | 6.51 |
| 2173 | 19.5 | 2.93 | 26.9 | 3.6 | 0.79 |
| 2174 | 19.2 | 2.88 | 26.5 | 3.6 | 0.82 |
| Av value | | | | | 2.4 |

^a H₃PO₄-wetted opaque vessel. ^b Assumed value based upon data of experiments no. 2161 and 2162.

ture of the present diffusion studies

$$D_{12} = \frac{0.533}{p(\text{in atm})} \text{cm}^2 \text{sec}^{-1} \quad (8)$$

The effective rate constant for the surface reaction is obtained from the model presented by Mitchell and Zemansky.¹⁹ The surface reaction rate for a cylindrical reaction volume of finite length with a surface efficiency of unity for atom recombination is given by

$$k_s = \left\{ \frac{\pi^2}{l^2} + \frac{5.78}{r^2} \right\} D_{12} \text{sec}^{-1} \quad (9)$$

where in our experiments the length, l , and the radius, r , were the same and equal to 1.5 cm. Therefore

$$k_w(M) = \frac{k_s p}{RT} = 0.16 M^{-1} \text{sec}^{-1} \quad (10)$$

when the total pressure is expressed in terms of the total molar concentration, (M).

3.0. Experimental Results

Detailed descriptions of the apparatus and technique have been previously reported.^{4,15,20-23}

3.1. Termolecular Recombination of Atoms. Nitric oxide was selected as the third body for the quantitative measurement of a termolecular rate constant because it is a very effective quencher (deactivator) of excited iodine atoms²⁴ and the most efficient chaperon (third body) for recombination.¹⁴

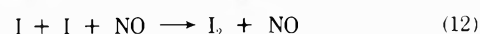
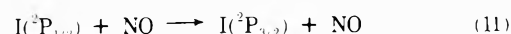


TABLE II: Summary of Rate Constants Calculated to Evaluate the Reaction Order of I₂ Formation in the Unwetted Opaque Vessel^a

| Expt no. | Reactant mixture | P _T , Torr | I(² P _{1/2}) + CH ₃ I k _B × 10 ⁻⁶ , M ⁻¹ sec ⁻¹ | I + I + M k _M × 10 ⁻⁹ , M ⁻² sec ⁻¹ | I + I + wall k _w (M) × 10 ² , M sec ⁻¹ |
|-------------------|----------------------------------|-----------------------|--|---|---|
| 0 to 4 msec Data | | | | | |
| 1716 | CH ₃ I + 0.5Kr + 25He | 40.2 | 3.4 | 15 | 26 |
| 1718 | CH ₃ I + 0.5Kr + 25He | 39.4 | 6.7-8.3 | 33 | 44-55 |
| 1720 | CH ₃ I + 0.5Kr + 25He | 19.6 | 0.66 | 3.9-7.0 | 1.1 |
| 1722 | CH ₃ I + 0.5Kr + 25He | 19.3 | 10.3 | 80 | 16 |
| 1730 | CH ₃ I + 0.5Kr + 51He | 34.6 | 3.4 | 9.9-12 | 9.3 |
| 0 to 35 msec Data | | | | | |
| 1710 | CH ₃ I + 0.5Kr + 25He | 43.1 | 1.1 | 4.5 | 8.9 |
| 1712 | CH ₃ I + 0.5Kr + 25He | 42.3 | 1.1 | 2.8 | 8.6 |
| 1724 | CH ₃ I + 0.5Kr + 25He | 19.0 | 2.6 | 21 | 4.0 |
| 1726 | CH ₃ I + 0.5Kr + 25He | 18.5 | 4.3-5.7 | 56 | 6.3-8.3 |
| 1728 | CH ₃ I + 0.5Kr + 51He | 35.4 | 1.7-2.1 | 5.8 | 4.5-5.5 |
| 1734 | CH ₃ I + 0.5Kr + 51He | 34.6 | 1.7 | 7.9 | 4.1 |
| | | | | | Av 6.3 |

^a Best agreement for the late time data is obtained for diffusion-controlled, surface recombination of atoms.

Reaction 11 was expected to be considerably faster than any other reaction of I(²P_{1/2}); in addition, reaction 12 should account for most all of the I₂ formation. Therefore, the second-order behavior prescribed by eq 6 and 7 should be followed.

Experiments were performed in which the NO/CH₃I ratio and the total pressure were varied. Figure 1 shows the second-order plots for two experiments, using data points taken off smooth curves drawn through the spectrometer-measured ion intensities for I₂ as a function of time. Figure 1 indicates that the reaction rate does increase upon the addition of more NO. A tabulation of the third-order rate constants calculated for 11 nitric oxide experiments is given in Table I. The total per cent decomposition of CH₃I was measured and used to calculate the absolute value of (I₂)_t, assuming that reaction 12 was the only source of I₂. The contributions to termolecular recombination by Kr, I₂, and CH₃I could be neglected in the data analysis because the values of k_M(M) are three, three, and five orders of magnitude, respectively, less than k_{NO}(NO).¹⁷ An average value of k_{NO} equal to 2.4 (±1.4) × 10¹³ M⁻² sec⁻¹ was obtained.

3.2. Surface Recombination of Atoms. The occurrence of the surface recombination of iodine atoms was first recognized in a set of experiments which were designed to measure both the bimolecular reaction of excited iodine atoms with methyl iodide and the termolecular recombination of atoms. A black glass reaction vessel²¹ was being used for the first time and without any H₃PO₄ wetting.²⁵ Two groups of experiments were conducted: one group used 50-μsec data sampling intervals and recorded data for 4 msec; the second group used 800-μsec data sampling intervals and recorded data for 35 msec. For each time group of experiments, the reaction conditions were varied first by decreasing the total pressure to one-half at the same He/CH₃I ratio and second by increasing the He/CH₃I ratio by adding helium and increasing the total pressure.

The rapid initial formation of I₂, which is characteristic of the excited iodine atom reaction 1, was not observed. The long time (0-35-msec) formation of I₂ was found to be first order with respect to iodine atoms and inversely proportional to total pressure, as shown in Figure 2. A quantitative summary of rate constants, calculated assuming

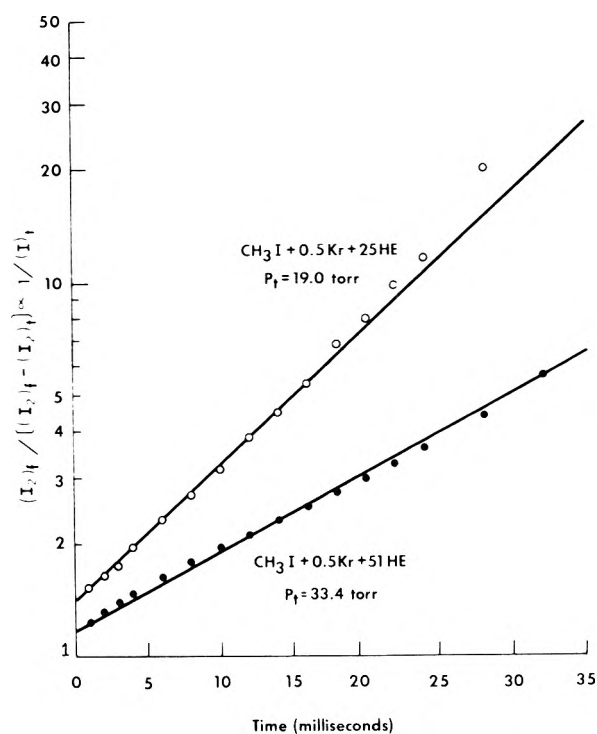


Figure 2. First-order plot of I₂ formation due to surface recombination of I atoms as a function of added He and total pressure. Unwetted black glass reaction vessel.

the three different mechanisms of I₂ formation, is shown in Table II. Data accumulated in the initial stages (0-4-msec) of the reaction showed no consistency with any of the three mechanisms. However, the 0-35-msec data provided agreement within a factor of 2 among the rate constants calculated for a first-order, diffusion-controlled surface recombination of atoms.

An average value of k_w(M) = 0.063 M sec⁻¹ was obtained, which compares reasonably well for a diffusion measurement to the Chapman-Enskog value of 0.16 M sec⁻¹. Discrepancies of this magnitude are not uncommon for theoretical calculations of halogen atom interactions with inert gases when the Lennard-Jones (6-12) potential is used.²⁶ Donovan and Husain^{7,12} and Abrahamson, *et al.*,¹³ have reported a similar occurrence of diffusion of ex-

cited iodine atoms to the reaction vessel walls in inert gas systems. Conversion of our rate constant $k_w(M)$ to a diffusion coefficient yields a value of $0.23 \text{ cm}^2 \text{ sec}^{-1}$ at 300 K and 1 atm for atomic iodine in helium; the value determined by Abrahamson, *et al.*, is $0.95 \text{ cm}^2 \text{ sec}^{-1}$.

The nonunity values of the intercepts in Figure 2 probably indicates that some I₂ was formed early in time by the excited iodine atom reaction 1 before collisional deactivation of the excited atoms occurred.

4.0. Conclusions

The agreement obtained in this study between the measured and the literature or theoretical values of the rate constants for both the termolecular and the surface recombination of iodine atoms provides additional evidence for the capability of the flash photolysis and time-resolved mass spectrometry technique to yield quantitative kinetic data.

The complexity of the methyl iodide system in flash photolysis and in continuous photolysis is obvious from the large number of articles in the literature. In most previous studies, however, the fate of the iodine atoms has been considered to be simply the termolecular recombination to I₂ by whatever third bodies were present. We have now shown that the deactivation of excited iodine atoms and the formation of molecular iodine can be as complex as the chemistry of the methyl radical reactions. In particular, I₂ may be formed by the bimolecular reaction of excited iodine atoms with methyl iodide, by the termolecular recombination of atoms, or by the surface recombination of atoms. The experimental conditions determine which reaction dominates.

Surface recombination dominates when an easily diffusible medium such as helium is used as a diluent, when the reaction vessel is small and the walls are untreated and exhibit a high efficiency for surface reactivity, and when the relative partial pressures of efficient chaperon molecules are low. Termolecular recombination dominates when diffusion and surface reaction are negligible, when effective quenching molecules for I(²P_{1/2}) deactivation are present, and when efficient chaperon molecules are available for IM complex formation. Bimolecular chemical reaction dominates when surface reaction is made negli-

ble by a wetting agent and when an ineffective quenching chaperon molecular such as helium is used to dilute the system. The latter conditions were employed in our earlier reports.^{3,15}

Acknowledgments. The author gratefully acknowledges D. M. Haaland and F. K. Truby for valuable discussions and J. M. Freese for assistance with the experiments.

References and Notes

- (1) This work supported by the U. S. Atomic Energy Commission.
- (2) For a review of the methyl radical reactions, see J. R. Major and J. R. Simons, *Advan. Photochem.*, **2**, 137 (1964).
- (3) J. V. V. Kasper and G. C. Pimentel, *Appl. Phys. Lett.*, **5**, 231 (1964).
- (4) (a) R. T. Meyer, *J. Chem. Phys.*, **46**, 4146 (1967); (b) *J. Phys. Chem.*, **72**, 1533 (1968).
- (5) S. J. Riley and K. R. Wilson, *Discuss. Faraday Soc.*, **53**, 132 (1972).
- (6) R. J. Donovan and D. Husain, *Nature (London)*, **206**, 171 (1965).
- (7) R. J. Donovan and D. Husain, *Trans. Faraday Soc.*, **62**, 11 (1966).
- (8) R. J. Donovan, F. G. M. Hathorn, and D. Husain, *J. Chem. Phys.*, **49**, 953 (1968).
- (9) R. J. Donovan, F. G. M. Hathorn, and D. Husain, *Trans. Faraday Soc.*, **64**, 3192 (1968).
- (10) R. J. Donovan and D. Husain, *Trans. Faraday Soc.*, **62**, 2023 (1966).
- (11) J. J. Deakin and D. Husain, *J. Chem. Soc., Faraday Trans. 2*, **68**, 1603 (1972).
- (12) R. J. Donovan and D. Husain, *Trans. Faraday Soc.*, **62**, 1050 (1966).
- (13) E. W. Abrahamson, L. J. Andrews, D. Husain, and J. R. Wiesenfeld, *J. Chem. Soc., Faraday Trans. 2*, **68**, 48 (1972).
- (14) G. Porter, Z. G. Szabo, and M. G. Townsend, *Proc. Roy. Soc., Ser. A*, **270**, 493 (1962).
- (15) D. M. Haaland and R. T. Meyer, *Int. J. Chem. Kinet.*, in press.
- (16) G. Porter and J. A. Smith, *Proc. Roy. Soc., Ser. A*, **261**, 28 (1961).
- (17) G. Porter, *Discuss. Faraday Soc.*, **33**, 198 (1962).
- (18) J. O. Hirschfelder, C. F. Curtiss, and R. B. Bird, "Molecular Theory of Gases and Liquids," Wiley, New York, N. Y., 1954, pp 539, 567, 1110, 1127.
- (19) A. C. G. Mitchell and M. W. Zemansky, "Resonance Radiation and Excited Atoms," Cambridge University Press, New York, N. Y., 1934, p 247.
- (20) R. T. Meyer, *J. Sci. Instrum.*, **44**, 422 (1967); *J. Chem. Phys.*, **46**, 967 (1967).
- (21) J. M. Freese and R. T. Meyer, *Rev. Sci. Instrum.*, **39**, 1764 (1968).
- (22) R. T. Meyer, *Rev. Sci. Instrum.*, **35**, 1064 (1964).
- (23) R. T. Meyer, C. E. Olson, and R. R. Berlind, paper presented at the Fourteenth Annual Conference on Mass Spectrometry and Allied Topics, Dallas Texas, 1966. Sandia Laboratories Report No. SC-R-66-928, Albuquerque, N. Mex., Aug 1966.
- (24) R. J. Donovan and D. Husain, *Trans. Faraday Soc.*, **62**, 2987 (1966).
- (25) E. A. Ogryzlo, *Can. J. Chem.*, **39**, 2556 (1961).
- (26) J. A. Blake, R. J. Browne, and G. Burns, *J. Chem. Phys.*, **53**, 3320 (1970).

Pulse Radiolytic Study of Ni^+ . Nickel-Carbon Bond Formation

M. Kelm, J. Lilie, A. Henglein,* and E. Janata

Hahn-Meitner-Institut für Kernforschung Berlin GmbH, Bereich Strahlenchemie, 1 Berlin 39, Germany

(Received November 20, 1973)

Publication costs assisted by Hahn-Meitner-Institut für Kernforschung Berlin

Deaerated aqueous solutions of NiSO_4 were irradiated with ^{60}Co γ rays or by single pulses of high-energy electrons. The solutions contained aliphatic alcohols, diethyl ether, *c*-pentane, or formate as scavengers for OH and H radicals. Metallic nickel was precipitated from some of these solutions upon γ irradiation. Reactions between Ni^+ and organic radicals leading to organic nickel compounds were observed in the pulse experiments using both optical and conductimetric detection methods. The rate constants of reactions of Ni^+ with organic radicals are of the order of $10^9 \text{ M}^{-1} \text{ sec}^{-1}$. The reaction $2\text{Ni}^+ \rightarrow \text{Ni} + \text{Ni}^{2+}$ was not observed under these conditions. Nickel formation is attributed to the attack of radicals on the organic nickel compounds. These compounds can be oxidized by H_2O_2 with rate constants of 10^4 – $10^6 \text{ M}^{-1} \text{ sec}^{-1}$. They react slowly with water, the lifetime being somewhat less than 1 sec in the cases of methanol and ethanol and longer in the other cases. Only the $\cdot\text{CH}_2\text{C}(\text{CH}_3)_2\text{OH}$ radical does not form a complex but is rapidly reduced to yield isobutene. The complex formed from Ni^+ and CO_2^- rapidly picks up a proton.

Introduction

Abnormal valency states of metals which play an important role as inhibitors or catalysts in chemical reactions can be produced by reactions of the hydrated electron with metal ions. Divalent metal cations such as Ni^{2+} are reduced this way to form unstable monovalent cations such as Ni^+ . These monovalent ions have an absorption band at 300 nm and act as powerful reductants. Ni^+ , for example, was found to react with oxygen, nitrous oxide, hydrogen peroxide, and haloaliphatic compounds. The rate constants of such processes were measured in pulse radiolytic experiments by recording the decay of the Ni^+ absorption in solutions containing both Ni^{2+} and the reactant.¹⁻⁸ The products of these reactions have not yet been investigated, however.

Irradiation of a solution containing a divalent metal ion often leads to the precipitation of the corresponding metal.⁹ The yield is generally significant only if an organic OH scavenger is simultaneously present. Some metal ions such as, Co^{2+} , Ni^{2+} , and Cu^{2+} , were found to increase the yield of formaldehyde at the expense of glycol during the radiolysis of methanol. This effect was ascribed to complex formation between the divalent metal ions and methanol radicals, $\dot{\text{C}}\text{H}_2\text{OH}$.¹⁰ An interaction of Ni^+ ions also formed in these solutions with methanol radicals was not considered.

In the present investigations, steady γ irradiation and pulse radiolysis experiments were carried out to obtain more detailed information about the mechanisms of the reduction of Ni^{2+} in aqueous solutions and of reactions of Ni^+ with various radicals produced simultaneously from dissolved organic solutes. In the γ irradiations, the amount of nickel precipitated under various conditions was determined. In the pulse radiolysis experiments, conductimetric observation of the intermediates in addition to the conventional optical absorption measurements yielded decisive information. Earlier conductimetric observations had confirmed the reaction of the hydrated electron with Ni^{2+} , but no conclusion about the mechanism of formation of metallic nickel could be drawn from these measurements.¹¹

Experimental Section

All solutions were prepared with triply distilled water. NiSO_4 , methanol, *c*-pentane, ethanol, 2-propanol, and diethyl ether (Merck p.a.) and sodium formate (Riedel p.a.) were used without further purification. The solutions were flushed with purified argon for about 2 hr to remove air.

The solutions (1.925 l.) were irradiated in the field of a 20,000 Ci ^{60}Co source at a dose rate of 5.5×10^5 rads/hr. The precipitated nickel was filtered under exclusion of air, washed with water and with acetone, dried under vacuum, and its weight determined. In order to check whether the precipitate was pure metallic nickel, the precipitate was dissolved in dilute hydrochloric acid and titrated complexometrically with EDTA (titriplex III).

In some of the experiments, the pH of the solution was kept constant during irradiation by automatic addition of small amounts of 1 M NaOH solution. The pH of the solution was continuously measured with a glass electrode. The output voltage of the pH meter (Knick, Model 26) was fed into a comparator controlling a small pump which automatically injected the NaOH solution. The solution was flushed with argon during irradiation in order to assure rapid distribution of the injected liquid.

The pulse radiolysis equipment has already been described¹² (1.6-MeV electrons from a Van de Graaff generator; pulse duration: 0.5–5 μsec ; beam current: 25 mA; dose per μsec of pulse: about 1500 rads). Since the base conductivity of the NiSO_4 solution used was rather high, the dc method¹³ for recording the conductivity could not be applied. We used the 10-MHz method, details of which have recently been reported,¹⁴ with a different cell because of the lower electron energy. Figure 1 shows the dimensions of the double cell and the scheme of the ac bridge. The upper part of the cell was irradiated while the lower part served as a blank. The cell was shielded such that the electron beam penetrated only the space between the upper two platinum electrodes. The analyzing light passed through at right angles to the beam and to the electric field. The electron beam penetrated the solution to a depth of about 5 mm. The cell constant and absorbed dose were always determined before and after a run of ex-

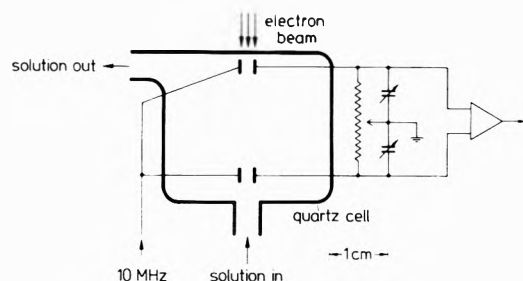


Figure 1. The double cell for conductivity measurements in pulse radiolysis and the main components of the ac bridge.

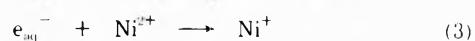
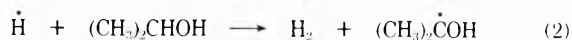
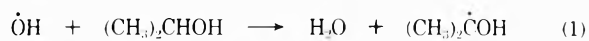
periments using a 10^{-4} M tetranitromethane solution containing 5% 2-propanol.¹³ Knowing the yield and extinction coefficient of the $C(NO_2)_3^-$ ion formed ($G = 6.0$; $\epsilon_{350nm} 1.4 \times 10^4 M^{-1} cm^{-1}$) and the molar conductivity of the $H^+ - C(NO_2)_3^-$ ion pair ($390 mol^{-1} ohm^{-1} cm^2$ at 25°) the cell constant and absorbed dose could be calculated from the observed signals after the pulse.

Results and Discussion

γ Radiolysis. Propanol Containing Solutions. Figure 2a shows the amount of nickel which precipitated from a solution containing 5×10^{-2} M NiSO₄ and 5×10^{-1} M 2-propanol. After a short induction period, the amount of nickel increases with dose. A G value of 0.7 atoms per 100 eV of absorbed energy is calculated from the initial slope of the curve after the induction period. The curve starts to level off toward the horizontal axis after rather short irradiation times. This effect can be attributed to the formation of protons during irradiation which dissolve part of the precipitated nickel. As can be recognized from Figure 2b, a linear relationship exists between the amount of precipitated nickel and the time of irradiation if the pH of the solution is kept constant by automatic addition of NaOH. The G value calculated from the slope of curve b is equal to 1.7 nickel atoms per 100 eV.

The nickel precipitate partially dissolved if oxygen was bubbled through the solution after irradiation. However, after filtration and drying under exclusion of air, the metal was no longer reactive toward oxygen. Analysis showed the precipitate to be practically pure metal.

The following equations describe the processes which are expected to occur upon γ irradiation



The rate constants of reactions 1 and 2 are known as 1.2×10^9 and $5 \times 10^7 M^{-1} sec^{-1}$, respectively.¹⁵ The hydrated electron reacts with the Ni²⁺ ion with $k = 2.3 \times 10^{10} M^{-1} sec^{-1}$.⁴ e_{aq}^- scarcely reacts with 2-propanol and OH is not reactive toward Ni²⁺. Reaction 3 is expected to occur with the yield of the hydrated electron which is 2.7/100 eV in dilute solutions. At the high nickel ion concentration used, additional electrons may be scavenged in the spurs. It thus appears from the observed yield of 1.7 atoms of nickel/100 eV, that the yield of Ni is half of that of intermediate Ni⁺. The dismutation reaction



which was already proposed by other authors² would explain the yield of 1.7/100 eV. However, reasons against the occurrence of reaction 4 will be given below.

Experiments were also carried out with a solution con-

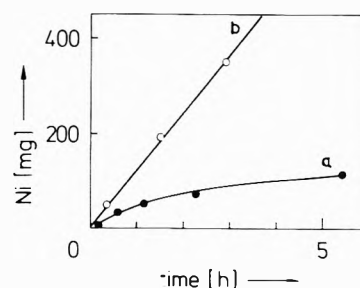
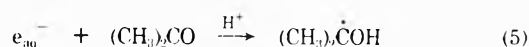


Figure 2. Amount of precipitated nickel as a function of time: solution 1.925 l of 0.05 M NiSO₄ plus 0.5 M 2-propanol; dose rate 5.5×10^5 rads/hr; curve a, without compensation of pH changes during irradiation (initial pH 5.5); curve b, with compensation by automatic NaOH injection (pH 5.5).

taining 0.5 M 2-propanol as OH and H scavenger, 0.5 M acetone as e_{aq}^- scavenger, and 10^{-3} M NiSO₄. Under these conditions, practically all the hydrated electrons react with acetone to form the 2-propanol radical



which is therefore the only species that could subsequently react with the nickel ion. No nickel, however, was precipitated from this solution. It is concluded that the 2-propanol radical does not react with Ni²⁺ under our conditions. The pulse radiolysis experiments described below led to the same conclusion.

Other Organic Solutes. Similar experiments were carried out with solutions containing the organic compounds listed in Table I. Integral G values for 3 hr of irradiation are shown in the table. Practically no nickel was formed when methanol, 2-methyl-2-propanol, and diethyl ether were present. In the absence of an organic additive, the formation of nickel was also suppressed. A rather high yield was observed for the sodium formate containing solution. The precipitated nickel was extremely fine and could be filtered only after addition of silicic acid. The nickel redissolved rapidly if oxygen was admitted to the irradiated solution.

These results indicate that the formation of nickel from Ni⁺ must be more complicated than described by eq 4. If the organic additive only scavenged OH radicals and H atoms and did not interfere with reactions 4, the yield should be independent of the nature of the organic additive. The results, however, indicate a strong influence of the nature of the organic solute. One can only understand this influence, if one assumes an interaction of the radicals formed by OH and H attack on the organic solute with the Ni⁺ ions formed in reaction 3. Depending on the redox behavior of the organic radical, this interaction may result in the formation of Ni or Ni²⁺ from Ni⁺. This problem will further be examined in the pulse radiolysis experiments described below. In solutions containing formate, the CC_2^- radicals formed by OH attack may in part be able to reduce Ni²⁺ ions at the high nickel ion concentration used.⁸ This reduction may contribute to the rather large yield of precipitated nickel of Table I.

Isobutene was traced as a final product of radiolysis of the 2-methyl-2-propanol containing solution. The solution was flushed with a stream of argon and the volatile compounds of the gas stream were frozen out at -190° . They were afterwards dissolved in CS₂ and analyzed gas chromatographically and by measuring the consumption of added bromine. A G value of 1.3 for isobutene was found which has to be regarded as lower limit, since isobutene

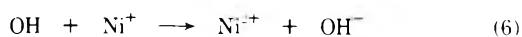
TABLE I: The 100-eV Yields of Nickel Formed in Solutions Containing Various Organic Additives

| Organic additive | 100-eV yield of Ni |
|--|--------------------|
| | <0.05 |
| 10 ⁻¹ M methanol | <0.05 |
| 10 ⁻¹ M diethyl ether | <0.05 |
| 10 ⁻¹ M ethanol | 0.19 |
| 10 ⁻¹ M 2-propanol | 0.44 |
| 10 ⁻¹ M 1-butanol | 0.22 |
| 10 ⁻¹ M sodium formate | 1.9 |
| 10 ⁻¹ M 2-methyl-2-propanol | <0.05 |

formed during irradiation might partly have been attacked by reactive intermediates. Furthermore, losses may have occurred during the process of separation of isobutene from the solution.

Pulse Radiolysis. Solutions without Organic Additive. Figure 3a shows oscillograms of the absorption at 300 nm and of the conductivity of an irradiated 10⁻⁴ M NiSO₄ solution. The solution was deaerated with argon and contained no OH scavenger. Both the optical absorption and the conductivity increased during the 1 μsec duration of the pulse since practically all the hydrated electrons react during the pulse. Taking the yield of the hydrated electron in dilute solution as $G = 2.7$, an extinction coefficient of 6000 M⁻¹ cm⁻¹ at 300 nm was calculated from the absorption signal immediately after the pulse. The observed conductivity increase of 290 cm² ohm⁻¹ mol⁻¹ corresponds to the formation of 2.7 H⁺ ions/100 eV (350 cm² ohm⁻¹ mol⁻¹), if a plausible value of -60 cm² ohm⁻¹ mol⁻¹ is assumed for the conductivity difference between Ni²⁺ and Ni⁺. The optical absorption as well as the conductivity decrease faster with increasing dose. After 1 msec, the two signals still retain about 25% of their values immediately after the pulse. They then slowly decay toward zero in the 10⁻² sec range.

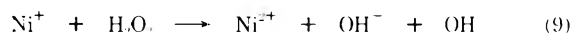
The decrease in optical absorption and in conductivity is attributed to the reactions



However, part of the OH radicals can undergo combination to form H₂O₂



Since Ni⁺ and OH are formed in about equal amounts, not all of the Ni⁺ ions can be reoxidized by the OH radical. About 25% of Ni⁺ remain after the OH radicals have disappeared. This amount of Ni⁺ is then reoxidized by the hydrogen peroxide formed partly by reaction 8 and partly as a molecular product of irradiation during the pulse



This reaction is known to be relatively slow.⁷

The curves of Figure 3a were analyzed quantitatively using an analog computer. The rate constant of reaction 8 is known as $2k = 1.0 \times 10^{10} \text{ M}^{-1} \text{ sec}^{-1}$.¹⁵ Agreement with the curves of Figure 3a was obtained, if a value of $2 \times 10^{10} \text{ M}^{-1} \text{ sec}^{-1}$ was assumed for the rate constant of reaction 6. A rate constant of $5 \times 10^7 \text{ M}^{-1} \text{ sec}^{-1}$ was obtained for reaction 9 by analysis of the slow decay in the 10⁻² sec range mentioned above. This constant is in agreement with a value obtained by other authors.⁷

2-Methyl-2-propanol as OH Scavenger. OH reacts with 2-methyl-2-propanol with $k = 2.5 \times 10^8 \text{ M}^{-1} \text{ sec}^{-1}$.¹⁵ The reaction mainly consists in the abstraction of an H atom

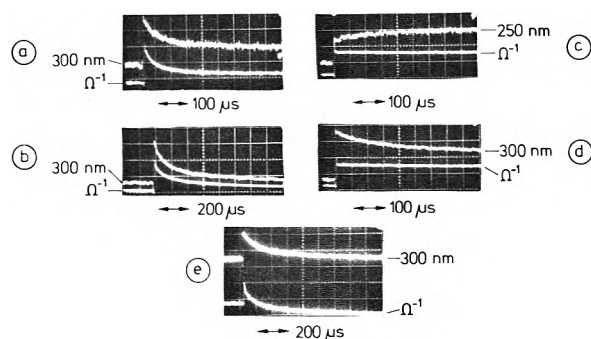
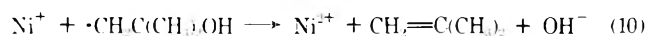


Figure 3. Oscillograms showing the time dependence of the optical absorption and conductivity of nickel solutions under various conditions: (a) 10⁻⁴ M NiSO₄, no OH scavenger; (b) 10⁻⁴ M NiSO₄, 0.5 M 2-methyl-2-propanol; (c and d) 10⁻⁴ M NiSO₄, 0.1 M methanol; (e) 5 × 10⁻⁵ M NiSO₄, 5 × 10⁻⁵ M sodium formate.

to form a β alcohol radical.¹⁶ Figure 3b shows that the optical absorption at 300 nm and the conductivity of an irradiated solution increase during the pulse and then rapidly decrease toward zero. The concentration of 2-methyl-2-propanol was high enough (5 × 10⁻² M) to ensure a half-life of OH of less than 1 μsec. The decrease after the pulse therefore cannot be caused by OH radicals, but must be due to a reaction of ·CH₂C(CH₃)₂OH with Ni⁺. The following reaction is postulated



The formation of isobutene and OH⁻ has recently been postulated for the cathodic reduction of ·CH₂C(CH₃)₂OH.¹⁷ The OH⁻ ion formed consumes a proton to form water. This explains the decrease in conductivity after the pulse. The observation of isobutene as a final product of γ radiolysis is also explained by reaction 10. Using a G value of 2.7 for Ni⁺ as well as for ·CH₂C(CH₃)₂OH, a rate constant of 3 × 10⁹ M⁻¹ sec⁻¹ was calculated from the second-order decay in Figure 3b. This rate constant is essentially higher than the rate constant of $k = 7 \times 10^8 \text{ M}^{-1} \text{ sec}^{-1}$ ¹⁶ for the interaction of two ·CH₂C(CH₃)₂OH radicals.

Another conclusion may be drawn from these experiments. If reaction 4 was fast, with a rate constant of the order of 10⁹ M⁻¹ sec⁻¹, it could compete successfully with reaction 10. Under these conditions, the optical absorption at 300 nm would again decrease rapidly if Ni does not absorb at the wavelength. The conductivity, however, would not change during reaction 4, since a Ni²⁺ ion has about the same conductivity as two Ni⁺ ions (it should be remembered that most of the conductivity in Figure 3b is due to the protons formed during the pulse). Since the conductivity signal in Figure 3b decayed parallel to the absorption signal, it must be concluded that reaction 4 does not occur under our conditions.

Methanol, Ethanol, 2-Propanol, Diethyl Ether, and c-Pentane as OH Scavengers. Typical optical absorption and conductivity vs. time curves are shown in Figure 3c and 3d for an irradiated methanol containing solution. The conductivity again increases immediately after the pulse (corresponding to the conductivity of a proton and the difference in Ni²⁺/Ni⁺ conductivities), but now remains constant for several milliseconds. The 300-nm absorption of Ni⁺ decreases after the pulse. At the same rate, an absorption is built up at 250 nm. The rate is proportional to the dose of the pulse. Similar effects were observed with solutions containing ethanol, 2-propanol, and

TABLE II: Rate Constants of Reactions Occurring in the Irradiated Solutions^a

| Organic additive | $R \cdot + R \cdot 2k10^9$, $M^{-1} \text{ sec}^{-1}$ | % Ni ⁺ consumed in reaction 11 | Ni ⁺ + R · $k10^9$, $M^{-1} \text{ sec}^{-1}$ | NiR ⁺ + H ₂ O ₂ k , $M^{-1} \text{ sec}^{-1}$ | NiR ⁺ + H ₂ O k , sec^{-1} |
|------------------|---|--|--|---|--|
| Methanol | 2.4 | 81 | 4.2 (4.2) | 7.3×10^3 | 7 |
| Ethanol | 2.3 | 80 | 2.3 (3.8) | 2.3×10^4 | 5 |
| 2-Propanol | 1.4 | 68 | 1.4 (1.3) | 1.1×10^6 | <1 |
| Diethyl ether | 0.7 | 72 | (0.8) | 1.3×10^3 | <1 |
| Formate | 0.9 | | 6.6 | | <1 |
| c-Pentane | 2.0 | 48 | 2.8 (0.8) | $<5 \times 10^6$ | 49 |

^a The values in row 4 are calculated from the observed decay and built up, the values in parentheses are calculated from rows 2 and 3.

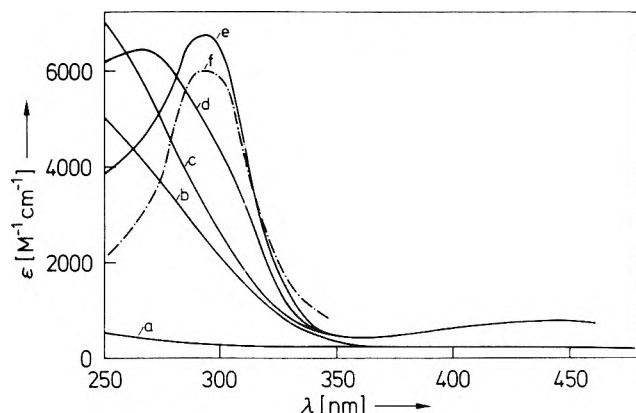


Figure 4. Absorption spectrum immediately after the pulse (f) and 500 μsec later in a solution of 10⁻⁴ M NiSO₄ and (a) formate, (b) 2-propanol, (c) methanol, (d) ethanol, and (e) diethyl ether as OH scavengers.

diethyl ether. These effects can be understood if one postulates that most of the Ni⁺ ions react with organic radicals. In the case of methanol we may write



This reaction explains the decrease in 300-nm absorption, the simultaneous increase in the 250-nm absorption (which is attributed to NiCH₂OH⁺), and the constancy of the conductivity (no proton is consumed in reaction 11; Ni⁺ and NiCH₂OH⁺ probably have similar molar conductivities).

The rate constant of reaction 11 was calculated as $4.2 \times 10^9 \text{ M}^{-1} \text{ sec}^{-1}$ (under the assumption that Ni⁺ was present with $G = 2.7$ and the organic radical R with $G = 3.2[G(\text{H}) + G(\text{OH})]$ after the pulse) by using a computer program to integrate the differential equations for the different parallel reactions. The rate constants for the reactions of Ni⁺ with the radicals formed from various organic compounds are listed in the fourth row of Table II. The spectrum of the solution immediately after the pulse always contained the 300-nm band of Ni⁺ with ϵ 6000 M⁻¹ cm⁻¹. After several hundred microseconds, i.e., when the second-order decay in the 300-nm absorption was complete, the solutions had different spectra which are attributed to the nickel organic compounds. Figure 4 shows the corrected spectrum of Ni⁺ immediately after the pulse (curve f) and of various nickel organic compounds (curves b–e). The small corrections which had to be made included (a) the correction for the known spectrum of the organic radicals present besides Ni⁺ immediately after the pulse and (b) the correction for the remaining Ni⁺ that escaped reaction 11 after several hundred microseconds. The fact that part of the Ni⁺ ions escape reaction 11 is explained in terms of reaction of the organic radicals with each other. The rate constants of these competing reac-

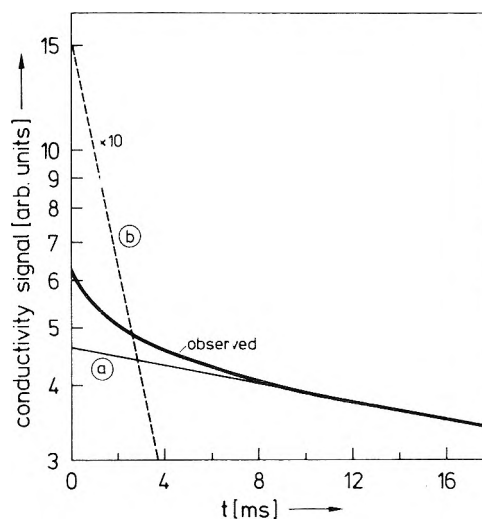


Figure 5. Semilogarithmic plot of the conductivity as a function of time: solution $5 \times 10^{-4} \text{ M NiSO}_4$; $5 \times 10^{-3} \text{ M 2-propanol}$; $10^{-5} \text{ M H}_2\text{O}_2$ (curves a and b: first-order components of the observed curve).

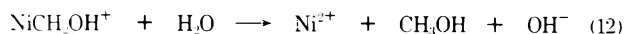
tions are listed in the first row of Table II. They were taken from the literature.¹⁶

The following procedure was carried out in order to determine the percentage of Ni⁺ that did not react with the organic radicals. A solution was pulse irradiated which contained 10⁻⁵ M H₂O₂ in addition to the nickel sulfate ($5 \times 10^{-4} \text{ M}$) and the organic solute such as 2-propanol ($5 \times 10^{-3} \text{ M}$). The added hydrogen peroxide did not disturb the primary processes of eq 1, 2, and 3 in which Ni⁺ and (CH₃)₂COH radicals are formed. It also did not interfere with the reaction between Ni⁺ and the organic radicals (eq 11). However, the Ni⁺ ions that escaped this reaction will now slowly be reoxidized by H₂O₂. The time required for this oxidation should be about 2 msec at the H₂O₂ concentration of 10⁻⁵ M and using the value of $5 \times 10^7 \text{ M}^{-1} \text{ sec}^{-1}$ for the rate constant of reaction 9. Figure 5 shows a semilogarithmic plot of the observed conductivity after the pulse on a rather compressed time scale. A decrease in conductivity is indeed observed over several milliseconds which is attributed to reaction 9 (the OH⁻ ion formed in reaction 9 consumes a proton and thus the conductivity is decreased). However, when this reaction is practically complete, the conductivity slowly decreases further. With increasing H₂O₂ concentration both decreases became proportionally faster. The slow decrease in conductivity in Figure 5 at times longer than 10 msec is attributed to reaction of hydrogen peroxide with the nickel organic compound NiC(CH₃)₂OH⁺ (formed in the first few hundred microseconds analogously to eq 11). In this oxidation of the complex, Ni²⁺ is formed and a proton is consumed.

Curve analysis as shown in Figure 5 was carried out. The extrapolation of the slow decrease at longer times yielded the straight line a, the intercept of which with the ordinate axis is a measure of the amount of the nickel organic compound formed. Subtraction from the observed curve gave the straight line b, the intercept of which is a measure of the Ni^+ ions that escaped reaction with 2-propanol radicals and were oxidized by H_2O_2 . It was concluded that 68% of the Ni^+ ions reacted with the 2-propanol radicals. The rate constant of the oxidation of the organic nickel compound by H_2O_2 could be calculated from the slope of curve a in Figure 5. A value of $1.1 \times 10^6 \text{ M}^{-1} \text{ sec}^{-1}$ was obtained. The slope of curve b was in agreement with that expected from the H_2O_2 concentration and the rate constant of $5 \times 10^7 \text{ M}^{-1} \text{ sec}^{-1}$ of reaction 9.

Similar experiments were carried out with the other organic solutes. As may be seen from the third row in Table II, except for *c*-pentane, always more than two-thirds of the Ni^+ ions formed originally reacted with the organic radicals. The rate constants for oxidation of the organic nickel compounds by H_2O_2 are listed in the fifth row of the table. Using the values of the second and third row of Table II, the rate constant of reaction 11 could be calculated with the aid of an analog computer. The calculated values are given in parentheses in the fourth row. They agree fairly well with those obtained directly by analyzing the decay of the 300-nm absorption and the increase of the 250-nm absorption as described above.

The 250-nm absorption and conductivity of Figure 3d faded very slowly by a first-order process in the 0.1-sec range (in the absence of additional hydrogen peroxide). This effect is attributed to the hydrolysis of the nickel organic compound



The conductivity decreases since the OH^- ion formed neutralizes a proton. Experiments were carried out with higher H^+ concentrations down to pH 3. No acceleration of reaction 12 could be observed. Similar observations were made with other organic solutes, where a faster decay was observed only for *c*-pentane. The rate constants of hydrolysis are listed in the sixth row of Table II.

No increase in the 300-nm absorption and in the conductivity was observed in the pulse irradiation of a solution containing $5 \times 10^{-4} \text{ M}$ NiSO_4 , $5 \times 10^{-1} \text{ M}$ 2-propanol, and 10^{-1} M acetone. The 2-propanol radical which is the only species formed in this solution apparently does not reduce Ni^{2+} . This conclusion had already been drawn above from the observation that no nickel was precipitated from such solution upon γ irradiation.

Formate as OH Scavenger. Figure 3e shows the dependence of the 300-nm absorption and of the conductivity on time for a pulse irradiated solution containing $5 \times 10^{-5} \text{ M}$ sodium formate and $5 \times 10^{-5} \text{ M}$ NiSO_4 at pH 5.0. The rate of decay of the 300-nm absorption increased with dose and was independent of the formate concentration. The decay of the conductivity after the pulse occurred at the same rate as that of the optical absorption if the pH was lower than 5. At pH values between 5 and 6, the conductivity decreased somewhat slower than the optical absorption. At shorter wavelengths an increase in absorption could be detected which was as fast as the decrease at 300 nm. Figure 4a shows the spectrum of the solution after 500 μsec , *i.e.*, after the decay at 300 nm, which is again attributed to an organic nickel compound. This spectrum can still be observed several seconds after the pulse. The

height of the conductivity signal after the pulse corresponds to the formation of 2.7 protons, 2.7 Ni^+ ions, and disappearance of 2.7 Ni^{2+} ions per 100 eV. OH produces the CO_2^- radical anion in its attack on the formate ion. No significant conductivity change is produced in this reaction. When a nickel compound is formed according to



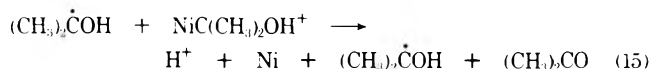
the conductivity should decrease by about $100 \text{ cm}^2 \text{ ohm}^{-1} \text{ mol}^{-1}$. The conductivity signal observed immediately after the pulse (which is mainly caused by H^+ formed during the pulse) should therefore decrease by only about 40% during the disappearance of Ni^+ . It can, however, be seen from Figure 3e, that the conductivity signal decreases much more markedly and even reaches negative values. After about 1 msec the signal reaches a final value of $-100 \text{ cm}^2 \text{ ohm}^{-1} \text{ mol}^{-1}$ (using $G = 2.7$). This effect can only be understood in terms of the pick-up of one proton by the nickel compound

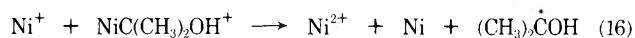


This reaction also explains the delay of the decay in conductivity at pH values higher than 5. Since the negative conductivity signal was still observed 10 sec after the pulse, it must be concluded that NiCO_2H^+ has a much longer lifetime. Measurements at longer times after the pulse could not be carried out with the present equipment. (Because of the short penetration of the 1.6-MeV electrons, the irradiated volume between the platinum electrodes in Figure 1 was rather small. Diffusion of long-lived particles formed by radiation out of the irradiated volume between the electrodes limits the time of observation to less than 10 sec after the pulse.) It may finally be mentioned that the buffer capacity of formate at pH 5.0 and at the low concentration used has only a slight influence on the conductivity changes produced by a pulse of irradiation. All experimental data were corrected for this effect. Since the Ni^+ absorption was as high in the formate containing solution as expected from the yield of 2.7 of the hydrated electron, it can be concluded that additional Ni^+ formation by reaction of the CO_2^- ion with Ni^{2+} did not occur. As mentioned above, this reaction might have taken place to a certain extent only in the γ irradiation experiments in which a much higher Ni^{2+} concentration was used and where the lifetime of the radicals with respect to mutual deactivation was much longer than in the pulse experiments.

Concluding Remarks

The question still remains as to how metallic nickel is formed in some of the solutions upon γ irradiation. No nickel precipitate was observed in the single pulse experiments. Since reaction 4 cannot compete with the reaction between Ni^+ and the organic radicals, another mechanism has to be found. Because of their long lifetime with respect to hydrolysis, the stationary concentration of the organic nickel compounds will be much higher than those of Ni^+ and the organic radicals during γ irradiation. It seems therefore plausible to postulate that many Ni^+ ions and organic radicals will be scavenged by the nickel compound when a certain concentration of the latter has been built up. We formulate reactions for the 2-propanol containing solution





Both reactions would occur more easily as the reducing power of the organic radical is increased. It is known that the reducing power of the radicals decreases in the sequence $\text{CO}_2^- > (\text{CH}_3)_2\dot{\text{C}}\text{OH} > \text{CH}_3\dot{\text{C}}\text{OH} > \dot{\text{C}}\text{H}_2\text{OH}$.^{18,19} The yield of nickel given in Table I shows the same trend. Reaction 15 enhances the disproportionation between two organic radicals. It may have played an important role in the experiments on the influence of nickel on disproportionation and combination of alcohol radicals mentioned above.¹⁰

Since OH attacks the organic solutes used in this work predominantly at the CH bond in α position to the functional group,²⁰ carbon radicals are produced and therefore carbon-nickel bonds are postulated for the complexes from Ni⁺ and the radicals. These complexes are thus quite similar to the organic chromium complexes which have been observed and in some cases isolated from aqueous solutions.²¹⁻²⁴ One of the methods of formation of such complexes, *i.e.*, production of organic radicals by OH which subsequently react with Cr(II),²⁴ is in principle similar to our method. The pulse radiolysis method has also been used in the studies on chromium complexes to measure the rate constants of complex formation from Cr(II) and various radicals.²⁵ The rate constants for α alcohol radicals were of the order of $10^8 \text{ M}^{-1} \text{ sec}^{-1}$, *i.e.*, about ten times slower than the rate constants for the corresponding Ni⁺ + radical reactions shown in Table II. The spectra of the chromium complexes contained a strong absorption band around 280 nm and a weaker one at about 400 nm. The nickel complexes have similar uv absorptions, the extinction coefficient being nearly three times as high as that of the chromium complexes. We were also able to see a weak absorption in the visible range at about 400 nm ($\epsilon \sim 300 \text{ M}^{-1} \text{ cm}^{-1}$, Figure 4). The rate constant of hydrolysis seems to be lower for the chromium than for the nickel complexes. The complex $\text{CrCH}_2\text{OH}^{2+}$, for example, has a rate constant of $0.7 \times 10^{-4} \text{ sec}^{-1}$,²⁴ while the nickel complex NiCH_2OH^+ decays with $k = 7 \text{ sec}^{-1}$. In order to observe the acceleration of the decay of chromi-

um complexes by H⁺ ions, concentrations of the latter of more than 0.09 M had to be used.²⁴ Such high H⁺ concentrations could not be applied in our work, since the hydrated electron is scavenged by H⁺ and cannot be used to reduce Ni²⁺.

Acknowledgment. The authors thank Dr. H. Möckel and M. Wilhelm for their assistance in the gas chromatographic analysis and the irradiation techniques.

References and Notes

- (1) J. H. Baxendale and R. S. Dixon, *Proc. Chem. Soc.*, 148 (1963).
- (2) G. E. Adams, J. H. Baxendale, and J. W. Boag, *Proc. Chem. Soc.*, 241 (1963).
- (3) J. H. Baxendale and R. S. Dixon, *Z. Phys. Chem. (Frankfurt am Main)*, **43**, 161 (1964).
- (4) J. H. Baxendale, E. M. Fielden, and J. P. Keene, *Proc. Roy. Soc., Ser. A*, **286**, 320 (1965); *Proc. Chem. Soc.*, 242 (1963).
- (5) J. H. Baxendale, J. P. Keene, and D. A. Stott, *Chem. Commun.*, 715 (1966).
- (6) M. Anbar and P. Neta, *J. Chem. Soc. A*, 841 (1967).
- (7) D. Meyerstein and W. A. Mulac, *J. Phys. Chem.*, **72**, 784 (1968).
- (8) G. V. Buxton, F. Dainton, and D. R. McCracken, *J. Chem. Soc., Faraday Trans. 1*, **69**, 243 (1973).
- (9) W. A. Phillip and S. J. Marsik, NASA TND-5880 (1970); NASA TND-5213 (1969).
- (10) W. Brackman, F. van de Graats, and P. J. Smit, *Recl. Trav. Chim. Pays-Bas*, **83**, 1253 (1964).
- (11) G. C. Barker and P. Fowles, *Trans. Faraday Soc.*, **66**, 1661 (1970).
- (12) A. Henglein, W. Schnabel, and J. Wendenburg, "Einführung in die Strahlenchemie," Verlag Chemie, Weinheim, 1969.
- (13) G. Beck, *Int. J. Radiat. Phys. Chem.*, **1**, 361 (1969).
- (14) J. Lilie and R. Fessenden, *J. Phys. Chem.*, **77**, 674 (1973).
- (15) M. Anbar and P. Neta, *Int. J. Appl. Radiat. Isotopes*, **18**, 493 (1967).
- (16) M. Simic, P. Neta, and E. Hayon, *J. Phys. Chem.*, **73**, 3794 (1969).
- (17) K. M. Bansal, A. Henglein, E. Janata, and R. M. Sellers, *Ber. Bunsenges. Phys. Chem.*, **77**, 1139 (1973).
- (18) K.-D. Asmus, A. Wigger, and A. Henglein, *Ber. Bunsenges. Phys. Chem.*, **70**, 862 (1966).
- (19) J. Lilie, G. Beck, and A. Henglein, *Ber. Bunsenges. Phys. Chem.*, **75**, 458 (1971).
- (20) K.-D. Asmus, H. Möckel, and A. Henglein, *J. Phys. Chem.*, **77**, 1218 (1973).
- (21) F. A. L. Anet and E. Leblanc, *J. Amer. Chem. Soc.*, **79**, 2649 (1957).
- (22) J. K. Kochi and D. Buchanan, *J. Amer. Chem. Soc.*, **87**, 853 (1965).
- (23) R. G. Crombs and M. D. Johnson, *J. Chem. Soc. A*, 177 (1966).
- (24) W. Schmidt, J. H. Swinehart, and H. Taube, *J. Amer. Chem. Soc.*, **93**, 1117 (1971).
- (25) H. Cohen and D. Meyerstein, *Chem. Commun.*, 320 (1972).

Radiolysis and Photolysis of the Hydrogen Peroxide-*p*-Nitrosodimethylaniline-Oxygen System¹

M. Hatada, I. Kraljic, A. El Samahy, and C. N. Trumbore*

Department of Chemistry, University of Delaware, Newark, Delaware 19711 (Received August 20, 1973)

Publication costs assisted by the University of Delaware

The γ ray radiolysis and ultraviolet photolysis of aerated solutions of *p*-nitrosodimethylaniline (RNO) containing hydrogen peroxide have been studied and compared. The same intermediate, the OH radical, appears to be solely responsible for the destruction of the RNO molecule in both the photolysis and radiolysis systems. Identical competition kinetics are found between RNO and hydrogen peroxide for the OH radical over a wide range of both RNO and hydrogen peroxide concentrations. Hydrated electron scavenging by high concentrations of hydrogen peroxide yields an intermediate which has the same kinetic behavior as that from the hydrogen peroxide photolysis. Evidence is given that the previously reported G values for radiolytic destruction of RNO were too low since one or more products of the reaction with OH absorb at 440 nm. However, the relative rate constants obtained from competition kinetics are not altered when this is taken into account, provided OH competitors *completely* scavenge the RNO bleaching reaction. An absolute quantum yield of 0.92 ± 0.10 is found for RNO destruction in aerated H₂O₂ solutions. This value would also be equal to the quantum yield for H₂O₂ decomposition, assuming the same stoichiometry as in the radiolysis. However, this would be larger by a factor of 2 than that which is commonly accepted. The reasons for this discrepancy may be mechanistic but, if so, the difference between the radiolysis and photolysis mechanisms is unexplained.

Introduction

Kraljic and Trumbore² demonstrated the potential of aqueous, air-saturated *p*-nitrosodimethylaniline (RNO) as a system for studying OH radical reaction rate constants. Kraljic³ further showed in preliminary studies the similarities between relative OH rate constants in radiolysis, hydrogen peroxide photolysis, and Fenton reagent (Fe²⁺ + H₂O₂) action in air-saturated RNO solutions. Later, two groups investigating the pulse radiolysis of RNO solutions cast doubts upon the use of RNO as a standard OH competitor. Dainton and Wiseall⁴ and Baxendale and Kahn⁵ independently studied the pulse radiolysis of RNO and reported extensive secondary back reactions with RNO by radicals formed from OH and a solute initially in competition with RNO for the OH. However, it was also reported that such reactions rarely occur under the conditions originally proposed by us,² namely, in oxygen-containing solutions where both hydrogen atoms and electrons are scavenged by the oxygen and do not further react with RNO.

In continuing investigations into the detailed reaction mechanism of RNO and OH, we have shown⁶ certain anomalies in the radiation chemistry of both neutral and acidic solutions of RNO, especially when RNO concentrations are varied. Yields in the two pulse radiolysis studies vary widely in the absence of oxygen, but are within experimental error in the presence of oxygen. Both pulse radiolysis studies confirmed our initial assumption² that O₂⁻ did not attack RNO and that the initial 440-nm bleaching was due to attack by the OH radical, with a G value of 2.6–2.7. It was, therefore, surprising to find a lower-than-expected net $G(-\text{RNO})$ of 1.1–1.2^{2,4} for γ radiolysis, less than half of the reported G_{OH} value.

Because of the above anomalies, the hydrogen peroxide photolysis method for generating OH radicals was chosen

for detailed kinetic studies to show whether some of the radiation chemistry anomalies would be eliminated. The primary yields in the ultraviolet photolysis of hydrogen peroxide appeared to be well established.^{7–11} The radiation chemistry of the same system was studied over a wide range of RNO and H₂O₂ concentrations in order to further test concentration effects.

Experimental Section

A Hanovia low-pressure mercury arc lamp (735A-7) with a Corning CS 7-54 filter was used as the source of ultraviolet light. The solutions to be photolyzed were placed in 10-mm silica absorption cells, positioned reproducibly on an optical bench, and photolyzed at room temperature ($23 \pm 1^\circ$). The concentration of RNO was determined spectrophotometrically at 440 nm ($\epsilon_{\text{RNO}}^{440}$ 33,500 for pH greater than 5).

Actinometry was performed in all cases with a uranyl oxalate actinometer.¹² By inserting a Corning CS 0-54 filter, which transmits light only above 313 nm between the lamp source and cell, it was possible with appropriate corrections to determine the input intensity to the cell at 313 nm separately and, hence, to determine the 254-nm photon intensity by the difference between the measured intensity with and without the CS 0-54 filter. An independent method employed for evaluating the absolute photon fluxes at the two wavelengths was by the use of two uranium oxalate actinometers in series. The agreement between these two independent methods was quite good (2% or less), and the photon intensity input at 254 and 313 nm was thus determined as 0.96×10^{16} and 1.35×10^{16} photons min⁻¹ ml⁻¹, respectively.

The light absorbed by H₂O₂ in aqueous solution of H₂O₂ and RNO was calculated from the following derived equation, assuming Beer's law is valid in the RNO and

TABLE I: Molar Extinction Coefficients (ϵ) of the Solutes at Various Wavelengths

| | 254 nm | 313 nm | 440 nm |
|-------------------------------|--------|--------|--------|
| RNO ^a | 2230 | 1550 | 33,500 |
| H ₂ O ₂ | 19 | 0.52 | |

^a Unprotonated form (above pH 5).**H₂O₂ concentration regions employed**

$$I_{H_2O_2} =$$

$$\sum_i \frac{c_{H_2O_2} \epsilon_{H_2O_2}^i}{c_{H_2O_2} \epsilon_{H_2O_2}^i + c_{RNO} \epsilon_{RNO}^i} \{1 - 10^{-(c_{H_2O_2} \epsilon_{H_2O_2}^i + c_{RNO} \epsilon_{RNO}^i) I_0^i L}\} I_0^i \quad (1)$$

where $I_{H_2O_2}$ is the number of quanta absorbed by hydrogen peroxide in the solution in photons ml⁻¹ min⁻¹, c and ϵ are the concentration of the solute and molar extinction coefficient of the solute indicated by the subscripts, and I_0^i is the flux input to the cell where the superscript i refers to the wavelength (*i.e.*, 254 or 313 nm). The values of ϵ used in this equation are given in the Table I. Equation 1 was experimentally verified. The number of 313-nm photons absorbed by H₂O₂ is shown to be less than 10% of the 254-nm photons absorbed by H₂O₂ in most of the solutions investigated.

The experimental details of the Co-60 γ radiation experiments are the same as reported previously.²

Eastman Kodak White Label RNO was used after several recrystallizations or as synthesized as described previously.² A 10⁻³ M RNO stock solution was stable for a period of up to several weeks.

Liquid chromatographic separations of the products of the RNO photolysis and radiolysis were obtained using a custom-built liquid chromatograph employing an ultraviolet detector and a 1-m ETH Permaphase column.¹³ The solvent systems used were either alcohol or acetonitrile-water.

The pH of the alkaline solutions was adjusted by the addition of small amounts of Na₂B₄O₇ solution for pH 9. (Yields of radiolysis have been shown to be pH independent between pH 5 and 10.⁵) All reagents were of analytical reagent grade purity. Triply distilled water was used in the preparation of all solutions. All solutions were air saturated.

Results and Discussion

First, it was necessary to establish at which concentrations of H₂O₂ and RNO there was little or no detectable chemical dark reaction. In addition, it was necessary to establish the photochemical behavior of RNO toward light of the wavelengths used in the photolysis. Preliminary experiments showed that 4 or 5 $\times 10^{-5}$ M RNO is stable in the presence of up to 1 to 3 $\times 10^{-2}$ M H₂O₂ for periods which provide sufficient time for the photolysis or radiolysis of the RNO solution and spectrophotometry of the photolyzed solution. However, at higher H₂O₂ concentrations, bleaching of the RNO did occur in periods which were not entirely negligible in comparison with the total time necessary to conduct a complete photolysis and quantitative analysis of the RNO bleaching yield. Corrections were made by using blanks of unirradiated RNO-H₂O₂ solutions. RNO solutions were shown to be stable upon irradiation with the filtered ultraviolet light containing 313- and 254-nm photons in that observable changes

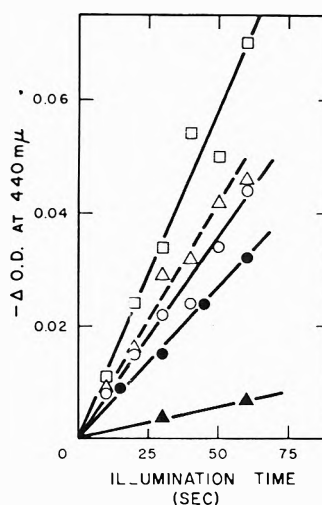


Figure 1. Change in optical density at 440 nm in *p*-nitrosodimethylaniline RNO-O₂-H₂O₂ solutions as a function of illumination time and H₂O₂ concentration: □, (RNO) = 5.0 $\times 10^{-5}$ M, (H₂O₂) = 0.058 M; Δ, (RNO) = 5.0 $\times 10^{-5}$ M, (H₂O₂) = 0.144 M; ○, (RNO) = 4.7 $\times 10^{-5}$ M, (H₂O₂) = 0.60 M; ●, (RNO) = 5.0 $\times 10^{-5}$ M, (H₂O₂) = 2.67 $\times 10^{-3}$ M; ▲, (RNO) = 5.0 $\times 10^{-5}$ M, (H₂O₂) = 5.3 $\times 10^{-4}$ M; photon flux = 2.21 $\times 10^{16}$ quanta ml⁻¹ min⁻¹. All solutions are air saturated, pH 6.

in optical density were not detected during the short photolysis times employed. Longer irradiation times did result in small amounts of RNO bleaching.

Photolytic Results in the RNO-H₂O₂-O₂ System. In RNO-H₂O₂-O₂ solutions, the optical density at the RNO absorption maximum (440 nm) was decreased with increasing exposure time of these solutions to ultraviolet light. As seen in Figure 1, at a given light intensity, the decrease in optical density was dependent upon the H₂O₂ concentration: (the higher the concentration of H₂O₂, the faster the destruction of RNO). However, at a concentration of H₂O₂ higher than 0.06 M, increasing the H₂O₂ concentration led to a reduced rate of destruction of RNO. This observation shows that in the lower H₂O₂ concentration region, the increased rate of bleaching of RNO is related to the increased absorption of ultraviolet light by H₂O₂ and, hence, more OH radicals will be formed to react with RNO. However, at larger H₂O₂ concentrations, H₂O₂ itself reacts with OH radicals and introduces a competition for the OH radical reaction with RNO.

The quantum yield for the destruction of the RNO, $\Phi(-RNO)$, was calculated

$$\Phi(-RNO) = \frac{(-\Delta \text{abs}^{440} / \text{min})(6.02 \times 10^{23})}{(I_{H_2O_2})(\epsilon_{RNO}^{440})(10^{23})} \quad (2)$$

where $-\Delta \text{abs}^{440} / \text{min}$ is the magnitude of the initial (negative) slope of the absorbance at 440 nm *vs.* illumination time plot, and $I_{H_2O_2}$ is the fraction of the photon flux absorbed by the hydrogen peroxide in the system calculated from eq 1.

Figure 2 shows the effect of the intensity of the absorbed light on $\Phi(-RNO)$. In this experiment, the intensity of ultraviolet light was changed by one order of magnitude by changing the distance between the light source and the cell. No intensity dependence on $\Phi(-RNO)$ was observed at lower H₂O₂ concentration, although there is a discernable intensity dependence for a hydrogen peroxide concentration of 0.12 M. This fact, along with relatively

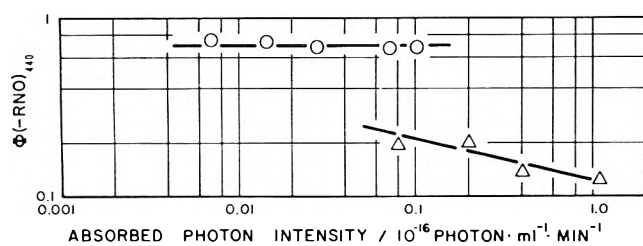


Figure 2. Effect of absorbed photon intensity on the quantum yield (measured at 440 nm) for the destruction of RNO: ○, (RNO) = $5.5 \times 10^{-5} M$, (H_2O_2) = $1.54 \times 10^{-3} M$; △, (RNO) = $5.0 \times 10^{-5} M$, (H_2O_2) = $5.3 \times 10^{-4} M$; photon flux = 2.21 rated, pH 6.

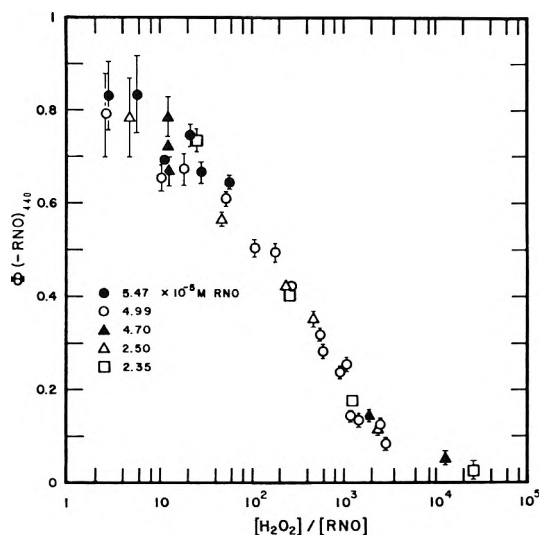
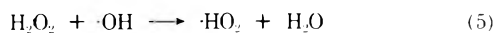
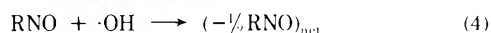


Figure 3. Effect of competition between H_2O_2 and RNO for OH radical on the quantum yield for bleaching at 440 nm. Solutions were air saturated, pH 6. (See text for correction to these values.)

smaller values of $\Phi(-RNO)$, argues against the possibility of a chain mechanism^{7,8} in the RNO- H_2O_2 system at low H_2O_2 concentrations. In Figure 3, values of $\Phi(-RNO)_{440}$ obtained at various concentrations of H_2O_2 and RNO are plotted *vs.* $\log (H_2O_2)/[RNO]$. These were the quantum yields calculated from the bleaching at 440 nm. The curve in this figure can be explained by the following simple competition reactions



Equation 4 is written with the indicated stoichiometry based upon results in the radiolytic RNO system,² which requires that two OH radicals be consumed for the net destruction of one RNO molecule (see next section). Equation 7 can be derived from the above set of reactions.

$$\frac{1}{\Phi(-RNO)} = \frac{2}{\Phi(\cdot OH)} \left[1 + \frac{k_5 (H_2O_2)}{k_4 (RNO)} \right] \quad (7)$$

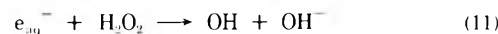
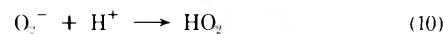
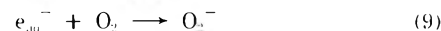
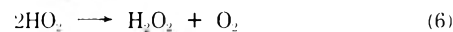
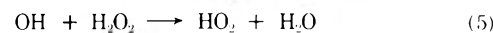
From the least-squares slope taken from the plot of $\Phi(-RNO)^{-1}$ and $(H_2O_2)/(RNO)$ shown in Figure 4, the relative rate constant ratio of the reaction 5 and 4, k_5/k_4 , is determined as 3.6×10^{-3} , in excellent agreement with that expected (3.6×10^{-3}),¹⁴ and the intercept of the line, 2.0/

$\Phi(\cdot OH)$ is 1.4, yielding $\Phi(\cdot OH) = 1.43$. This is seen to be slightly lower than anticipated from Figure 3, but since the experimental error is largest at the very low values of H_2O_2 concentration, we take the extrapolated least-squares value as more accurate.

If it is assumed that this quantum yield of OH radicals is a measure of all the OH radicals which escape geminate recombination in the photolytic decomposition of H_2O_2 , then the net quantum yield for hydrogen peroxide decomposition would be half of the above value, or 0.72 ± 0.07 . Since this value was in disagreement with all other values in the literature,⁷⁻¹¹ we decided to examine the implication of the wavelength dependence of $G(-RNO)$, measured at wavelength λ (around 440 nm) in the ^{60}Co γ radiolysis.¹⁵ These studies implied that the products of the radiolysis may absorb significantly at 440 nm, where all optical bleaching measurements were taken for the H_2O_2 photolysis studies. Dainton and Wisell's product analysis⁴ was based upon high total doses and a crude steam bath evaporation in air of irradiated solutions followed by thin layer chromatography. This analysis was suspect since, from our experiments, RNO and some of its products were easily decomposed during thin layer chromatography. After much unsuccessful effort to separate RNO from its products using thin layer and gas-liquid chromatography, a liquid chromatography system was found,¹³ which allowed separation and quantitative analysis of the RNO separated from its H_2O_2 photolysis and radiolysis products. The results of these quantitative studies showed that because of product absorbance at 440 nm a correction factor of 1.28 needed to be applied to $\Phi(-RNO)_{440}$ (the quantum yield calculated from the 440-nm bleaching only), thus yielding a new, corrected value of 0.92 ± 0.10 for the quantum yield for RNO destruction. Assuming the stoichiometry found from the radiolytic studies,^{2,4,5} namely, the net destruction of one RNO molecule for every two OH radicals, the quantum yield for scavenged OH radicals would be 1.84, and the quantum yield for disappearance of H_2O_2 would be 0.92 ± 0.10 (see ref 16).

The Radiolytic System RNO- H_2O_2 - O_2 . Table II represents values of $G(-RNO)$ found in the ^{60}Co γ radiolysis of aqueous, air-saturated, pH 9 solutions containing variable concentrations of H_2O_2 and RNO.

The results of these experiments may be interpreted in terms of the reactions



Equation 13 may be derived from the above set of equations.

$$\frac{1}{G(-RNO)} = 2 \left[1 + \frac{k_5 (H_2O_2)}{k_4 (RNO)} \right] \times \left[\frac{1}{(G_{e_{aq}^-}/1 + [k_9(O_2)/k_{11}(H_2O_2)]) + G_{OH}} \right] \quad (13)$$

where $G(-RNO)$, G_{OH} and $G_{e_{aq}^-}$ are, respectively, the

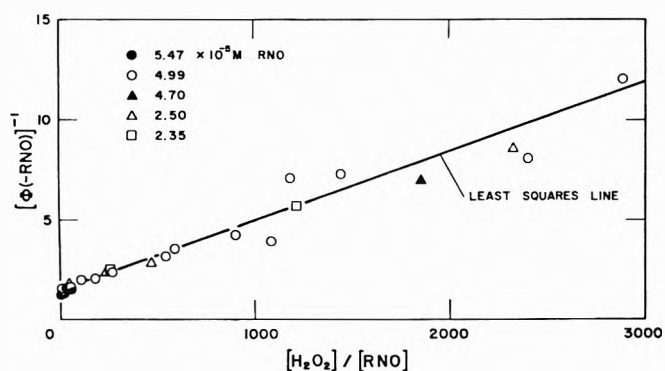


Figure 4. Test of simple competition kinetics (eq 7 in text) between RNO and H₂O₂ for the photolytic intermediate, OH. Data are taken from Figure 3.

net yields of radiolytic destruction of RNO, and the primary yields of the OH radical and the hydrated electron, both normally found to be approximately 2.7.¹⁴ We apply the same correction factor (1.28) used in the photolysis results to all values of $G(-RNO)_{440}$ (taken from initial slopes of spectrophotometric data at 440 nm) since the kinetics of formation of at least one common product of photolysis and radiolysis is found to be identical.¹³ Thus, we are able to test the validity of eq 12 by setting $G_{OH} = 2.7$,¹⁴ $k_9/k_{11} = 1.53$,¹⁴ and $k_5/k_4 = 0.0036$ ¹⁴ and calculating for all corrected $G(-RNO)$ values the best least-squares fit for $G_{e_{aq}^-}$. This procedure yields a value for $G_{e_{aq}^-}$ of 2.6, in good agreement, within experimental error, with the accepted value of this yield at these solute concentrations.¹⁴ Therefore, this agreement is taken as justification for the assumed mechanism since both RNO and H₂O₂ concentrations were varied over wide limits.

Thus, even when OH radicals originate from electron scavenging by H₂O₂, the assumed reaction mechanism and kinetic parameters remain the same as that in the hydrogen peroxide photolysis, except possibly for the RNO stoichiometry with respect to the OH radical.

Conclusions

The combined radiation and photochemical studies would appear to confirm a common competition mechanism in which hydrogen peroxide and RNO compete for an intermediate in an early process, the outcome of which exclusively determines the net yield of destruction of RNO. From these results, it is demonstrated that the oxidizing radical from radiolysis, the product of hydrated electron scavenging by hydrogen peroxide, and the ultraviolet photolysis product of hydrogen peroxide solutions are kinetically equivalent in the rate-determining competition steps. The stoichiometry of the reaction of RNO with this radical from two different sources (e_{aq}^- scavenging by H₂O₂ and OH from radiolysis of H₂O) is fixed at a net destruction of one RNO molecule for every two OH radicals.

TABLE II: Radiolytic Yields in the RNO-H₂O₂-O₂ System

| $1/G(-RNO)_{440}$ | $(H_2O_2)_0/[RNO]$ | $(O_2)_0/(H_2O_2)_0^a$ |
|-------------------|--------------------|------------------------|
| 0.86 | 0.75 | 6.7 |
| 0.79 | 2.5 | 2.0 |
| 0.71 | 7.5 | 0.67 |
| 0.64 | 25.0 | 0.2 |
| 0.67 | 75.0 | 0.067 |
| 0.97 | 250.0 | 0.02 |
| 1.53 | 750.0 | 0.0067 |
| 0.84 | 0.375 | 6.7 |
| 0.79 | 1.250 | 2.0 |
| 0.69 | 3.75 | 0.67 |
| 0.61 | 12.5 | 0.2 |
| 0.60 | 37.5 | 0.067 |
| 0.69 | 125.0 | 0.02 |
| 1.02 | 375.0 | 0.0067 |
| 0.82 | 1.5 | 6.7 |
| 0.77 | 5.0 | 2.0 |
| 0.73 | 15.0 | 0.67 |
| 0.67 | 50.0 | 0.2 |
| 0.75 | 100.0 | 0.1 |
| 1.35 | 500.0 | 0.02 |

^a All solutions were air saturated (2.5×10^{-4} M O₂) pH 9.

Since the ratio of rate constants (k_5/k_4) is, within experimental error, the same in both the radiation and photochemical systems, the common rate-determining steps may be concluded to be reactions 4 and 5. The reasons for the possible different net stoichiometries in the two systems ($-1/2$ RNO per OH in the radiation chemistry *vs.* -1 RNO per OH⁷⁻¹¹ in the photochemical system) may lie in the secondary and tertiary processes following reactions 4 and 5. Dainton and Rowbottom¹⁶ report the only quantum yield which is in agreement with our results.

References and Notes

- (1) This research was supported in part by the U. S. Atomic Energy Commission.
- (2) I. Kraljic and C. N. Trumbore, *J. Amer. Chem. Soc.*, **87**, 2547 (1965).
- (3) I. Kraljic in "The Chemistry of Ionization and Excitation," G. R. A. Johnson and G. Scholes, Ed., Taylor and Francis, London, 1967, p 303.
- (4) F. S. Dainton and B. Wiseall, *Trans. Faraday Soc.*, **64**, 695 (1968).
- (5) J. H. Baxendale and A. A. Kahn, *Int. J. Radiat. Phys. Chem.*, **1**, 11 (1969).
- (6) S. Shah, C. N. Trumbore, B. Giessner, and W. Park, *Advan. Chem. Ser.*, **No. 81**, 321 (1968).
- (7) J. H. Baxendale and J. A. Wilson, *Trans. Faraday Soc.*, **53**, 344 (1957).
- (8) J. L. Weeks and M. S. Matheson, *J. Amer. Chem. Soc.*, **78**, 1273 (1956).
- (9) D. H. Vorman and J. C. Chen, *J. Amer. Chem. Soc.*, **81**, 4141 (1959).
- (10) J. P. Hunt and H. Taube, *J. Amer. Chem. Soc.*, **74**, 5999 (1952).
- (11) M. Daniels, *J. Phys. Chem.*, **66**, 1473 (1962).
- (12) J. G. Calvert and J. N. Pitts, "Photochemistry," Wiley, New York, N. Y., 1966, p 786.
- (13) A. Lindemanis, J. DeStefano, and C. N. Trumbore, unpublished results.
- (14) I. Dragančić and Z. Draganić, "The Radiation Chemistry of Water," Academic Press, New York, N. Y., 1971.
- (15) J. E. Fanning, unpublished results.
- (16) F. S. Dainton and J. Rowbottom, *Trans. Faraday Soc.*, **49**, 1160 (1953).

Pulse Radiolysis Studies of Chloride Complexes of Thallium(II). Absorption Spectra and Stability Constants of TlCl^+ , TlCl_2 , and TlCl_3^-

R. W. Dodson and H. A. Schwarz*

Chemistry Department, Brookhaven National Laboratory, Upton, New York 11973 (Received November 19, 1973)

Publication costs assisted by Brookhaven National Laboratory

Three chloride complexes of Tl(II) have been identified in a study of the effect of chloride ion on the spectrum of Tl(II) produced by pulse radiolysis. Absorption maxima are found at 263 and 342 nm for TlCl^+ , at 280 and 342 nm for TlCl_2 , and at 304 and 362 nm for TlCl_3^- . The stability constants of the three complexes are 6.2×10^4 , 1900, and $13 M^{-1}$, respectively. The rate constant for dissociation of TlCl^+ into Tl^{2+} and Cl^- is $1.4 \times 10^5 \text{ sec}^{-1}$ and the rate constant for the reverse reaction is $9 \times 10^9 M^{-1} \text{ sec}^{-1}$. The Tl(II) produced by the radiation pulse disappears by disproportionation to Tl(I) and Tl(III) at diffusion-controlled rates. The rate constant for oxidation of Tl(I) by Cl_2^- is $5 \times 10^9 M^{-1} \text{ sec}^{-1}$. The rate constant for reduction of TlCl_2^+ by hydrogen atoms is $5 \times 10^8 M^{-1} \text{ sec}^{-1}$, and is $2 \times 10^9 M^{-1} \text{ sec}^{-1}$ for the other three Tl(III) complexes: TlCl_2^+ , TlCl_3 , and TlCl_4^- . These hydrogen atom rate constants are larger than that for Tl^{3+} , contrary to expectations based on free-energy considerations. It is proposed that the preferred reduction path is by ligand abstraction whenever possible. It was found that the principal product of H atom reduction of TlCl_2^+ is Tl^{2+} , not TlCl^+ , in support of this mechanism.

Introduction

Chloride ion has a marked effect on the rates of redox reactions involving Tl(III). The general features are a retardation of the reaction at low chloride concentration and a catalysis at high concentration. Examples are the oxidation of Tl(I) (the exchange reaction),²⁻⁷ Cr(II),⁸ Fe(II),^{9,10} U(IV),¹¹ and Os(II)(dipy)₃.¹² Some of these reactions involve Tl(II) as an intermediate (for instance, the reaction with Fe(II)) while others do not (for instance, the exchange reaction). Tl(III) forms strong chloride complexes and this fact is undoubtedly involved in the explanation of the rate effects. The question naturally arises whether Tl(II) also forms chloride complexes which affect the course and rate of reaction. In a study of the oxidation of Fe(II) by Tl(III) Duke and Bornong¹⁰ suggested that this is the case and that the Tl(II) complexes are somewhat less stable than the corresponding Tl(III) complexes.

Pulse radiolysis offers an opportunity to study complexes of Tl(II). Tl(II) can be produced in aqueous solution by reduction of Tl(III) with hydrogen atoms and by oxidation of Tl(I) with hydroxyl radicals. The absorption spectra of Tl(II) in neutral solution¹³ and in perchloric acid solution¹⁴ have already been observed. We have looked for and observed systematic effects of chloride ion on the spectrum of Tl(II). These effects show the existence of three chloride complexes and lead to estimates of their stability constants. We have measured the rate of relaxation toward equilibrium of the first complex and the rates of hydrogen atom reduction of Tl(III).

Experimental Section

Materials. Stock solutions of perchloric acid and of hydrochloric acid were prepared by diluting "Baker Analyzed" reagents with triple distilled water. Solutions 5, 3, and 1 M were standardized by titration with standard sodium hydroxide. More dilute solutions of hydrochloric acid were made by further quantitative dilution. These were restandardized, volumetrically with standard sodium

hydroxide and gravimetrically by precipitation of silver chloride. Thallous nitrate was prepared by dissolving thallium metal in nitric acid and recrystallizing, or was obtained from Alfa Inorganics. Thallous perchlorate was precipitated from a solution of the nitrate by adding perchloric acid. Some preparations were freed from traces of copper and silver by precipitating a small fraction of the thallium with hydrogen sulfide from slightly alkaline solution. In all preparations of thallous perchlorate the final purification steps were precipitation with perchloric acid, followed by three recrystallizations from triple distilled water. The removal of trace copper and silver had no discernible effect on the results obtained in the present investigation. Stock solutions of thallous perchlorate were prepared by dissolving weighed amounts of dry TlClO_4 in triple distilled water; the concentration was checked by bromate titration. Stock solutions of thallium(III) perchlorate were prepared by anodic oxidation of thallium(I) perchlorate in perchloric acid. Thallium(I) was determined by bromate titration, and total thallium was also determined by this method after reduction of thallium(III) with formaldehyde. Solutions for radiolysis were prepared by mixing known volumes of the stock solutions and, when needed, triple distilled water.

Pulse Radiolysis Equipment. A 2-MeV Van de Graaff was used as the electron source for experiments to measure absorption spectra and disproportionation kinetics. The analyzing light came from a 30-W deuterium lamp pulsed for 10 msec to a light level seven times the quiescent level. The light passed through the sample three times, then to a $f/3.5$ high-intensity monochromator and to the photomultiplier. The PM signal was amplified, sent to a digital transient recorder, and then to magnetic tape for later processing.

The sample was in a 2 cm \times 2 cm \times 0.8 cm quartz cell with a 2-mm capillary neck 5 mm long and was placed in an aluminum box to eliminate the effects of stray current on the charge measurement. Solutions were degassed by bubbling with Ar or brought to 50 μM O_2 by bubbling

with 5% O₂ in N₂. The cell was loosely stoppered after degassing to prevent air contamination. All irradiations were done at room temperature (23°).

The dose given the samples was calibrated by FeSO₄ dosimetry and was usually near 200 rads per pulse. Many pulses (40 or more) could be given to a sample without changing the initial absorbance after the pulse; a maximum of 12 were used. Only two pulses were given to the more dilute chloride samples to minimize the effect of complexing the chloride with Tl(III) produced in the reaction. The change in free chloride after the pulse was 10% in the worst case and no correction was made for the effect.

A 1.9-MeV Febetron (10⁻⁷ sec pulse length) was used as the electron source for the other kinetic studies. The analyzing light source was a pulsed xenon arc. The light, after passing through the sample (4 cm), left the accelerator vault and was focussed onto the monochromator. A 30° quartz prism was inserted 30 cm before the monochromator to predisperse the light sufficiently to minimize scattered light problems in the monochromator. The photomultiplier was mounted on a base containing a 6-nsec rise time amplifier and the amplified signal was sent to a Lecroy waveform digitizer which transferred the waveform to magnetic tape. Most of the Febetron experiments used about 5000-rad pulses.

Results

Spectra and Stability Constants. Pulse radiolysis of thallium(I) solutions and of thallium(I)-thallium(III) mixtures produces a light absorption due to thallium(II) lasting for several hundred microseconds at low doses. Absorption spectra of thallium(II) in 1 M HClO₄¹⁴ and in three HClO₄-HCl mixtures (1 M total acid) are given in Figure 1.

The absorbance produced in Tl(I)-Tl(III) solutions followed a second-order decay. The absorbance at the end of the pulse (4 μsec length) was found by the second-order kinetic analysis, and thus depends on all the data, not just the observation immediately after the pulse. This absorbance was corrected for the slight decay which occurred during the pulse (always less than 1%).

Oxygen was added to solutions of Tl(I) to provide a known fate, HO₂, for hydrogen atoms. A comparison with deaerated solutions did not produce evidence for H atom interference, although the results were somewhat less reproducible and the kinetics less regular in the absence of O₂. The decay in the presence of O₂ had a first-order component and was adequately represented empirically for two half-lives as a first-order decay with a constant term

$$A = A_1 e^{-k_1 t} + A_2$$

The absorbance at the end of the pulse is A₁ + A₂. This value was corrected for the reaction which occurred during the pulse and for absorption by the HO₂ present to give the absorbance of the Tl(II). The pseudo-first-order rate constant *k* at the doses used was about 3.5 × 10³ sec⁻¹ at low chloride concentration but rose appreciably at chloride concentrations above 2 × 10⁻⁴ M, reaching 3.2 × 10⁴ at 0.4 M chloride. The approximate first-order nature of the decay does not mean that all the Tl(II) is reacting with O₂. In fact, at low chloride concentrations, the rate of decay is almost independent of whether O₂ is present or not. The increase in rate constant at high chloride concentration is due to reaction of Tl(II) chloride complexes with oxygen

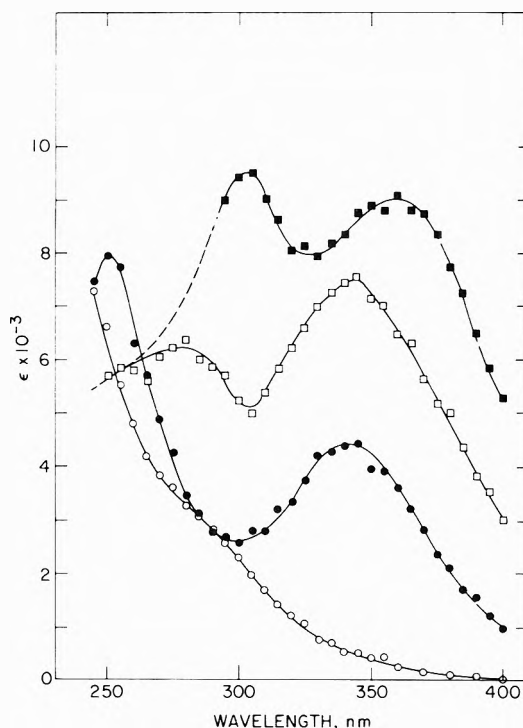
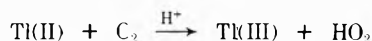


Figure 1. Absorption spectra of Tl(II), derived from pulse radiolysis of solutions containing various chloride concentrations: open circles, 10⁻³ M Tl(I), 5 × 10⁻⁵ M O₂, no Tl(III), no chloride; filled circles, 10⁻³ M Tl(I), 5 × 10⁻⁵ M O₂, no Tl(III), 10⁻⁴ M HCl; open squares, 10⁻³ M Tl(I), 5 × 10⁻⁵ M O₂, no Tl(III), 5.1 × 10⁻³ M HCl; filled squares, 6 × 10⁻⁴ M Tl(I), 3 × 10⁻⁴ M Tl(III), 0.4 M HCl. All solutions are 1 M acid, the balance of acid being HClO₄. The dashed line continuation below 295 nm of the upper curve is estimated from studies of Tl(I) solutions which yielded a spectrum similar in shape but not identical with that reported here (see text).



which is borne out by the appearance of absorption in the region 250–280 nm due to Tl(III) chloride complexes stoichiometrically equivalent to the Tl(II) reacting with oxygen. The Tl(II) probably disappears at low chloride concentration by disproportionation and by reaction with HO₂



which would add a first-order component because HO₂ is formed in excess of Tl(II) (yields of 3.65 molecules per 100 eV (*G_H*) vs. 2.85 (*G_{OH}*)) and HO₂ is relatively stable with respect to disproportionation.

The extinction coefficients were found from

$$\epsilon = A_0/lc$$

where A₀ is the absorbance due to Tl(II), *l* is the light path length (6.1 cm), and *c* is the total Tl(II) concentration produced by the pulse, calculated from the dosimetry and known yields. The assumed yield of Tl(II) from Tl(I) solution is 2.85 ions per 100 eV (*i.e.*, *G_{OH}*), and from Tl(I)-Tl(III) mixtures is 6.5 (*i.e.*, *G_{OH}* + *G_H*).

With Tl(I)-Tl(III) mixtures observations much below 300 nm were not possible because of the light absorption by the chloride complexes of Tl(III). Also, uncertainties in stability constants for these complexes introduced an error into the estimation of free chloride ion concentrations when the total chloride was much below 10⁻³ M. Consequently the useful range of the mixtures was limited. Ex-

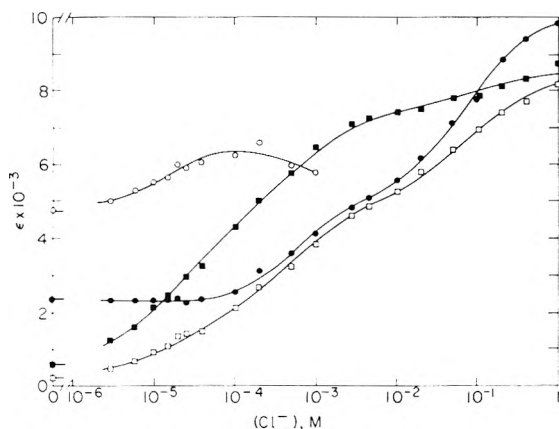


Figure 2. Variation of Tl(II) extinction coefficient with free chloride concentration at four wavelengths: open circles, 260 nm; filled circles, 300 nm; filled squares, 340 nm; open squares, 380 nm. Data at 10^{-3} M Cl^- and below obtained from 10^{-3} M Tl(I), 5×10^{-5} M O_2 solutions; data from 10^{-3} M Cl^- to 0.1 M Cl^- obtained from 10^{-3} M Tl(I), 5×10^{-4} M Tl(III) solutions; data at 0.1 M Cl^- and above obtained from 6×10^{-4} M Tl(I), 3×10^{-4} M Tl(III) solutions. The curves are least-squares fits of eq 4 to the data.

Extinction coefficients determined from the mixtures should be the same as those from the Tl(I) solutions. This was found to be the case for 10^{-3} and 5×10^{-3} M free chloride solutions, for which extinction coefficients from Tl(I) solutions averaged 1.6% higher than from Tl(I)-Tl(III) solutions, an effect less than experimental error. The two methods do not agree at higher chloride. Solutions containing 10^{-4} M Tl(I) and 0.4 M chloride ion gave erratic spectra, about 20% larger near 360 nm and 30–40% larger near 300 nm than the top curve of Figure 1. In 10^{-3} M Tl(I), 0.4 M Cl^- , the disagreement was greater. Thallium(I) concentration had little effect on extinction coefficients when Tl(III) was present. A solution containing 2.1×10^{-4} M Tl(I), 6.0×10^{-4} M Tl(III), 0.4 M Cl^- , and 0.6 M HClO_4 gave results identical with the upper curve of Figure 1 (for which the thallos concentration is 3 times larger) above 320 nm, although the peak at 302 nm appeared to be 5% larger. We do not understand the problem with Tl(I) solutions at high chloride concentration (except that chloride complexes of Tl(I) are present). The agreement between methods at 5×10^{-3} M Cl^- and below suggests the results to be trustworthy in that region. The lack of Tl(I) concentration effect in Tl(I)-Tl(III) solutions suggests that the results obtained with these solutions are trustworthy in the high chloride range.

The spectrum in the absence of Cl^- is the same as presented earlier.¹⁴ There is no peak in the observable range of the spectrum. The spectrum from solutions containing 10^{-4} M Cl^- shows a peak at 250 nm and a peak at 340 nm, which we ascribe to TlCl^+ . The first peak shifts to 280 nm and the 340-nm peak is much larger in 5.1×10^{-3} M Cl^- solutions indicating a second complex; and in 0.4 M Cl^- the first peak shifts further to 302 nm and the second peak shifts to 360 nm, indicating a third complex.

Further evidence for these complexes is seen in Figure 2, in which extinction coefficients at four wavelengths are given as a function of free chloride concentration from 3×10^{-6} to 1 M Cl^- . The growth of the first complex may be seen in the region of 10^{-5} M Cl^- at 260, 340, and 380 nm. The lack of change in ϵ at 300 nm indicates the wavelength is near an isosbestic point of Tl^{2+} and TlCl^+ . The spectral changes continue as the chloride ion concentra-

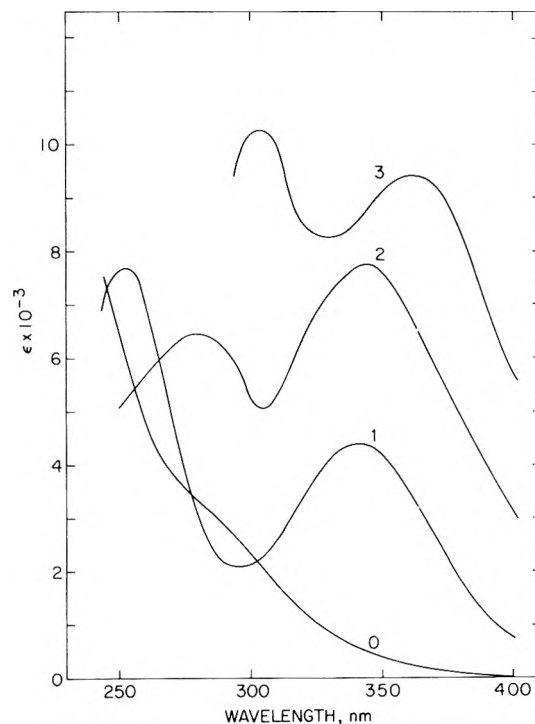
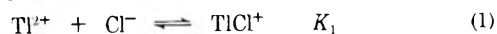


Figure 3. Absorption spectra of the individual Tl(II) chloride complexes derived from spectra of Figure 1 and stability constants of Table I: curve 0, Tl^{2+} ; curve 1, TlCl^+ ; curve 2, TlCl_2^+ ; curve 3, TlCl_3^- .

tion is increased. Effects of the formation of a second complex are most clearly seen below 10^{-3} M, in the increase in ϵ at 300 nm. Since this wavelength is near an isosbestic point of Tl^{2+} and TlCl^+ , the increase in ϵ below 10^{-3} M cannot be due to continued growth of TlCl^+ , and shows the formation of a second complex, TlCl_2^+ . The growth of the third complex is seen near 0.1 M Cl^- .

The three equilibria are



and the stability constants are defined by

$$K_1 = [\text{TlCl}^+]/[\text{Tl}^{2+}][\text{Cl}^-]$$

$$K_2 = [\text{TlCl}_2^+]/[\text{TlCl}^+][\text{Cl}^-]$$

$$K_3 = [\text{TlCl}_3^-]/[\text{TlCl}_2^+][\text{Cl}^-]$$

The variation of ϵ with chloride concentration is

$$\epsilon_{\text{obsd}} = \frac{\epsilon_0}{D} + \frac{\epsilon_1 K_1 [\text{Cl}^-]}{D} + \frac{\epsilon_2 K_1 K_2 [\text{Cl}^-]^2}{D} + \frac{\epsilon_3 K_1 K_2 K_3 [\text{Cl}^-]^3}{D} \quad (4)$$

where

$$D = 1 + K_1 [\text{Cl}^-] + K_1 K_2 [\text{Cl}^-]^2 + K_1 K_2 K_3 [\text{Cl}^-]^3$$

and the ϵ 's are the extinction coefficients for the complexes with 0, 1, 2, and 3 chlorides. The results plotted in Figure 2 were fit to eq 4 by non-linear least-squares analysis, all values of ϵ_{obsd} being given equal weight. The stability constant estimates were not appreciably different whether all four wavelengths were used, just the data at 300, 340, and 380 nm or just those at 340 and 380 nm. The "best values" of the stability constants are given in Table

TABLE I: Stability Constants of Chloride Complexes of Thallium in Three Oxidation States

| Oxidation state | Medium | K_1 | K_2 | K_3 | K_4 |
|----------------------|----------------------------|-------------------------------|------------------------------|-------------|------------|
| Tl(I) ^a | 4 M (NaClO ₄) | 0.8 | 0.2 | 0.1 | |
| Tl(II) ^b | 1 M (HClO ₄) | $(6.2 \pm 0.7) \times 10^4$ | 1900 ± 400 | 13 ± 3 | |
| Tl(III) ^c | 0.5 M (HClO ₄) | $(5.22 \pm 0.19) \times 10^6$ | $(1.25 \pm 0.1) \times 10^5$ | 553 ± 8 | 44 ± 9 |

^a R. O. Nilsson, *Ark. Kemi*, **10**, 363 (1956). Numerous other estimates are listed in *Chem. Soc., Spec. Publ.*, No. 17, 294, 295 (1964). ^b This work. A fourth complex, $K_4 < 1$ is not excluded. ^c The values of K_1 and K_2 are those of ref 17 which also gives $K_3 = 482 \pm 60$ and $K_4 = 65.3 \pm 7$. For K_3 and K_4 we have a preference for the values of ref 18 which are those listed above. A species containing five chlorides, with $K_5 \approx 0.1-0.4$ has been proposed by D. L. Horrocks and A. F. Voigt, *J. Amer. Chem. Soc.*, **79**, 2440 (1957), and by R. M. Walters and R. W. Dodson.¹⁸

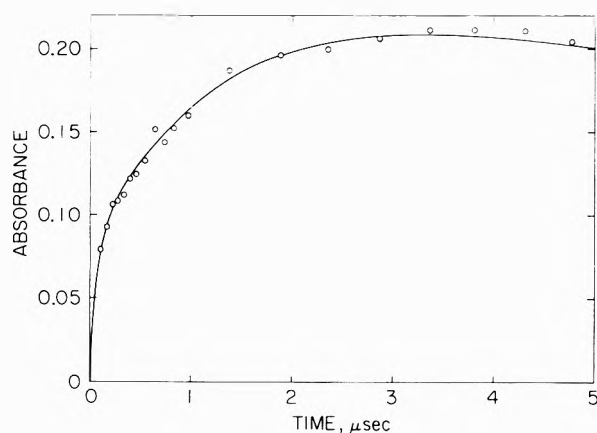


Figure 4. Growth of absorbance at 280 nm following pulse radiolysis of a solution containing 3×10^{-4} M Tl(III), 7.3×10^{-3} M total HCl, and 0.99 M HClO₄. The predominant Tl(III) species in this solution is TlCl₃. Solid curve is sum of two exponential growths modified by a second-order decay. These results (and those of the next two figures) were obtained from five to ten separate experiments using varying time scales with 50% overlap between scales. Each experiment yielded 19 points on the time curve. Accurate dosimetry was unavailable for these experiments, and the curves were normalized vertically to give the best fit with each other. All points in a time band (equal to interpoint spacing) were averaged to produce the points that are plotted.

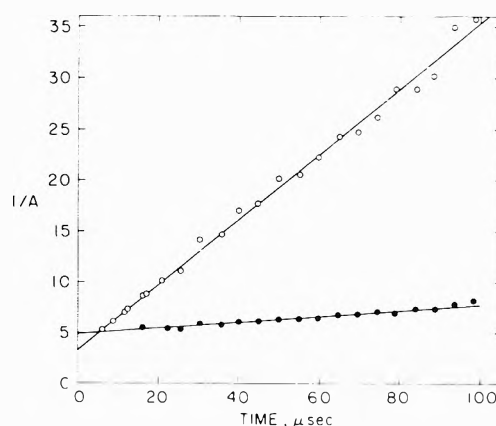
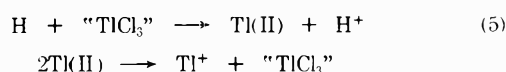


Figure 5. Second-order decay following growth in pulse radiolyzed Tl(III) solutions: open circles, a continuation of the data of Figure 4 (280 nm); filled circles, absorption at 290 nm from solution containing 3.00×10^{-3} M Tl(III), 3.00×10^{-3} M total HCl, 1 M HClO₄ (in which predominant Tl(III) species is TlCl₂⁺).

I along with stability constants for Tl(III) and Tl(I) chloride complexes. The values for Tl(II) were based on data at 300, 340, and 380 nm in view of the lack of data above 10^{-3} M Cl⁻ at 260 nm. The spectra of the individual complexes, derived from the data of Figures 1 and 2, are given in Figure 3.

Kinetics. Earlier work¹⁴ established that hydrogen atoms react with Tl³⁺ with a rate constant of 3.9×10^7 M⁻¹ sec⁻¹. It is of interest to know the rate constants for reaction of the H atoms with the Tl(III) chloride complexes. The growth of absorbance at 280 nm in a solution containing predominantly (65%) TlCl₃ complex is shown in Figure 4. This rapid growth is followed by a slower second-order decay (beyond 5 μsec), as shown in Figure 5. For the reaction scheme ("TlCl₃" refers to the various chloride complexes present)



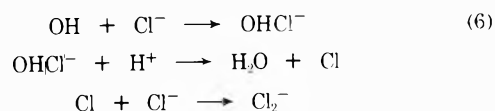
(plus other radical-radical reactions)

the variation of absorbance with time should be representable by

$$A = A_0(1 - e^{-\alpha[\text{Tl(III)}]_0 t}) \frac{1}{1 + \alpha t}$$

where α includes the effects of second-order radical-radical reactions. This form can be derived if all radical-radi-

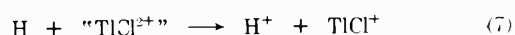
cal reactions are assumed to have the same rate constant. From Figure 5, α is found to be 1.0×10^5 sec⁻¹. It is not possible to give a detailed interpretation of α in terms of the individual second-order processes. Knowing the magnitude of α , we can now analyze Figure 4. The growth data cannot be fit with a single exponential. The solid curve is calculated for a very fast rise with a rate constant of 1.4×10^7 sec⁻¹ and a slower rise with a rate constant of 5.5×10^5 sec⁻¹. A reasonable explanation of the rapid rise is that it is due to absorption by Cl₂⁻ formed by the reactions¹⁵



Reaction 6 is rate controlling under our conditions. The free chloride concentration in this solution is 6×10^{-3} M, and from the 1.4×10^7 sec⁻¹ rate constant we estimate k_6 to be 2×10^9 M⁻¹ sec⁻¹. Jayson, Parsons, and Swallow¹⁵ give k_6 as 4×10^9 M⁻¹ sec⁻¹. Our estimate is based mainly on two points and the discrepancy is not serious.

The slower rise is due to reaction 5, $k_5[\text{Tl(III)}] = 5.5 \times 10^5$ sec⁻¹, from which $k_5 = 2 \times 10^9$ M⁻¹ sec⁻¹.

The situation is remarkably different in a Tl(III) solution at low free chloride (1×10^{-6} M) ("TlCl₂⁺") in which the species TlCl₂⁺ predominates. The decay of the absorbance after 20 μsec is much slower than found in "TlCl₃" solution, as shown by the lower curve of Figure 5. The time dependence of the absorbance between 2 and 20 μsec (Figure 6) is wavelength dependent, the absorbance decreasing with time at 340 nm while increasing slightly at 290 nm. Apparently the reaction



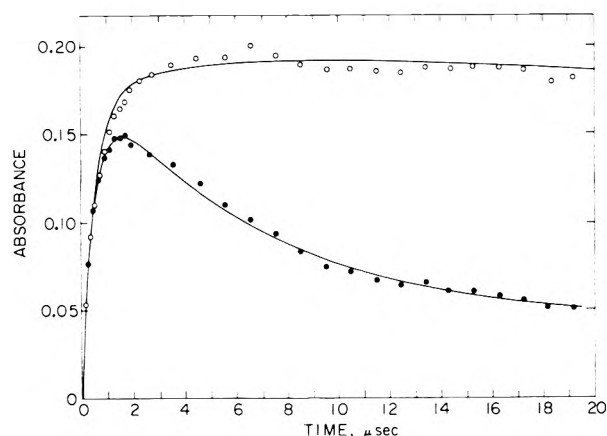
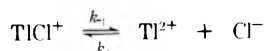


Figure 6. Growth and decay of absorbance at 290 (open circles) and 340 nm (filled circles) following pulse radiolysis of solution containing $3.00 \times 10^{-3} M$ Tl(III), $3.00 \times 10^{-3} M$ total HCl, and $1 M$ HClO₄ (same solution as lower curve of Figure 5). Solid curves are sums of exponential growth and decay.

produces TlCl⁺ at a concentration far in excess of that which would be in equilibrium with $10^{-6} M$ free chloride. The relaxation to equilibrium



would lead to the observed large decrease in absorbance at 340 nm and a slight increase at 290 nm, as may be seen by reference to the spectra of Figure 3. The rise in absorbance in the first 2 μsec can be attributed to reaction 7. The kinetic equation developed from reactions 7 and 1 predicts that the absorbance should be expressed as the sum of a first-order growth with rate constant $k_7[\text{Tl(III)}]$ and a first-order relaxation with rate constant $k_r = k_{-1} + k_1[\text{Cl}^-]$.

$$A = A_1(1 - e^{-k_7[\text{Tl(III)}]t}) + A_2(1 - e^{-k_r t}) \quad (8)$$

The solid lines in Figure 6 are computed on this basis with a slight correction for the slow second-order decay (Figure 5). The value of $k_7[\text{Tl(III)}]$ was $1.9 \times 10^6 \text{ sec}^{-1}$, from which k_7 is $6 \times 10^8 M^{-1} \text{ sec}^{-1}$. The value of $k_{-1} + k_1[\text{Cl}^-]$ was $1.5 \times 10^5 \text{ sec}^{-1}$ and $[\text{Cl}^-]$ was $1 \times 10^{-6} M$ (calculated from solution composition and stability constants of thallium(III) chloride complexes). The stability constant K_1 , $6.2 \times 10^4 M^{-1}$, is equal to k_1/k_{-1} , so we find $k_{-1} = 1.4 \times 10^5 \text{ sec}^{-1}$ and $k_1 = 9 \times 10^9 M^{-1} \text{ sec}^{-1}$. This treatment ignores the fact that the chloride released in the reaction, about $10^{-5} M$, is far in excess of the equilibrium concentration. However, because of the strong buffering action of the Tl(III), the equilibrium concentration of free chloride would be shifted only a few per cent. On the reasonable assumption that the complexing reaction of the Tl(III) is diffusion controlled the relaxation of the Tl(III) equilibrium should be essentially complete in 10^{-7} sec , a period much shorter than the observation time. The treatment also neglects reactions of the hydroxyl radical, *i.e.*, those with Tl(I) and Tl(II) as well as recombination. Some justification for this neglect is to be found in the compensating character of the reactions with Tl(I) and Tl(II). We have not been able to devise a mechanism which accounts for the qualitative difference in behavior at 290 and 340 nm by reactions of the hydroxyl radical.

The coefficient A_1 in eq 8 represents the limiting absorbance that would be obtained if the relaxation process

TABLE II: Fraction (F) of Tl(II) Formed as TlCl⁺ by Reaction of Hydrogen Atoms with Tl(III) as a Function of Chloride Concentration

| [Tl(III)], mM | Total [Cl ⁻], mM | Fraction of Tl(III) present as | | | F |
|------------------|------------------------------------|--------------------------------|--------------------|--------------------------------|------|
| | | Tl ³⁺ | TlCl ²⁺ | TlCl ₂ ⁺ | |
| 10.0 | 4.9 | 0.52 | 0.47 | 0.01 | 0.46 |
| 10.0 | 7.5 | 0.29 | 0.67 | 0.04 | 0.43 |
| 10.0 | 9.9 | 0.12 | 0.76 | 0.12 | 0.59 |
| 3.0 | 3.0 | 0.12 | 0.76 | 0.12 | 0.61 |
| 10.0 | 13.2 | 0.03 | 0.63 | 0.34 | 0.72 |

were very slow. It may be related to the composition of the Tl(II) produced in reaction of H with Tl(III) by

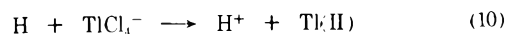
$$A_1 = \{F\epsilon(\text{TlCl}^+) + (1 - F)\epsilon(\text{Tl}^{2+})\}l[\text{Tl(II)}]$$

where F is the fraction of Tl(II) produced as TlCl⁺. The value of F for the "TlCl²⁺" solution is 0.54, determined from the values of A_1 at 290 (0.176) and at 340 nm (0.188). This solution contains 12% of the Tl(III) as TlCl₂⁺, 12% as Tl³⁺, and 76% as TlCl²⁺. Four other solutions, $10^{-2} M$ in Tl(III) and $1 M$ in total acid with varying proportions of HCl, were examined to determine how F varies with solution composition. The absorbances past the peak in the rate curve at 340 nm were extrapolated to zero time to approximate A_1 values for each solution and wavelength. The solution compositions and resulting values of F are given in Table II. Increase in the TlCl₂⁺ content of the solutions causes an increase in F .

Two other thallium(III) solutions, containing predominantly TlCl₂⁺ and TlCl₄⁻ species, respectively, were also examined, but in less detail than the TlCl²⁺ and TlCl₃ solutions. The rate constant for reaction 9

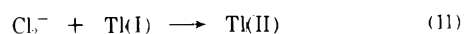


was found to be $2 \times 10^9 M^{-1} \text{ sec}^{-1}$ and for reaction 10



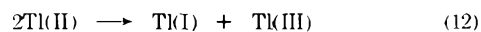
was also found to be $2 \times 10^9 M^{-1} \text{ sec}^{-1}$.

The rate constant for the oxidation of Tl⁺ by OH has been determined to be $1.0 \times 10^{10} M^{-1} \text{ sec}^{-1}$.¹⁴ The corresponding reaction with Cl₂⁻ would be



This reaction was studied in a solution containing deaerated $3 \times 10^{-4} M$ Tl(I) and $0.99 M$ HCl. The absorbance at 260 nm increased after the pulse in a first-order process with a rate constant of $1.5 \times 10^6 \text{ sec}^{-1}$, from which $k_{11} = 5 \times 10^9 M^{-1} \text{ sec}^{-1}$. The absorbance at 340 nm, the peak of the Cl₂⁻ spectrum, was 0.179 immediately after the pulse and decreased to 0.157 at 2 μsec with the same rate constant as that found at 260 nm. We associate this change with reaction 11, so that 0.179 is the absorbance of the Cl₂⁻ which produces Tl(II) with an absorbance of 0.157 in 0.99 M HCl. The extinction coefficient of Tl(II) at 340 nm in this medium, from Figure 2, is 8450, consequently we find $\epsilon(\text{Cl}_2^-)$ to be $8450 \times 0.179/0.157$ or 9600 at 340 nm. This may be compared with 8800 found by Jayson, Parsons and Swallow,¹⁵ and 12,500 found by Anbar and Thomas.¹⁶

After thallium(II) is produced in deaerated solutions containing both Tl(I) and Tl(III), and has relaxed toward equilibrium of its complexes with chloride, it disappears by a second-order disproportionation reaction



as noted earlier in connection with the spectra and stabil-

TABLE III: Disproportionation Rate Constants for Tl(II)

| Free $[\text{Cl}^-]$, M | λ | $10^{-5}k_{12}/\epsilon$ | 10^9k_{12} |
|----------------------------|-----------|--------------------------|--------------|
| 0.0010 | 300 | 6.55 | 2.69 |
| 0.0010 | 380 | 6.21 | 2.44 |
| 0.0028 | 300 | 5.49 | 2.64 |
| 0.0028 | 380 | 5.59 | 2.59 |
| 0.0046 | 300 | 5.31 | 2.69 |
| 0.0046 | 380 | 5.61 | 2.74 |
| 0.0097 | 300 | 5.01 | 2.79 |
| 0.0097 | 380 | 5.11 | 2.73 |
| 0.0204 | 300 | 4.52 | 2.78 |
| 0.0204 | 380 | 4.67 | 2.72 |
| 0.0502 | 300 | 3.50 | 2.50 |
| 0.0502 | 380 | 3.95 | 2.53 |
| 0.100 | 300 | 3.01 | 2.37 |
| 0.200 | 300 | 2.65 | 2.36 |
| 0.400 | 300 | 1.92 | 1.81 |
| 0.400 | 390 | 2.83 | 1.85 |
| 0.400 | 400 | 3.62 | 1.94 |
| 0.980 | 300 | 1.97 | 1.85 |

ity constants. Values of k_{12} obtained from runs at various chloride concentrations are given in Table III. Although multiple pulsing had no effect on initial absorbances after a pulse, we did note a slight increase in k/ϵ values (5–10%) over the course of a dozen pulses. Consequently Table III includes only results from the first four pulses on any sample. The rate constants are wavelength independent and vary only slightly with chloride concentration.

Discussion

The experiments involved a wide range of chloride concentration, and it is appropriate to consider the reliability of the concentration scales for total chloride and for free chloride. The total chloride concentration was calculated from the concentration of the standardized stock solutions of HCl and the volumetric dilution factors. The random error resulting from analytical and volumetric errors was estimated in a representative case to be about 0.5%. A more important source of error when the concentration of added chloride was very low is trace halide impurity in the perchloric acid. We believe this to have been not more than micromolar on the basis of the following considerations. (i) Figure 1 shows that Tl(II) in perchlorate solution absorbs light only weakly in the neighborhood of 350 nm with no sign of a spectral peak. In the presence of $10^{-4} M$ chloride the extinction coefficient is increased about tenfold (more at higher wavelengths) and a peak at 340 nm is well developed. From the magnitude of K_1 ($6 \times 10^4 M$) and with the extreme assumption that all of the absorbance found in this region with the perchlorate solution was in fact due to TlCl^+ it follows that the free chloride must have been less than $2 \times 10^{-6} M$. (ii) A perchlorate stock solution $1 \times 10^{-3} M$ in Tl(I) and $1 M$ in HClO_4 was carefully examined by turbidimetric analysis employing silver nitrate. It was estimated that total $[\text{Cl}^-]$ in this solution was less than $1 \times 10^{-6} M$. A least-squares analysis of the data assuming $1 \times 10^{-6} M$ chloride impurity gave $K_1 = 6.6 \times 10^4 M^{-1}$, a 6% increase, and negligible change in the other stability constants. We conclude, therefore, that no serious error in the stability constants arises from chloride impurity.

The free chloride concentration is the difference between total chloride and that complexed by Tl(III). The necessary stability constant data are not available for $1 M$ HClO_4 medium, and we have used values for $0.5 M$ HClO_4 , which are well determined.^{17,18} In the solutions

used for estimating extinction coefficients and stability constants the greatest fractional uncertainty was for a particular solution $2.21 \times 10^{-3} M$ in total chloride, $0.502 \times 10^{-3} M$ in Tl(III), and $1.00 \times 10^{-3} M$ in Tl(I), for which we calculate a free chloride concentration of $1.01 \times 10^{-3} M$. A calculation with stability constants of Tl(III) chloride complexes in $3 M$ HClO_4 medium¹⁷ gives $0.8 \times 10^{-3} M$. It seems reasonable to infer that the error in the calculated value of free chloride concentration in this solution probably does not exceed 10%. The effect is greater (up to a factor of 2) with some of the solutions used to examine the reaction of H atoms with Tl(III), in which Tl(III) concentration is much greater than chloride concentration. However, the exact value of free chloride concentration is not critical in these cases.

The absorption peaks near 340 nm in Figure 1 resemble the peak in the absorption spectrum of Cl_2^- , both in position and in shape. The Cl_2^- formed in our solutions reacts with $10^{-3} M$ Tl(I) with a pseudo-first-order rate constant of $k_{11}[\text{Tl(I)}]$, or $5 \times 10^6 \text{ sec}^{-1}$. Thus the Cl_2^- lifetime is only $0.14 \mu\text{sec}$ and Cl_2^- cannot be responsible for the long-lived species of Figures 1 and 2.

The rate constant for formation of the TlCl^+ complex from Tl^{2+} and Cl^- , k_1 , was observed to be $9 \times 10^9 M^{-1} \text{ sec}^{-1}$, which is certainly near the diffusion limit for the reaction. It would seem reasonable to suppose that k_2 and k_3 are also diffusion limited (about $10^{10} M^{-1} \text{ sec}^{-1}$). With this assumption the dissociation rate constants for TlCl_2 and TlCl_3^- , k_{-2} and k_{-3} , can be estimated from the stability constants to be $5 \times 10^7 \text{ sec}^{-1}$ ($10^{10}/K_2$) and 10^9 sec^{-1} ($10^{10}/K_3$). Consequently, the relaxation times of these two equilibria are very short. The relaxation time of the first equilibrium is the only one which might be long enough to affect the results of Figures 1 and 2. Any such effect was neglected in the treatment of the data. The lowest chloride concentration in Figure 1 is $10^{-4} M$, for which the relaxation rate constant, $k_{-1} + k_1[\text{Cl}^-]$, is $1 \times 10^6 \text{ sec}^{-1}$. The time from the middle of the pulse until the first data are collected in these experiments is $7 \mu\text{sec}$, and relaxation is complete within 0.1% (e^{-7}) at the end of that time. The data of Figure 2 extend to lower chloride concentrations, for which relaxation effects might be more serious. The estimate of the first stability constant is most sensitive to data at chloride concentrations near $1/K_1$, $1.6 \times 10^{-5} M$. The relaxation rate constant is $2.8 \times 10^5 \text{ sec}^{-1}$ at this concentration, so the equilibrium is 86% relaxed before data collection begins and 99% relaxed before disproportionation and reaction with HO_2 decrease the absorbance by 5%. Such errors in the first part of the curve would lead to a negligible error in the estimate of the absorbance of the fully relaxed solution, measured as initial absorbance from a first order fit of data over two half-lives.

Certain correlations appear in the stability constants given in Table I. There is a vertical correlation between values for Tl(III) and Tl(II), i.e., the ratio of K_1 for Tl(III) to K_1 for Tl(II) is 84, the ratio of K_2 's is 66 and the ratio of K_3 's is 44. This correlation suggests that Tl(II) might have a K_4 of about 1. Our results extend to $1 M$ Cl^- and offer no evidence for such a value, but within the accuracy of the data, the fourth complex certainly could exist. There is also a hint of diagonal correlation between Tl(III) and Tl(II); that is, stability constants for similar charge types are equal within a factor of about 3. This correlation certainly does not extend to Tl(I) complexes.

The disproportionation rate constants given in Table

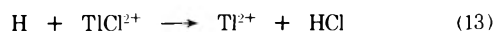
III, determined for chloride concentrations varying from 10^{-3} to $1 M$, must contain significant contributions from $\text{TlCl}^+ + \text{TlCl}_2$, $\text{TlCl}_2 + \text{TlCl}_2$, $\text{TlCl}_2 + \text{TlCl}_3^-$, and $\text{TlCl}_3^- + \text{TlCl}_3^-$. (The TlCl^+ present in $10^{-3} M \text{Cl}^-$ is only 30% of all Tl(II) and so contribution from $\text{TlCl}^+ + \text{TlCl}^+$ should be small.) Of the four reactions listed above, only the last is a reaction between charged species. The diffusion-limited rate constant for the others is $k_{\text{diff}} = 4\pi DR \times 6.02 \times 10^{20}$, where D is the diffusion coefficient of the Tl(II) species (about $1.5 \times 10^{-5} \text{cm}^2 \text{sec}^{-1}$) and R is the reaction radius (about 3 Å). Thus the diffusion-limited rate constant is estimated to be $3.4 \times 10^9 M^{-1} \text{sec}^{-1}$, a value only slightly greater than the values of k_{12} given in Table III. The diffusion limit for $\text{TlCl}_3^- + \text{TlCl}_3^-$ in $1 M$ ionic strength should be slightly smaller, due to charge repulsion, and indeed k_{12} decreases slightly at high Cl^- . It was previously suggested¹⁴ that the reaction $\text{Tl}^{2+} + \text{Tl}^{2+}$ is diffusion limited, and its small value ($1.9 \times 10^8 M^{-1} \text{sec}^{-1}$) is due to the fact that it is a reaction between ions of high charge.

The observed rate constants for reaction of hydrogen atoms with Tl(III) in solutions containing predominantly TlCl_2^+ , TlCl_3 , or TlCl_4^- were all $2 \times 10^9 M^{-1} \text{sec}^{-1}$. Consequently the rate constants for reaction with these individual species are also $2 \times 10^9 M^{-1} \text{sec}^{-1}$. The constant K_7 , determined in a solution containing 12% Tl^{3+} , 76% TlCl_2^+ , and 12% TlCl_2^+ was appreciably lower, $6 \times 10^8 M^{-1} \text{sec}^{-1}$. This rate constant may be expressed in terms of those of the individual complexes as

$$k_7 = k(\text{Tl}^{3+})\alpha(\text{Tl}^{3+}) + k(\text{TlCl}_2^+)\alpha(\text{TlCl}_2^+) + k(\text{TlCl}_2^+)\alpha(\text{TlCl}_2)$$

where the α 's are the fractions of Tl^{3+} present as the indicated species, 0.12, 0.76, and 0.12 respectively, and $k(\text{Tl}^{3+})$ is $3.9 \times 10^7 M^{-1} \text{sec}^{-1}$,¹⁴ and $k(\text{TlCl}_2^+)$ is $2 \times 10^9 M^{-1} \text{sec}^{-1}$. We find from the above equation that $k(\text{TlCl}_2^+)$ is $5 \times 10^8 M^{-1} \text{sec}^{-1}$.

The order of reactivities of these complexes with hydrogen atoms, $k(\text{TlCl}_4^-) \sim k(\text{TlCl}_3) \sim k(\text{TlCl}_2^+) > k(\text{TlCl}_2^+) \gg k(\text{Tl}^{3+})$, is parallel to the order of reactivity of ferric chloride complexes with hydrogen atoms:¹⁹ $k(\text{FeCl}_2^-) > k(\text{FeCl}_2^+) \gg k(\text{Fe}^{3+})$. It is also known that $k(\text{FeOH}^{2+}) \gg k(\text{Fe}^{3+})$.²⁰ Such orders of reactivity are not expected from free-energy considerations;²¹ that is, if a reactant is stabilized by complexing to a greater extent than the product, the rate constant of a reaction involving the complex should be smaller, not larger, than the similar reaction with the uncomplexed substance. Electron transfer reactions involving H might be expected to be slow, in spite of the usually large free-energy changes available, because serious rearrangement of the reactants is required to realize the free-energy change; that is, the reaction product H_9O_4^+ is much different from the starting material, $\text{H} + 4\text{H}_2\text{O}$. The presence of chloride or other ligand offers a new pathway for the reaction, ligand abstraction, which involves little immediate reorganization of the water, for instance



If chlorine abstraction takes place, the product Tl(II) should be the aquo form, Tl^{2+} . Data on this point may be obtained from Table II. The fraction, F , of Tl(II) formed as TlCl^+ from hydrogen atom reduction of mixtures of TlCl_2^+ and TlCl_2^+ is seen to be always less than unity, but increases with increasing $\alpha(\text{TlCl}_2^+)$. The fraction, f_1 , of reactions of hydrogen atoms with Tl(III) which are with TlCl_2^+ in any solution is

$$f_1 = k(\text{TlCl}_2^+)\alpha(\text{TlCl}_2^+) / [k(\text{Tl}^{3+})\alpha(\text{Tl}^{3+}) + k(\text{TlCl}_2^+)\alpha(\text{TlCl}_2^+) + k(\text{Tl}_2^+)\alpha(\text{TlCl}_2^+)]$$

(and there is a similar equation for f_2 , reaction with TlCl_2^+). If F_1 and F_2 are the fraction of reactions of H with TlCl_2^+ and TlCl_2^+ which yield TlCl^+ as a product, then

$$F = F_1 f_1 + F_2 f_2$$

The values of F_1 and F_2 , determined from the data of Table II, are 0.4 and 0.9 with estimated errors of ± 0.1 . F_2 is expected to be 1, because even if the initial Tl(II) product of the reaction was TlCl_2 it would relax to TlCl^+ in about 10^{-7}sec , as mentioned earlier in the Discussion.

F_1 might be expected to be zero on the basis of reaction 13, but this is clearly impossible. The HCl will dissociate very rapidly, since HCl is a strong acid, before the HCl and Tl^{2+} have diffused very far apart. There is a high probability that the chloride ion will then react with the Tl^{2+} to form TlCl^+ . Monchick²² gives the probability of such reaction to be approximately R/r where R is the separation of Tl^{2+} and Cl^- when they react and r is the separation at the time the Cl^- is formed by ionization of HCl. If, in our case, the entire 40% of Tl(II) produced as TlCl^+ is attributed to this process, then r is 7.5 Å, if R is assumed to be about 3 Å. In other words, the HCl diffuses about 4.5 Å before dissociating. The lifetime of the HCl may be found from $r^2 = 4Dt$. The diffusion constant will be about $3 \times 10^{-5} \text{cm}^2 \text{sec}^{-1}$, and so t is about 10^{-11}sec , or the rate constant for dissociation of HCl is 10^{11}sec^{-1} . The recombination rate constant for H^+ and Cl^- will be $10^{10} M^{-1} \text{sec}^{-1}$ or less, so that we estimate the pK of HCl to be -1 or less.

Hogfeldt²³ estimates the pK of HCl to be between -1 and -2.6 , based on Hammett acidity function measurements and nmr measurements. (Bell²⁴ gives values of -6 to -7 , based on vapor pressure studies.) We conclude that our results are entirely consistent with the ligand abstraction mechanism for hydrogen atom reactions.

Acknowledgment. We are grateful to David R. Comstock for assistance in the experimental work.

References and Notes

- (1) Work performed under the auspices of the U. S. Atomic Energy Commission
- (2) G. Harbottle and R. W. Dodson, *J. Amer. Chem. Soc.*, **73**, 2442 (1951).
- (3) L. Eimer and R. W. Dodson, Brookhaven National Laboratory Quarterly Progress Report No. 93(S-8), 67, 1951.
- (4) C. H. Brubaker, K. O. Groves, J. P. Mickel, and C. P. Knop, *J. Amer. Chem. Soc.*, **79**, 4441 (1957).
- (5) B. Baysal, *Actes Congr. Int. Catal.*, 2nd, 1960, 559 (1961).
- (6) S. Gilks, T. E. Rogers, and G. M. Waind, *Trans. Faraday Soc.*, **57**, 1371 (1961).
- (7) G. Nord-Waind, *Proc. Symp. Coord. Chem.*, 1964, 437 (1965).
- (8) G. Dulz, Ph.D. Dissertation, Columbia University, 1963.
- (9) O. L. Forchheimer and R. P. Epple, *J. Amer. Chem. Soc.*, **74**, 5772 (1952).
- (10) F. R. Duke and B. Bornong, *J. Phys. Chem.*, **60**, 1015 (1956).
- (11) A. C. Harkness and J. Halpern, *J. Amer. Chem. Soc.*, **81**, 3526 (1959).
- (12) D. H. Irvine, *J. Chem. Soc.*, 1841 (1957).
- (13) B. Cercek, M. Ebert, and A. J. Swallow, *J. Chem. Soc. A*, 612 (1966).
- (14) H. A. Schwarz, D. Comstock, J. K. Yandell, and R. W. Dodson, *J. Phys. Chem.*, **78**, 488 (1974).
- (15) G. G. Jayson, B. J. Parsons, and A. J. Swallow, *J. Chem. Soc. Faraday Trans. 1*, **69**, 1597 (1973).
- (16) M. Anbar and J. K. Thomas, *J. Phys. Chem.*, **68**, 3829 (1964).
- (17) M. J. M. Woods, P. K. Gallagher, Z. Z. Hugus, and E. L. King, *Inorg. Chem.*, **3**, 1313 (1964).
- (18) R. M. Walters and R. W. Dodson in "Solvent Extraction Chemistry," D. Dyrssen, J.-O. Liljensin, and J. Rydberg, Ed., North-Holland, Amsterdam, 1967, p 71.
- (19) H. A. Schwarz, *J. Amer. Chem. Soc.*, **79**, 534 (1957).

- (20) W. G. Rothschild and A. O. Allen, *Radiat Res.*, **8**, 101 (1958).
(21) R. A. Marcus, *Ann. Rev. Phys. Chem.*, **15**, 155 (1964).
(22) L. Monchick, *J. Chem. Phys.*, **24**, 381 (1956).

- (23) E. Hogfelt, *J. Inorg. Nucl. Chem.*, **17**, 302 (1961).
(24) R. P. Bell, "The Proton in Chemistry," Cornell University Press, Ithaca, N. Y., 1959, p 8.

Electron Spin Resonance of γ Irradiation Induced Free Radicals in Polyvinylpyridines

J. C. Ronfard Haret,^{1,2} A. Lablache Combier,² and C. Chachaty*¹

Service de Chimie-Physique, C.E.N. de Saclay, B.P. No. 2, 91190, Gif-Sur-Yvette, France and Laboratoire de Chimie Organique Physique, Université des Sciences et Techniques de Lille, 59650, Villeneuve D'Ascq, France (Received November 19, 1973)

Publication costs assisted by the Commissariat à l'Energie Atomique

Free radicals formed by γ irradiation of polyvinylpyridines in bulk or in glassy solutions have been identified by electron spin resonance. In neutral alcoholic solutions, pyridinyl radicals produced by hydrogen addition to nitrogen are selectively formed. Analysis of esr spectra shows that the methine proton of the chain is located in the plane of the pyridyl ring. When these polymers are irradiated in glassy concentrated hydrochloric acid, the nitrogens being protonated, hydrogen atom addition occurs to a ring carbon with formation of an azacyclohexadienyl radical. Likewise vinylpyridinyl and methylazabenzyl radicals are formed when vinylpyridine monomers are irradiated in neutral and acidic matrices, respectively. The hyperfine coupling parameters determined from these radicals formed in specific conditions allowed the assignment of the spectra of bulk irradiated polymers to pyridyl and pyridinyl radicals.

I. Introduction

One of the main problems in the study of the radiolytic degradation or reticulation of polymers is the identification of the radicals formed under irradiation.

Vinyl polymers with aromatic side groups can give radicals from addition or abstraction of hydrogen or even ions radicals, stable at low temperatures. The esr spectra recorded after radiolysis of such polymers may be quite complex and it is sometimes difficult to identify unambiguously the different radicals formed.

A convenient approach to this problem is to produce selectively, under different experimental conditions, the radicals expected to be formed by radiolysis. Their characteristic esr spectrum may be then useful for the assignment of the spectra of the irradiated polymer. In the case of polystyrene, for example, the cyclohexadienyl radical produced under irradiation by hydrogen addition to the 2 carbon of the ring has been identified by comparison of its esr spectrum with that of the radical formed selectively by reaction of hydrogen atoms on polystyrene fluffs in a gas flow.^{3a}

Several radicals may be expected to be formed under γ irradiation of polyvinylpyridines (PVP): pyridinyl or azacyclohexadienyl radicals by addition of hydrogen to the ring, azabenzyl or pyridyl radicals by hydrogen abstraction on the α carbon of the chain or the ring, respectively. The formation of radical cations has also been suggested,^{3b} but it may be ruled out, considering more recent works on pyridine itself.^{4a}

In order to identify the esr spectra of PVP irradiated in bulk, the above mentioned radicals were selectively generated by γ irradiation of the polymers in several glassy solutions at 77°K. In some cases, related radicals were also obtained from small molecules such as vinyl- or alkylpyridines.

II. Experimental Section

Most of our experiments have been carried out on chemically synthesized polymers. Isotactic P2VP was obtained by polymerization initiated by phenylmagnesium bromide.^{4b} Atactic P2VP and P4VP were prepared by free radical polymerization initiated by azobisisobutyronitrile.

Esr experiments were performed at 9200-9300 MHz using Strand Labs 601 BX and Varian V 4502-9 esr spectrometers. The samples were degassed and sealed in quartz tubes, then γ irradiated at 77°K with 10 kCi ⁶⁰Co source (doses of 1-2 Mrads).

Measurement were carried out first at 77°K, then at variable temperature. Sometimes samples were examined again at 77°K, after annealing, to check whether the changes observed with temperature are reversible or not.

III. Analysis of the Esr Spectra

In most cases the esr spectra of radicals from polyvinylpyridines were poorly resolved and the hyperfine coupling constants were deduced from the overall width and second moments of the spectra,⁵ then verified by computer simulation. The coupling constants which could not have been obtained by these ways were estimated from spin densities calculations. These parameters were then slightly modified until a reasonable agreement between calculated and experimental spectra was reached.

For the heterocyclic radicals under study the overall width of the spectrum is

$$\Delta H = 2A_{N_{11}} + \sum_i a_i^{11} \quad (1)$$

where $A_{N_{11}}$ is the axial component of the nitrogen coupling tensor and a_i^{11} the coupling constant of proton i . ΔH is measured between the apex of the outermost lines of the experimental spectrum (first derivative of absorption).

TABLE I: Characteristics of the ESR Spectra of Polymers Irradiated in Bulk

| Polymer spectrum | Isotactic P2VP | | Atactic P2VP | | P4VP | |
|--|------------------|------------------|------------------|------------------|------------------|------------------|
| | Triplet | Singlet | Triplet | Singlet | Triplet | Singlet |
| Proportion, % | 18 | 82 | 26 | 74 | 24 | 76 |
| Total width, G | 72 ^a | 50 ^b | 72 ^a | 50 ^b | 72 ^a | |
| Second moments, G ² (with respect to $g = 2.0032$) | 500 ^a | 120 ^b | 500 ^a | 120 ^b | 530 ^a | 100 ^b |
| | | 141 ^a | | 137 ^a | | 120 ^a |

^a At 123°K. ^b At 243°K.

The contribution of the hyperfine coupling to the second moment M_2 of an esr spectrum is⁵

$$\langle \Delta H^2 \rangle_{\text{hf}} = \frac{1}{3} \sum_i \sum_u n_i S_i A_{u,i}^2 \quad (2)$$

$A_{u,i}$ is the principal component of the coupling tensor of nucleus i along axis u and S_i is a constant. $S_i = 1/4$ for $I = 1/2$ (proton), $S_i = 2/3$ when $I = 1$ (nitrogen, deuterium), n_i is the number of equivalent nuclei.

The contribution of the line width is $\lambda^2/4$, where λ the distance between points of maximum and minimum slope of a gaussian line. It is evaluated by optimization of the calculated spectrum compared to the experimental one. Usually $\lambda^2/4 \leq 6 \text{ G}^2$.

The contribution of the anisotropy of the g tensor is⁶

$$\langle \Delta H^2 \rangle_g = \frac{H_0^2}{5} \left[\epsilon_x^2 + \epsilon_y^2 + \epsilon_z^2 + \frac{2}{3} (\epsilon_x \epsilon_y + \epsilon_x \epsilon_z + \epsilon_y \epsilon_z) \right] \quad (3)$$

H_0 is the value of the magnetic field with respect to which the second moment is calculated and g_0 the corresponding g value. ϵ_x , ϵ_y , and ϵ_z are $g_u/g_0 - 1$ where g_u is the principal component of the g tensor along an axis x , y , or z . In the present case $H_0 = 3280 \text{ G}$ and $g_0 = 2.0032$ which corresponds to the acridine coal reference sample.

Among radicals studied here, pyridinyl radicals may be assumed to have the largest g anisotropy, on account of the relatively large spin density on nitrogen.

Assuming for the sake of simplicity that g is axially symmetric, g_{\perp} will be the smallest principal component of the tensor, perpendicular to the plane of the ring.⁷ g_{\parallel} is given by the average position of the two outermost lines of the spectrum, with respect to H_0 . The g_{\perp} component cannot be measured directly from line positions. We have therefore determined the isotropic value of g , g_{iso} , from the first moment of the spectrum with respect to H_0 ⁶

$$M_1 = -H_0(g_{\text{iso}}/g_0 - 1) \quad (4)$$

For the values of H_0 and g_0 given above it is found for P2VP and P4VP pyridinyl radicals that $M_1 = -0.83 \pm 0.01 \text{ G}$ and therefore that $g_{\text{iso}} = 2.0037 \pm 0.0002$. g_{\perp} being equal to 2.0033 ± 0.0002 , we get $g_{\perp} = 1/2(3g_{\text{iso}} - g_{\parallel}) = 2.0044 \pm 0.0002$. Relation 3 gives $\langle \Delta H^2 \rangle_g = 1.7 \text{ G}^2$.

It may be therefore expected that the contribution of g anisotropy will not exceed 2 G^2 for most of the free radicals under study. The uncertainty on the experimental value of the second moment is about 5%, and the contribution of the g tensor anisotropy may be therefore neglected.

The main contribution to the second moment of the spectra of irradiated PVP is thus the hyperfine coupling of the protons and of the nitrogen. The coupling of π protons bonded to carbons adjacent to the conjugated system is

nearly isotropic as in the case of aliphatic β protons,⁸ and their individual contribution to M_2 will be $a^2/4$. On the other hand, the anisotropy of the coupling of σ protons directly bonded to the conjugated system has to be taken into account for the calculation of the theoretical values of M_2 as well as for the simulation of esr spectra.

For the σ proton of a $-\text{CH}-$ fragment we have chosen the following principal values⁹ of the coupling tensor: $A_x^{\text{H}} \approx a_{\text{H}}$ along the axis of the $2p$ π orbital of the adjacent carbon, $A_z^{\text{H}} \approx 0.5a_{\text{H}}$ along the C-H bond, and $A_y^{\text{H}} \approx 1.5a_{\text{H}}$ perpendicular to the xz plane.

For a N-H fragment, we have taken likewise¹⁰ $A_x^{\text{H}} \approx a_{\text{H}}$, $A_z^{\text{H}} = 0.4a_{\text{H}}$, $A_y^{\text{H}} = 1.6a_{\text{H}}$.

According to eq 2, the contribution of $(a_{\text{CH}}^{\text{H}})^2/4$ and $(a_{\text{NH}}^{\text{H}})^2/4$ to M_2 must be weighted by a factor 1.17 and 1.23, respectively.

Spin densities were calculated by the method of McLachlan.¹¹ The coulomb $\alpha = \alpha_0 + h\beta_0$ and resonance $\beta = k_{ij}\beta_0$ integrals, used in the preliminary HMO calculation, are given in the literature.¹² They are listed under each of the tables giving the spin densities. Unless otherwise specified $h = 0$ and $k_{ij} = 1$. The parameter λ of the interatomic exchange integral was taken equal to 1.1.¹³

The coupling constants (in gauss) are related to spin densities by the following equations

$$a_{\text{CH}}^{\text{H}} = Q_{\text{CH}}^{\text{H}} \rho_{\text{C}} \quad (5)$$

with $-25 \text{ G} < Q_{\text{CH}}^{\text{H}} < -28 \text{ G}^{14}$

$$a_{\text{N}} = 28 \rho_{\text{N}} \quad (6)$$

for a sp^2 hybridized nitrogen

$$a_{\text{NH}}^{\text{H}} = -32 \rho_{\text{N}} \quad (7)$$

The angular dependence of the coupling of π protons is given by the relations^{14,15}

$$a_{\pi}^{\text{H}} = 58 \rho_{\text{C}} \cos^2 \theta \quad (8)$$

$$a_{\pi}^{\text{H}} = 55 \rho_{\text{N}} \cos^2 \theta$$

where θ is the angle between plane H-C-C or H-C-N and the axis of the orbital of the unpaired electron, centered on a carbon or nitrogen of the conjugated system.

The computer simulation of the spectra was carried out using the program of Lefebvre and Maruani.⁶ The anisotropy of the coupling of σ protons was taken into account by using the principal values quoted above. The relative orientation of the tensors was deduced from the assumed geometry of the radicals. The nitrogen coupling tensor was supposed axially symmetric around the direction perpendicular to the plane of the ring. We took usually $A_{\text{N}}/A_{\perp} = 5.5$.

IV. Results and Discussion

1. *Irradiation of Polymers in Bulk.* At 77°K, before annealing, the spectra of irradiated P2VP and P4VP are

TABLE II: Total Width and Second Moments in Pyridinyl Radicals

| Compound | Solvent | Temp, °K | Total width, G | Second moment, G ² |
|---------------------------|---|----------|----------------|-------------------------------|
| 2-Vinylpyridine (2VP) | C ₂ D ₃ OD | 96 | 44 | 97 |
| | C ₂ H ₅ OH | 96 | 49 | 114 |
| 4-Vinylpyridine (4VP) | C ₂ D ₃ OD | 96 | 42 | 93 |
| | C ₂ H ₅ OH | 96 | 47 | 101 |
| Isotactic or atactic P2VP | CH ₃ OD + 10% D ₂ O | 105 | 44 | 90 |
| | C ₂ H ₅ OH | 105 | 50 | 115 |
| P4VP | CD ₃ OD + 10% D ₂ O | 105 | 38 | 72 |
| | C ₂ H ₅ OH | 105 | 45 | 97 |
| Pyridine ^a | C ₂ D ₃ OD | 105 | 52 | 116 |
| | C ₂ H ₅ OH | 105 | 59 | 140 |

^a From ref 14.

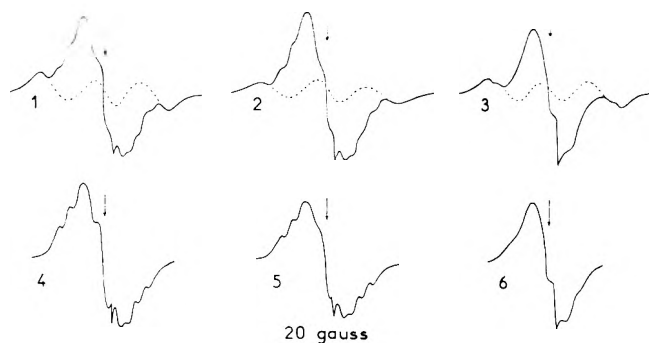


Figure 1. ESR spectra of polyvinylpyridines irradiated at 77°K: (1, 4) atactic P2VP; (2, 5) isotactic P2VP; (3, 6) P4VP. The spectra 1, 2, and 3 are recorded at 123°K, the spectra 4, 5, and 6, at 243°K. The dotted lines correspond to the difference between the spectra initially recorded at 123°K (upper line) and the spectra obtained at this temperature after warming at 243°K. Vertical arrows: $g = 2.0032$.

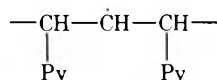


Figure 2. ESR spectra of pyridinyl radicals trapped in alcohol matrices: (1 and 2) P4VP in C₂H₅OH and CD₃OD, respectively ($T = 105^\circ\text{K}$); (3 and 4) computed spectra corresponding respectively to 1 and 2 (see Table III). Vertical arrow $g = 2.0032$.

triplets with a predominant central line. These spectra appear to be formed by the superposition of the signals of two radicals. The side peaks disappear either by uv photolysis (250–300 nm), with a decrease in the overall concentration of radicals, or by warming at 180°K. The spectrum of the remaining radicals can be observed up to 350°K. For P4VP it is a wide structureless band, but for P2VP, the hyperfine structure, although poorly resolved, allows its assignment as it will be shown below. No differences were observed between the spectra of atactic and isotactic P2VP.

Let us denote as A the part of the spectrum disappearing at 180°K (triplet) and B the spectrum remaining at room temperature. The relative contributions of A and B have been determined on spectra recorded at 123°K by subtracting from the spectra of samples kept at this temperature, that of samples annealed 12 mn at 225°K and then cooled to 123°K. Table I gives some characteristics of spectra A and B and their relative intensities.

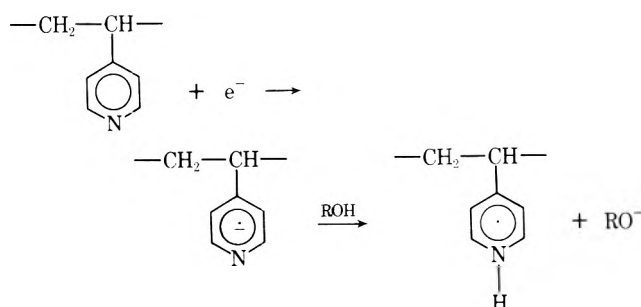
From the structure of these spectra, it may be concluded that they do not correspond to alkyl radicals such as



On the other hand, as mentioned above, we have to consider the possible formation, under irradiation, of azabenzyl, pyridyl, pyridinyl, or azacyclohexadienyl radicals. Only the pyridyl radicals, which are very reactive, cannot be obtained separately from the polymers. In the case of pyridine itself, it has only been obtained at 4°K in an argon matrix.¹⁶

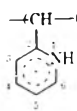
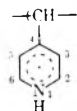
2. Selective Formation of the Radicals from PVP. (a) Pyridinyl Type Radicals. These radicals are derived from PVP by addition of hydrogen atom to the nitrogen of a pyridine ring. As for pyridine,¹⁴ they are formed by irradiation of the polymer in alcoholic glassy matrices at 77°K.

Pyridinyl radicals results from electron capture followed by protonation of the radical anion as shown by the disappearance of the signal of the solvated electron normally observed in irradiated glassy alcohol.



The coupling constants of the hydrogen bonded to nitrogen, and indirectly that of nitrogen (eq 6 and 7), are given by the difference in width of the spectra of the radicals formed in protonated and deuterated matrices. The other coupling constants have been deduced from the

TABLE III: Spin Densities and Coupling Constants in Polyvinylpyridinyl Radicals

| Free radical | Coupling constants, G | | | Spin densities | | |
|---|-----------------------|---|--|--|--------------|--------|
| | Exptl values | Values from simulated spectra | Calcd ^a | Exptl | Calcd | |
|  P2VP | 1 | $a_H = 6$ $a_N = 5.5$ $A_{N\parallel} = 12.5$ $A_{N\perp} = 2.7$ | $a_H = -6.5$ $a_N = 6.0$ $A_{N\parallel} = 13.5$ $A_{N\perp} = 2.7$ | $a_H = -6.96$ $a_N = 6.09$ $A_{N\parallel} = 13.5$ $A_{N\perp} = 2.4$ | 0.19 | 0.217 |
| | 2 | | | | | 0.217 |
| | 3 | | | | $a_H = 1.48$ | -0.053 |
| | 4 | $a_H = 12$ | $a_H = -12$ | $a_H = -12.2$ | 0.43 | 0.436 |
| | 5 | | | $a_H = 2.04$ | | -0.073 |
| | 6 | $a_H = 5$ | $a_H = -6$ | $a_H = -7.17$ | 0.18 | 0.256 |
|  P4VP | 1 | $a_H = 7.0$ $a_N = 6.5$ $A_{N\parallel} = 14.5$ $A_{N\perp} = 2.7$ | $a_H = -7.5$ $a_N = 7.0$ $A_{N\parallel} = 14.5$ $A_{N\perp} = 2.7$ | $a_H = -7.08$ $a_N = 6.19$ $A_{N\parallel} = 13.7$ $A_{N\perp} = 2.4$ | 0.22 | 0.221 |
| | 2 and 6 | $a_H = 6$ | $a_H = -5.5$ | $a_H = -6.83$ | 0.21 | 0.244 |
| | 3 and 5 | | | $a_H = 2.00$ | | -0.071 |
| | 4 | | | | | 0.433 |
| | | | | | | |

^a From theoretical spin densities calculated with $h(C_2)$ or $h(C_4) = -0.05$, $h(*NH^*) = 1.2$, $h(C-N) = 1$.

overall width and second moment of the spectra (Table II).

The case of P4VP γ irradiated in ethanol matrix will now be discussed in detail. After disappearance of the solvent radical by warming at $\sim 120^\circ\text{K}$, a spectrum with an overall width $\Delta H_H = 45$ G or $\Delta H_D = 38$ G is observed, depending whether the matrix is $\text{C}_2\text{H}_5\text{OH}$ or $\text{C}_2\text{D}_2\text{OD}$, therefore $a_{NH^*H} = \Delta H_H - \Delta H_D = 7$ G. Relation 7 gives $\rho_N = 0.22$, $a_N = 6.2$ G, then $A_{N\perp} = 2.5$ G, $A_N = 13.7$ G. The second moment of the spectrum of the P4VP pyridinyl radical is 72 G² with a contribution of 44 G² from nitrogen coupling and 5 G² from line width ($\lambda \sim 4.5$ G).

Neglecting the contribution of protons 3 and 5 which is expected to be low (see Table III), that of proton 2 and 6 and of the α proton of the chain will be (relation 2)

$$\frac{7}{12}a_{H_{2,6}}^2 + \frac{(a_H^\alpha)^2}{4} = 23 \text{ G}^2 \quad (9)$$

The contribution of these protons to the overall width of the spectrum is

$$2a_{H_{2,6}} + a_H^\alpha = 11 \text{ G} \quad (10)$$

relations 9 and 10 give $a_{2,6}^H = 5.1$ G, $a_H^\alpha = 0.8$ G.

The computer simulation of the spectra (Figure 2) gives the best agreement for $a_{H_{2,6}} = 5.5$ G, $a_H^\alpha = 0.0$ G. Taking $Q_{CH^*H} = -28$ G, we find $\rho_{2,6} = 0.19$ G and therefore $\rho_4 = 1 - 2\rho_{2,6} - \rho_N = 0.4$ in agreement with calculated spin densities (Table III).

The spin density on carbon 4 is large enough to assume from the small coupling of the α proton of the chain ($0.0 < a_H < 0.8$ G) that it is located in the plane of the pyridyl ring, whose orientation is thus well defined, with respect to the chain.

The hyperfine coupling constants of the 2-polyvinylpyridinyl radical, which has no symmetry axis, cannot be deduced by such a straightforward manner from the width and second moment of its spectrum (Figure 3).

Assuming that the α proton of the chain is located in the plane of the adjacent ring ($a_H^\alpha \approx 0$), it has been found by computer simulation of the spectra and spin densities calculated that $a_{NH^*H} = 6$ G, $a_N = 5.5$ G ($A_N = 12.5$ G, $A_{N\perp} = 2.4$ G), $a_4^H = 12$ G, $a_6^H = 5$ G, and a_3^H and $a_5^H \leq 1$ G.

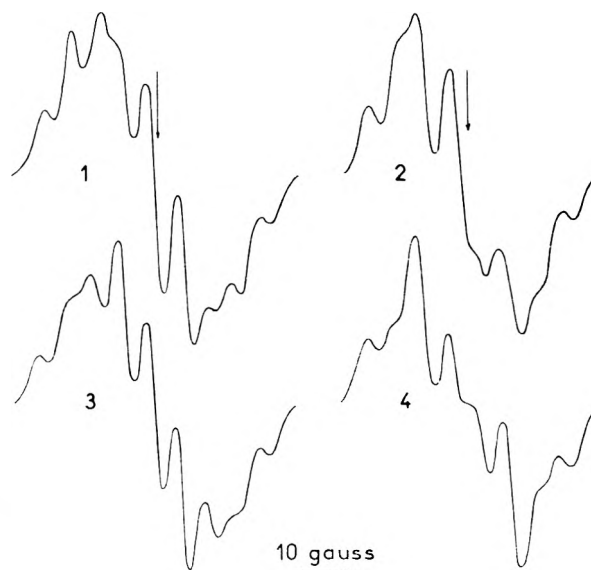


Figure 3. ESR spectra of poly-2-vinylpyridinyl radicals at 105°K : (1) $\text{C}_2\text{H}_5\text{OH}$ matrix, (2) CD_3OD matrix, (3 and 4) computed spectra corresponding respectively to 1 and 2 (see Table III).

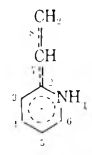
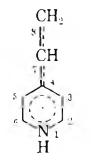
It may be pointed out as expected, that the spin densities and coupling constants of PVP pyridinyl radicals are very close to that found previously for the pyridinyl radical trapped in an alcohol glassy matrix.¹⁴

When 2- and 4-vinylpyridines are γ irradiated in alcohol matrices, it could be expected by analogy with styrene¹⁷ that an azabenzyl type radical should be formed by addition of a hydrogen atom to a vinyl double bond. The coupling constant of the added proton, of the order of 6-7 G, is however more consistent with its attachment to the ring nitrogen.

This point has been confirmed by the calculation of spin densities and the computer simulation of the spectra from optimized coupling parameters and relative orientation of the tensors deduced from the most likely geometry of vinylpyridinyl type radicals (see Table IV).

The 2-vinylpyridinyl radical has two stereoisomers depending upon the orientation of the vinyl double bond

TABLE IV: Spin Densities and Coupling Constants in Vinylpyridinyl Radicals

| Free radical | | Coupling constants, G | | | Spin densities | |
|---|---|---|--|--|----------------|--------|
| | | Exptl values | Values from simulated spectra | Calcd ^a | Exptl | Calcd |
|  | 1 | $a_H = 5.0$ $a_N = 4.8$ $A_{N\parallel} = 11.0$ $A_{N\perp} = 2.0$ | $A_H = -5.5$ $a_N = 4.8$ $A_{N\parallel} = 11.0$ $A_{N\perp} = 2.0$ | $a_H = -5.55$ $a_N = 4.87$ $A_{N\parallel} = 11.5$ $A_{N\perp} = 2.2$ | 0.17 | 0.174 |
| | 2 | | | | | 0.250 |
| | 3 | | $a_H = 2$ | $a_H = 2.26$ | | -0.081 |
| | 4 | | $a_H = -6$ | $a_H = -6.27$ | | 0.224 |
| | 5 | | $a_H = -1$ | $a_H = -0.75$ | | 0.027 |
| | 6 | | $a_H = -2$ | $a_H = -1.79$ | | 0.064 |
| | 7 | | | $a_H = 0.53$ | | -0.019 |
| | 8 | | $a_H = -9.5$ | $a_H = -10$ | | 0.360 |
|  | 1 | $a_H = 5$ $a_N = 4.8$ $A_{N\parallel} = 11$ $A_{N\perp} = 2$ | $a_H = -5.5$ $a_N = 4.8$ $A_{N\parallel} = 11$ $A_{N\perp} = 2.0$ | $a_H = -4.8$ $a_N = 4.2$ $A_{N\parallel} = 9.3$ $A_{N\perp} = 1.7$ | 0.17 | 0.150 |
| | 2 | | $a_H = -2.5$ | $a_H = -2.72$ | | 0.097 |
| | 3 | | | $a_H = -0.73$ | | 0.026 |
| | 4 | | | | | 0.280 |
| | 5 | | | $a_H = 0.50$ | | -0.018 |
| | 6 | | $a_H = -5$ | $a_H = -4.17$ | | 0.149 |
| | 7 | | | $a_H = 0.1$ | | -0.004 |
| | 8 | | $a_H = -9.5$ | $a_H = -10.5$ | | 0.376 |

^a From theoretical spin densities calculated with $h(C_3) = 0.17$ (4-vinylpyridinyl) $h(*NH^+) = 1.2$, $k(C_2-C_7)$ or $k(C_4-C_7) = 0.8$.

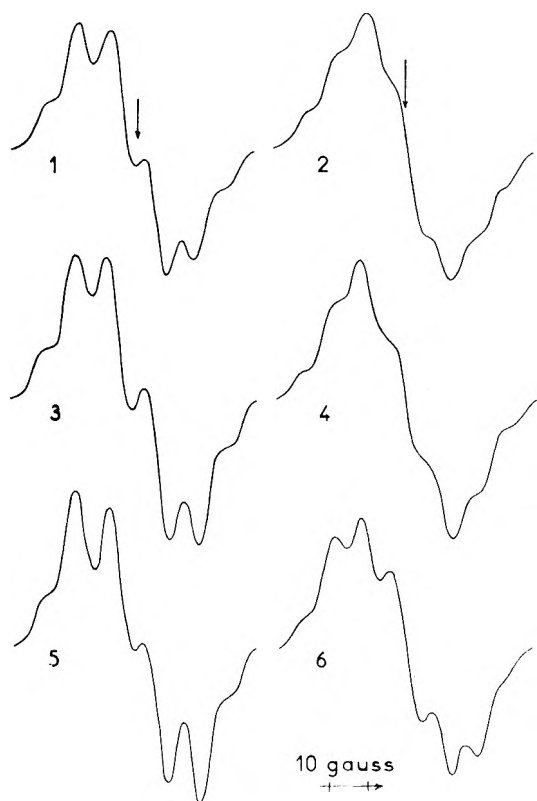


Figure 4. Spectra of 2 vinylpyridinyl radicals: spectra 1 and 2 correspond to radicals trapped at 96°K in C₂D₅OD and C₂H₅OH, respectively; spectra 3-6 are computed from data of Table IV for the two possible planar stereoisomers (3 and 4 stereoisomer II, 5 and 6 stereoisomer I, see text).

with respect to the ring. The comparison of the experimental spectrum with those calculated for these two forms shows clearly that the stereoisomer II is predominant (Figure 4)^{17a}. Both stereoisomers of the 2-vinylpyridinyl

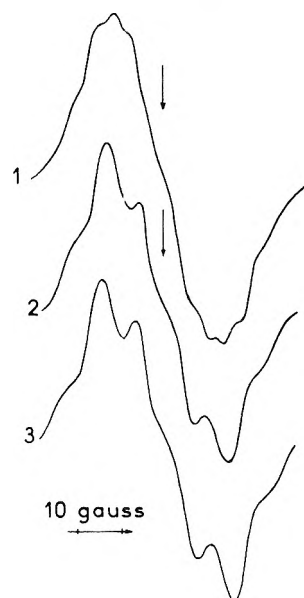
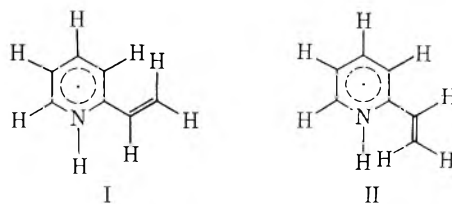


Figure 5. Spectra of 4-vinylpyridinyl radicals: (1) 96°K in C₂H₅OH matrix; (2) 96°K, C₂D₅OD matrix; (3) computed spectrum corresponding to 2.

yl radical show the same spin density distribution and therefore have esr spectra of same width and second moment.



The structural differences between their spectra can be only explained by an effect of the relative orientation of the coupling tensors of protons 1 and 8. The spectra of

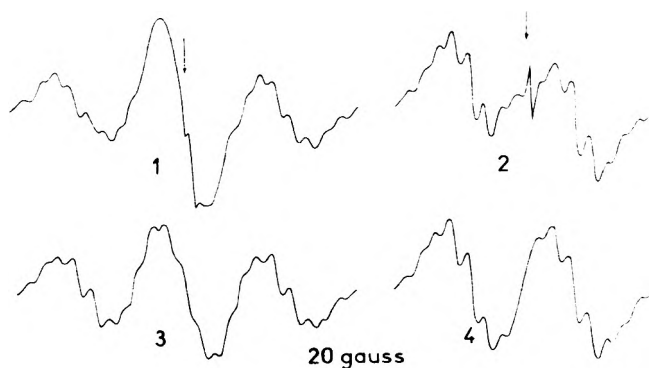


Figure 6. Spectra of 4-azacyclohexadienyl radical from P2VP: (1) 105°K, HCl-H₂O matrix; (2) 105°K DCl-D₂O matrix; spectra 3 and 4 are computed from data of Table VI (column 4); spectrum 4 results from the superposition of the spectra obtained for the two sets of coupling constants of the -CHD- group denoted I and II in this table.

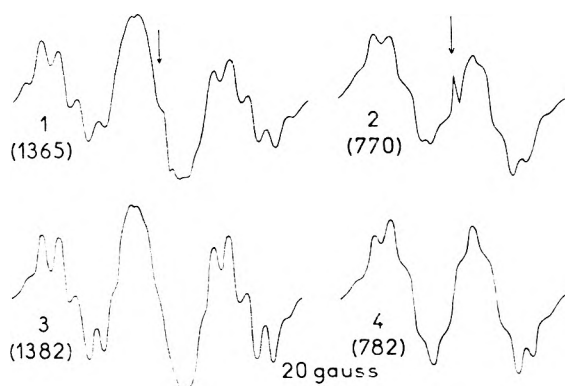


Figure 7. Spectra of 2-azacyclohexadienyl radical from P4VP: (1) 105°K, HCl-H₂O matrix; (2) 105°K DCl-D₂O matrix; spectra 3 and 4 are the corresponding computed spectra (see Table VIII). The nonequivalence of methylene proton is taken into account. Spectrum 4 results from the superposition of the spectra corresponding to the two possible stereoisomers. In parentheses are the second moments of the spectra.

radicals I and II become actually similar when proton 1 is substituted by a deuterium.

A similar effect has been already reported for randomly oriented allyl type radicals.¹⁸ It may be applied to the identification of cis and trans isomers of such radicals.

(b) *Azacyclohexadienyl Type Radicals.* To avoid the formation of pyridinyl radicals by hydrogen addition to nitrogen, it is necessary to protonate pyridine in acidic medium. Thus the γ radiolysis at 77°K of pyridine in a glassy matrix of concentrated hydrochloric acid (8–12 M) gives rise to azacyclohexadienyl radicals by addition of a hydrogen atom to a carbon.^{19,20}

When P2VP and P4VP are irradiated under these conditions, we observe a spectrum, whose main hyperfine structure is a triplet if the matrix is protonated, or a doublet in the case of a deuterated matrix. The splitting of 50–60 G is actually characteristic of the coupling of a methylene proton of a cyclohexadienyl type radical^{21,22} (Figures 6 and 7).

The overall width of the spectra of azacyclohexadienyl radicals derived from P2VP or P4VP is

$$\Delta H_H = 2A_N + a_{NH}^H + \Sigma a_{CH}^H + 2a_{CH_2}^H + a_H^{\alpha} \quad (11)$$

For the same radicals formed in a deuterated matrix the width will be

TABLE V: Total Width of Spectra and Coupling Constants of Methylene Protons of Azacyclohexadienyl Radicals from PVP

| Substrate | ΔH_{HCl} , G | $a_H^{CH_2}$, G | ΔH_{DCl} , G | a_H^{CHD} , G |
|---------------------------|----------------------|------------------|----------------------|-----------------|
| Isotactic or atactic P2VP | 192 | 122 | 136 | 60 |
| P4VP | 155 | 100 | 110 | 46 |

$$\Delta H_D = 2A_{N||} + \Sigma a_{CH}^H + 2a_{CHD}^D + a_{CHD}^H + a_H^{\alpha} \quad (12)$$

where Σa_{CH}^H is the sum of the coupling constants of protons attached to sp² carbons. The values of ΔH_H and ΔH_D for both polymers are given in Table V.

The apparent value of a_{CHD}^H is slightly different from $a_{CH_2}^H$. Moreover Figures 6 and 7 show that the structure of the central peak of the triplet of azacyclohexadienyl radicals is not the same as for the side bands. These two facts suggest that the two protons of the methylene groups are not equivalent, as will be shown later.

There is an obvious analogy between the esr spectrum of P2VP γ radiolyzed in an acidic matrix¹⁹ and that of the 4-azacyclohexadienyl radical derived from pyridine. The coupling of the α proton of the macromolecular chain attached to the 2 carbon of the ring is unresolved on account of the small spin density at this point (see Figure 6 and Table VI). For the same reason the coupling of the proton directly bonded to C₂ is not observed in the case of pyridine.

In the case of P4VP, the hydrogen addition may occur on C₂ or C₃. Addition to carbon 4 may be ruled out since the esr spectrum is a triplet. The calculations of spin densities and the computer simulation of the spectrum show clearly that the radical observed is the 2-azacyclohexadienyl radical (Figure 7, Table VI).

The coupling constants of the methylene protons of azacyclohexadienyl radicals derived from P2VP and P4VP have been deduced from the spin densities on carbon or nitrogen atoms adjacent to this group, using the relation²³

$$a_{CH_2}^H = Q(\rho^{1/2} + \rho'^{1/2})^2 \cos^2 \theta \quad (13)$$

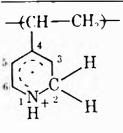
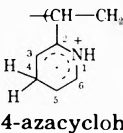
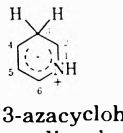
with $Q = 58$ G for -CH₂- in positions 3 and 4 (two adjacent carbons) and $Q' = (58 + 55)/2 = 56.5$ G in position 2 (-CH₂- adjacent to nitrogen and carbon 3).

The nonequivalence of the two hydrogen atoms of the methylene group, which is not observed in the case of the cyclohexadienyl radical, is probably related to a slight distortion of the ring due to the presence of nitrogen. It can be easily seen that each of the azacyclohexadienyl radicals derived from the PVP has two stereoisomers giving the same esr spectrum in the case of fully protonated radicals, and four stereoisomers, forming two pairs of magnetically equivalent radicals, when the methylene group is monodeuterated (Figure 8). The different coupling constants of the protons or deuterons of the methylene group have been determined by successive approximations in the search for the best agreement between experimental and simulated spectra (Table VI).

Finally it may be noted that the spin densities for the azacyclohexadienyl radicals protonated on the nitrogen are almost the same as those calculated for their neutral form, which have not been observed under our experimental conditions.

(c) *Azabenzyl Type Radicals.* Azabenzyl radicals from P2VP and P4VP are not selectively formed by γ irradiation of the polymers, however, it cannot be excluded that

TABLE VI: Coupling Constants and Spin Densities of Azacyclohexadienyl Radicals from Polyvinylpyridines

| Free radicals | Spin densities | | Coupling constants, G | | |
|---|----------------|---|-----------------------|---|---|
| | A ^a | B ^b | A ^a | B ^b | |
|  2-azacyclohexadienyl | 1 | 0.217 | 0.22 | $a_H = -6.7$ $a_N = 5.0$ $A_{N } = 13.2$ $A_{N\perp} = 2.4$ $a_H = 50.5^c$ $a_D = 3.1^c$ $a_H = -11$ | $a_H = -7$ $a_N = 6.1$ $A_{N } = 13$ $A_{N\perp} = 2.7$ $a_H = 47.5$ $a_D = 8.3$ (I) $a_H = 52.5$ $a_D = 7.6$ (II) $a_H = -12$ |
| | 2 | (C) -0.028 (H ₂) 0.101 | | | |
| | 3 | 0.385 | 0.43 | | |
| | 4 | -0.056 | | $a_H = -9$ | $a_H = -9$ |
| | 5 | 0.318 | 0.32 | $a_H = 2.6$ | $a_H = -3$ |
| | 6 | 0.065 | 0.10 | | |
|  4-azacyclohexadienyl | 1 | 0.293 | 0.31 | $a_H = -10$ $a_N = 8.8$ $A_{N } = 19.5$ $A_{N\perp} = 3.5$ | $a_H = -10$ $a_N = 9.3$ $A_{N } = 20$ $A_{N\perp} = 4$ |
| | 2 | -0.054 | | | |
| | 3 | 0.365 | 0.357 | $a_H = -10.3$ | $a_H = -10$ |
| | 4 | { (C) -0.030 (H ₂) 0.115 | | $a_H = 63.5^c$ | $a_H = 60$ $a_D = 9.8$ (I) |
| | 5 | 0.365 | 0.321 | $a_D = 10.2^c$ | $a_H = 62$ $a_D = 9.4$ (II) |
| | 6 | -0.054 | -0.07 | $a_H = -10.3$ | $a_H = -9$ |
|  3-azacyclohexadienyl | 1 | -0.20 | | $a_H = 3.8$ | $a_H = -3.4$ |
| | 2 | 0.378 | | $a_H = -10.6$ | $a_H = 54.3^c$ |
| | 3 | (C) -0.034 (H ₂) 0.118 | | | |
| | 4 | 0.406 | | $a_H = -11.4$ | |
| | 5 | -0.135 | | $a_H = 3.8$ | |
| | 6 | 0.388 | | $a_H = -10.9$ | |

^a From spin densities calculated with $h(C(H_{\alpha})) = -0.1$, $h(C(H_{\beta})) = -0.5$, $h(N-H^+) = 1.1$ (or $h(-N=) = 0.8$ see text), $k(C-CH_2) = k(CH_2-NH) = 0.8$, $k(C(H_2)) = 2.5$. ^b From simulation of esr spectra. ^c Calculated from relation 13 with $\theta = 60$ and 120° .

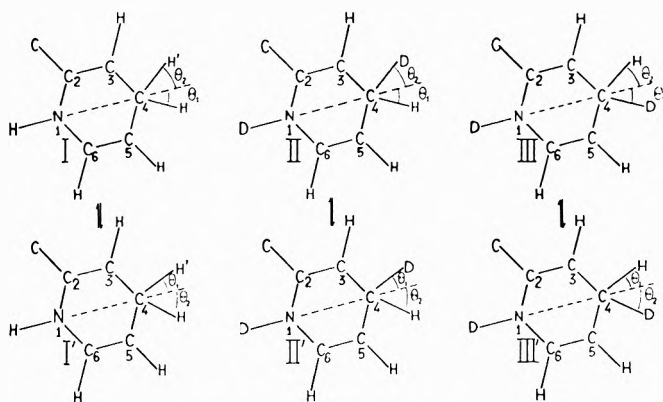


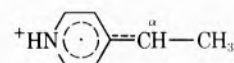
Figure 8. Conformational isomerism of 4-azacyclohexadienyl radical from P2VP due to the nonequivalence of methylene protons. Isomers I and I', II and III', and II' and III and magnetically equivalent. A similar figure could be given for 2-azacyclohexadienyl radical from P4VP.

they are formed together with other radicals since the recorded spectra correspond to several superimposed signals (Figure 1).

The hyperfine structure of the spectra of azabenzyl radicals from these polymers cannot be predicted since many conformations seem possible, according to the orientation of C_β-H_β bond of the chain, with respect to the axis of the 2p π unpaired electron orbital on the α carbon. We have however determined the characteristic hyperfine coupling parameters of such radicals, from the esr spectra of methylazabenzyl radicals produced by hydrogen addition to the vinyl double bond of the monomers.

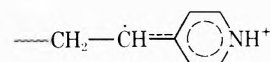
In order to avoid the hydrogen atom addition to the nitrogen, 2VP and 4VP monomers have been irradiated in

glassy hydrochloric acid (~9 M) at 77°K. The nitrogen being protonated, hydrogen addition occurs as expected on the vinyl double bond, giving a radical such as



MO calculations show that the protonation of nitrogen introduces only a small change in the spin density distribution.

The difference between the overall width of the esr spectra of methyl-2- or -4-azabenzyl radicals formed in HCl-H₂O matrix or DCl-D₂O matrix gives $a_{H}^{Me} = 19$ G, $\rho_{H} = 0.65$ and therefore $15 < a_H^\alpha < 18$ G (relations 5 and 8). The nonequivalence of a_{H}^{Me} and a_H^α coupling constants is masked by the line width so that binomial quintets or quartets are observed in the case of protonated and deuterated matrices, respectively (Figures 9 and 10). Characteristic triplets of growing chain radicals such as

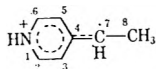


due to the addition of methyl azabenzyl radical to monomer molecules are also observed on warming above 140°K (see Figure 9, spectra 3 and 6).

The hyperfine structure due to the ring protons of azabenzyl radicals has been analyzed on the much more resolved spectra of methyl-4-azabenzyl radicals from γ irradiated ethylpyridines in glassy acidic matrices, after elimination by warming of the azacyclohexadienyl radicals formed simultaneously (Figure 10). Table VII shows the results relative to methyl-4-azabenzyl radicals.

The coupling constants thus determined for an azabenzyl type radical allow an estimation to be made of the

TABLE VII: Spin Densities and Coupling Constants in Protonated Methyl-4-azabenzyl Radical

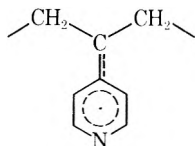


| Position | 1 | 2 and 6 | 3 and 5 | 4 | 7 |
|-----------------------------------|---|---------|------------------------|--------|--|
| Exptl coupling constants, G | $A_{N\parallel} = 9.4$ $A_{N\perp} = 1.6$ $a_N = 4.2$ $a_{H^{NH}} = 4.7$ | | $a_{H\parallel} = 4.7$ | | $a_{CH_3^H} = 15.5$ $a_{CH_3^H} = 19.0$ |
| Spin densities | 0.15 | | 0.17 | | 0.65 |
| Calcd Spin densities ^a | 0.138 | 0.000 | 0.145 | -0.027 | 0.601 |

^a With $h(C_7) = -0.2$, $h(^*CH_3) = -0.1$, $h(C^*(H_3)) = -0.5$, $h(^*NH^+) = 1.2$ (or $h(-N=) = 0.8$ see text), $k(C_4-C_7) = 1.1$, $k(C_7-C_8) = 0.76$, $k(C\equiv C_2) = 2.0$.

width and second moment of similar radicals from PVP, provided that the conformation of the chain at the vicinity of the α proton is known.

For that purpose, we have performed INDO calculations²⁴ to find the most stable conformation of the radical



The corresponding energy minimum is obtained for dihedral angles (see above) $\theta = 60$ and 120° , giving $a_{\beta^H} = 9.5$ G (relation 8). It may be easily calculated from relations 1 and 2 that the esr spectrum of such a radical, in that conformation, should have an overall width of 62 G and a second moment of 120 G². Very similar results have been found for the corresponding azabenzyl radical from P2VP.

V. Conclusion

It now becomes possible, taking into account the data assembled for all the radicals under study, to assign more safely the esr spectra of P2VP and P4VP irradiated in bulk (see Figure 1).

The total width of these spectra is clearly not consistent with the presence of azacyclohexadienyl type radicals, which could explain the triplet structure. For both polyvinylpyridines, this triplet may be assigned to the corresponding 2-pyridyl radical: its overall width is 74 G and its second moment, 600 G², very close therefore to the corresponding values derived on the 2-pyridyl radical itself, from the data of Kasai and McLeod.¹⁶

It has been shown¹⁶ that this last radical may be photolyzed at 4°K in an argon matrix to give a vinyl type radical. Such a radical has not been observed in the present work although the triplet assigned to the pyridyl radical disappears under photolysis subsequent to γ irradiation.

The photolysis of the pyridyl radicals from P2VP and P4VP induces a decrease in the total concentration of radicals. It seems likely that this effect is related to the photoionization of pyridyl radicals followed by the scavenging of the released electrons by any radicals trapped in the polymer, giving a diamagnetic ion

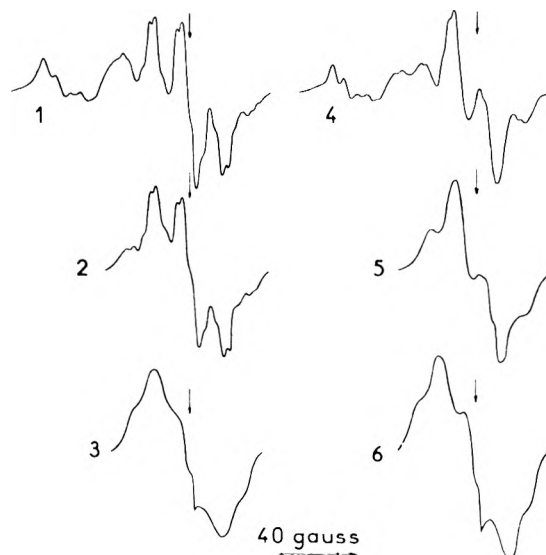
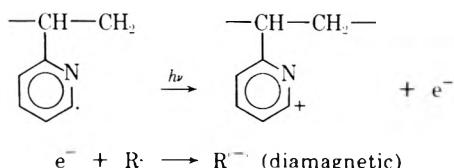


Figure 9. Variation with temperature of the esr spectra of 2-vinylpyridine on HCl-H₂O matrix (spectra 1-3) and DCl-D₂O matrix (spectra 4-6): (1 and 4) 77°K before warming; (2 and 5) 105°K after warming at 140°K; (3 and 6) 105°K after warming at 145°K. Spectra 1 and 4 are partially superimposed to that of Cl₂⁻.

The local concentration of free radicals trapped in γ irradiated polymers is known to be larger (10^{18} - 10^{19} radicals ml⁻¹)²⁵ than the average concentration of 10^{17} - 10^{18} radicals obtained in usual irradiation conditions. Furthermore the electron affinity of a free radical is generally larger than that of the parent diamagnetic compound (see, for example, ref 26).

The narrowest component of the esr spectrum of PVP irradiated in bulk (Figure 1) may be assigned either to a pyridinyl type radical formed by hydrogen addition, or to an azabenzyl type radical produced by hydrogen abstraction on the α carbon of the aliphatic chain. The most probable conformation of this last radical (see above) gives about the same width and second moment as for pyridinyl radicals. However the resolution of the spectrum of the radical from P2VP becomes sufficient above 150°K to assign it unambiguously to a pyridinyl radical. It is therefore reasonable to assume that this radical is formed in the case of P4VP as well.

Acknowledgments. We thank Professor C. Loucheux from the University of Lille for providing us samples of polymers used in this study and the Delegation Generale à

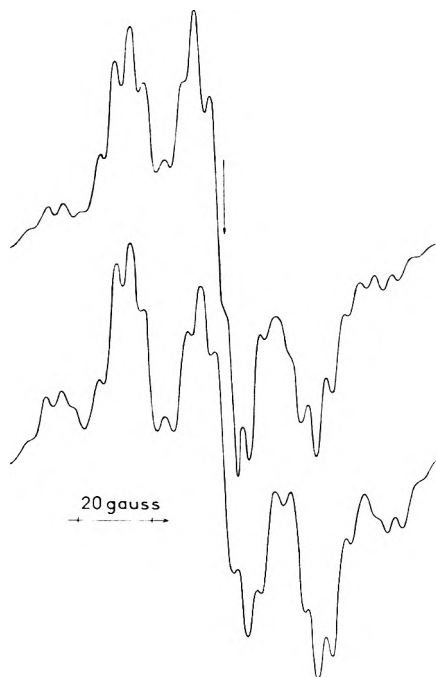


Figure 10. Upper spectrum shows γ irradiated ethyl-4-pyridine (HCl 12 M, 77°K). The lower spectrum is computed for the $^+\text{HNC}_5\text{H}_4\text{-CH-CH}_3$ radical (see Table VII).

la Recherche Scientifique et Technique for its financial support (Grant No. 7270064).

We are also indebted to Professor C. Parkányi for his help in the translation of the manuscript.

References and Notes

- (1) Service de Chimie-Physique.
- (2) Laboratoire de Chimie Organique Physique.
- (3) (a) L. A. Wall and R. B. Ingalls, *J. Chem. Phys.*, **41**, 1112 (1964); (b) C. David, A. Verhasselt, and G. Geuskens, *Polymer*, **9**, 521 (1968).
- (4) (a) H. J. Bower, J. A. McFae, and M. C. R. Symons, *Chem. Commun.*, 542 (1967); (b) G. Natta, G. Mazzanti, P. Longi, and G. Dall'Asta, and F. Bernardini, *J. Polym. Sci.*, **51**, 487 (1961).
- (5) G. Vincow and P. Johnson, *J. Chem. Phys.*, **39**, 1143 (1963).
- (6) R. Lefebvre and J. Maruani, *J. Chem. Phys.*, **42**, 1480 (1965).
- (7) H. M. McConnell and R. E. Robertson, *J. Phys. Chem.*, **61**, 1018 (1957).
- (8) W. Derbyshire, *Mol. Phys.*, **5**, 225 (1962).
- (9) J. R. Morton, *Chem. Rev.*, **64**, 453 (1964).
- (10) (a) J. R. Morton, *J. Phys. Chem. Solids*, **24**, 209 (1963); (b) J. R. Rowlands and D. H. Whiffen, *Nature (London)*, **193**, 61 (1962).
- (11) A. D. McLacalan, *Mol. Phys.*, **3**, 233 (1960).
- (12) (a) A. Streitwieser, "Molecular Orbital Theory for Organic Chemists," Wiley, New York, N. Y., 1961; (b) B. Eda, R. J. Cook, and D. H. Whiffen, *Trans. Faraday Soc.*, **60**, 1497 (1964).
- (13) A. R. Buick, T. S. Kemp, and T. J. Stone, *J. Phys. Chem.*, **74**, 19, 3439 (1970).
- (14) C. Chachaty, *J. Chim. Phys.*, **64**, 608 (1967).
- (15) H. Fischer, *Z. Naturforsch. A*, **20**, 428 (1965).
- (16) P. H. Kasai and D. McLeod, *J. Amer. Chem. Soc.*, **94**, 720 (1972).
- (17) C. Chachaty, *J. Chim. Phys.*, **64**, 614 (1967).
- (17a) Note Added in Proof. A recent high-resolution nmr study of 2-vinylpyridine shows that this compound has the cis structure corresponding to radical II (J. B. Rowbotham and T. Schaefer, *Can. J. Chem.*, **52**, 136 (1974)).
- (18) C. Chachaty and J. Maruani, *Can. J. Chem.*, **44**, 2631 (1966).
- (19) H. J. Bower, J. A. McRae, and M. C. R. Symons, *J. Chem. Soc. A*, 2696 (1968).
- (20) C. Chachaty and A. Forchioni, *C.R. Acad. Sci., Ser. C*, **264**, 1421 (1964).
- (21) R. W. Fessenden and R. H. Schuler, *J. Chem. Phys.*, **39**, 2147 (1963).
- (22) Pyridinyl type radicals are also observed for concentrations of PVP > 0.5 M, due to the scavenging of electrons by the pyridinium ions.
- (23) D. H. Whiffen, *Mol. Phys.*, **6**, 223 (1963).
- (24) J. A. Pople and D. L. Beveridge, "Approximate Molecular Orbital Theory," McGraw-Hill, New York, N. Y., 1970.
- (25) B. G. Ershov, in "Actions Chimiques et Biologiques des radiations," Vol. XIV, Masson et Cie, Paris, 1969, Chapter 4.
- (26) V. I. Vedenev, "Bond Energies, Ionization Potentials and Electron Affinities," Arnold, London, 1967.

The Influence of True Chemical Equilibrium on the Viscosity-Mobility Product of Electrolytes

Paul Hemmes

Department of Chemistry, Rutgers University, Newark, New Jersey 07102 (Received November 9, 1973)

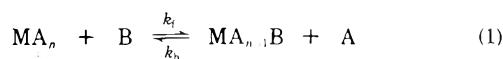
Equations have been derived which relate the Walden product of ionic mobility and solvent viscosity to the solvent composition in mixed solvents. It is assumed that a true chemical reaction occurs between the ion and the components of the solvent. In certain cases, the Walden product will exhibit maxima or minima as a function of composition. The results cannot be used for the evaluation of the equilibrium constant for the chemical process.

The product of the ionic mobility and the solvent viscosity (hereafter called the Walden product¹) has long been used as a measure of ion-solvent interactions. Since the mobility at infinite dilution is usually measurable, the Walden product is independent of ion-ion interactions. It is well known that classical theories of electrolytes are grossly naive with regard to the model used for the sol-

vent. In the most elementary treatment it is easy to show that the continuum solvent model leads to the prediction that Walden's product is a constant. Theoretical refinements by Zwanzig² have improved upon the elementary model by incorporating dynamic features of the solvent molecules into the theory. The influence of true chemical equilibrium has not previously been considered quantita-

tively. Qualitatively it is expected that chemical equilibrium will cause major deviations of Walden's product from a constant value. This prediction will now be examined. All subsequent discussion will deal with mixed solvents. Considerations of the influence of ionic isomerizations and change of coordination number in a pure solvent must await the refinement of the theoretical treatment of ion-solvent interactions.

Suppose an ion M is present in vanishing small concentration in a mixed solvent composed of two types of molecules A and B. Also assume that the coordination number of the ion is n and that both A and B are monodentate. Consider the process in which the ion is present in pure A and then B is added. The following equilibrium is then established



The equilibrium constant for this process is

$$K = (MA_{n-1}B)(A)/(MA_n)(B)$$

Hence the ratio of ionic species is determined by the solvent composition since the concentration of A and B are both assumed to be very much greater than the concentration of ions. The problem which is to be considered now is as follows. How is the Walden product influenced by this process? Mathematically this is most easily demonstrated by considering first a diffusion process.

Theoretical

The following derivation is based on a method used by Kacena and Matousek.³ For simplicity we will take $(MA_n) = C_M$, $(MA_{n-1}B) = C_{MB}$, and $(B) = C_B$. In eq 1, k_f and k_b are the forward and reverse rate constants of the reaction. The stability constant for the reaction, K , is equal to k_f/k_b . Over any arbitrary time interval τ the metal ion will be present in the uncomplexed form (MA_n) for a certain fraction of this interval τ_M . The fraction of time it is in the complexed form will be τ_{MB} . These fractions are measures of the lifetime of the species. Hence, assuming that C_B is large

$$\tau_M = 1/k_f C_B$$

$$\tau_{MB} = 1/k_b$$

Hence $\tau_{MB}/\tau_M = k_f C_B/k_b = KC_B = C_{MB}/C_M$.

The average displacement, Δ , of a particle of lifetime τ is given by the Einstein-Smoluchowski equation

$$\Delta_i = (2D_i\tau)^{1/2}$$

where D_i is the diffusion coefficient of the species. When two species are present which interconvert rapidly compared to the time scale of the experiment the mean quadratic displacement is

$$\Delta^2 = \Delta_M^2 + \Delta_{MB}^2 = 2\bar{D}\tau$$

$$\Delta^2 = 2D_M\tau_M + 2D_{MB}\tau_{MB}$$

where \bar{D} is the mean diffusion coefficient and is the quantity measured by any slow experiment. That is, \bar{D} is measured whenever the time required for the experiment is very much greater than the lifetime of the longest-lived species.

A comparison of terms gives

$$\bar{D} = D_M \frac{\tau_M}{\tau} + D_{MB} \frac{\tau_{MB}}{\tau}$$

$$\bar{D} = (D_M + D_{MB}KC_B) \frac{\tau_M}{\tau}$$

but $\tau = \tau_M + \tau_{MB} = (1 + KC_B)\tau_M$ thus

$$\bar{D} = \frac{D_M + D_{MB}KC_B}{1 + KC_B} \quad (2)$$

The mean diffusion coefficient therefore is simply the concentration weighted average of D_M and D_{MB} . Equation 2 has been derived independently for a number of electrochemical processes^{4,5} and has been used to evaluate ionic association constants.⁶

Applications to Electrical Conductance Measurements

We can express \bar{D} in terms of the equivalent conductance by means of the Nernst-Einstein equation. Also, so as to remove any restrictions on the relative amounts of A and B (except that they be much greater than the concentration of ions) we can express eq 2 in terms of mole fraction units. Hence

$$\bar{\lambda}_0 = \frac{\lambda_{0M} + (\lambda_{0MB}K - \lambda_{0M})X_B}{1 + (K - 1)X_B} \quad (3)$$

where K is, of course, in mole fraction units.

If we now assume that both species obey the Walden product ($\lambda_0\eta = k$, where η is the solvent viscosity and k , a constant) we have

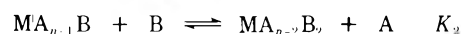
$$\bar{\lambda}_0\eta = W = \frac{k_M + (k_{MB}K - k_M)X_B}{1 + (K - 1)X_B} \quad (4)$$

Equation 4 predicts that W will vary with X_B despite the fact that both species obey the Walden product. Only for the special case of $k_{MB} = k_M$ will W be independent of composition.

Unfortunately the variation of W with composition will depend upon the details of the ion solvent interaction. For example, if B is a bidentate ligand while A is monodentate, then the reaction is



Under such conditions, eq 4 will not apply. Furthermore if more than one molecule of B reacts to produce more than one product, we have



etc. For the case of two stages of association, as above, we have

$$W = \frac{k_M + (k_{MB}K_1 - k_M)X_B + k_{MB_2}K_1K_2X_B^2}{1 + (K_1 - 1)X_B + K_1K_2X_B^2} \quad (5)$$

If eq 5 is differentiated with respect to X_B and the derivative set equal to zero, it is found that a maximum or minimum will be found for all values of X_B which satisfy the equation

$$X_B = \frac{-Q \pm (Q^2 - 4RS)^{1/2}}{2R}$$

where $Q = 2K_1K_2(k_{MB_2} - k_M)$, $R = K_1K_2(k_{MB_2}K_1 - k_{MB_2} - k_{MB}K_1 + k_M)$, and $S = K_1(k_{MB} - k_M)$. Hence from the above it is seen that the formation of more than one type of solvated complex ion will produce maxima and/or minima in the Walden product for single ions. Obviously if the other ion is also subject to chemical reactions with the solvent,

then the Walden product for the electrolyte Λ_{∞} will be a highly complex function of composition.

It seems unlikely that the variation of W with composition could be utilized for the measurements of the various K values. Rather what is needed is the independent determination of K from spectral measurements combined with conductance measurements of W in both pure solvents if possible and then in mixtures. Naturally any method for estimating the diffusion coefficients (polarography, chronopotentiometry, etc.) could also be used by suitable modification of the above equations.

Acknowledgment. The author wishes to thank the Research Council of Rutgers University for a grant which helped support this work.

References and Notes

- (1) P. Walden, *Z. Phys. Chem.*, **55**, 207, 246 (1906).
- (2) R. Zwanzig, *J. Chem. Phys.*, **52**, 3625 (1970).
- (3) V. Kacena and L. Matousek, *Collect. Czech. Chem. Commun.*, **18**, 294 (1953).
- (4) Z. Zabransky, *Collect. Czech. Chem. Commun.*, **24**, 3075 (1959).
- (5) N. Tanaka and A. Yomada, *Z. Anal. Chem.*, **224**, 117 (1957).
- (6) W. Lyness and P. Hemmes, *J. Inorg. Nucl. Chem.*, **35**, 1392 (1973).

An Empirical Intermolecular Potential Energy Function for Water

Lester L. Shipman² and Harold A. Scheraga*

Department of Chemistry, Cornell University, Ithaca, New York 14850 (Received November 7, 1973)

An empirical intermolecular potential energy function for water has been derived using data from pertinent available experimental and theoretical studies. The data utilized include the lattice energy of ice, X-ray structure of ice, compressibility of ice, intermolecular vibrational frequencies of ice, gas-phase dipole moment, gas-phase quadrupole moments, gas-phase infrared and microwave structure of the water monomer, and the localized molecular orbital structure of the water monomer. Expressions have been derived which relate various macroscopic thermodynamic properties to the intermolecular potential energy function. The contributions of the zero-point vibrational energy of ice to several of the above properties have been examined. Potential energy *vs.* O...O distance curves for various water dimers have been calculated and compared with large basis set *ab initio* quantum mechanical results. The need for an adequate treatment of the quantum mechanical nature of the intermolecular motions in the water dimer in the calculation of the second virial coefficient is discussed.

I. Introduction

In studies of the interactions of water molecules with each other and with other (solute) molecules, it is helpful to have an approximate empirical intermolecular potential for water. Among the many empirical intermolecular potentials that have been developed, the one upon which attention has been centered most recently is that of Ben-Naim and Stillinger³ (BNS), which has been applied to liquid water by Rahman and Stillinger,^{4,5} Weres and Rice,⁶ and Lentz, *et al.*⁷ These studies with the BNS potential have furthered our understanding of the structure and dynamics of liquid water. Although the BNS potential has been applied with considerable success to studies of liquid water, several defects in the potential have been identified,⁶⁻⁸ including the overestimation of the magnitude of the librational frequencies of tetracoordinated water molecules and the related overly strong tendency to form perfect tetrahedral coordination through hydrogen bonding. Also, the BNS potential was derived on a classical mechanical basis, whereas the intermolecular motions among water molecules are definitely of a quantum mechanical nature,⁶ as will be shown in section VIII.

In the present paper, we present a derivation of a physically reasonable potential for water, based on a wide variety of experimental and theoretical data, with a view toward being able to reproduce and account for the most

pronounced features of the structure and dynamical behavior of water in isolated dimers, trimers, etc., as well as in the liquid and solid states. The data utilized include the equilibrium O...O distance of ice,⁹ the lattice energy of ice, compressibility of ice, intermolecular vibrational frequencies of ice, gas-phase dipole moment, gas-phase quadrupole moments, gas-phase infrared and microwave structure of the water monomer, and the localized molecular orbital structure of the water monomer.

In order to relate macroscopic quantities such as the lattice energy of ice to the intermolecular potential, it has been necessary to start with relations from equilibrium thermodynamics and derive formulas which relate certain macroscopic data to the intermolecular potential. Contributions from the zero-point intermolecular vibrational energies have been considered explicitly in this derivation.

The potential is used to study the potential energy of a water dimer, the second virial coefficient of water vapor and, in another paper,¹⁰ the intermolecular vibrational modes of ice I.

II. Functional Form of the Potential

The empirical potential energy function derived in this study is pairwise additive; *i.e.*, the potential energy of an aggregate of water molecules is the sum of the potential energy of all pairs of water molecules in the aggregate.

Since three-body and higher order interactions have not been considered explicitly in the derivation of the potential here, the potential is best classified as an "effective" pair potential. The potential consists of two basic components, an electrostatic and an exp-6 component, as shown in eq 1, where U is the total potential energy.

$$U = U_{es} + U_{exp6} \quad (1)$$

The exponential form for the nonbonded repulsion was chosen, rather than the R^{-12} form, because of the need to fit the zeroth, first, and second derivatives to experimental quantities, and the exponential form was found to be more satisfactory for this than the R^{-12} form. The electrostatic component has the form

$$U_{es} = \sum_{i < j}^N U_{es}(i, j) \quad (2)$$

for interactions *in vacuo*, where N is the number of water molecules interacting, and $U_{es}(i, j)$ is the electrostatic energy of interaction between the water molecules i and j . Since, as will be shown in section IV, there are seven point charges on each water molecule, $U_{es}(i, j)$ has the form

$$U_{es}(i, j) = \sum_{k=1}^7 \sum_{l=1}^7 \frac{q_k q_l}{R_{kl}} \quad (3)$$

where q_k and q_l are the k th point charge on water molecule i and the l th point charge on water molecule j , respectively, and R_{kl} is the distance between q_k and q_l . The exp-6 component has the form

$$U_{exp6} = \sum_{i < j}^N A \exp(-CR_{ij}) - B/R_{ij}^6 \quad (4)$$

where A , B , and C are constants and R_{ij} is the distance between the centers of masses of water molecules i and j .

III. Geometry of the Water Molecule

The nuclear geometry was taken as the one determined from infrared and microwave studies¹¹ of the water monomer.¹² The O-H bond length is 0.95718 Å and the H-O-H bond angle is 104.523°.

IV. The Electrostatic Component

The positions and number of point charges on each water molecule were assigned to be qualitatively consistent with the localized molecular orbital structure of the water monomer.¹³ In this structure, a pair of electrons resides in a tightly bound inner shell orbital on oxygen, a pair of electrons resides in each of the two O-H bonding orbitals, and a pair of electrons resides in each of the two lone pair orbitals. Accordingly, a point charge of $+e$ was placed on each of the hydrogen nuclei, a charge of $+6e$ was placed on the oxygen nucleus ($+8e$ nuclear charge plus $-2e$ electronic charge), and point charges of $-2e$ were placed in each of the two O-H bonding regions and in each of the two lone pair regions. This system of charges is qualitatively similar to the system of point charges suggested by Hirschfelder, Curtiss, and Bird¹⁴ from the localized molecular orbital study of water monomer by Duncan and Pople.¹⁵ The precise locations of the extranuclear charges were determined as described in section VI.

There are initially 17 parameters to be fixed in the potential energy function, corresponding to the O-H bond length, the H-O-H bond angle, the x, y, z coordinates of the four outer-shell electron pairs, and the parameters A ,

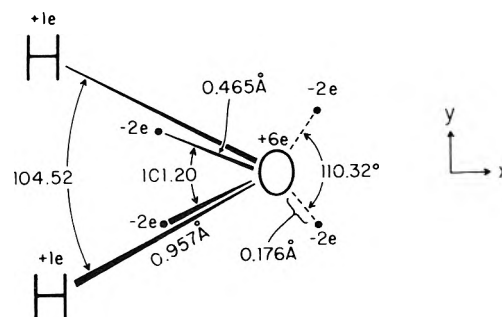


Figure 1. Positions of the seven point charges within the water molecule. All distances have been rounded to the nearest 0.001 Å and all angles have been rounded to the nearest 0.01°. The hydrogens and bonding pairs are in the xz plane and the lone pairs in the xy plane.

B , and C of the exp-6 component. The O-H bond length and the H-O-H bond angle are chosen as the experimental values given in section III, leaving 15 parameters to be fixed. In the coordinate system chosen (the derivation being independent of this choice), the water molecule lies in the xz plane, with the dipole moment vector along the x axis and the oxygen at the origin (see Figure 1). The positions of the four outer-shell electron pairs were constrained to the symmetry of the water molecule (C_{2v}), eliminating eight parameters to be fixed and leaving seven. In particular, the bonding electron pairs are constrained to lie in the xz plane, fixing each of their y coordinates as zero. The bonding electron pairs are constrained to reflect into each other through the xy plane; thus, knowledge of the x and z coordinates of one bonding pair implies knowledge of the x and z coordinates of the second bonding pair. The lone pairs are constrained to lie in the xy plane, fixing each of their z coordinates as zero. The lone pairs are constrained to reflect into each other through the xz plane; thus knowledge of the x and y coordinates of one lone pair implies knowledge of the x and y coordinates of the second lone pair.

Of the seven remaining parameters, three are A , B , and C of the exp-6 component (to be determined as described in section V). The final four parameters are fixed by constraining the positions of the bonding and lone pair charges to reproduce the experimental gas-phase dipole moment¹⁶ (1.884 D), two quadrupole moments^{17,18} (θ_{aa} , θ_{bb} , and θ_{cc} are equal to 2.72, -0.32 , and -2.40×10^{-26} esu cm^2 , respectively, but only two are independent since $\theta_{aa} + \theta_{bb} + \theta_{cc} = 0$), and (as will be described in section VI) the average librational frequency of ice.

V. The Exp-6 Component

After fixing the positions of the bonding and lone pair point charges (as will be described in section VI), the three adjustable parameters (A , B , and C) of the exp-6 component are obtained from the equilibrium O...O distance (R) of ice, the lattice energy of ice, and the isothermal compressibility (κ) of ice. Before relating these experimental quantities to the intermolecular potential, U , we obtain an expression for the molar volume, V , of ice as a function of R .

1. *Relation between R and V .* The space group for the oxygen atoms of ice¹⁹ is $D_{6h}^4(P6_3/mmc)$ but, because of the disorder of the positions of the hydrogens²⁰ (statistically there are 3/2 ways that each water molecule can orient at its lattice site), strictly speaking, ice belongs to no space group. However, we know that all possible arrange-

ments of hydrogens in ice must have approximately the same energy.²⁰ In the present study, we have considered only that particular arrangement of hydrogens that corresponds to the smallest hexagonal unit cell for ice;²¹ the space group for this arrangement is $C_{6h}^3(P6_3cm)$, and there are 12 water molecules per unit cell.²²

If the ice lattice were perfectly tetrahedral (*i.e.*, if all nearest-neighbor O...O distances were equal and all O-O-O angles between neighbors were tetrahedral), the molar volume would be a function only of R . We consider here how closely we can fit the observed lattice constants (a , b , and c) of ice under the assumption that ice has a perfect tetrahedral lattice. The low temperature lattice constants, which change very slowly with temperature near $T = 0^\circ\text{K}$, are $a = b = 4.4968 \text{ \AA}$ and $c = 7.3198 \text{ \AA}$ from X-ray diffraction on polycrystalline ice.²³ A nearest-neighbor O...O distance of 2.7493 \AA in a perfect tetrahedral lattice gives $a = b = 4.4896 \text{ \AA}$ and $c = 7.3315 \text{ \AA}$, which deviates from the observed values by only 0.16% in each of the lattice constants. Therefore, to a good approximation, we consider ice to be a perfect tetrahedral lattice with $R = 2.7493 \text{ \AA}$ at $T = 0^\circ\text{K}$. For a perfect tetrahedral lattice, the volume of 1 mol (N_0 water molecules) of ice is given by

$$V = 8(3)^{1/2}N_0R^3/9 \quad (5)$$

2. *Relations between Macroscopic Properties of Ice and U.* We now derive the equations which relate the equilibrium values of R , the lattice energy, and compressibility of ice to the intermolecular potential, U . We begin with the following relation for a one-component system²⁴

$$(\partial E/\partial V)_T = T(\partial S/\partial V)_T - P \quad (6)$$

where E is the internal energy, V is the volume, T is the absolute temperature, S is the entropy, and P is the pressure. At $T = 0^\circ\text{K}$, this reduces to

$$(\partial E/\partial V)_{T=0^\circ\text{K}} = -P \quad (7)$$

since it is physically reasonable to expect the residual entropy of ice to be constant or slowly varying for small changes of volume from the equilibrium volume; *i.e.* $(\partial S/\partial V)_T$ is not expected to be infinite at $T = 0^\circ\text{K}$. At $T = 0^\circ\text{K}$, the internal energy, E , may be expressed as

$$E = U + \Delta Z_{\text{intra}} + Z_{\text{inter}} \quad (8)$$

where U is the potential energy (relative to zero potential energy for infinitely separated water molecules), ΔZ_{intra} is the change in intramolecular zero-point energy in going from the vapor phase to ice, and Z_{inter} is the total intermolecular vibrational zero-point energy of ice. Since there is no vapor at 0°K , $P = 0$, and since all water molecules are in their ground state (*i.e.*, ice) at 0°K , it follows from eq 7 and 8 that

$$\left(\frac{\partial U}{\partial V}\right)_{T=0^\circ\text{K}} + \left[\frac{\partial(\Delta Z_{\text{intra}})}{\partial V}\right]_{T=0^\circ\text{K}} + \left(\frac{\partial Z_{\text{inter}}}{\partial V}\right)_{T=0^\circ\text{K}} = 0 \quad (9)$$

Since ice can be assumed to be a perfect tetrahedral lattice, eq 9 may be rewritten (with the aid of eq 5) as

$$\left(\frac{\partial U}{\partial R}\right)_{T=0^\circ\text{K}} + \left[\frac{\partial(\Delta Z_{\text{intra}})}{\partial R}\right]_{T=0^\circ\text{K}} + \left(\frac{\partial Z_{\text{inter}}}{\partial R}\right)_{T=0^\circ\text{K}} = 0 \quad (10)$$

Now, let us consider the second derivative²⁴ of E with respect to V , *viz.*

$$\left(\frac{\partial^2 E}{\partial V^2}\right)_T = \frac{1}{\kappa V} + T \left[\frac{\partial(\alpha/\kappa)}{\partial V}\right]_T \quad (11)$$

where α is the coefficient of thermal expansion, and the other terms have been defined previously. Since it is physically reasonable to expect that (α/κ) does not become infinite for small changes in volume away from the equilibrium value at $T = 0^\circ\text{K}$, the second term on the right-hand side of eq 11 vanishes. With the aid of eq 5, eq 11 may be rewritten as

$$\left(\frac{\partial^2 E}{\partial R^2}\right)_{T=0^\circ\text{K}} = \left[\frac{8(3)^{1/2}N_0R}{\kappa}\right] + \frac{2}{R} \left(\frac{\partial E}{\partial R}\right)_{T=0^\circ\text{K}} \quad (12)$$

The second term on the right in eq 12 is identically equal to zero at the equilibrium value of R and, with the aid of eq 8, we arrive at

$$\left(\frac{\partial^2 U}{\partial R^2}\right)_{T=0^\circ\text{K}} + \left[\frac{\partial^2(\Delta Z_{\text{intra}})}{\partial R^2}\right]_{T=0^\circ\text{K}} + \left(\frac{\partial^2 Z_{\text{inter}}}{\partial R^2}\right)_{T=0^\circ\text{K}} = \frac{8(3)^{1/2}N_0R}{\kappa} \quad (13)$$

The lattice energy of ice (defined as U at $T = 0^\circ\text{K}$) has been estimated by Whalley^{25,26} to be -14.08 kcal/mol . The compressibility of ice, extrapolated to $T = 0^\circ\text{K}$ from the empirical κ vs. T relation of Dantl,²⁷ is $(9.3 \pm 1.4) \times 10^{-12} \text{ cm}^2 \text{ dyn}^{-1}$, and the value calculated from the empirical elastic constants vs. temperature relations of Proctor²⁸ (extrapolated to $T = 0^\circ\text{K}$) is $(9.2 \pm 0.2) \times 10^{-12} \text{ cm}^2 \text{ dyn}^{-1}$. Combining these results by weighting them by the inverse of their respective experimental errors, we take the compressibility of ice at $T = 0^\circ\text{K}$ to be $(9.2 \pm 0.4) \times 10^{-12} \text{ cm}^2 \text{ dyn}^{-1}$.

As a first approximation, we assume that

$$\left[\frac{\partial(\Delta Z_{\text{intra}})}{\partial R}\right]_{T=0^\circ\text{K}} + \left(\frac{\partial Z_{\text{inter}}}{\partial R}\right)_{T=0^\circ\text{K}} = 0 \quad (14)$$

and

$$\left[\frac{\partial^2(\Delta Z_{\text{intra}})}{\partial R^2}\right]_{T=0^\circ\text{K}} + \left(\frac{\partial^2 Z_{\text{inter}}}{\partial R^2}\right)_{T=0^\circ\text{K}} = 0 \quad (15)$$

The validity of these assumptions will be examined in section VII. With these assumptions, eq 10 and 13 reduce to eq 16 and 17, respectively. The experimental values of R and κ have been instituted on the right-hand side of eq 13.

$$(\partial U/\partial R)_{T=0^\circ\text{K}} = 0 \quad (16)$$

$$\left(\frac{\partial^2 U}{\partial R^2}\right)_{T=0^\circ\text{K}} = 60 \text{ kcal mol}^{-1} (\text{\AA})^{-2} \quad (17)$$

$R = 2.7493 \text{ \AA}$

Equations 16 and 17, together with the experimental estimate^{25,26} of the lattice energy of ice, *viz.*

$$U_{T=0^\circ\text{K}} = -14.08 \text{ kcal mol}^{-1} \quad (18)$$

are three conditions that make it possible to fix the values of A , B , and C of the exp-6 component for a given set of charge positions. For computational purposes, the lattice energy U was taken as $(\frac{1}{2})(\frac{1}{2})$ of the sum of the potential energies of interaction of each of the 12 water molecules in the central unit cell with all other water molecules (including those in the central unit cell) in a section of the ice lattice consisting of $5 \times 5 \times 5$ unit cells (1500 water molecules).

VI. Determination of the Charge Positions

At this point in the derivation of the intermolecular po-

tential energy function, four parameters remain to be fixed. These parameters vary the positions of the bonding and lone pair electronic charges. Three of these parameters are fixed by requiring that the charges match the dipole and quadrupole moments, as indicated in section IV. The remaining parameter (required to determine the positions of the charges uniquely) is obtainable because the calculated librational frequencies of ice²⁹ depend on the positions of the bonding and lone pair electronic charges. The positions of these charges were varied until the average of the calculated librational frequencies of a central water molecule, vibrating in the field of its four nearest neighbors in ice, was near the mean librational frequency of ice, and the computed gas-phase dipole and quadrupole moments matched the experimental values. The librational frequencies were calculated using a model of a central water molecule and its four nearest neighbors in their ice arrangement at $R = 2.7493 \text{ \AA}$. The harmonic force constant matrix (including the mass) for the motions of the central water molecule (with the four outer molecules held stationary, as in the computations of Lentz, *et al.*,^{8,29}) was calculated numerically, and subsequent diagonalization of this matrix gave the normal frequencies (calculated as $1/(2\pi c)$ times the square roots of the eigenvalues of the harmonic force constant matrix, with c being the velocity of light).

The librational peak of ice is broad with the highest intensity at 840 cm^{-1} in the infrared³⁰ and at 780 cm^{-1} in the Raman spectrum.²⁵ Unlike the infrared and Raman spectra, the inelastic neutron scattering spectrum is not severely restricted by selection rules and, therefore, should be more representative of the actual frequency distribution. Several of the most recent values³¹⁻³⁷ for the approximate position of the librational peak (or peaks) in the inelastic neutron scattering spectrum are listed in Table I. It should be noted that only one peak was observed in some studies, but two distant peaks in others.

A thermodynamic analysis of the heat capacity of ice³⁸ suggests that the mean librational frequency is 650 cm^{-1} . It is clear from the infrared, Raman, inelastic neutron scattering, and thermodynamic data summarized here that the position of the librational peak (or peaks) of ice is known only approximately. We have selected a value of 700 cm^{-1} as a reasonable one for the mean librational frequency, and we have used this frequency to fix the last remaining parameter in the potential energy function. The particular value of 700 cm^{-1} was chosen to give the most weight to the peak observed in the $600\text{--}700\text{-cm}^{-1}$ range in the inelastic neutron scattering spectrum and to the 650-cm^{-1} estimate from the heat capacity analysis, while still giving some weight to the peak in the $800\text{--}1000\text{-cm}^{-1}$ range of the inelastic neutron scattering spectrum.

The intermolecular vibrational frequencies, calculated using the completely derived potential for the vibrations of a central water in the field of its four, fixed, nearest neighbors, are 188, 192, 205, 660, 714, and 730 cm^{-1} . The first three frequencies are hindered translations, and the last three are librations; it should be noted that the average of the calculated librational frequencies is 701 cm^{-1} , according to our imposed constraint.

The empirical intermolecular potential energy function derived here is completely specified by eq 1-4 and Table II, which gives the values for the parameters of the potential energy function. The positions of the charge centers in the water molecule are shown in Figure 1. Hereafter in this paper, this empirical intermolecular potential energy

function for water will be referred to as the "SS" potential.

VII. Volume Dependence of the Vibrational Zero Point Energies of Ice

It has been assumed that the intra- and intermolecular vibrational zero-point energy contributions to the first and second derivatives of the internal energy with respect to R sum to zero (see eq 14 and 15). It is the purpose of this section to discuss the validity of these assumptions. Consider the first and second derivatives of the intermolecular zero-point energies with respect to R . For the vibration of a central water molecule in the field of its four fixed nearest neighbors, Z_{inter} has been calculated (at $R = 2.6493$, 2.7493 , and 2.8493 \AA) as the sum over the six values of $hc\omega/2$, where the ω 's are the fundamental frequencies (in cm^{-1}) calculated in the manner described in section VI. The three computed values of Z_{inter} were fit by a parabola, and the following derivatives obtained

$$\left[\frac{\partial Z_{\text{inter}}}{\partial R} \right]_{T=0^\circ\text{K}}^{R=2.7493\text{\AA}} = -4.0 \text{ kcal mol}^{-1} (\text{\AA})^{-1} \quad (19)$$

and

$$\left[\frac{\partial^2 Z_{\text{inter}}}{\partial R^2} \right]_{T=0^\circ\text{K}}^{R=2.7493\text{\AA}} = 5.8 \text{ kcal mol}^{-1} (\text{\AA})^{-2} \quad (20)$$

Unfortunately, the first and second derivatives of ΔZ_{intra} with respect to R are unknown. It is for precisely this reason that we have elected (as a computational device) to absorb the contributions of the zero-point vibrational energies to the volume dependence of E entirely into U through the assumptions of eq 14 and 15.

It is physically reasonable to expect that the first derivatives of the intra- and intermolecular zero-point energies with respect to R tend to sum to zero and that the second derivatives of the intra- and intermolecular zero point energies tend to sum to zero for the following reasons. ΔZ_{intra} and Z_{inter} are both zero for large values of R , and have opposite signs and are of the same order of magnitude (-1.19 and 3.95 kcal/mol , respectively²⁵) at the equilibrium value of R (2.7493 \AA). ΔZ_{intra} and Z_{inter} would be expected to have larger rates of change with respect to R nearer the equilibrium value of R than at larger values of R because they arise from hydrogen bonding, a short-range interaction. Thus, it is reasonable to assume that $[\partial(\Delta Z_{\text{intra}})/\partial R]_{T=0^\circ\text{K}}$ and $(\partial Z_{\text{inter}}/\partial R)_{T=0^\circ\text{K}}$ have opposite signs and that $[\partial^2(\Delta Z_{\text{intra}})/\partial R^2]_{T=0^\circ\text{K}}$ and $(\partial^2 Z_{\text{inter}}/\partial R^2)_{T=0^\circ\text{K}}$ have opposite signs at the equilibrium value of R . In section XI, an experiment is suggested which should give information about the volume dependence of the zero-point vibrational energies.

VIII. Formation of a Water Dimer

The smallest unit that can be used to examine the behavior of the six-dimensional (three rotational and three translational degrees of freedom) water-water potential is a water dimer. The dependence of the SS potential energy on R for the perpendicular plane linear dimer (PePLD), parallel plane linear dimer (PaPLD), perpendicular plane bifurcated dimer (PePBD), parallel plane bifurcated dimer (PaPBD), and tetrahedral linear dimer (TLD) has been examined. These dimers are shown in Figure 2, and their SS potential energy *vs.* R curves are shown in Figure 3, together with the results of large basis set *ab initio* cal-

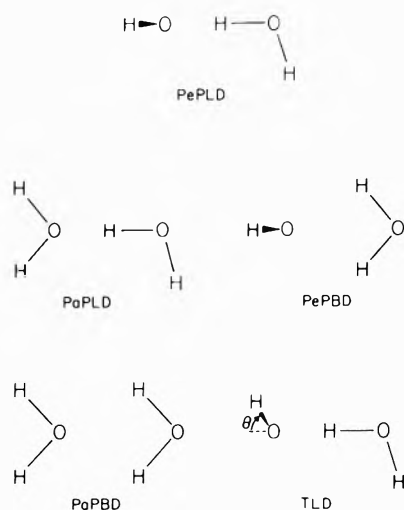


Figure 2. Various water dimers considered here. For those water molecules for which only a single hydrogen is shown, a second hydrogen lies directly behind the one shown, and its position is determined by reflecting the hydrogen shown through the plane of the paper. $\theta = (\frac{1}{2}) \arccos(-\frac{1}{3})$ in the special case of the TLD.

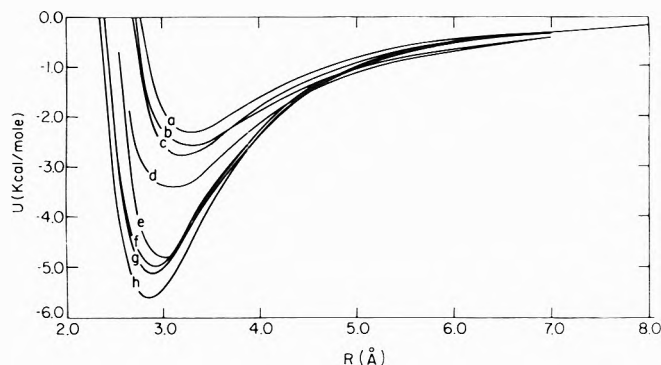


Figure 3. Potential energy curves for various water dimers as calculated from the SS potential and from the potentials of large basis set *ab initio* calculations by Diercksens.^{39,40} (a) PaPBD (SS); (b) PaPBD (*ab initio*); (c) PePBD (SS); (d) PePBD (*ab initio*); (e) PePLD (*ab initio*); (f) PaPLD (SS); (g) PePLD (SS); (h) TLD (SS).

calculations by Diercksens.^{39,40} We do not mean to imply here that the minima with respect to R in Figure 3 correspond to minima in the six-dimensional space, since all degrees of freedom are not included in Figure 3; in fact, most of the dimers studied here correspond to saddle points on the six-dimensional potential energy surface.⁴¹

Before comparing the SS and *ab initio* results, several defects in the *ab initio* results should be mentioned here, since these defects must be considered when deciding how close the agreement between the results of the SS potential and the large basis set *ab initio* potential should be expected to be. First, the *ab initio* calculations do not include dispersion energy. Second, the *ab initio* curves are lower in energy than the SS curves at large values of R because the potential energy in this region is predominantly dipole-dipole interaction energy, and the *ab initio* wave function overestimates the dipole moment of the isolated water molecule by 17% (2.206 D⁴⁰ compared to the experimental value of 1.884 D¹⁶), making the dipole-dipole interaction energy 37% too large (since the dipole-dipole interaction energy is proportional to the square of the dipole moment).

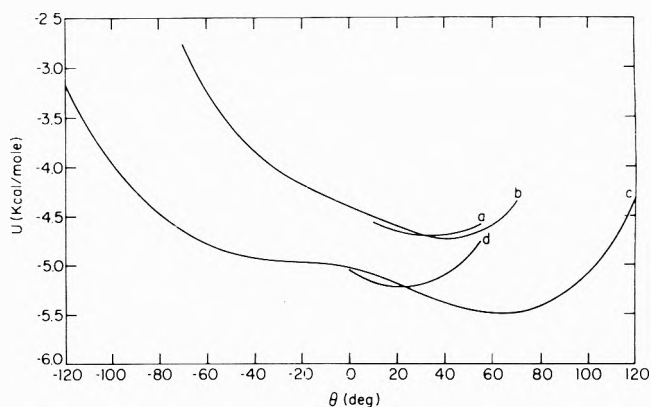


Figure 4. Potential energy vs. θ (at $R = 3.00 \text{ \AA}$) for the SS potential and for the potentials from available large basis set *ab initio* calculations. θ is defined in the TLD drawing of Figure 2: (a) *ab initio*;^{39,40} (b) *ab initio*;⁴² (c) SS; (d) *ab initio*.⁴⁴

On the repulsive side of the potential, the shape of the SS and *ab initio* curves are visibly quite similar. Both results show that the position of the minimum moves to larger values of R as the stability of the dimer decreases. For the TLD, the minima in the SS and *ab initio*^{42,43} curves are at $R = 2.86$ and 3.00 \AA , respectively.

Figure 4 shows the dependence of the SS potential energy on θ at $R = 3.00 \text{ \AA}$ (θ is defined in the drawing of the TLD structure in Figure 2), together with the results of large basis set *ab initio* calculations.^{39,40,42,44} Both the SS and *ab initio* curves are visibly quite similar. Both the region near the TLD, and the curvature of the SS potential curve is less than that of the *ab initio* curves. The minimum⁴⁵ is located at approximately 37, 41, 63, and 22° for the *ab initio* curve of Diercksens,^{39,40,46} the *ab initio* curve of Hankins, *et al.*,⁴² the SS potential curve, and the *ab initio* curve of Kollman and Allen,⁴⁴ respectively. It is of interest that the dependence of U on θ for the BNS potential (shown in Figure 11 of ref 3) exhibits *two* minima near the tetrahedral values of $\pm 55^\circ$ with an intervening maximum at 0° ; this behavior is in qualitative disagreement with the results of both the *ab initio* and SS potentials.

In order to assess the possible quantum mechanical nature of the intermolecular vibrations of a water dimer, the normal vibrational frequencies at the minimum very near the TLD on the six-dimensional potential energy surface were calculated. The potential energy was minimized with respect to all six intermolecular degrees of freedom for this local minimum, the harmonic force constant matrix (including the mass) was calculated numerically and diagonalized, and the frequencies were obtained by multiplying the square root of each of the six nonzero eigenvalues of the harmonic force constant matrix by $1/(2\pi c)$. The resulting frequencies were 681, 451, 183, 114, 105, and 63 cm^{-1} . The potential energy at the minimum was found to be 5.8 kcal mol^{-1} , and the intermolecular zero-point energy ($hc/2$ times the sum of the six frequencies in cm^{-1}) was calculated from the above frequencies to be 2.3 kcal mol^{-1} , some 40% of the distance from the bottom of the potential energy well toward the dissociation limit. In order for the intermolecular vibrations to be treated classically, $h\nu/kT$ must be much less than unity for each of the six intermolecular vibrations. Figure 5 shows plots of $h\nu/kT$ for each of the six intermolecular frequencies as a function of temperature. It can be seen that two of the vibrations are of a decidedly quantum mechanical nature

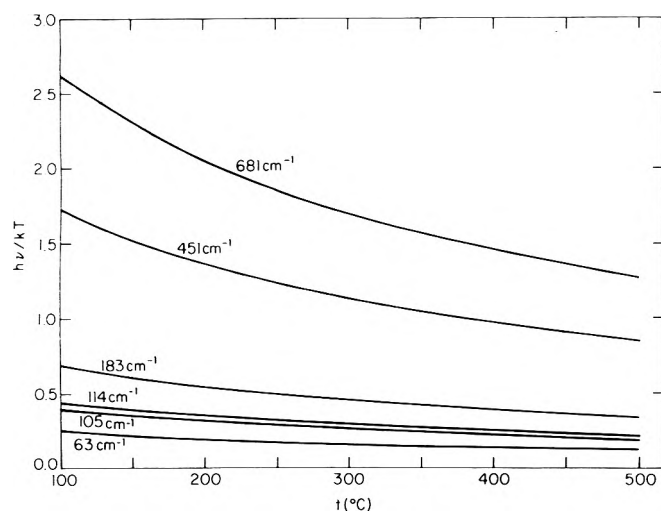


Figure 5. $h\nu/kT$ (where T is absolute temperature) as a function of centigrade temperature for the six intermolecular vibrational modes of a water dimer found very near the TLD on the six-dimensional potential energy surface.

and the other four might be treated classically in an approximate, though not rigorous, manner because $h\nu/kT$ is not much less than unity for these four frequencies throughout the temperature range shown.

IX. Compressive Effect in Ice

As pointed out by Momany, *et al.*,⁴⁷ the long-range attractive forces between a central molecule in a crystal and other molecules beyond its nearest neighbors constitute a compressive force which reduces the equilibrium intermolecular distance compared to that in, say, a dimer. In order to examine the magnitude of this compressive effect in ice, we consider the forces which balance in determining the equilibrium value of R in ice at $T = 0^\circ\text{K}$.

The potential energy U may be divided into a contribution, U_{NN} , from nearest neighbors and a contribution, U_{R} , from the remainder of the crystal.

$$U = U_{\text{NN}} + U_{\text{R}} \quad (21)$$

The roles of U_{NN} and U_{R} in determining the equilibrium value of R are quite different, in that U_{NN} leads to a repulsive force and U_{R} to an attractive force. From eq 16 and 21, we have

$$\left(\frac{\partial U_{\text{NN}}}{\partial R}\right)_{T=0^\circ\text{K}} + \left(\frac{\partial U_{\text{R}}}{\partial R}\right)_{T=0^\circ\text{K}} = 0 \quad (22)$$

This is not a strict equality because of the omission of the zero-point vibrational energy contributions. The forces, F_{NN} and F_{R} , corresponding to the energy components, U_{NN} and U_{R} , are the negatives of the first derivatives in the first and second terms, respectively, in eq 22. Rearranging, and rewriting eq 22 in terms of the forces, we obtain

$$F_{\text{NN}} \approx -F_{\text{R}} \quad (23)$$

i.e., the nearest-neighbor force is repulsive to about the same extent as the force from the rest of the crystal is attractive. This leads to a "compressive effect" wherein nearest neighbors are closer together at equilibrium in ice than they are at equilibrium as isolated dimers.⁴⁷ For example, the equilibrium value of R in ice (both experimentally and from the SS potential) is $\approx 2.75 \text{ \AA}$ and the equilibrium value of R in the TLD (computed with the SS po-

TABLE I: Recent Inelastic Neutron Scattering Results for the Librational Peak of Ice

| Investigators | Frequency, ^a cm ⁻¹ | Ref |
|-------------------------|---|-----|
| Bajorek, <i>et al.</i> | 601 | 31 |
| Burgman, <i>et al.</i> | 600–810 ^{b,c} | 32 |
| Prask, <i>et al.</i> | 650,900 | 33 |
| Harling | 726 | 34 |
| Renker and Blankenhagen | 640,820 ^b | 35 |
| Thaper, <i>et al.</i> | 653,840 | 36 |
| Blankenhagen | 690,970 ^b | 37 |

^a The librational peak is quite broad. ^b Read from frequency distribution figures by the present authors, and rounded to the nearest 10 cm⁻¹. ^c Broad plateau.

tential) is $\approx 2.86 \text{ \AA}$, a compressive effect in ice of $\approx 0.11 \text{ \AA}$.

X. Second Virial Coefficient

The second virial coefficient, $B(T)$, is a measure of the intermolecular pair potential, and is a quantity that can be determined experimentally. The results of section VIII show that the intermolecular vibrations of the water dimer are quantum mechanical, not classical, in nature, and it follows that a quantum mechanical formulation should be used to calculate $B(T)$. Unfortunately, a rigorous calculation using a quantum formulation is not computationally feasible at this time since a knowledge of the intermolecular vibrational states from the ground state to the dissociation limit is needed for the quantum treatment. In view of this, $B(T)$ has been calculated here for various potentials, using the classical formulation. The classical expression⁴⁸ for water is

$$B(T) = -\frac{N_0}{4\pi^2} \int_0^{2\pi} \int_0^\pi \int_0^{2\pi} \int_0^\pi \int_0^\pi \int_0^\pi [e^{-U(r,\theta,\phi,\alpha,\beta,\gamma)/kT} - 1] r^2 \sin \theta \sin \beta \, dr \, d\theta \, d\phi \, d\alpha \, d\beta \, d\gamma \quad (24)$$

where N_0 is Avogadro's number, U is the potential energy of interaction between water molecule no. 1 and water molecule no. 2, the spherical coordinates r , θ , and ϕ define the position of the center of mass of water molecule no. 2 (the center of mass of water molecule no. 1 being at the origin), α , β , and γ are the Euler angles which specify the rotation of water molecule no. 2 with respect to water molecule no. 1, k is Boltzmann's constant, and T is the absolute temperature. The Euler angle rotations are carried out in a very specific manner; water molecule no. 2 is rotated by α about its c axis, then by β about its b axis, and finally by γ about its c axis, where b and c are principal axes.

The calculation of $B(T)$ may be simplified by breaking the integral down into four intervals in r as shown in Table III. U is so positive in interval no. 1 that $e^{-U(r,\theta,\phi,\alpha,\beta,\gamma)/kT} \ll 1$ (for the temperature range and potentials studied here), and hence the water molecules may be considered to behave like rigid spheres in interval no. 1. In this rigid-sphere interval, the six-dimensional integral may be evaluated analytically⁴⁹ to give $10.1 \text{ cm}^3 \text{ mol}^{-1}$. In intervals no. 2 and 3, the six-dimensional equivalent of the rectangle method for one dimension has been used to perform the integration numerically using equally spaced points. The accuracy of this integration method has been verified by comparing the numerical results with the analytical results for two 1.884 D dipoles interacting in interval no. 3. U is essentially a dipole-dipole interaction energy in interval no. 4 for the potentials studied

TABLE II: Parameters of the Intermolecular Potential Energy Function

| Electrostatic component | Coordinates, Å | | | Charge |
|---|----------------|------------|------------|--------|
| | x | y | z | |
| O nucleus | 0.000000 | 0.000000 | 0.000000 | +6e |
| H nucleus | -0.5858502 | 0.000000 | 0.7569498 | +1e |
| H nucleus | -0.5858502 | 0.000000 | -0.7569498 | +1e |
| Bonding pair | -0.2954276 | 0.000000 | +0.3596594 | -2e |
| Bonding pair | -0.2954276 | 0.000000 | -0.3596594 | -2e |
| Lone pair | 0.1005610 | 0.1444746 | 0.000000 | -2e |
| Lone pair | 0.1005610 | -0.1444746 | 0.000000 | -2e |
| Center of mass | -0.0655591 | 0.000000 | 0.000000 | |
| Exp-6 component ^a | | | | |
| $A = 0.6700663 \times 10^6 \text{ kcal/mol}$ | | | | |
| $B = 0.2835012 \times 10^4 \text{ kcal mol}^{-1} (\text{Å})^{-6}$ | | | | |
| $C = 3.2530000 (\text{Å})^{-1}$ | | | | |

^a The exp-6 component has a minimum energy of -0.79 kcal/mol at 3.45 Å .

TABLE III: Intervals for Integration of Eq 24

| Interval no. | Interval range, Å | Integration method |
|--------------|-------------------|----------------------------|
| 1 | $0 \leq r \leq 2$ | Analytical (rigid sphere) |
| 2 | $2 < r < 4$ | Numerical (fine grid) |
| 3 | $4 \leq r \leq 7$ | Numerical (coarse grid) |
| 4 | $7 < r$ | Analytical (dipole-dipole) |

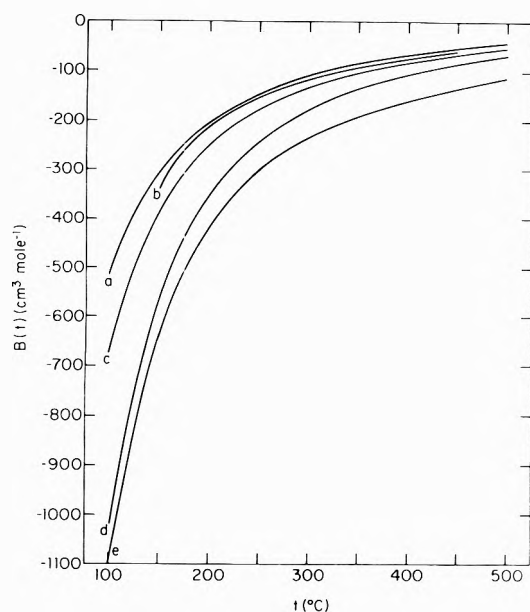


Figure 6. Second virial coefficient of water vs. temperature as determined experimentally and as calculated classically from various empirical intermolecular potentials for water: (a) BNS potential;³ (b) experimental;⁵¹ (c) 1.06 scaled BNS potential;⁴ (d) ST2 potential;⁵⁰ (e) SS potential.

here, and the six-dimensional integral can be evaluated analytically⁴⁹ for dipole-dipole interactions. The potentials, for which $B(T)$ has been calculated here, are the BNS potential,³ the 1.06 scaled BNS potential,⁴ the ST2 potential,⁵⁰ and the SS potential. The results are shown in Figure 6 along with the experimental results of Kell, *et al.*⁵¹

The curve for $B(T)$, calculated using the classical formulation and the BNS potential, fits the experimental $B(T)$ curve reasonably well because the parameters of the BNS potential were varied during the derivation of the BNS potential to obtain this fit. The SS potential, on the other hand, was derived without use of $B(T)$ data, since it

was felt in advance that the classical formulation of $B(T)$ might be invalid for water.

There are at least two effects that contribute to the rather large deviation between the theoretical $B(T)$ curve (calculated classically from the SS potential) and the experimental curve. First, the decidedly quantum mechanical nature of some of the intermolecular vibrational modes of the water dimer would contribute a positive correction to the calculated curve of Figure 5. Second, the three-body interactions in ice (which are attractive^{42,43}) have been absorbed into the SS potential, making the potential an "effective" pair potential and leading to an overestimation of the stability of the water dimer, and this would contribute a positive correction to the calculated curve of Figure 5. There is at least one effect that opposes the two effects just mentioned. The O-H stretching intramolecular vibrations should have lower frequencies in the hydrogen-bonded water dimer than they have in the isolated monomer, thus stabilizing the dimer, and this would contribute a negative correction to the calculated curve of Figure 5. At this time, we are unable to assess the magnitudes of any of these three corrections. However, a comparison of the experimental curve and the $B(T)$ curve calculated classically from the SS potential leads to the obvious conclusion that the sum of the first two corrections exceeds that of the third.

XI. Conclusions

A new empirical intermolecular potential (SS potential) has been derived by use of a variety of experimental data and by taking account of quantum effects (by use of eq 8 and the arguments used to render eq 14 and 15 plausible). The SS potential has been compared to large basis set *ab initio* potentials for a water dimer. It has been shown that some of the intermolecular vibrational modes of water are definitely of a quantum mechanical nature.

The results of the present study point out a fundamental difference in the nature of hydrogen bonding between various molecules. In a water-water hydrogen bond, the light masses of the vibrational modes which are primarily hydrogen motions lead to large vibrational zero-point energies. In fact, it has been calculated here that the ground state of a water dimer is approximately 40% of the distance from the bottom of the potential well toward the dissociation limit. Ammonia is an example of another molecule that may have large intermolecular vibrational zero-point energies. At the other extreme, a hydrogen bond (*e.g.*, N-H...O=C) between two portions of a protein molecule involves such large masses at each end of

the hydrogen bond that the ground state for intermolecular vibrations should be quite near the bottom of the potential energy well. It follows that zero-point vibrational energies play an important role in the determination of hydrogen bond strengths for systems with intermolecular vibrational modes with light reduced masses and stiff potentials. The importance of the zero-point vibrational energies in the hydrogen bond strength of water has been discussed in some detail by Eisenberg and Kauzman⁵² and Hagler, Scheraga, and Nemethy.⁵³

The quantum mechanical nature of the motions in aggregates of water molecules, as described here, leads to the view that the results of classical molecular dynamics calculations on water should be interpreted with caution since the (possibly important) quantum effects have been left out. Similarly, hydrogen bond strengths calculated from wave functions should not be compared directly to experimental values unless the zero-point energies are taken into account.

The volume dependence of the zero-point vibrational energies should be susceptible to an experimental determination by measuring the O...O distance (using X-ray crystallography) and the intra and intermolecular vibrational frequencies (using infrared spectroscopy) as the pressure is increased. Care would need to be taken to assure that ice I_h were the form under study since increased pressure eventually would result in transitions to more densely packed forms of ice.

Acknowledgment. We are indebted to Drs. B. R. Lentz, F. A. Momany, and G. C. C. Niu for many helpful, informative discussions.

References and Notes

- (1) This work was supported by research grants from the National Science Foundation (No. GB-28469X3), and from the National Institute of General Medical Sciences of the National Institutes of Health, U. S. Public Health Service (No. GM-14312).
- (2) NIH Postdoctoral fellow 1972-1974.
- (3) A. Ben-Naim and F. H. Stillinger in "Water and Aqueous Solutions: Structure, Thermodynamics and Transport Processes," R. A. Horne, Ed., Wiley-Interscience, New York, N. Y., 1972, p 303.
- (4) A. Rahman and F. H. Stillinger, *J. Chem. Phys.*, **55**, 3336 (1971).
- (5) F. H. Stillinger and A. Rahman, *J. Chem. Phys.*, **57**, 1281 (1972).
- (6) O. Weres and S. A. Rice, *J. Amer. Chem. Soc.*, **94**, 8983 (1972).
- (7) (a) B. R. Lentz, A. T. Hagler, and H. A. Scheraga, *J. Phys. Chem.*, in press; (b) B. R. Lentz, Ph.D. Thesis, Cornell University, Aug 1973.
- (8) B. R. Lentz, A. T. Hagler, and H. A. Scheraga, *J. Phys. Chem.*, to be submitted for publication.
- (9) Throughout this paper, "ice" is taken to mean "ice I_h."
- (10) L. L. Shipman and H. A. Scheraga, *J. Phys. Chem.*, to be submitted for publication.
- (11) W. S. Benedict, N. Gailar, and E. F. Plyer, *J. Chem. Phys.*, **24**, 1139 (1956).
- (12) Experimental data are given to the number of significant figures reported in the experimental studies cited. This does not mean that the potential is sensitive to all the significant figures given.
- (13) C. W. Kern and M. Karplus in "Water, A Comprehensive Treatise," Vol. 1, F. Franks, Ed., Plenum Press, New York, N. Y., 1972, p 41.
- (14) J. O. Hirschfelder, C. F. Curtiss, and R. B. Bird, "Molecular Theory of Gases and Liquids," Wiley, New York, N. Y., 1954, p 1032.
- (15) A. Duncan and J. Pople, *Trans. Faraday Soc.*, **49**, 217 (1953).
- (16) M. Lichtenstein, V. E. Derr, and J. J. Gallagher, *J. Mol. Spectrosc.*, **20**, 391 (1966).
- (17) J. Verhoeven and A. Dynamus, *J. Chem. Phys.*, **52**, 3222 (1970).
- (18) These are the "Buckingham-type" quadrupole moments, and are in the principal axes coordinate system. See A. D. Buckingham, *Quart. Rev. Chem. Soc.*, **13**, 183 (1959).
- (19) W. H. Barnes, *Proc. Roy. Soc. Ser. A*, **125**, 670 (1929).
- (20) L. Pauling, *J. Amer. Chem. Soc.*, **57**, 2680 (1935).
- (21) P. G. Owston, *Advan. Phys.*, **7**, 171 (1958).
- (22) J. D. Bernal and R. H. Fowler, *J. Chem. Phys.*, **1**, 515 (1933).
- (23) R. Brill and A. Tippe, *Acta Crystallogr.*, **23**, 343 (1967).
- (24) G. N. Lewis and M. Randall, "Thermodynamics and the Free Energy of Chemical Substances," McGraw-Hill, New York, N. Y., 1961, pp 665-666.
- (25) E. Whalley in "Physics and Chemistry of Ice," E. Whalley, S. J. Jones, and L. W. Gold, Ed., Royal Society of Canada Publication, Ottawa, 1973, p 73.
- (26) A number of pieces of experimental information were used to estimate the lattice energy of ice. Among these were the intramolecular normal vibrational frequencies in the vapor, the intramolecular normal vibrational frequencies in ice, the intermolecular vibrational frequencies of ice, the heat of vaporization from liquid to zero pressure gas at 25°, the difference in ideal gas enthalpy between 25° and 0°K, heat capacity data for the liquid between 0 and 25°, heat of fusion, and heat capacity data for ice between 0°K and 0°.
- (27) G. Dantl in "Physics of Ice," N. Riehl, B. Bullemer, and H. Engelhardt, Ed., Plenum Press, New York, N. Y., 1969, p 227.
- (28) T. M. Proctor, Jr., *J. Acoust. Soc. Amer.*, **39**, 972 (1966).
- (29) The use of the potential function here to compute the librational frequencies is similar to the procedure of Lentz, *et al.*⁸ who previously tested another potential function by computing the frequencies of hydrogen-bonded water molecules.
- (30) J. E. Bertie and E. Whalley, *J. Chem. Phys.*, **40**, 1637 (1964).
- (31) A. Bajorek, J. A. Janik, J. M. Janik, I. Natkaniec, K. Parlinski, Y. N. Pokotilovskii, M. Sudnik-Hryniewicz, V. E. Komarov, R. P. Ozerov, and S. P. Solov'ev, "Inelastic Scattering of Neutrons," Vol. 2, International Atomic Energy Agency, Vienna, 1968, p 143.
- (32) J. O. Burgman, J. Scisinski, and K. Skold, *Phys. Rev.*, **170**, 808 (1968).
- (33) H. Prask, H. Boutin, and S. Yip, *J. Chem. Phys.*, **48**, 3367 (1968).
- (34) O. K. Harling, *J. Chem. Phys.*, **50**, 5279 (1969).
- (35) B. Renker and P. v. Blankenhagen in ref 27, p 287.
- (36) C. L. Thaper, A. Sequeira, B. A. Dasannacharya, and P. K. Iyengar, *Phys. Status Solidi*, **34**, 279 (1969).
- (37) P. v. Blankenhagen, *Ber. Bunsenges. Phys. Chem.*, **76**, 891 (1972).
- (38) A. J. Leadbetter, *Proc. Roy. Soc. Ser. A*, **278**, 403 (1965).
- (39) G. H. F. Diercksen, *Chem. Phys. Lett.*, **4**, 373 (1969).
- (40) G. H. F. Diercksen, *Theor. Chim. Acta*, **21**, 335 (1971).
- (41) A study, in which the water dimers corresponding to minima and saddle points on the six-dimensional potential energy surface are located and characterized, is being completed by L. L. Shipman, J. C. Owicki, and H. A. Scheraga, *J. Phys. Chem.*, to be submitted for publication.
- (42) D. Hankins, J. W. Moskowitz, and F. H. Stillinger, *J. Chem. Phys.*, **53**, 4544 (1970).
- (43) B. R. Lentz and H. A. Scheraga, *J. Chem. Phys.*, **58**, 5296 (1973).
- (44) P. A. Kollman and L. C. Allen, *J. Chem. Phys.*, **51**, 3286 (1969).
- (45) The position of the minimum was estimated by means of a three-point fit of the data to a parabola in each case.
- (46) A point at $\theta = 0^\circ$ is shown in Figure 4 of ref 40 (*i.e.*, Diercksen calculated the dimer energy at $\theta = 0^\circ$ also). However, this point at $\theta = 0^\circ$ has not been included here since the nuclear geometry used by Diercksen in calculating the energy for this point was different from the monomer geometry used for the other points.
- (47) F. A. Momany, L. M. Carruthers, R. F. McGuire, and H. A. Scheraga, *J. Phys. Chem.*, submitted for publication.
- (48) Reference 3, p 315.
- (49) Reference 14, p 210.
- (50) F. H. Stillinger and A. Rahman (private communication from F. H. Stillinger) have derived this potential, and applied it to a study of the molecular dynamics of water. The results are better than the results for the BNS potential.
- (51) G. S. Kell, G. E. McLaurin, and E. Whalley, *J. Chem. Phys.*, **48**, 3805 (1968).
- (52) D. Eisenberg and W. Kauzman, "The Structure and Properties of Water," Oxford University Press, New York, N. Y., 1969, p 137.
- (53) A. T. Hagler, H. A. Scheraga, and G. Nemethy, *J. Phys. Chem.*, **76**, 3229 (1972).

Electrical Conductance and Ultrasonic Relaxation for Lithium Perchlorate in Tetrahydrofuran

Paul Jagodzinski¹ and Sergio Petrucci*

Department of Chemistry, Polytechnic Institute of New York, Brooklyn, New York 11201 (Received July 2, 1973; Revised Manuscript Received December 13, 1973)

Electrical conductance (10^{-5} to $1 M$) at 25, -15 , and -30° and ultrasonic absorption (0.05 – $0.5 M$) in the frequency range 5 – 330 MHz at 25, -15 , and -30° have been measured for LiClO₄ in tetrahydrofuran (THF). The electrical conductance data reveal the presence of a minimum that can be interpreted and evaluated by the Fuoss-Kraus theory of triple ion formation (up to $\sim 0.1 M$). Numerical evaluation of ion pair and triple ion pair constants were made. The ultrasonic relaxation data are interpreted as due to the process of formation of triple ions, the barrier of activation energy for the process being comparable to the one for viscous flow.

Introduction

Electrolytes solutions in media of low dielectric constants were investigated by audio-frequency electrical conductance methods in the 1930's by Fuoss and Kraus in a series of classic papers.^{2a} Later, Davies^{2b} reexamined some of the same systems by dielectric relaxation techniques giving qualitative evidence of the molecular complexities of these systems through the appearance of distribution of relaxation processes. It was of interest to study the same system by classical and by modern kinetic tools, in order to determine the molecular dynamics involved.

For this purpose, the system of LiClO₄ in THF has been investigated by both audio-frequency electrical conductance and by radio frequency ultrasonic absorption measurements. The results of each method will be discussed.

Experimental Section

Materials. Tetrahydrofuran (Matheson Coleman and Bell) was distilled under a nitrogen atmosphere over a 60% K-Na alloy in a 3-ft Vigreux column. It was found that distillation over Na was ineffective, the melting point of Na being higher than the boiling point of the solvent. A 60% K-Na alloy is liquid at the boiling temperature of the solvent and provides good surface contact between liquid and metal. The central third of the THF distillate was collected and stored under nitrogen. The density of the distilled THF at 25.0° was $0.8819 \pm 5 \times 10^{-5}$ g/cc; the literature values^{3,4} range from 0.880 to 0.883 g/cc.

Anhydrous reagent grade LiClO₄ (Smith, Cleveland, Ohio) was dried to constant weight at $\sim 190^\circ$. It was stored in sealed bottles; contact with the atmosphere for weighing lasted only 30 sec or less. Redrying the material at $\sim 190^\circ$ for 1–2 days after being weighed gave no changes in weight. Further, LiClO₄·3H₂O reagent grade (Smith, Cleveland, Ohio) was dehydrated at 75° under 0.1 mm pressure. A $0.25 M$ solution of this material in THF gave conductance values within 0.2% of the values reported in Figure 1.

Solutions for conductance work more concentrated than $50 \times 10^{-4} M$ were prepared individually by weighing both salt and freshly distilled solvent. This was done to avoid possible changes of conductance due to aging or formation

of peroxides. Each value of the reported conductance at $c = 50 \times 10^4 M$ and higher was obtained from individual solutions.

For the solutions of concentration lower than $5 \times 10^{-3} M$, a "concentration" method was used. The stock solution was added by weight burets to the solvent in the conductance cell. A drybox filled with purified N₂ was used in all the operations involving cell filling and solution transfer.

Procedure and Instrumentation. The density of the solutions at 25° was required to convert molalities to molarities. At both -15 and -30° the difference between the density of the solutions and the pure solvent was within $\pm 0.2\%$ of the values at 25.0° . A special pycnometer with a capillary stem and a bulb (acting as a reservoir to allow for the liquid expansion upon thermal reequilibration to room temperature) was used for the density measurements at -15 and -30° .

Each reported value of the density was obtained by averaging a double determination. The average error was found to be $\pm 5 \times 10^{-5}$ g/cc using thermostats with $\pm 2 \times 10^{-2}^\circ$ of precision and a Mettler H-6 balance. The capacity of the pycnometers was approximately 50 cc.

The equipment for the conductance work has been described elsewhere.⁵

Conductance measurements were made at three temperatures: 25.000 ± 0.001 , -15 ± 0.01 , and $-30 \pm 0.01^\circ$. At 25° the previously reported⁵ fluctuation of $\pm 0.005^\circ$ were decreased by circulating water previously thermostated at $24.00 \pm 0.05^\circ$ through a 40-ft spiral of 1-in. i.d. copper tubing (immersed in the oil bath close to the thermostat walls). The room temperature was maintained as $23 \pm 1^\circ$ by a York 3-ton air conditioning unit.

The conductance cells used had constants of $0.1142 + 6 X_s$ and $0.2794 + 12 X_s$ cm⁻¹ with X_s the total specific conductance of the solutions. For the solutions of concentration below $50 \times 10^{-4} M$ it was necessary to insert a 30-k Ω shunt (GR510 Series) in parallel with the cell. The resistances of the solutions were measured at 1000, 2000, and 5000 Hz. For the diluted solutions linear extrapolation to zero frequency was performed since parallel losses may be the main sources of error. At higher concentrations, extrapolation of the resistance to infinite frequency by a R vs. $1/f^{1/2}$ plot was made, where f is the frequency

in Hz. Electrode polarization becomes the increasingly important source of error with increasing electrolyte concentration. In all cases the differences between either R_0 , R_∞ , or any of the R 's were not larger than $\pm 0.1\%$.

Solutions for ultrasonic measurements were prepared by first weighing the salt and then diluting in volumetric flasks. Only fresh solutions were used. Duplicate measurements were always made with newly prepared solutions. Whenever differences larger than the sensitivity of the method were noticed, the results were rejected. The equipment and experimental details have been previously described.^{5,6} For measurements above 200 MHz at 25° a new interferometric cell with two 1-in. delay lines was used. The moving crystal connected to the delay line traveled over a high-precision horizontal slide (Automatic Gages, Rochester, N. Y.) ensuring maintenance of parallelism within few seconds of an arc for travel of 1 in. A precision micrometer (Boeckeler Instruments, Tucson, Ariz.) allowed readings of these displacements to within $\pm 1 \times 10^{-4}$ in. Temperature was maintained at 25° by circulating thermostated water through a jacket surrounding the cell. The temperature was measured by a thermocouple probing directly into the solution during the measurements. Plots of attenuation in decibels *vs.* distance increments at the frequency of 330 MHz were perfectly linear and repetitive runs gave results for the absorption coefficient of sound within $\pm 2\%$. At the lowest frequencies, 9 and 5 MHz, it is important to avoid diffraction errors. Accordingly, the distance between the sending and receiving crystal was kept within the Fresnel zone. A calibrated Kai attenuator (Model 1/432C) that could be varied by fractions of 1 dB (down to 0.1 dB) was used. The attenuator was put in series with the cell and changes in the attenuator settings were compensated by changes in the distance between the crystals of the cell. In this way, the maximum distance between the two crystals could be kept within the limit $0.5R^2/\lambda$, with R the radius of the sending crystal and λ the wavelength. Further, plots of the attenuation (in dB) *vs.* distance were linear for all the data reported in this work.

Results and Discussion

I. Electrical Conductance. After the molalities of the stock solutions used for conductance work were determined in a non-linear least-squares program was fitted to the following data at 25°: $m = 0, 0.11464, 0.28773, 0.57898, \text{ and } 1.17988$ mol/kg of solvent and $\rho = 0.88196, 0.89115, 0.90376, 0.92480, \text{ and } 0.96690$ g/cc. The program fits the data according to the relation $\rho(\text{g/cc}) = 0.88206 + 0.0758m - 0.00353m^2$, from which the molalities of the solutions used for the conductance work were converted to molarities c at 25°.

For the lower temperatures it was found that the ratio $(\rho^{\text{solution}}/\rho^{\text{solvent}})^{25} = (\rho^{\text{solution}}/\rho^{\text{solvent}})^{25}$ within $\pm 0.2\%$. A similar functional form of ρ on m was therefore assumed for the solutions at the lower temperatures

In Figure 1A, the plots of $\log \Lambda$ *vs.* $\log c$ are shown at 25, -15, and -30°. Although the data at low concentrations ($c \leq 9 \times 10^{-4} M$) approximate the requirement⁷ of slope = -0.50 (required by an electrolyte heavily associated to a neutral ion pair), they diverge *positively* from this slope at increasing concentrations.⁸ Eventually the $\log \Lambda$ *vs.* $\log c$ plot goes through a minimum, a sign of the existence of conducting triple ions. Also above 0.5 M at 25°, where data are available, the $\log \Lambda$ *vs.* $\log c$ plot

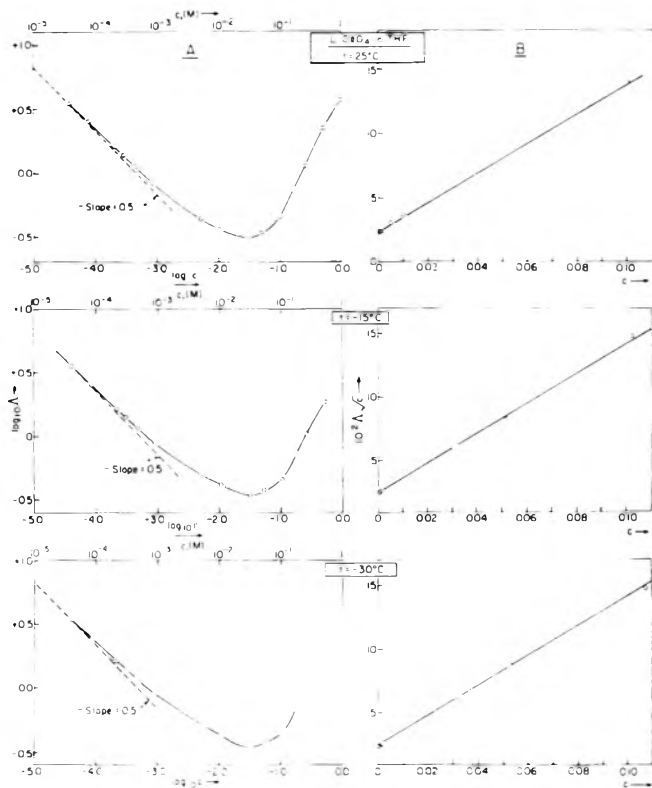


Figure 1. $\log \Lambda$ *vs.* $\log c$ (A) and $\Lambda c^{1.2}$ *vs.* c (B) for LiClO_4 in THF at 25, -15, -30°.

shows a downward concavity possibly indicating the appearance of quadrupoles.

The conductance data were treated as follows. At low concentrations ($c \leq 9 \times 10^{-4} M$) the Fuoss-Kraus method^{9a} for association to ion pairs has only been tentatively applied. Plots of F/Λ *vs.* $c \Delta f_{\pm}^2/F$ are shown in Figure 2. These plots are approximately linear. Least-squares analysis should give $1/\Lambda_0$ as intercept and K_A/Λ_0^2 as slope. It is apparent that the intercept gives the wrong value of Λ_0 . In fact at 25° it gives $\Lambda_0 = 17.88 \Omega^{-1} \text{ cm}^2 \text{ equiv}^{-1}$ whereas from the data of Szwarc, *et al.*,^{9b} $\lambda^0(\text{Li}^+) = 36.6 \Omega^{-1} \text{ cm}^2 \text{ equiv}^{-1}$. According to Justice and Treiner $\lambda^0(\text{ClO}_4^-)$ is 119.5 giving $\Lambda^0(\text{LiClO}_4)$ of $156.1 \Omega^{-1} \text{ cm}^2 \text{ equiv}^{-1}$. (The value $\lambda^0(\text{ClO}_4^-) = 119.5$ was obtained as follows. Justice and Treiner¹⁰ determined $\Lambda^0(\text{Bu}_4\text{NClO}_4) = 162.6 \Omega^{-1} \text{ cm}^2 \text{ equiv}^{-1}$ in THF at 25°. Micheletti¹¹ reports $\Lambda^0(\text{Bu}_4\text{NBPh}_4) = 82.97$ and $\Lambda^0(i\text{Am}_3\text{BuNBPh}_4) = 79.66 \Omega^{-1} \text{ cm}^2 \text{ equiv}^{-1}$ at 25° in THF. Taking $\lambda^0(i\text{Am}_3\text{BuN}) = \lambda^0(\text{BPh}_4)$ one calculates $\lambda^0(\text{Bu}_4\text{N}) = 82.97 - 39.83 = 43.14$ and $\lambda^0(\text{ClO}_4^-) = 162.6 - 43.14 = 119.5 \Omega^{-1} \text{ cm}^2 \text{ equiv}^{-1}$.)

Szwarc, *et al.*,^{9b} worked in the concentration region from 10^{-6} to $10^{-4} M$ therefore avoiding the complication of triple ions. They reported that when data at higher concentrations were plotted according to the Fuoss-Kraus method a downward trend appeared. The failure to describe the ionic equilibria in terms of ion pairs and free ions alone was also predicted theoretically by Fuoss^{7,12} for concentrations higher than $c_0 = 3.2 \times 10^{-7} D^3$. In our case, $D = 7.39$ at 25° which gives $c_0 = 1.3 \times 10^{-4} M$, almost at the lowest limit of our concentrations. Tentative runs at concentrations below $0.4 \times 10^{-4} M$ were abandoned because the resistance was too high to be measured with accuracy. Correction of the solvent conductance would have implied a several per cent correction to the

TABLE I: Triple Ion Analysis of LiClO₄ in THF

| <i>t</i> , °C | Λ^0 , $\Omega^{-1} \text{ cm}^2 \text{ equiv}^{-1}$ | $K_A \times 10^{-7}$, M^{-1} | K_T , M^{-1} | a_T (eq 3) $\times 10^3$, cm | a_T^- (eq 4) $\times 10^3$, cm | a_T (eq 5) $\times 10^3$, cm |
|---------------|---|---------------------------------|------------------|---------------------------------|-----------------------------------|---------------------------------|
| 25 | 156.1 ^a | 4.84 ± 0.19 | 153 ± 3 | 5.27 ± 0.02 | 3.63 ± 0.02 | 4.62 ± 0.02 |
| -15 | (97.3) ^b | 1.50 ± 0.12 | 139 ± 5 | 5.14 ± 0.03 | 3.53 ± 0.02 | 4.47 ± 0.03 |
| -30 | (78.6) ^b | 0.93 ± 0.10 | 133 ± 9 | 5.10 ± 0.07 | 3.50 ± 0.04 | 4.44 ± 0.06 |

^a Value calculated from literature data. See text. ^b Values calculated from the Walden rule retaining $\Lambda^0 = 156.1$ at 25°.

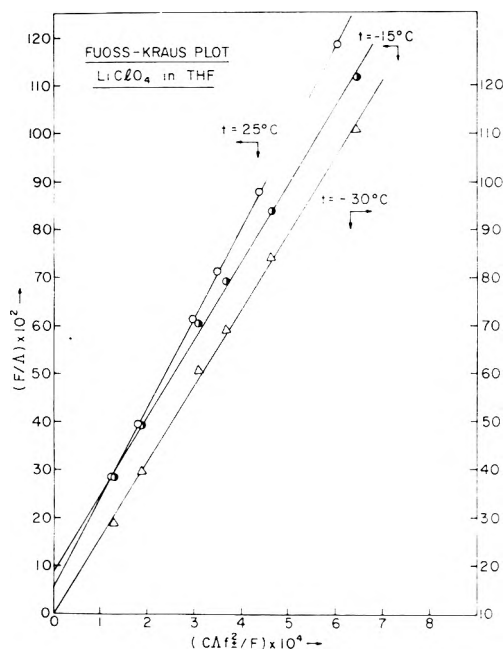


Figure 2. Fuoss-Kraus plot: F/Λ vs. $c\Lambda^2/F$.

total conductance. In fact Szwarz's association constant for LiBPh₄ is $\sim 1.25 \times 10^4 M^{-1}$, more than three orders of magnitude lower than the one for LiClO₄ as reported below. Therefore in THF, LiClO₄ is a weaker electrolyte than LiBPh₄ and its electrical conductance is far lower at $c = 10^{-4}$ to $10^{-5} M$.

It should be noticed that using $\Lambda^0 = 156.1 \Omega^{-1} \text{ cm}^2 \text{ equiv}^{-1}$ at 25°, $\Lambda^0 = 97.3$ at -15°, and $\Lambda = 78.6$ at -30° (from the Walden rule), the slopes of the Fuoss-Kraus plots yield a K_A of 4.57×10^7 at 25°, 1.53×10^7 at -15°, and $0.98 \times 10^7 M^{-1}$ at -30°, respectively. These figures are in surprisingly good agreement with the results given below and based on triple ion formation analysis. Therefore, it seems that the presence of triple ions rather than the slope of a Fuoss-Kraus plot affects the determination of Λ_0 (because of its functional form in the intercept).

Analysis by the Fuoss-Kraus theory^{2a} of triple ion formation has been performed according to the relation

$$\Lambda\sqrt{c} = \frac{\Lambda_0}{\sqrt{K_A}} + \frac{\Lambda_T^0 K_T}{\sqrt{K_A}} c \quad (1)$$

where Λ_T^0 is the conductance of the two triple ions ($\Lambda_T^0 = \lambda^0(\text{Li}(\text{ClO}_4)_2^-) + \lambda^0(\text{Li}_2(\text{ClO}_4)^+)$), and K_T is the formation constant of the triple ions

$$K_T = \frac{[\text{Li}(\text{ClO}_4)_2^-]}{[\text{LiClO}_4][\text{ClO}_4]} = \frac{[\text{Li}_2(\text{ClO}_4)^+]}{[\text{LiClO}_4][\text{Li}^+]}$$

In the above a symmetrical approximation is assumed for the coordination of the triple ions.^{2a} Also Λ_T^0 is assumed to be $\Lambda_T^0 = (1/3)\Lambda^0$. Plots of $\Lambda c^{1/2}$ vs. c are shown in Figure 1B. These plots are approximately linear up to the

concentration of 0.1 M after which a strong positive deviation from linearity appears.¹³ Linear least-squares analysis (solid line) of the linear portion of the plots give the slopes and intercepts from which K_A and K_T are calculated as reported in Table I.

Correlation of the K_A 's in the form of $\log K_A$ vs. $1/DT$ according to the Fuoss^{14a} function

$$K_A = K_0 e^b = \frac{4\pi N a^3}{3000} \exp\left(\frac{|z_1 z_2| e^2}{a D k T}\right) \quad (2)$$

gives $a = 1.81 \times 10^{-8}$ cm where a is the minimum approach distance between ions in the ion pair.

Based on the Fuoss-Kraus ion pair analysis, one gets $a = 1.95 \times 10^{-8}$ cm. These figures are in reasonable accord with the sum of the crystallographic radius of Li^+ $r_{\text{Li}} = 0.68 \times 10^{-8}$ cm and the Cl-O distance, $r_{\text{ClO}} = 1.65 \times 10^{-8}$ cm, namely, $\Sigma r = 2.33 \times 10^{-8}$ cm. Thus from the exponential part of eq 2 (see footnote 16a), one would conclude that some contact between ion pairs for LiClO₄ probably exists. The same conclusion was reached for LiBPh₄ by Szwarz, *et al.*,^{9b} in comparing data for LiBPh₄ with data for NaBPh₄. However judging from the Stokes radius r_+ = 4.9×10^{-8} cm it would seem that Li^+ is solvated in THF, whereas $r_- = 1.5 \times 10^{-8}$ cm is in fair accord with the r_{ClO} distance.

Next the correlation of the triple ion association constants K_T should be tried. There are two theories of association for triple ion formation. Both are based on the assumption of a continuum for the solvent and on ion-dipole interaction energy, but use different models.

The first theory by Kraus and Fuoss of 1933^{2a} retains the Bjerrum model and conceives of a triple ion as an entity held together by electrostatic interactions. In particular the ion pair and the free ion are considered to be associated into a triple ion when the parameter $b_T = e^2/a_T D k T > 8/3$. a_T is the distance of minimum approach between the ion and the center of the ion pair dipole of internuclear separation a . According to the Debye-Hückel model one would expect $a_T = 1.5a$. (Assuming ion pairs at distance a is consistent with the Bjerrum model at low dielectric constants. It has been pointed out^{14b} that the average distance for ion pairs $\langle r \rangle = a[1 + (1/b)] \simeq a$ for large b , or, for small D .) According to the triple ion theory,^{2a} it is not necessary that an ion and a dipole be in actual contact to be considered as a triple ion. In fact, triple ions were considered to exist^{2a} up to the minimum of their probability distribution function, namely, up to the distance $R > a_T$. The triple ion association constant according to the original 1933 theory^{2a} is given by the expression

$$K_T = \frac{2\pi N a_T^3}{1000} I(b_T) \quad (3)$$

where $I(b_T)$ is a double integral which has been tabulated^{2a} for a wide range of values of b_T .

In 1959 Fuoss proposed⁷ a new theory for triple ion for-

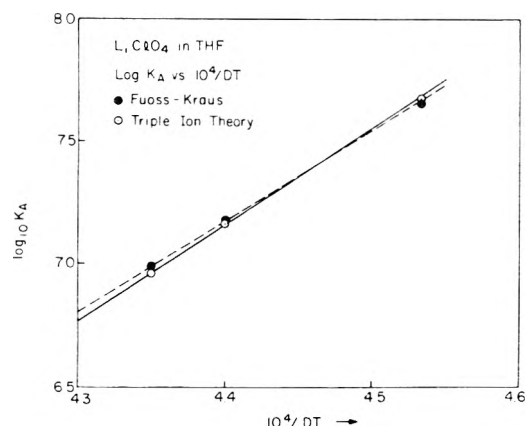


Figure 3. Log K_A vs. $1/DT$ for LiClO_4 in THF. The dashed line refers to the Fuoss-Kraus analysis shown in Figure 2. The solid line refers to the results of the triple ion analysis.

mation based on the definition that only ions in direct contact with a dipole ion pair should be considered as triple ions.

When an ion is in contact with an ion pair, the energy U becomes⁷ $U = e^2/2aD$ (for a 1:1 electrolyte). The triple ion formation constant is given by the expression

$$K_T = \frac{Nv_2}{1000} e^{-3} e^{b/2} = \frac{N\pi a^3}{1000} e^{-3} \exp\left(\frac{e^2}{2aDkT}\right) \quad (4)$$

where $v_2 = \pi a^3$ is the volume of the ion pair assumed to be a cylinder of radius $a/2$ and height $4a$. The factor e^{-3} stands for $\exp(-3R/2)$ which corresponds,⁷ according to the authors to the entropy changes due to the loss of three degrees of translational freedom upon formation of a triple ion. Vibrational degrees of freedom were excluded by the model, because it was argued that if vibration occurs, the contact between the ions breaks.⁷

Apart from obvious misprints,⁷ in the assignment of the number of rotational degrees of freedom for both ion pairs and triple ions, we believe the factor e^{-3} should read $e^{-3/2}$ in eq 4. If one accepts the statement⁷ that the net entropy change per mole is $-3R/2$ ($3RT/2$ for the entropy was clearly a misprint⁷) the factor to be introduced in the K_T expression namely $\exp(\Delta S/R)$ gives $e^{-3/2}$ not e^{-3} as reported.⁷

We also believe that the same result for K_T can be achieved unambiguously by modification of the model to include the vibrational degrees of freedom. Spectroscopic evidence¹⁵ for vibrational motion of ion pairs in THF has been documented in the literature.¹⁵

A linear diatomic molecule (ion pair) possesses three degrees of freedom for translation and $3n - 3 = 3$ internal degrees of freedom. Of these, two are for rotation, and one for vibration. A linear triple ion will have $3n - 3 = 6$ internal degrees of freedom. Of these, two are for rotation and four for vibration, specifically the symmetrical and asymmetrical stretching modes and the two degenerate bending modes.

In terms of the corresponding average internal energy, this can be expressed by the relations for linear molecules.

$$\text{triple ion} \quad U = \frac{3}{2}RT + RT + (3n - 5)RT = \frac{13}{2}RT$$

$$\text{ion pair} \quad U = \frac{3}{2}RT + RT + (3n - 5)RT = \frac{7}{2}RT$$

$$\text{free ion} \quad U = \frac{3}{2}RT$$

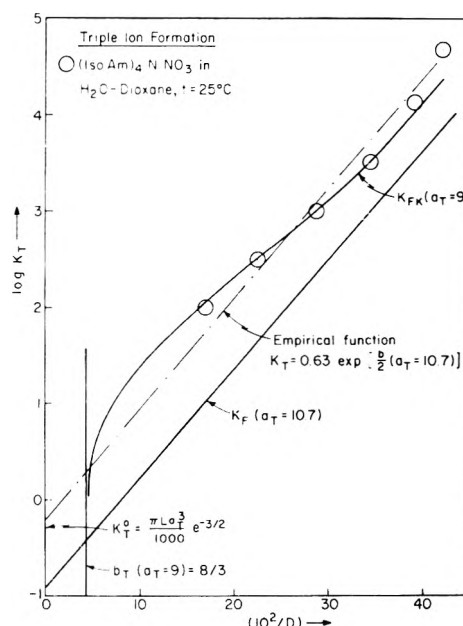


Figure 4. Log K_T vs. $1/D$ for $i\text{Am}_4\text{N-NO}_3$ in $\text{H}_2\text{O-dioxane}$ at 25° . Solid sigmoid line is the Bjerrum-Fuoss eq 3. Solid straight line is the Fuoss eq 4. Dashed straight line is the calculated least-squares function. Arrow indicates the intercept calculated according to eq 5.

The change in internal energy upon formation of a triple ion from an ion pair and a free ion will be $\Delta U = 3RT/2$, namely, a gain of $3RT/2$ per mole of triple ion formed. The triple ion formation constant expression should then be multiplied by a factor $\exp(-\Delta U/RT) = e^{-3/2}$, since $\Delta U_{\text{total}} = \Delta U_{\text{electr}} + \Delta U_{\text{freedom}} = (e^2/2aD) + 3RT/2$ and $K_T \propto \exp(-\Delta U_{\text{total}}/RT)$.

In the above, the ions, ion pairs and triple ions are considered immersed in a continuum of permittivity D .⁷ The solvent has been excluded from participating in the association process. Volume changes have also been neglected. This last approximation is equivalent to equalize the Helmholtz and Gibbs free energy changes $\Delta A = \Delta G$ and to equate internal energy changes to enthalpy changes $\Delta U = \Delta H$. The expression for K_T should then read

$$K_T = \frac{N\pi a^3 e^{-3/2}}{1000} = K_T^0 e^{b/2} \quad (5)$$

It is of interest to test eq 3-5 against experimental data. The only system where extensive data are available is tetraisoamylammonium nitrate in $\text{H}_2\text{O-dioxane}$ at 25° .¹⁶

Figure 4 shows these data¹⁶ displayed as $\log K_T$ vs. $10^4/D$. The solid sigmoid line is the Fuoss-Kraus eq 3 (marked K_{FK}) showing the asymptotic limit to $\log K_T \rightarrow -\infty$ for the value of D corresponding to $b_T = 8/3$. The value of $a_T = 9 \times 10^{-8}$ cm has been retained from the original paper.^{2a} The dashed straight line is the function calculated by least-squares analysis assuming linearity between $\log K_T$ and $1/D$ (eq 4). The intercept however is equal to 0.63 which is larger than the value predicted by eq 4, namely, 0.1155. This last figure is obtained by using $a = 10.7 \times 10^{-8}$ cm. This in turn is the calculated value from the computed slope (dashed line) of $\log K_T$ vs. $1/D$ (Figure 4). In Figure 4, the solid straight line represents the 1959 eq 4 retaining the value of $a = 10.7 \times 10^{-8}$ cm.

It is noteworthy that by using eq 5 with $a = 10.7 \times 10^{-8}$ cm one obtains $K_T^0 = 0.52$ in better accord with the extrapolated value 0.63 from the linear least-squares analy-

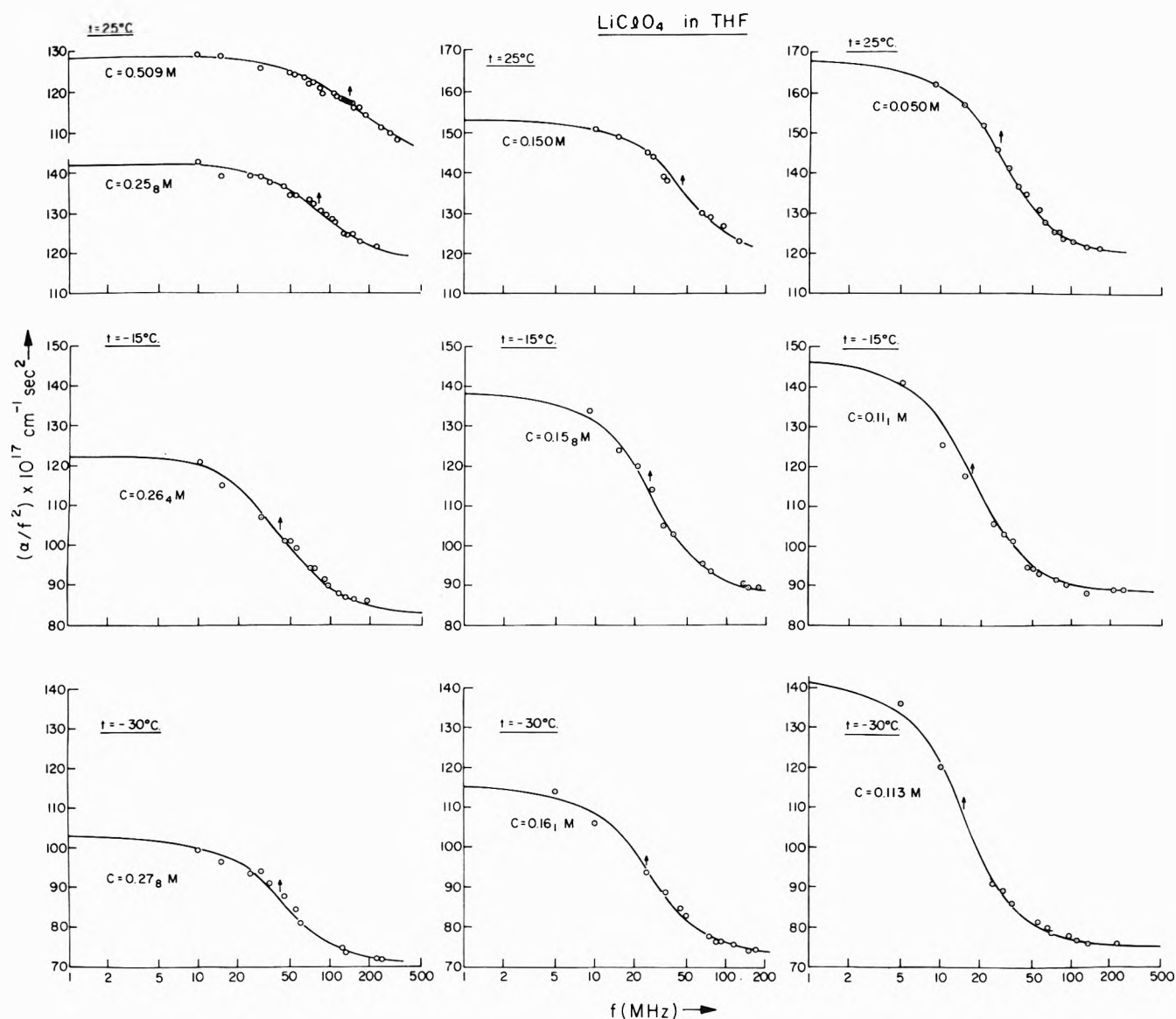


Figure 5. α_0/f^2 vs. the frequency f (MHz) for LiClO₄ in thf at 25, -15, -30°.

sis. In Figure 4 the calculated intercept $K_T^0 = 0.52$ is indicated by an arrow.

It is noteworthy that eq 5 eliminates the need to introduce⁷ further parameters like the ion-solvent energy E_s . This quantity was introduced⁷ in eq 4 in the form of $\exp(-E_s/kT)$ to account for the experimental intercept 0.63. It is significant that E_s resulted as $E_s = 1.7kT$, namely, $e^{1.7}$. This value is close to the factor $e^{1.5}$ which distinguishes eq 5 from eq 4.

Fitting eq 3 to the results of K_T for LiClO₄ in THF (Table I) gives the values for a_T reported in Table I which average to $a_T = (5.2 \pm 0.7) \times 10^{-8}$ cm. Similarly, the fit of eq 5 to the data of LiClO₄ in THF gives as an average $a_T = (4.5 \pm 0.1) \times 10^{-8}$ cm (Table I). Equation 4 gives $a_T = (3.55 \pm 0.07) \times 10^{-8}$ cm.

All these figures are larger than expected on the basis of the axiom^{2a} $a_T = 1.5a \sim 3.0 \times 10^{-9}$ cm.^{16a}

II. Ultrasonic Relaxation. The results of ultrasonic absorption measurements, α (cm⁻¹ neper), for LiClO₄ in THF are reported in Figures 5 and 6. These data are expressed both as α/f^2 vs. the frequency f (MHz) and as $\alpha_{exc}\lambda$ vs. the frequency f . α_{exc} is the excess absorption

TABLE II: Ultrasonic Properties of THF^a

| t , °C | $(\alpha_0/f^2) \times 10^{17}$, cm ⁻¹ sec ² | u , m/sec | Frequency range, MHz |
|----------|--|-------------|-------------------------|
| -50 | 62 ± 1.6 | | 15-145 |
| -30 | 79 ± 1 | 1531 ± 19 | 10-155 |
| -15 | 90.6 ± 2 | 1457 ± 3 | 15-145 |
| 25 | 132 ± 3 | 1269 ± 9 | 15-290 |
| 35 | 140 ± 3 | 1232 ± 15 | 10-230 |
| 45 | 160 ± 4 | 1178 ± 12 | 15-125 |

^a The values of α_0/f^2 are averaged over the frequency range reported. No systematic trend was noticed in this range. α_0 is the sound absorption coefficient (neper cm⁻¹); u the sound velocity (meter/sec).

coefficient, $\alpha_{exc} = \alpha - \alpha_\infty$ where α_∞ is the high-frequency value of α . λ is the wavelength $\lambda = u/f$ with u the sound velocity in solution approximated to the one in the pure solvent at the same temperature. The reason for disregarding the solvent α_0/f^2 values (Table II) is because LiClO₄ causes large depressions of sound absorption at high frequency with respect to the absorption of the solvent, an effect increasing with concentration (Table III).¹⁷

The relaxation parameters were calculated as follows.

TABLE III:^a Ultrasonic Results for LiClO₄ in THF

| <i>t</i> ₁ , °C | <i>c</i> , M | <i>f</i> _R , MHz | <i>B</i> × 10 ¹⁷ , cm ⁻¹ sec ² | μ _{max} 10 ⁵ | <i>k</i> _f × 10 ⁻⁹ , M ⁻¹ sec ⁻¹ | <i>k</i> _r × 10 ⁻⁸ , sec ⁻¹ |
|----------------------------|--------------|-----------------------------|---|----------------------------------|--|--|
| 25 | 0.509 | 144 | 106 | 198 | (1.60 ± 0.10) | (0.81 ± 0.28) |
| | 0.258 | 83 | 118.5 | 124 | | |
| | 0.150 | 46 | 118 | 102 | | |
| | 0.050 | 28.5 | 120 | 86 | | |
| -15 | 0.264 | 42 | 83 | 119 | (1.02 ± 0.08) | |
| | 0.158 | 26 | 88 | 95 | | |
| | 0.111 | 17 | 89 | 70.5 | | |
| | 0.278 | 42 | 71 | 103 | | |
| -30 | 0.161 | 25 | 73 | 78.4 | (0.92 ± 0.13) | |
| | 0.113 | 15 | 76 | 75 | | |
| | | | | | | |

^a The values reported for the *B*'s are reliable to within ±1 × 10⁻¹⁷ cm⁻¹ sec². The values reported for the *f*_r's and μ_{max} are reliable within ±5–10% tending toward the latter figure at the lowest concentration. *f*_R is the relaxation frequency, *B* the background sound absorption, and μ_{max} the maximum excess sound absorption coefficient times the wavelength at *f* = *f*_R.

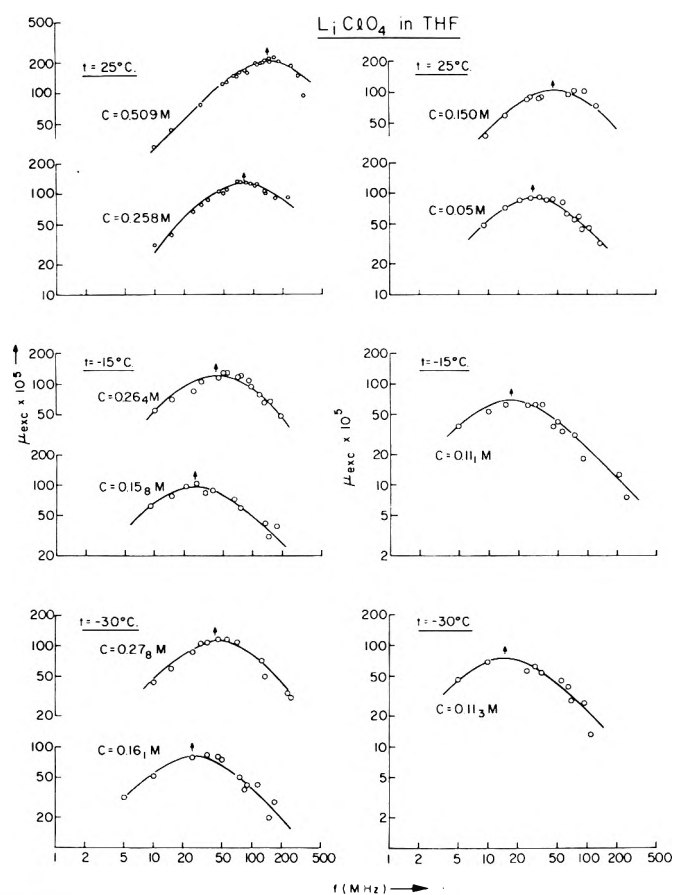


Figure 6. $\mu_{exc} = \alpha_{exc}\lambda$ vs. the frequency *f* (MHz) for LiClO₄ in THF at 25, -15, and -30°.

From the graph α/f^2 vs. *f* (Figure 5) a value of $B = \alpha_{\infty}/f^2$ for each system was estimated. The quantity $\mu = \alpha_{exc}\lambda$ was then calculated at each frequency. For a process following a single relaxation one has

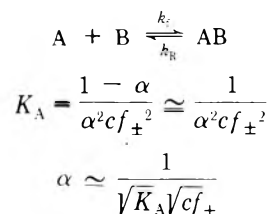
$$\mu = \alpha_{exc}\lambda = 2\mu_{max} \frac{f/f_R}{1 + (f/f_R)^2} \quad (6)$$

with *f*_R the relaxation frequency and μ_{max} the maximum excess sound absorption per wavelength. Plots of μ vs. *f* are shown in Figure 6. A template analysis gave the solid lines according to eq 6. The fit of the parameters μ_{max} and *f*_R was checked by recalculating α/f^2 vs. *f* (solid lines in Figure 5) according to the function

$$\frac{\alpha}{f^2} = \frac{A}{1 + (f/f_R)^2} + B = \frac{2\mu_{max}/\lambda f_R}{1 + (f/f_R)^2} + \frac{\alpha_{\infty}}{f^2} \quad (7)$$

Another check on the estimated parameters was performed by recalculating *B* as the difference $(\alpha/f^2)_{expt} - \{\alpha_{\infty}/[1 + (f/f_R)^2]\}$. The fit was accepted only if the calculated *B* was independent of frequency and if the averaged *B* agreed with the estimated starting value of *B* to within 1 × 10⁻¹⁷ cm² sec⁻¹. The estimated uncertainty in *A* and *f*_R is ±5–10%.

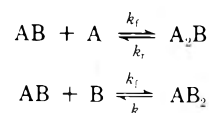
The observed relaxation process was interpreted as follows: the conductance data indicate the presence of two major complex species in the concentration range of this ultrasonic study, namely, ion pairs and triplets. One could advance the hypothesis that the observed relaxation is due to ion pairs in equilibrium with free ions. This hypothesis, however, cannot be sustained for the following reasons. A very high association constant *K*_A, as in the present case, would require approximate linearity¹⁸ between τ⁻¹ and *c*^{1/2} (τ is the relaxation time, τ⁻¹ = 2π*f*_R). This is shown below schematically.



Also

$$\tau^{-1} = k_f(c_A + c_B)f_{\pm}^2 + k_r = 2\alpha k_f c f_{\pm}^2 + k_r \approx \frac{2k_f}{\sqrt{K_A}} f_{\pm} \sqrt{c} + k_r \approx \frac{2k_f}{\sqrt{K_A}} \sqrt{c} + k_r \quad (8)$$

Our experimental data however (Figure 7) show linearity between τ⁻¹ and *c*. This can be explained assuming that the observed relaxation process is due to an ion pair in equilibrium with a triple ion according to one of the two equivalent schemes



In this case¹⁸

$$\tau^{-1} \approx k_f(c_{AB} + c_B) + k_r$$

where

$$c_{AB} \cong (1 - \alpha)c = \left(1 - \frac{1}{\sqrt{K_A} \sqrt{cf_{\pm}}}\right)c$$

$$c_B \cong \alpha c = \frac{\sqrt{c}}{\sqrt{K_A} f_{\pm}}$$

then

$$c_{AB} + c_B \cong c - \frac{\sqrt{c}}{\sqrt{K_A} f_{\pm}} + \frac{\sqrt{c}}{\sqrt{K_A} f_{\pm}} = c$$

and

$$\tau^{-1} \cong k_f c + k_r \quad (9)$$

In the definition of $c_B \cong \alpha c$ one has ignored the single activity coefficient of B . This may be justified in view of the low concentration of free ions. In the above calculation, the small correction to c_{AB} and c_B due to the formation of the triple ions have been neglected in view of the relatively small K_T . Results of k_f and k_r (when measurable), according to relation 9 obtained by linear least-squares analysis, are reported in Table III. The solid lines in Figure 7 are calculated τ^{-1} vs. c functions at 25, -15, and -30°.

A plot of $\log k_f$ vs. $1/T$ is shown in Figure 7A. The apparent Arrhenius activation energy is $E_a = 1.5 \pm 0.2$ kcal/mol. This figure is comparable with the one calculated from the equation given by Metz and Glines³ for the temperature dependence of the viscosity of THF.

$$\log \eta = -3.655 + \frac{393}{T}$$

From which $E_a = 393 \times 2.3 \times R = 1.79$ kcal/mol. The above indicates that the forward process is diffusion controlled. An alternate interpretation should be considered, namely, the hypothesis that the observed process corresponds to the formation of $(\text{LiClO}_4)_2$ quadrupoles. The scheme $2AB = (\text{AB})_2$ leads to an approximate proportionality between τ^{-1} and c . In fact, $\tau^{-1} = 2c_{AB}k_f + k_r$ and $2c_{AB} \cong 2c(1 - \alpha) \cong 2c$. However, that the formation of quadrupoles is not the source of the relaxation phenomenon will be demonstrated in the subsequent discussion of the concentration dependence of μ_{max} .

The conclusion from the above is that the diffusion-controlled formation of triple ions is the source of the ultrasonic relaxation phenomenon. It is then natural to compare the rate constants for the forward process to theoretically calculable rate constants for diffusion-controlled rate processes. The Smoluchowski-Debye¹⁹ theory for rigid spheres gives for the rate constant

$$k_D = \frac{4\pi N}{1000} (D_A + D_{AB})(r_A + r_{AB}) \frac{b}{1 - e^{-b}} M^{-1} \text{sec}^{-1}$$

where $b = |z_A z_{AB}| e^2 / a_T D k T$. In our case $b = 0$ and the above equation reduces itself to the original Smoluchowski¹⁹ equation for rigid uncharged spheres. Introducing²⁰ the Stokes-Einstein relations $D_A = kT/6\pi\eta r_A$ and $D_{AB} = kT/6\pi\eta r_{AB}$ gives

$$k_D = \frac{2NkT}{3000\eta} \left(2 + \frac{r_{AB}}{r_A} + \frac{r_A}{r_{AB}}\right) M^{-1} \text{sec}^{-1} \quad (10)$$

If one takes $r_A = r_{AB}$ it gives $k_D = 8NkT/3000\eta = 1.4 \times 10^{10} M^{-1} \text{sec}^{-1}$, a figure which is an order of magnitude larger than the experimental forward rate constant.

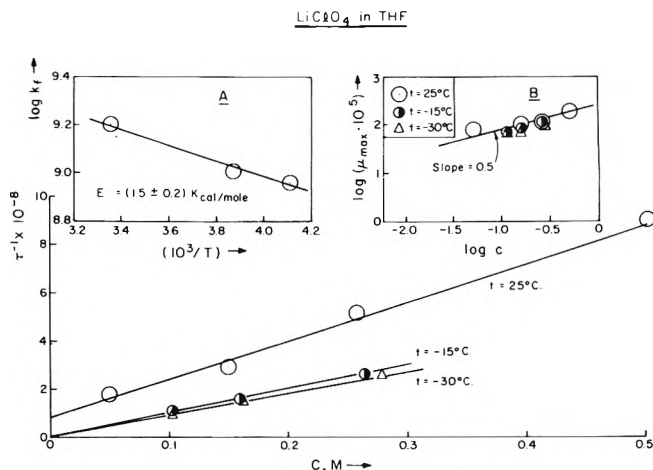


Figure 7. Plot of τ^{-1} vs. c (M) for LiClO_4 in THF: insert A, plot of $\log k_f$ vs. $1/T$; insert B, plot of $\log \mu_{\text{max}}$ vs. $\log c$.

Alternatively, one may calculate the radii of the ions from the Stokes relation $r = 0.82|z|/\lambda^0 \eta 10^{-8}$, obtaining $r_{\text{Li}} = 4.9 \times 10^{-8}$ cm and $r_{\text{ClO}_4} = 1.5 \times 10^{-8}$ cm. Assuming $r_{AB} = a \cong 2 \times 10^{-8}$ cm; as found by conductance measurements and the relation $K_A \propto e^b$, one obtains for $A = \text{Li}^+$, $k_D = 1.74 \times 10^{10} M^{-1} \text{sec}^{-1}$ (eq 10). Similarly, assuming the formation of AB_2 with $B = \text{ClO}_4^-$ one obtains

$$k_D = \frac{2NkT}{3000\eta} \left(2 + \frac{r_{AB}}{r_B} + \frac{r_B}{r_{AB}}\right) = 1.47 \times 10^{10} M^{-1} \text{sec}^{-1}$$

Objections could be raised to using the solvent viscosity in the Smoluchowski equation. To clarify this point the viscosity of solutions of LiClO_4 in THF at $25 \pm 0.02^\circ$ was measured. An Ubbelohde suspended level viscometer was calibrated with conductance water and methanol distilled over Al amalgam. With the calibrated viscometer the viscosity of THF resulted 0.4583 ± 0.0008 cP. Solutions of LiClO_4 in THF of concentrations 0.02997, 0.1009, 0.1713, 0.2523, 0.5044, and 1.0132 M gave viscosities 0.4734 ± 0.0009 , 0.4918 ± 0.0011 , 0.5143 ± 0.0006 , 0.5450 ± 0.0024 , 0.6405 ± 0.0017 , and 0.9625 ± 0.0021 cP, respectively. The viscosity of the solutions in the range 0–0.5 M changes by a factor of only 1.4. This ensures that the viscosity is not the factor responsible for the lower rate constant with respect to the value calculated above according to the Debye-Smoluchowski theory.

The applicability of the Smoluchowski equation was further checked by calculating $D^0(\text{Li})$, $D^0(\text{ClO}_4)$, and $D^0(\text{LiClO}_4)$ from the Nernst relations between diffusion coefficients and limiting conductances. The result for k_D remained in the range $1\text{--}1.5 \times 10^{10} M^{-1} \text{sec}^{-1}$. It seems therefore, that all attempts of calculating k_D lead to values which are one order of magnitude larger than the observed value of $k_f = 1.6 \times 10^9 M^{-1} \text{sec}^{-1}$ at 25° .

An alternate approach²¹ for the calculation of k_f is to use the Eyring theory in which

$$k_f = \frac{kT}{h} \exp\left(-\frac{\Delta G_{el}^*}{kT}\right) \quad (11)$$

ΔG_{el}^* is the free energy of activation which can be calculated from the interaction energy between an ion and a neutral dipole. For a model of a charge ϵ at a distance r from a center of a dipole of charge separation a , Gurney²² reports the following calculation for the interaction energy

$$E_{\text{id}} = \frac{\epsilon\mu/a}{\left(r + \frac{a}{2}\right)D} - \frac{\epsilon\mu/a}{\left(r - \frac{a}{2}\right)D} = -\frac{\epsilon\mu}{\left(r^2 - \frac{a^2}{4}\right)D} = \frac{|z|e\mu}{\left(r^2 - \frac{a^2}{4}\right)D}$$

where μ/a is one of the charges of the dipole, $[r + (a/2)]$ is the distance between the charge ϵ and the furthest point on the dipole that has the same sign as ϵ . Similarly $[r - (a/2)]$ is the distance between the charge ϵ and the opposite charge of the dipole. It is assumed that both charge and dipole are immersed in a continuum of permittivity D .

From conductance data and the relation $K_A \propto e^b$ the center to center distance, a , in the ion pair is $a \approx 2 \times 10^{-8}$ cm. Then $\mu = a|z|e = 9.6 \times 10^{-18}$ esu cm. The distance between the center of the ion and the center of the dipole has been estimated from conductance data to be $r \approx a_T \approx 5 \times 10^{-8}$ cm (eq 3). Assuming that in the ground state the ion and dipole are so far apart that their r^2 interaction energy is negligible, then $\Delta G_{e1}^* \approx E_{\text{id}} = 25.94 \times 10^{-14}$ erg; $(\Delta G_{e1}^*/kT) = 6.31$ and $k_f = 6.2 \times 10^{12} \times 1.82 \times 10^{-3} = 11.3 \times 10^9 M^{-1} \text{sec}^{-1}$ whereas the experimental value for k_f at 25° is $1.6 \times 10^9 M^{-1} \text{sec}^{-1}$. However, the theoretical value is extremely sensitive to the choice of the parameter r . For instance, a change in r to the value $r = 4.5 \times 10^{-8}$ cm (eq 5, Table I) would result in $k_f = 2.4 \times 10^9 M^{-1} \text{sec}^{-1}$ which agrees with the experimental value.

Although agreement between the observed and calculated value of k_f can be obtained, it seems unlikely that the simple rigid sphere-rigid dipole model is satisfactory in describing the system. The fact that the activation energy follows the diffusion-controlled requirement for the energy barrier while the rate constant is slower than expected from the rigid spheres model¹⁹ suggests that there is some preexponential factor in the rate constant expression lowering its value, namely, some entropic factor.

Scrutiny of both models assumed above shows that in both cases *rigid spheres* or *rigid dipoles* were assumed whereas it is entirely possible that some internal degree of freedom is present in the activated state. Accordingly, the following approach may prove applicable.

As mentioned in the section on conductance, we may consider the triple ion to be a linear triatomic molecule with $3n - 3 = 6$ internal degrees of freedom. This molecule will have two rotational degrees of freedom and four vibrational degrees of freedom. In the activated state, one of these four degrees of vibration will be converted into a translational degree of freedom along the reaction coordinate. In the activated state, the triple ion will have three degrees of freedom for translation, two for rotation and three for vibration. In the initial ground state the ion pair will have three degrees of freedom for translation, two for rotation, and one for vibration. The free ion will have three degrees of freedom for translation (assuming it to be a rigid sphere). Then calling f_t , f_R , and f_v the respective partition functions per degree of freedom, the Eyring theory gives

$$k_f = \frac{kT}{h} K^* = \frac{kT}{h} \frac{f_t^3 f_R^2 f_v^3}{f_t^6 f_R^2 f_v} e^{-E^0/RT} = \frac{f_t^3 kT}{f_t^3 h} e^{-E^0/RT} \quad (12)$$

E^0 is the energy barrier at the absolute zero. Assuming the functional form of the rate constant²³ $k_f = AT^m \exp$

$(-E^0/RT)$ with $m \approx 1/2$, we obtain $E^0 = E_a - mRT = 1.5 - 0.3 = 1.2$ kcal/mol or $k_f = (f_v^2/f_t^3) 6 \times 10^{12} e^{-1.2} = (f_v^2/f_t^3) \times 1.81 \times 10^{12} \text{cc molecule}^{-1} \text{sec}^{-1}$. The values of the partition functions in solution are not known any better than to within an order of magnitude. For small molecules and low temperature, $f_t = 10^8$, $f_R = 10^1$, and $f_v = 1,^{24}$ which gives $k_f \approx (1/10^{24}) \times 1.8 \times 10^{12} = 1.8 \times 10^{-12} \text{cc molecule}^{-1} \text{sec}^{-1}$ or $k_f \approx 1.1 \times 10^9 M^{-1} \text{sec}^{-1}$ which is in agreement with the experimental value of $1.6 \times 10^9 M^{-1} \text{sec}^{-1}$.

Although this calculation is approximate and strictly valid only for gases,²⁵ it shows that it is necessary to include internal molecular motions in the activated state. This leads to the proper order of magnitude for the rate constant with retention of the experimental Arrhenius activation energy $E_a = 1.5$ kcal/mol, comparable to the one for viscous flow. Furthermore, even by increasing f_t and f_v by one order of magnitude respectively,²⁴ to $f_t = 10^9$ and $f_v = 10$ we still have $k_f = (10^2/10^{27}) \times 1.8 \times 10^{12} = 1.8 \times 10^{-13} \text{cc molecule}^{-1} \text{sec}^{-1} = 1.1 \times 10^8 M^{-1} \text{sec}^{-1}$ which is lower than the experimental value not higher as predicted by the Smoluchowski rigid sphere theory.

Finally, we want to consider the concentration dependence of μ_{max} as further evidence of the triple ion formation interpretation of our results.

According to Eigen,¹⁸ the excess sound absorption per wave length for a process like $AB + B \rightarrow AB_2$ is given by

$$\mu = \frac{\pi (\Delta V_s)^2}{\beta_s} \frac{d\theta}{RT} \frac{d \ln K_T}{1 + \omega^2 \tau^2}$$

with

$$\frac{d\theta}{d \ln K_T} = \left[\frac{1}{[AB]} + \frac{1}{[B]} + \frac{1}{[AB_2]} + \frac{d \ln \gamma_{AB}}{dc_{AB}} + \frac{d \ln \gamma_B}{dc_B} + \frac{d \ln \gamma_{AB_2}}{dc_{AB_2}} \right]^{-1} \quad (13)$$

in the above β_s is the adiabatic compressibility, ΔV_s is the adiabatic volume change due to the process, θ is the reaction displacement of the concentration, K_T is the equilibrium constant, $\omega = 2\pi f$, and the γ 's are the activity coefficients contributions. Ignoring the latter

$$\mu_{\text{max}} = \frac{\pi (\Delta V_s)^2}{2\beta_s} \frac{1}{RT} \left[\frac{1}{[AB]} + \frac{1}{[B]} + \frac{1}{[AB_2]} \right]^{-1}$$

since $K_T = (AB_2)/(AB)(B)$

$$\mu_{\text{max}} = \frac{\pi (\Delta V_s)^2}{2\beta_s} \frac{K_T [AB][B]}{1 + K_T [B] + K_T (AB)} \approx \frac{\pi (\Delta V_s)^2}{2\beta_s} \frac{1}{RT} [B]$$

given $[AB] \gg [B]$ and $K_T [AB] \gg 1$. On the other hand, ignoring activity coefficients, one may write $K_A = [AB]/[A][B]$ and $[B] = [AB]^{1/2}/\sqrt{K_A} \approx c^{1/2}/\sqrt{K_A}$. Since $[A] = [B]$ given $K_{T1} = K_{T2}$. Then

$$\mu_{\text{max}} \approx \frac{\pi (\Delta V_s)^2}{2\beta_s} \frac{c^{1/2}}{RT \sqrt{K_A}} \quad (14)$$

In a plot of $\log \mu_{\text{max}}$ vs. $\log c$ should be linear with slope = 1/2.

In Figure 7 (insert B) this plot is shown by the solid arbitrary line having slope = 0.5. Least-squares analysis of our data at 25, -15, and -30° give respective slope 0.34, 0.60, and 0.36 or an average of 0.43 ± 0.14 which is in fair agreement with the predicted value.

In the alternative case of quadrupole formation we have¹⁸

$$2(AB) = (AB)_2$$

$$\mu_{\max} \cong \frac{\pi (\Delta V_s)^2}{2\beta_s RT} \left[\frac{2}{[AB]} + \frac{1}{[AB]_2} \right]^{-1}$$

defining $K_q = [AB]_2/[AB]^2$

$$\left[\frac{2}{[AB]} + \frac{1}{[AB]_2} \right]^{-1} = \left[\frac{2}{[AB]} + \frac{1}{K_q[AB]^2} \right]^{-1} = \frac{K_q[AB]^2}{2K_q[AB] + 1} \cong \frac{[AB]}{2}$$

if $2K_q[AB] > 1$. Then

$$\mu_{\max} \cong \frac{\pi (\Delta V_s)^2}{4\beta_s RT} [AB] \cong \frac{\pi (\Delta V_s)^2}{4\beta_s RT} c \quad (15)$$

A plot of $\log \mu_{\max}$ vs. $\log c$ should be approximately linear with slope equal to one instead of 0.5 as for the triple ion process. If the converse condition $2K_q[AB] < 1$ were to hold, then the expression for μ_{\max} would be proportional to $[AB]^2$, namely, to c^2

$$\mu_{\max} = \frac{\pi (\Delta V_s)^2}{2\beta_s RT} K_q c^2 \quad (16)$$

and a plot of $\log \mu_{\max}$ vs. $\log c$ should be approximately linear with slope equal to two instead of 0.5 as for the triple ion process.

References and Notes

- (1) This work is part of the thesis of P. Jagodzinski of partial fulfillment of the requirements for the Degree of Bachelor of Sciences, Polytechnic Institute of Brooklyn, 1973.
- (2) (a) R. M. Fuoss and C. A. Kraus, *J. Amer. Chem. Soc.*, **55**, 2387 (1933), and quoted literature; (b) M. Davies and G. Johnson, *Acta Chem. Scand.*, **18**, 1171 (1964), and literature quoted therein.
- (3) D. J. Metz and A. Glines, *J. Phys. Chem.*, **71**, 1158 (1967); E. Kuss, *Z. Angew. Phys.*, **7**, 376 (1955).
- (4) C. Carvajal, K. J. Tolle, J. Smid, and M. Szwarc, *J. Amer. Chem. Soc.*, **87**, 5548 (1965).
- (5) A. Fanelli and S. Petrucci, *J. Phys. Chem.*, **75**, 2649 (1971).
- (6) G. S. Darbari, M. R. Richelson, and S. Petrucci, *J. Chem. Phys.*, **53**, 859 (1970).
- (7) R. M. Fuoss and F. Accascina "Electrolytic Conductance," Interscience, New York, N. Y., 1959, Chapter XVIII.
- (8) It should be noted that if traces of water were present in the solvent at concentrations comparable to the electrolyte, the increase of permittivity D should cause a decrease in the concentration of triple ions. This in turn should cause a decrease in slope (Figure 1A) toward -0.5, not a deviation from this value as observed.
- (9) (a) R. M. Fuoss and C. A. Kraus, *J. Amer. Chem. Soc.*, **55**, 476 (1933); R. M. Fuoss, *ibid.*, **57**, 488 (1935); (b) D. N. Bhattacharyya, C. L. Lee, J. Smid, and M. Szwarc, *J. Phys. Chem.*, **69**, 608 (1965).
- (10) J. C. Justice and C. Freiner, *C. R. Acad. Sci.*, **269**, 1364 (1969).
- (11) C. Micheletti, Thesis, University of Paris, 1972.
- (12) R. M. Fuoss, *Chem. Rev.*, **17**, 27 (1935).
- (13) With the values reported in Table I for K_A and K_T one may calculate at $c = 0.1$ the ionic strength $I = \alpha c + \alpha_3 c = (\sqrt{c}/\sqrt{K_A}) + (K_T/\sqrt{K_A} c^{3/2}) = 7.4 \times 10^{-4} M$. This is still a rather reasonable value of the ionic strength I to apply the theory for triple ion formation expressed in the form of eq. 1.
- (14) (a) R. M. Fuoss, *J. Amer. Chem. Soc.*, **80**, 5059 (1958); (b) C. DeRossi, B. Sesta, M. Battistini, and S. Petrucci, *J. Amer. Chem. Soc.*, **94**, 2961 (1972); M. J. Pikal, *J. Phys. Chem.*, **75**, 663 (1971).
- (15) W. F. Edgell, J. Lyford, V. A. Barbetta, and C. I. Jose, *J. Amer. Chem. Soc.*, **93**, 6403 (1971), and previous literature quoted therein; M. J. Fenich and J. L. Wood, *J. Chem. Phys.*, **49**, 2358 (1968); J. C. Evans and G. Y-S. Lu, *J. Phys. Chem.*, **69**, 3223 (1965).
- (16) R. M. Fuoss, *J. Amer. Chem. Soc.*, **55**, 21 (1933).
- (17) (a) Note Added in Proof: However one must recognize that the value $a \cong 2 \times 10^{-8}$ cm has been obtained by the Denison-Ramsay proportionality (J. J. Denison and J. B. Ramsay, *J. Amer. Chem. Soc.*, **77**, 2615 (1955)), $K_A \propto e^b$, not considering the preexponential factor in eq. 2. By including the internal degrees of freedom of the ion pair, namely, two degrees of rotation and one of vibrational freedom, one may calculate the change in internal energy upon pairing

$$\Delta V = \left[\frac{5}{2} RT + RT - (3n - 5)RT \right] - 2 \left[\frac{5}{2} RT \right] = \frac{7}{2} RT - \frac{6}{2} RT = \frac{1}{2} RT$$

Then the corrected eq 2 should read

$$K_A = K_0 e^{-1/2} e^b = \frac{4\pi N a^3}{3000} e^{-1/2} e^b$$

Applying this expression to the data of K_A for LiClO₄ in THF (Table I), one obtains at $t = 25^\circ$, $a = 3.74 \times 10^{-8}$ cm; at $t = -15^\circ$, $a = 3.87 \times 10^{-8}$ cm; and at $t = -30^\circ$, $a = 3.95 \times 10^{-8}$ cm. The average is $a = 3.85 \times 10^{-8}$ cm. This figure, in turn, would predict $a_T = 1.5$, $a = 5.8 \times 10^{-9}$ cm. The numerical values of both a and a_T depend therefore on the theory used. This leads to the conclusion that the only significance of these figures is to be of the expected order of magnitude when compared to molecular models.

- (17) This effect may be due to ionic solvation. Solvent molecules coordinated around ions do not participate in the structural rearrangement of the solvent due to the passage of the sound wave. This is reflected in a decrease of the bulk viscosity η_v in the relation

$$\frac{\alpha_0}{f^2} = \frac{2\pi^2}{\omega^3} \left(\eta_v + \frac{4}{3} \eta \right)$$

with η the shear viscosity.

- (18) (a) M. Eigen and L. DeMaeyer in "Investigation of Rates and Mechanism of Reaction," Vol. 8, A. Weissberger, Ed., Wiley, New York, N. Y., 1963, Part II; (b) S. Petrucci in "Ion Interactions," Vol. II, Academic Press, New York, N. Y., 1971, Chapter II.
- (19) M. Von Smoluchowski, *Phys. Z.*, **17**, 557 (1916); P. Debye, *Trans. Electrochem. Soc.*, **82**, 265 (1942).
- (20) S. Petrucci, *J. Phys. Chem.*, **71**, 1174 (1967).
- (21) A. A. Frost and R. G. Pearson, "Kinetics and Mechanism," 2nd ed, Wiley, New York, N. Y., 1951, p 149.
- (22) R. W. Gurney, "Ionic Processes in Solutions," Dover Publications, New York, N. Y., 1953, p 264.
- (23) Reference 21, p 100 and Table 2, p 94.
- (24) Reference 21, Table 1, p 87.
- (25) Similar calculations for the ΔS of association of ions media of low D have been carried with success by Bruckenstein and Pettit.²⁶
- (26) L. D. Pettit and S. Bruckenstein, *J. Amer. Chem. Soc.*, **88**, 4783 (1966).

Theory of Ion-Complexing Effects in Ion-Exchange Column Performance¹

Frederick M. Golden, Klara I. Shiloh, Gerhard Klein, and Theodore Vermeulen*

Department of Chemical Engineering and Sea Water Conversion Laboratory, University of California, Berkeley, California 94720
(Received August 1, 1973)

Publication costs assisted by the National Science Foundation

A local-equilibrium analysis of ion-exchange behavior is carried out for a model three-cation system in which selectivity reversals occur through complex formation by two of the cations. The allowable differential composition paths, shown on a concentration grid, are used to determine the plateaus and the transitions (frequently composite) for given compositions of feed and presaturant. The relative directions of change of species concentration in the transitions are found to be interrelated by the partial derivatives of concentration, rather than by the selectivities as such. Some composition-profile routes occur for which the presence of selectivity reversal causes a ternary system to undergo three discrete transitions (rather than two) between the feed and the presaturant plateaus. Numerical trial, coupled with algebraic criteria, is required to determine which type of route is followed.

Introduction

Complexing between counterions and coions in ion-exchange systems is often useful in achieving desired separations. As an example, the use of complexing is the basis for practical separations of rare earths by ion exchange. In process applications it is desirable that selectivity of complexing enhance the selectivity of ion exchange. In fact, complexing will frequently enhance some selectivities and diminish others.

The purpose of this study has been to evaluate the behavior of complexing systems, both generally and illustratively, for predicting the concentration history of the column effluent and the composition profile in the column under local-equilibrium conditions. The boundary conditions assumed are that a constant-composition solution (the "feed") is supplied to a column, and that this column has a uniform initial composition (in equilibrium with a uniform "presaturant"). The conceptual system examined here includes a large measure of selectivity reversal; solutions of cases where less selectivity reversal occurs can be inferred quite readily from this rather complicated system. (Selectivity depends on overall behavior of counterion species; see eq 30-32.)

Local-equilibrium theory, used for this analysis, is based on the assumptions that the resin and the aqueous solution are in perfect equilibrium at each point in the column and that axial dispersion does not occur.^{2,3} While this theory does not provide the entire basis for column design, it does provide necessary information on which to base a treatment that takes column dynamics into account. Local-equilibrium analysis yields column profiles which comprise a series of transitions, or "waves" of changing composition, whose constituent compositions move through the column at well-defined velocities that are controlled by the specific coexisting resin and solution concentrations.⁴⁻⁶ The transitions are separated by plateaus, *i.e.*, regions of constant composition. Each transition may be *abrupt* (a step change of composition), *gradual* (a continuous sequence of equilibrium states), or *composite* (partly abrupt and partly gradual). Although these principles are now widely accepted, the need remains to

illustrate their application to representatively difficult examples such as the ones reported on here.

Finding the effluent-concentration history, or the composition profile in a column, involves constructing a composition-path diagram which shows the evolution of the coexisting concentrations of different component ions along each possible composition path. For ternary systems these possible paths fall into two families. Each family of paths comprises curves in the composition diagram that do not intersect other curves in the same family; thus each point in the diagram lies on two paths, one in each family.

In the idealized system adopted here to develop and demonstrate the theory, there are three exchangeable ions, M, N, and O, assumed to be cations. M and N each form a *neutral* complex with the single coion X. All the ions have the same charge number (*e.g.*, 1). For illustrative purposes, the exchange equilibrium constants and the complex stability constants have been chosen to provide the maximum number of selectivity reversals for this type of system, which is three. The premise is adopted that the uncomplexed anion X and the neutral complexes are excluded from the resin. The behavior of anionic (rather than neutral) complexes will also resemble qualitatively the model developed here.

Mathematical Foundations

Equilibria and Material Balances. The governing equations will now be stated, and put into a form suitable for computing the composition-path diagram. (A table of notation is appended, for convenient reference.) It is convenient to introduce two nondimensional concentrations. First, for the stationary phase

$$y_i = q_i/Q \quad (1)$$

Here q_i is the concentration of a species i in the resin in units of g -moles of i per gram of resin, and Q is the resin capacity ($= \sum q_i$). Also, for the mobile phase

$$x_i = c_i/\tilde{c}_X \quad (2)$$

with c_i the concentration of i in the aqueous phase in g -moles of i per liter of solution, and \tilde{c}_X the constant total

coion concentration both as complexes MX and NX and as free ion X

$$\tilde{c}_X = c_X + c_{MX} + c_{NX} \quad (3)$$

The *composition velocity* (a dimensionless combination of independent variables) relates the V and v values at which a particular composition is encountered

$$u = \frac{Q\rho v}{c_X(V - v\epsilon)} \quad (4)$$

Here V is the volume of feed which has entered the column in liters; v is the volume of column, measured from the inlet end, at which the composition occurs; ϵ is the fraction of column volume not occupied by resin; and ρ is the grams of resin per liter of column as packed. Both ϵ and ρ are treated as constants. Composition velocity also serves as a dimensionless column volume, and is a convenient variable against which to display equilibrium profiles inside the column. The reciprocal of u , called the throughput parameter T , is a dimensionless effluent volume against which effluent concentration histories can be displayed.

The chemical species present in the system are the ions M^{m+} , N^{m+} , O^{m+} , and X^{m-} , and neutral complexes MX and NX. The total concentrations of M and of N in the complexed plus uncomplexed form, in the mobile phase, are

$$\tilde{x}_M = x_{MX} + x_M \quad (5)$$

$$\tilde{x}_N = x_{NX} + x_N \quad (6)$$

Because the atoms of M are present in two molecular forms MX and M^{m+} in the mobile phase, these forms will usually be measured together, and must both be considered in any material balance. The totality of MX and M^{m+} comprise a *conserved species*. If, in the mobile phase, M^{m+} forms MX or is formed from MX without any interphase transfer of M^{m+} (the only transferable species), no change occurs in the concentration \tilde{x}_M of conserved species M. (The tilde mark used to identify a conserved species is omitted when a single normal species, e.g., O, is conserved.)

From these considerations, it follows that the continuity equation for ion exchange without complexing, given originally by DeVault,² is also valid for each of the conserved species M, N, and O. Along the path of any gradual transition, the composition velocity is a local function of the coexisting equilibrium concentrations

$$\frac{d\tilde{x}_M}{dy_M} = \frac{d\tilde{x}_N}{dy_N} = \frac{dx_O}{dy_O} = u \quad (7)$$

For the stated boundary conditions, the composition identified by each set of values of \tilde{x}_M , y_M , \tilde{x}_N , and y_N encountered in the transition remains intact as it advances through the column, and is said to be *coherent*.

Similarly, for abrupt (step) transitions, the characteristic velocity of the step is

$$\frac{\Delta\tilde{x}_M}{\Delta y_M} = \frac{\Delta\tilde{x}_N}{\Delta y_N} = \frac{\Delta x_O}{\Delta y_O} = u_\Delta \quad (8)$$

The ion-exchange equilibria are given by the separation factors, considered to be constant

$$\alpha_{MO} = \frac{y_M x_O}{y_M x_O} \text{ and } \alpha_{NO} = \frac{y_N x_O}{x_N y_O} \quad (9)$$

(It is evident that $\alpha_{ji} = 1/\alpha_{ij}$.) The complexing equilibria

are given by the dimensionless stability factors K_{iX} (assumed to be constant for each given \tilde{c}_X , as through the relation $K_{iX}\tilde{c}_X = \text{constant}$)

$$K_{MX} = \frac{x_{MX}}{x_M x_X} \text{ and } K_{NX} = \frac{x_{NX}}{x_N x_X} \quad (10)$$

Thus, in this treatment, both the separation factors and the stability factors are presumed to be independent of mole-fraction composition.

Selectivity is defined through a selectivity ratio $\tilde{\alpha}_{ij}$, analogous to α_{ij} but based on the total solution concentration of each conserved species (see eq 30-32). The selectivity ratio cannot remain constant when complexing occurs; this fact is especially evident for the case where α_{ij} , K_{iX} , and K_{jX} are all constant. A selectivity reversal occurs for species i and j when $\tilde{\alpha}_{ij} = 1$; i.e., when α shifts from values below unity

For a numerical illustration that will show three selectivity reversals, the following values of the parameters were chosen

$$\alpha_{MO} = 300; \alpha_{NO} = 10; K_{MX} = 800; K_{NX} = 20 \quad (11)$$

With these parameters, in the absence of complexing, the selectivity sequence would be MNO in decreasing order of affinity. Through the stored choice of constants, M is the species that forms the more stable complex. The MNO selectivity sequence applies when M is the principal cation, it being then only partly complexed, because but little X remains. As M diminishes, it becomes more completely complexed by X; this favors resin uptake of N and shifts the sequence to NMO. Diminution of both M and N reduces further the uptake of M (to give sequence NOM), and finally also reduces the uptake of N (to yield ONM).

Composition Paths and Composition Velocities. The general procedure for finding composition paths for gradual transitions involves the solution of an ordinary differential equation, obtained as follows. We consider \tilde{x}_M and \tilde{x}_N to be functions of y_M and y_N

$$\tilde{x}_M = f_M(y_M, y_N) \text{ and } \tilde{x}_N = f_N(y_M, y_N) \quad (12)$$

Now the total derivative of each \tilde{x} is taken; the component partial derivatives identified by symbols A, B, C, and D are each functions of composition

$$\frac{d\tilde{x}_M}{dy_M} = \frac{\partial f_M}{\partial y_M} + \frac{\partial f_M}{\partial y_N} \frac{dy_N}{dy_M} = A + B \frac{dy_N}{dy_M} \quad (13)$$

and

$$\frac{d\tilde{x}_N}{dy_N} = \frac{\partial f_N}{\partial y_M} \frac{dy_M}{dy_N} + \frac{\partial f_N}{\partial y_N} = C \frac{dy_M}{dy_N} + D \quad (14)$$

Equation 7 justifies equating these two total derivatives. The resulting relation is solved for dy_N/dy_M , to obtain two roots giving the directions of the two composition paths through a point specified by any two of y_M , y_N , \tilde{x}_M , and \tilde{x}_N .

$$\frac{dy_N}{dy_M} = \frac{d\tilde{x}_N}{d\tilde{x}_M} = \frac{D - A \pm \sqrt{(D - A)^2 + 4BC}}{2B} = \frac{2C}{A - D \pm \sqrt{(D - A)^2 + 4BC}} \quad (15)$$

(When either B or C is zero, the form that becomes indeterminate is avoided.)

The composition velocities may also be found, by combining eq 7, 13, and 15

$$u = A + B \left(\frac{dy_N}{dy_M} \right) = \frac{D + A + \sqrt{(D - A)^2 + 4BC}}{2} \quad (16)$$

The path corresponding to the plus signs, having the higher local velocity, is called the fast path. Likewise the path corresponding to the minus signs is called the slow path.

Special Conditions along Borders and at Watershed Points. Watershed points are compositions for which there is no distinction between the two composition-velocity roots; that is, where the square-root term just given becomes zero

$$(D - A)^2 + 4BC = 0 \quad (17)$$

Watersheds are junctions between a fast path and a slow path having the same direction dy_N/dy_M . For complexing systems defined by constant separation factors and constant complex-stability constants, the algebraic criteria indicate that such junctions occur along the borders of the composition diagram (where the ternary system has become a binary), not inside these borders. For all complexing systems of the present type, on the $y_M = 0$ border, $B = 0$; and on the $y_N = 0$ border, $C = 0$. Along each of these two borders, if a watershed point occurs, $A = D$. For the $y_O = 0$ border, the slope dy_N/dy_M of the composition path is -1 , and eq 15 yields $A - B + C - D = 0$; combining this condition with eq 17 yields the watershed criterion $B = -C$. The present system has two watersheds in the $y_N = 0$ border, one on the $y_M = 0$ border, and none on $y_O = 0$.

From eq 15 the slopes of the paths intersecting the $y_M = 0$ border, at the intersections, are

$$dy_N/dy_M = C/(A - D) \quad (18)$$

and the slopes of the paths intersecting the $y_N = 0$ border, at the intersections, are

$$dy_N/dy_M = (D - A)/B \quad (19)$$

The corresponding slopes for paths intersecting $y_O = 0$ are found to be C/B . Uses of these relations will be indicated in subsequent calculations.

Solution of Governing Equations. By using equilibrium and electroneutrality conditions and the conservation of coions, explicit solutions are found for the mobile-phase concentrations in terms of the stationary-phase concentrations

$$\tilde{x}_M = \frac{x_M}{x_X} (K_{MX} x_X^2 + x_X) \quad (20)$$

$$\tilde{x}_N = \frac{x_N}{x_X} (\bar{K}_{NX} x_X^2 + x_X) \quad (21)$$

where

$$\frac{x_M}{x_X} = \frac{\alpha_{OM} y_M}{(\alpha_{OM} - 1)y_M + (\alpha_{ON} - 1)y_N + 1} \quad (22)$$

$$\frac{x_N}{x_X} = \frac{\alpha_{ON} y_N}{(\alpha_{OM} - 1)y_M + (\alpha_{ON} - 1)y_N + 1} \quad (23)$$

$$x_X = \frac{\sqrt{1 + 4a} - 1}{2a} \quad (24)$$

and

$$a = K_{MX} \left(\frac{x_M}{x_X} \right) + K_{NX} \left(\frac{x_N}{x_X} \right) \quad (25)$$

An equation for x_O is needed in discussions of selectivity reversal

$$\frac{x_O}{x_X} = \frac{y_O}{(\alpha_{OM} - 1)y_M + (\alpha_{ON} - 1)y_N + 1} \quad (26)$$

The derivatives A , B , C , and D used in eq 13-16 can now be evaluated. The equations are not difficult to derive, and are omitted for the sake of brevity.

Detailed Analysis

Contours of Mobile-Phase Compositions. A complete description of the system is developed here and in the ensuing parts of this section from the foregoing relations and from constants of eq 11.

First, contours of mobile-phase concentrations (\tilde{x}_M , \tilde{x}_N , and x_X) are calculated in terms of y_M and y_N , and are plotted on triangular coordinates in Figures 1-3.

In Figure 1, the total concentration of M in solution is shown in the form of contours of constant \tilde{x}_M as a function of the resin-phase composition. They very roughly follow the contours of constant y_M , but have noticeable curvature. The locus of maximum y_M on these \tilde{x}_M contours is defined by the $B (= \partial \tilde{x}_M / \partial y_N) = 0$ curve which crosses the diagram somewhat parallel to the $y_O = 0$ border. Similar considerations apply to Figure 2, which gives contours of total N for the mobile solution phase. The contours of \tilde{x}_N , established by interpolation of calculated points, are roughly parallel to lines of constant y_N . The locus $C (= \partial \tilde{x}_N / \partial y_M) = 0$ matches the maximum y_N values on the \tilde{x}_N contours.

Contours of constant x_X , or nondimensional concentration of free coion, are shown in Figure 3. These contours are straight lines satisfying the relation

$$(\alpha_{OM} - 1 - K_{MX} \alpha_{OM} a) y_M + (\alpha_{ON} - 1 - K_{NX} \alpha_{ON} a) y_N + 1 = 0 \quad (27)$$

Substituting the constants of eq 11, one obtains

$$(299 + 800a) y_M + (270 + 600a) y_N + 1 = 0 \quad (28)$$

Here a , defined by eq 24, is given explicitly as

$$a = (1 - x_X) / x_X^2 \quad (29)$$

Thus the slope and intercepts of this family of contours depend only on x_X . (Equation 27 is obtained by eliminating mobile-phase concentrations from eq 25 by using eq 22 and 23, and simplifying.)

Also shown on Figure 3 are loci which occur along (or near) lines of constant x_X . Three of these are selectivity reversals, shown as dashed lines extending beyond the borders, and are discussed in the next section. The remaining three loci, determined by iterative calculations, locate the y extrema of \tilde{x}_M , \tilde{x}_N , and x_O contours. It was found (but to date, only numerically) that x_X is constant on the latter loci. On $B = 0$, $x_X = 0.230$; on $C = 0$, $x_X = 0.280$; and on $A - B + C - D = 0$, $x_X = 0.381$. It can be shown that, if x_X is held constant, these three loci all become straight lines on (y_M, y_N) coordinates, but these lines have not yet been proved to match eq 27 and 28.

Selectivity Reversals. The separation factors in terms of total solution concentrations have been made to vary with composition, by the occurrence of complexing. With the use of eq 22, 23, and 26, these separation factors may be

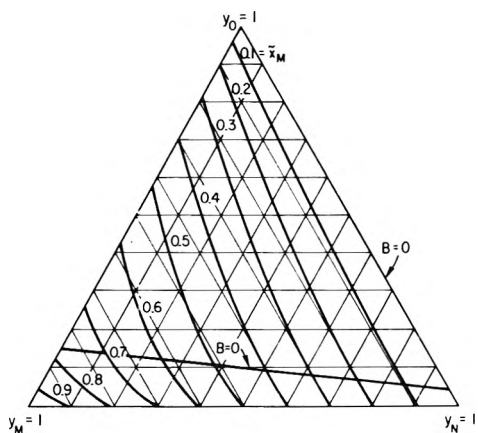


Figure 1. Equilibrium total solution concentration of M in relation to solid-phase composition.

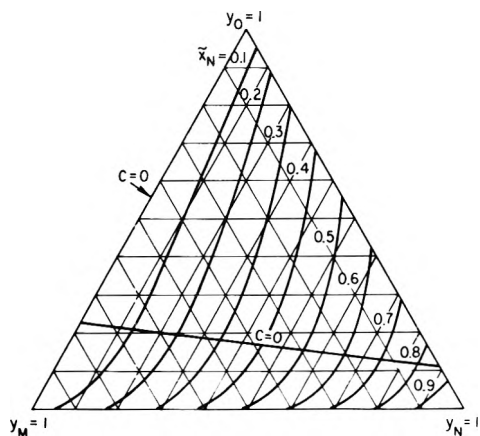


Figure 2. Equilibrium total solution concentration of N in relation to solid-phase composition.

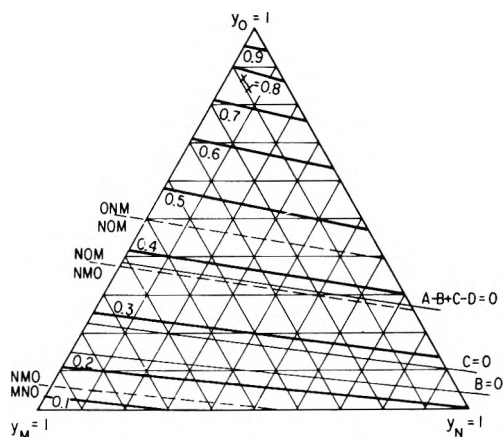


Figure 3. Equilibrium solution concentration of X (free coin) in relation to solid-phase composition.

expressed in terms of x_X

$$\tilde{\alpha}_{NM} = \frac{y_N \tilde{x}_M}{y_M \tilde{x}_N} = \alpha_{NM} \frac{K_{MX} x_X + 1}{K_{NX} x_X + 1} \quad (30)$$

$$\tilde{\alpha}_{OM} = \frac{y_O \tilde{x}_M}{y_M \tilde{x}_O} = \alpha_{OM} (K_{MX} x_X + 1) \quad (31)$$

$$\tilde{\alpha}_{ON} = \frac{y_O \tilde{x}_N}{y_N \tilde{x}_O} = \alpha_{ON} (K_{NX} x_X + 1) \quad (32)$$

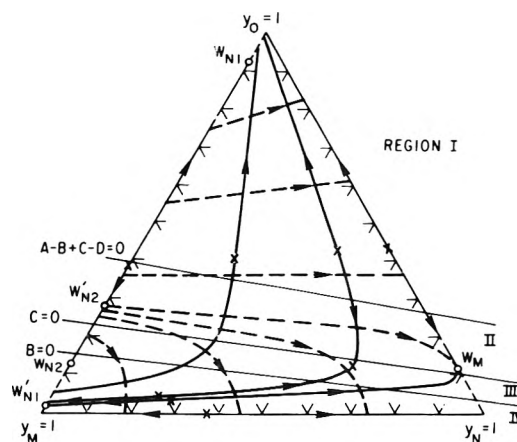


Figure 4. Composition paths in relation to solid-phase composition. Slow paths are solid lines, fast paths dashed. Regions have different combinations of composition-change increase or decrease for different counterions. Arrows show direction of downstream change in composition for gradual transitions.

Selectivity reversals occur where these separation factors are equal to unity, as has already been discussed. When $x_X = 0.145$, $\tilde{\alpha}_{NM} = 1$. This x_X contour is the locus on which the order of selectivity changes from MNO to NMO (components are listed in decreasing order of affinity for the resin). At $x_X = 0.3738$, $\tilde{\alpha}_{OM} = 1$, and the order of selectivity changes from MNO to NOM. At $x_X = 0.4500$, $\tilde{\alpha}_{ON} = 1$, and the order of selectivity changes from NOM to ONM. Thus, as the composition changes from pure M to pure O, the order of selectivity changes from one determined primarily by uncomplexed ions at low x_X to one determined by complexing at high x_X .

The order of selectivity is important in making a qualitative evaluation of the ability of the column to perform a given separation. Nevertheless, reversals are found here to have only an indirect effect on the mathematical description of the system, and they will be of no further import in this study. Instead, the profile behavior depends substantially on the extremum loci, as will be shown below.

Composition-Path Diagram. To obtain the composition paths, eq 15 has been integrated by stepwise calculation using a digital computer.⁹ Two families of composition paths result, shown in Figure 4. The family shown as dashed lines are fast paths corresponding to the plus sign in eq 15, while the family shown as solid lines are slow paths corresponding to the minus sign. Each family includes paths on the border of the diagram.

Watershed points, to be discussed below, appear on the borders as points of demarcation between families. The paths through watersheds W_{N1} and W_{N2} on the border $y_N = 0$ do not enter the three-component region of the diagram. However, the two composition paths through watershed W_M on the border $y_M = 0$ do penetrate the diagram. The intersections of these paths with the $y_N = 0$ border, W_{N1}' and W_{N2}' , are not watershed points.

All the fast paths emanate between watersheds W_{N1} and W_{N2} on the border $y_N = 0$. These paths intersect the other two borders at all points except between W_M and N. (M, N, and C are the vertices where the respective y 's become unity.) All the slow paths emanate from the border segment between W_{N2} and M. Some of these paths intersect the same border between W_{N1} and O, and the remainder, which emanate between W_{N1}' and M, intersect the $y_M = 0$ border between W_M and N.

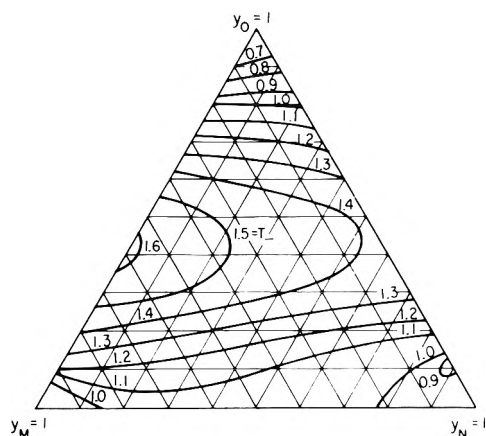


Figure 5. Throughput-parameter values along slow paths, in relation to solid-phase composition.

Figure 4 includes arrows indicating directions in which composition velocities increase. On the fast paths (dashed lines), the composition velocities increase in the direction away from the $y_N = 0$ border, and there are no extrema of u . On the slow paths, extrema occur where the composition paths are tangent to the T contours of Figure 5 (explained below). These extrema, indicated by small crosses, were found by trial computation of T on the paths. On the paths which intersect between W_M and N , a single maximum occurs. On the paths which intersect near O , there are three extrema (a maximum, a minimum, and a second maximum). For those which intersect near W_{N1} , the extrema nearer M have disappeared together, and only a maximum remains.

Also shown on this diagram are the loci $A - B + C - D = 0$, $C = 0$, and $B = 0$. Consistent with eq 15, where fast paths cross the locus $A - B + C - D = 0$, they become parallel to the $y_O = 0$ border. Where fast paths cross the locus $B = 0$, they become parallel to the $y_M = 0$ border. Where slow paths cross the locus $C = 0$, they become parallel to the $y_N = 0$ border.

A correlation based on these loci may be established for the relative directions of changes of concentrations along the differential composition paths. Although similar to the affinity cut rule⁵ developed for constant-separation-factor systems without complexing, the "direction cut" correlation is divorced from the order of selectivity in the system except at its limits. The loci divide the composition-path diagram into four regions, numbered I, II, III, and IV. Within each region, all species on one side of the vertical line in Table I change their concentrations in one direction, and species on the other side change in the opposite direction. In region II, for example, the composition-path diagram shows that along slow paths the M and N concentrations change in the same direction, while the O concentration changes oppositely. Along fast paths, M and O change in one direction, while N changes oppositely.

The sequence in Table I is the unique ordering that will produce a "direction cut" between the first and second species for slow paths and between the second and third species for fast paths. Whereas for a constant α system the concentration paths would always be gradual when the first-named species increased, the paths indicated by the sequences given in Table I are sometimes gradual and sometimes abrupt.

Watershed Points and Composition-Velocity Contours.

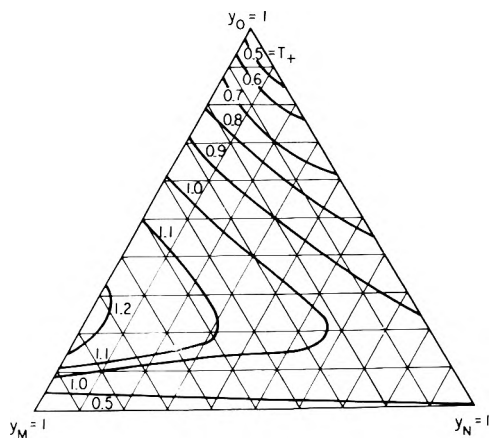


Figure 6. Throughput-parameter values along fast paths, in relation to solid-phase composition.

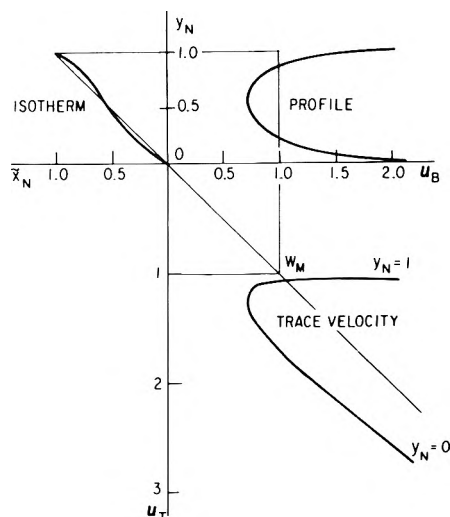


Figure 7. Fictitious concentration profile and behavior of trace amounts of M along the ON border.

Equation 16 gives two composition velocities for every composition (with the exception of watershed points, at which the two composition velocities become equal). The minus sign gives the smaller composition velocity, corresponding to a composition on a slow path. Contours of throughput ratio T_- (the reciprocal of composition velocity) for slow paths are plotted in Figure 5. Choice of the plus sign gives the larger velocity, which corresponds to a fast path, and T_+ contours for such paths are plotted in Figure 6. The two families of contours exhibit roughly the same properties (a ridge in the central region, a maximum T on the $y_N = 0$ border, a minimum at W_M).

The watershed points, at which composition velocities become equal, were located by trial and error, usually with four-place accuracy. Table II shows the coordinates of the watersheds. Two on the $y_N = 0$ border are designated W_{N1} and W_{N2} , and one on the $y_M = 0$ border is designated W_M .

Path Isotherms along Borders. The borders are composition paths along which binary exchange occurs between feed and presaturant containing the same two exchanging components.

Figures 7-9 summarize data along the $y_M = 0$, $y_N = 0$, and $y_O = 0$ borders. One of the curves given is the isotherm, showing resin-phase vs. mobile-phase concentra-

TABLE I: Relative Direction of Change of Concentration of the Three Exchanging Species

| Region | x_X at region boundary | Slow paths | Fast paths | Selectivity |
|--------|--------------------------|----------------|-------------|-------------|
| I | 0.381 | O N M (g; a) | O N M (g) | ONM, NOM |
| II | 0.280 | O M N (a) | O M N (a) | NMO |
| III | 0.230 | M O N (g; a) | M O N (a) | NMO |
| IV | | M N O (g) | M N O (g) | NMO, MNO |

TABLE II: Compositions and Composition Velocities of the Watershed Points

| Point | y_M | \bar{x}_M | y_N | \bar{x}_N | T | u |
|----------|--------|-------------|--------|-------------|--------|-------|
| W_{N1} | 0.0742 | 0.1534 | 0 | 0 | 0.6097 | 1.64 |
| W_{N2} | 0.873 | 0.795 | 0 | 0 | 1.190 | 0.840 |
| W_M | 0 | 0 | 0.8887 | 0.8421 | 0.9267 | 1.080 |

tions. Each isotherm crosses the 45° diagonal at a selectivity-reversal point, which is the intercept in Figure 3 of the corresponding selectivity-reversal locus. Near each selectivity reversal but not coincident with it, an inflection point occurs, where the binary composition velocity (u_B or $1/T_B$) reaches a minimum. Also shown are column profiles in the form y_i vs. u_B , which exhibit a minimum in u at the inflection-point composition. These profiles show that, for many feed and presaturated compositions, composite composition routes will occur which consist of both abrupt and gradual segments.

Ordinarily a composition route in a ternary system has three plateaus and two transitions. However, in some systems, for specific feeds and presaturant conditions, it has been suggested that there are four plateaus and three transitions. For systems with constant α 's and K 's, the only routes having this property traverse a watershed.⁸ A general test is now proposed for deciding whether a ternary composition route can traverse a watershed. At any one border composition, the binary composition velocity u_B may be either smaller or larger than the ternary composition velocity u_T on the internal path that passes through that border and composition point. Thus, the velocity associated with each composition in the resulting profile, u_B , will correspond to the fast velocity of the ternary system for some compositions and the slow velocity for others. For the test, a small amount of the third component is conceptually introduced, as a step change of composition in the feed or in the presaturation plateau. This step propagates in the column at a well-defined velocity u_T , which is the limiting velocity on a composition path which intersects the border. If u_B is the fast velocity of a border composition, u_T is the slow velocity, and vice versa. If, in the vicinity of the watershed composition, u_T is greater than u_B , the ternary composition route cannot traverse the watershed. Thus the effect is that the presence of the third component, adjacent to the watershed, allows the composition route to leave the border if u_T exceeds u_B .

These conclusions may be stated more completely in algebraic terms. If the binary transition is gradual, a ternary route traversing the watershed is possible if

$$\left| \frac{\partial u_T}{\partial u_B} \right|_{\text{border}} > 1 \tag{33}$$

but such a ternary route is impossible if

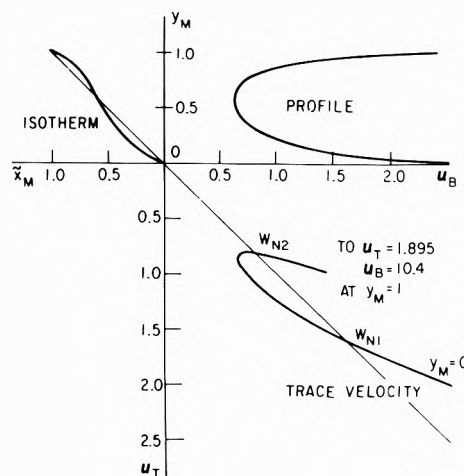


Figure 8. Fictitious concentration profile and behavior of trace amounts of N along the OM border.

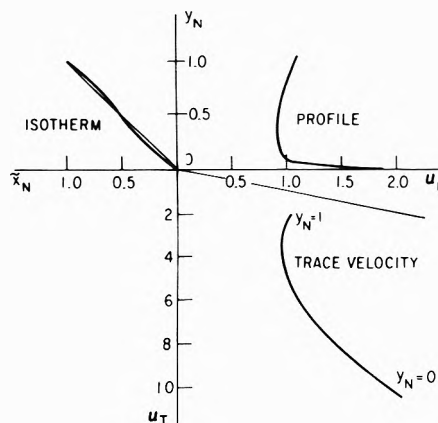


Figure 9. Fictitious concentration profile and behavior of O along the MN border.

$$\left| \frac{\partial u_T}{\partial u_B} \right|_{\text{border}} < 1 \tag{34}$$

If the binary transition is abrupt, a ternary route traversing the watershed is possible for at least some feed and presaturation conditions if

$$\left| \frac{\partial u_T}{\partial u_B} \right|_{\text{border}} < 0 \tag{35}$$

but such a ternary route is wholly impossible if

$$\left| \frac{\partial u_T}{\partial u_B} \right|_{\text{border}} > 0 \tag{36}$$

All these conclusions apply to compositions near the watershed. For more general situations, each case must be considered separately.

Each of Figures 7-9 shows the trace velocities as functions of the binary velocities along one of the borders. Figures 7 and 8 illustrate the properties of the watersheds

with respect to ternary transitions. At W_M the slope of the graph of u_T vs. u_B is negative. According to the above criteria, a ternary route through the watershed is possible for some feed and presaturation conditions when the binary transition is *abrupt*, but is not possible for *gradual* binary transitions. At W_{N1} and W_{N2} the derivative of u_T with respect to u_B is positive and less than unity. Thus ternary routes traversing these two watersheds are impossible, whether gradual or abrupt.

Orthogonal Representation

Representation of Model System. The topology of composition diagrams with two degrees of freedom has been investigated very generally by Tondeur¹⁰ with use of the orthogonal topological path grid as originated by Klein⁵ and Vermeulen. Using this approach, an orthogonal representation for the composition diagram of Figure 4 is shown in Figure 10 which preserves the topology of the exact trilinear coordinate diagram. The essential feature of this mapping is that all the composition paths of either fast or slow type are represented as a family of parallel lines. (Solid lines again represent slow paths, and dashed lines fast paths.)

The model system has three watershed points, W_M , W_{N1} , and W_{N2} . Paths entering the interior of the composition diagram do not emanate from W_{N1} and W_{N2} , but two such paths do pass through W_M and also intersect the $y_N = 0$ border at points W_{N1}' and W_{N2}' . In the schematic diagram of Figure 10, these topological features are preserved by placing the vertices of the original triangle and the watersheds W_{N1} and W_{N2} at those vertices of the polygon (here a hexagon) having an interior angle of 90° . Points W_{N1}' and W_{N2}' appear on straight sides of the polygon. The watershed W_M lies at the corner of the polygon with an interior angle of 270° .

Thus the effect of the watershed behavior is to divide the total composition diagram into three separate areas, each represented in Figure 10 by a square. For a constant-separation-factor system without complexing, the entire composition diagram would correspond to a single square. Within each one of the three squares of Figure 10, or indeed within either rectangle formed by adjacent squares, the separation route (in the event of gradual transitions) is constructed from the slow path through feed composition F and the fast path through presaturant composition P , with the intersection of these two paths representing the composition of the intermediate plateau. (When either of the transitions is partially or completely abrupt, the respective differential composition path is not followed exactly, but the abrupt path still lies in the vicinity of the fictitious gradual path.)

Our attention centers upon the more complex situation encountered when the feed and presaturant compositions lie in the squares that do not form a common rectangle, because now the "normal" route cannot be constructed. For example, if the feed composition F lies in square $MN W_M W_{N1}'$, but the presaturation point P lies in the square $W_M O W_{N1}' W_{N2}'$, no route exists involving a single switch from a slow to a fast path, because these paths do not intersect in the region of real concentrations.

For such cases Tondeur's suggestion of routes which traverse a watershed is examined here. Between a feed composition at F and a presaturation composition at P , two potential routes, $FP_1 W_M P_2 P$ and $FP_1' W_{N1}' W_{N2}' P_2' P$, are indicated in Figure 10 by

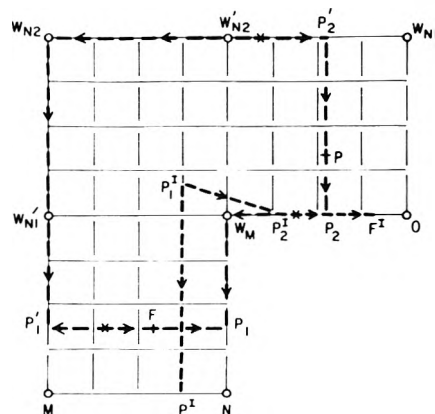


Figure 10. Orthogonal map of Figure 4, showing projected routes between low-O feed (F) and high-O presaturant (P), and between high-O feed (F') and low-O presaturant (P'). Traveling from F to P , or from F' to P' , arrows in the direction of travel indicate tendencies for gradual transition, and in opposite direction for abrupt transition.

long heavy dashes. Both these routes differ from ordinary routes in a ternary system, in having four plateaus and three transitions rather than the usual three plateaus and two transitions. Such routes are referred to here as Tondeur routes. The first route begins with a transition along a slow path from F to P_1 . At P_1 there is a switch to a fast path $P_1 W_M$, and the difference between the fast and slow composition velocities produces a plateau of composition P_1 . At W_M a switch occurs from a fast path $P_1 W_M$ upstream to a slow path $W_M P_2$ downstream. Ordinarily such a switch would be prohibited because the fast and slow composition velocities would occur in the wrong order; however, at W_M (and at watershed points in general) both velocities are equal and no plateau forms. At P_2 another switch takes place from a slow path $W_M P_2$ upstream to a slow path $P_2 P$ downstream, with plateau formation at P_2 . Similar considerations apply to route $FP_1' W_{N1}' W_{N2}' P_2' P$, with plateau formation at P_1' and P_2' and a traverse of watershed W_{N2} .

For a Tondeur route, the selectivity reversal, or the accompanying change in species behavior, appears to cause one of the components to act as two separate species which do not meet in the column. For the first route above, it is M that occurs in both the feed and the presaturant plateaus but disappears between them; for the second route, it is N . It can be noted that complexing produces a greater change in selectivity for M than for N . Considerations of this type made the route through W_M appear more likely, and this conclusion has been verified by the calculations that will be described here.

Representation of a System with Two Selectivity Reversals. The composition diagram for a model system resembling the system treated here was determined by Shiloh.¹¹ Her system, showing only two selectivity reversals ($ONM \rightarrow NOM \rightarrow NMO$), resulted from the following constants: $\alpha_{MO} = 150$; $\alpha_{NO} = 10$; $K_{MX} = 10,000$; $K_{NX} = 150$.

The pertinent triangular diagram and orthogonal representation are presented schematically in Figure 11. The diagram has been distorted to display more clearly its behavior in the region where y_O is small.

Computation of Composition Profiles

Feed Composition on $y_M = 0$ Border, and Presaturation Composition on $y_O = 0$ Border. An important objective is

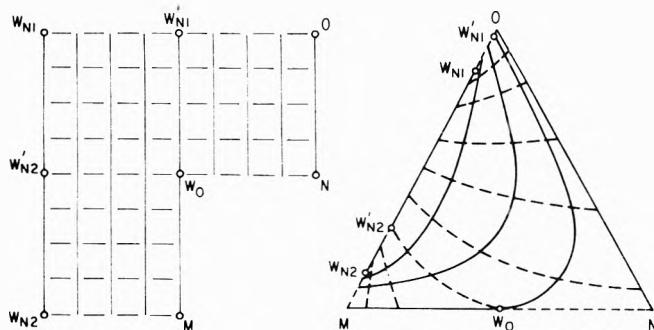


Figure 11. Composition-path diagram and auxiliary orthogonal map, for a case which has stronger association of M and N with coion X and consequently undergoes only two selectivity reversals

to find methods for passing directly from the composition-path diagram and collateral data to the local-equilibrium composition profile, without intermediate use of computations based on stage or dynamic models of the column. Such computations, unless skillfully used, are likely not to provide the required detail. The ensuing section discusses representative routes that have been computed from the composition-path diagram and then checked approximately by dynamic calculations.

A coherent profile has been determined between a feed point F^I lying within the area $W_MOW_{N1}W_{N2}'$ and a presaturant point lying within the area MNW_MW_{N1}' , shown in Figure 10. From the criteria of eq 33-36, such a route is deduced to have three plateaus and two transitions.

The feed composition was chosen on the $y_M = 0$ border: $y_M = 0$, $y_N = 0.7$, $y_O = 0.3$; $\bar{x}_M = 0$, $\bar{x}_N = 0.6768$, $x_O = 0.3232$. Also, the presaturant was chosen on the $y_O = 0$ border: $y_M = 0.1$, $y_N = 0.9$, $y_O = 0$; $\bar{x}_M = 0.1054$, $\bar{x}_N = 0.8946$, $x_O = 0$.

Several routes from F^I to P^I may be considered in principle, all of them beginning at F^I with a gradual transition; and ending at P^I , also with a gradual transition. However, the route cannot entirely follow the slow path through F^I via W_M to the intersection with the fast path through P^I , and proceed from there to P^I along that path; along this route and in the direction indicated, the composition velocity decreases from W_M to the intersection, so that an abrupt transition must occur. Two-transition possibilities to consider are (1) a composite transition upstream with the abrupt portion leading, and a gradual transition downstream; (2) a gradual transition upstream, and a composite transition downstream with the abrupt portion trailing; and (3) a combination of both types of composite transition.

In the first of these possibilities, the gradual transition would follow compositions along the slow path from F^I to some point P_2^I , yet to be established, between F^I and W_M . From P_2^I , the composition would change abruptly to that of a point P_1^I lying on the fast path through P^I (but not lying on the slow path through F^I) with the composition at P_1^I also still to be established. Figure 10 gives the topological representation of such a route. The conditions this type of route would have to satisfy in order to occur are that the slower composition velocity at P_2^I would equal the step velocity between the compositions at P_1^I and P_2^I for all components; and that the composition at P_1^I , which is that of the middle plateau zone, would lie on the fast path through P^I . Formally, this may be expressed as follows

$$\frac{d\bar{x}_i'}{dy_i'} = \frac{\bar{x}_i' - \bar{x}_i''}{y_i' - y_i''} \quad (i = M, N, O) \quad (37)$$

where \bar{x}_i' , y_i' represents a composition on the NO border (at P_2^I), and \bar{x}_i'' , y_i'' (at P_1^I) is a composition on the fast path through P^I .

At P_2^I , \bar{x}_M' and y_M' are zero. Moreover, along the fast path, \bar{x}_M'' happens to be very nearly proportional to y_M , so that $\bar{x}_M''/y_M'' = 1.050 \pm 0.003$. Equation 37 may thus be written in the form

$$d\bar{x}_N'/dy_N' = 1.050 \pm 0.003$$

where $d\bar{x}_N'/dy_N'$ is the reciprocal of the slope of the isotherm along the $y_M = 0$ border. The only solution for P_2^I between points F^I and N is $y_M' = 0$, $y_N' = 0.890$, $y_O' = 0.220$; $\bar{x}_M' = 0$, $\bar{x}_N' = 0.833$, $x_O' = 0.167$.

Now eq 37 becomes

$$\frac{0.833 - \bar{x}_N''}{0.880 - y_N''} = 1.05$$

This equation with the attendant equilibrium has been solved by trial, to give the composition at point P_1^I : $y_M'' = 0.099$, $y_N'' = 0.815$, $y_O'' = 0.096$; $x_M'' = 0.1047$, $x_N'' = 0.76$, $x_O'' = 0.125$. Computed column profiles and concentration histories are shown in Figures 12 and 13. Starting from the feed, y_N is seen to rise gradually to P_2^I , in accordance with the path isotherm of Figure 7 for the $y_M = 0$ border. A drop in y_N then occurs to the short plateau at P_1^I . The second transition shows y_N rising gradually from P_1^I along the fast path to the presaturation composition.

In the profile for species M, the gradual part of the slow transition does not affect M, and only the abrupt portion from P_2^I to P_1^I is seen. Plateau P_1^I is followed by the gradual fast transition, which passes through a shallow minimum (for which $B = 0$) at an intermediate point.

Also shown in Figures 12 and 13 are discrete points for an effluent concentration history and column profile, obtained with a method-of-characteristics computer program written by Clazie and Omatete.^{12,13} The computed results did not approach local equilibrium closely enough to separate the two transitions or to show the peak in N. However, a single jump in M from feed to P_1^I is clearly indicated, thus showing that the alternative possibility of two composite transitions is not needed. The possibility of a composite fast transition for test case 1 was also ruled out by finding that no u_Δ exists which would match the u for the fast path.

The two following cases involve changes in the opposite direction, like the path between F and P which was described earlier. One of those two cases yields a Tondeur route, having four plateaus and three transitions.

Tondeur Route through W_M . As stated above, Tondeur routes are possible through watershed W_M for particular ranges of feed and presaturation conditions. Such a route is demonstrated here, which corresponds to route $P_1W_MP_2$ in Figure 10.

Table III presents data for the $y_M = 0$ border: resin and aqueous concentrations of N, binary-composition velocities for exchange of N and O, and the trace-composition velocity for a very small transition along the path intersecting the border. Somewhat as shown for points P and F in Figure 10, the presaturation composition is assumed to be located at or near the composition-diagram border at $y_N = 0.80$, and the feed composition (feed 1) is at or near

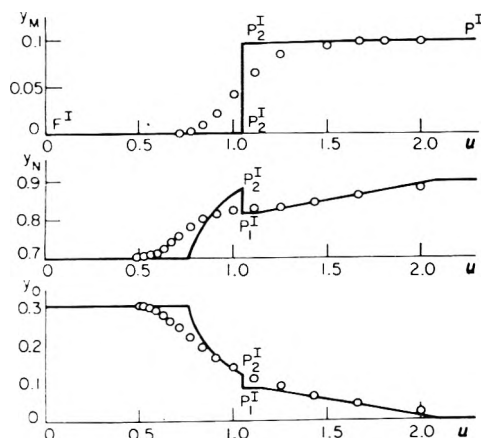


Figure 12. Counterion concentration profiles in column for calculated example having high-O feed and low-O presaturant.

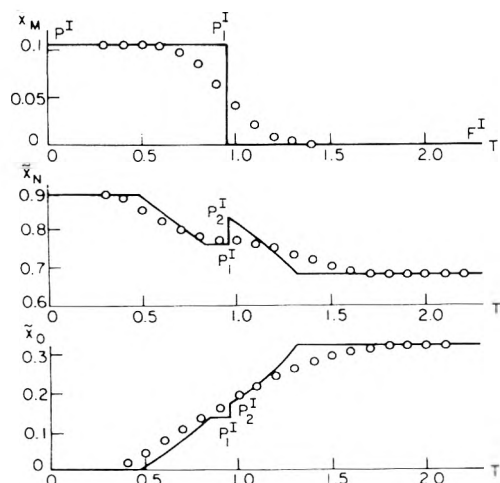


Figure 13. Counterion concentration histories leaving column for calculated example having high-O feed and low-O presaturant.

TABLE III: Tests for Locating a Tondeur Route through W_M

| y_N | \bar{x}_N | u_B | u_T | u_Δ | |
|--------|-------------|-------|-------|------------|-----------------|
| 0.8 | 0.75722 | 0.865 | 1.103 | | Presaturant |
| 0.8886 | 0.84200 | 1.078 | 1.079 | | |
| 0.8887 | 0.84210 | 1.079 | 1.079 | | Watershed W_M |
| 0.8888 | 0.84221 | 1.079 | 1.078 | | |
| 0.94 | 0.90331 | 1.332 | 1.072 | 1.042 | Feed 2 |
| 0.96 | 0.93145 | 1.488 | 1.072 | 1.089 | Feed 1 |
| 0.98 | 0.96320 | 1.699 | 1.072 | 1.144 | Feed 3 |

the border at $y_N = 0.96$. Then, from eq 8, the step velocity of the assumed binary-exchange transition is computed as $u_\Delta = 1.089$. The composition velocity of a trace in the feed (the upstream transition) is 1.072, less than u_Δ , while the composition velocity of a trace introduced in the presaturant (the downstream transition) is 1.103, greater than u_Δ . Hence a three-transition four-plateau profile is possible for this choice of feed and presaturation compositions.

A small change in feed composition to $y_N = 0.94$ (feed 2), with the same presaturation composition as before, gives the step velocity of the binary transition as 1.042. This velocity is ordered correctly with respect to the trace in the presaturant, but is not ordered correctly with respect to a trace step in the feed which moves at $u_T =$

1.072. Thus the feed trace converts the binary transition to a ternary transition, and destroys the Tondeur route.

A different small change in feed composition, to $y_N = 0.98$, gives a binary step velocity of 1.144. Now the step velocity of the binary is ordered correctly with respect to a step in the feed for which $u_T = 1.072$, but interferes with a step in the presaturant. Again a Tondeur route is impossible.

Further examination of the problem by use of this method indicates that the range of accessible Tondeur routes is quite limited. The narrowest possible jump is between presaturant at $y_{NP} = 0.83$ and feed at $y_{NF} = 0.91$ (qualitatively). At $y_{NP} = 0.80$, as just shown, feed between y_{NF} of 0.95 and 0.97 is accessible. At $y_{NP} = 0.70$, the feed value y_{NF} must be between 0.975 and 1.00. The widest possible jump is between presaturant at $y_{NP} = 0.53$ and $y_{NF} = 1.00$. For $y_{NF} = 0.97$, the accessible presaturant range is between $y_{NP} = 0.80$ and 0.72; whereas for $y_{NF} = 1.00$, y_{NP} lies between 0.70 and 0.53.

The Tondeur routes are not confined to feed and presaturant compositions close to the $y_M = 0$ border. However, for the abrupt transition to a presaturant in the upper part of the triangular diagram, the u_Δ will become progressively smaller than u_T as y_M increases, thereby reducing the accessible range. In the lower part of the diagram, because of the wide span of gradual transitions, solid-line paths extending to $y_{MF} = 0.7$ or even higher will still give Tondeur routes if their intersections at $y_M = 0$ fall within the ranges indicated above.

Tondeur routes are defined here as routes that (1) pass through a watershed point, thereby lying on a border, and (2) possess an extra transition (e.g., for a ternary system, three transitions rather than two). At present, for complexing of the type described here, no routes are known that satisfy conditions 1 without condition 2, or condition 2 without condition 1; but the possible existence of routes of either such type has not yet been formally disproved.

It is noteworthy that the non-Tondeur routes studied here usually exhibit one composite transition. When a non-Tondeur route changes into a Tondeur route, the extra plateau forms at the junction point between the gradual and abrupt segments of the composite transition. Thus a close similarity exists between Tondeur routes and nearby non-Tondeur routes.

Summary and Conclusions

The formation of complexes in a ternary ion-exchange system has been analyzed from the local-equilibrium viewpoint. The structure of the composition diagram and the underlying reasons for that structure have been demonstrated. Two new concepts have been introduced to facilitate this analysis: (1) the loci on which the partial derivatives of the equilibrium functions go to zero is important in deciding the relative directions of change of component concentrations along the differential composition path; (2) the graph of trace-composition velocity vs. binary velocity can be used to determine the possibility of a ternary composition route through a watershed, called a Tondeur route.

Representative composition routes have been computed from the composition-path diagram and concomitant information. Tondeur routes, in which the component with the greatest change in selectivity behaves as if it were two components, are seen to exist for special choices of feed and presaturation conditions; but other choices lead to

the normal two-transition routes, even when the topology of the differential paths qualitatively suggests a three-transition route.

Appendix. Notation

A, B, C, D = $\partial x_i / \partial y_j$ values, defined by eq 13-14
 c = fluid-phase concentration of anionic or molecular species
 \bar{c} = same, for sum of complexed and uncomplexed forms
 F = feed
 K = stability constant
 M, N, O = counterion species
 P = presaturant
 Q = resin capacity, equivalents/mass
 q = resin-phase concentration of an ionic species, equivalents/mass
 u = composition velocity, dimensionless; see eq 4
 V = fluid volume
 v = packed volume of resin
 W = watershed
 X = coion, complex forming
 x = relative fluid-phase concentration, c/\bar{c}_x
 \bar{x} = same, for sum of complexed and uncomplexed forms

y = relative resin-phase concentration, q/Q
 α = selectivity coefficient
 ϵ = void fraction
 ρ = resin bulk density, mass/packed volume

References and Notes

- (1) Sponsored by the Materials Research Division of the U. S. Office of Saline Water, and by the Engineering Chemistry Division of the National Science Foundation.
- (2) D. DeVault, *J. Amer. Chem. Soc.*, **65**, 532 (1943).
- (3) J. E. Walter, *J. Chem. Phys.*, **13**, 229 (1945).
- (4) E. Glueckauf, *Discuss. Faraday Soc.*, **7**, 12 (1949).
- (5) G. Klein, D. Tondeur, and T. Vermeulen, *Ind. Eng. Chem.*, **6**, 339 (1967).
- (6) F. Helfferich and G. Klein, "Multicomponent Chromatography," Marcel Dekker, New York, N. Y., 1970.
- (7) H. K. Rhee, R. Aris, and N. R. Amundson, *Phil. Trans. Royal Soc. London, Ser. A*, **267**, 419 (1970).
- (8) D. Tondeur, *Chem. Eng. J.*, **1**, 337 (1970).
- (9) This calculation was carried out by A. G. Sassi.
- (10) D. Tondeur, *J. Chim. Phys.*, **68**, 311 (1970).
- (11) K. I. Shiloh, M.S. Thesis, University of California, Berkeley, Calif., 1965.
- (12) R. N. Clazie, G. Klein, and T. Vermeulen, University of California Sea Water Conversion Laboratory Report No. 67-4, 1967; U. S. Office of Saline Water, Research and Development Progress Report No. 326, 1968.
- (13) O. O. Omatete, Ph.D. Dissertation, University of California, Berkeley, Calif., 1971.

Analysis of Inertial Effects on Electron Spin Resonance Spectra in the Slow Tumbling Region¹

G. V. Bruno and J. H. Freed*

Department of Chemistry, Cornell University, Ithaca, New York 14850 (Received November 19, 1973)

An analysis is given of the inertial effects (which arise from the coupling of the molecular orientational degrees of freedom to the molecular angular momentum) on ESR spectra of radicals in the model-sensitive slow tumbling region. The analysis is based on the stochastic-Liouville equation in combined spin, orientational, and angular momentum space, and it utilizes recently developed models of Langevin (or Brownian) diffusion and extended diffusion. The case of a simple line from an axial g tensor is studied in most detail. It is shown that the complete analysis for inertial effects in this case yields results similar to a very crude model of free diffusion found by Goldman, *et al.*, to be in good agreement with experimental results in their analysis of slow-tumbling nitroxide spectra. Results of Langevin and extended diffusion were virtually the same. However, results obtained for a familiar approximate inertial model, which neglects noncommutativity of the angular-velocity components, disagreed sharply with all other cases (including the even cruder free diffusion model derived from it) indicating that it is an unsatisfactory model. The less complete results obtained for the case of nitroxide spectra indicate similar conclusions.

I. Introduction

In a recent set of ESR experiments in the slow tumbling region where the ESR line shapes are no longer simple Lorentzians, it was found possible to distinguish between different models for the molecular reorientation.² The models considered were Brownian rotational diffusion, diffusion by molecular jumps of substantial angle, and a simplified model of free diffusion wherein the inertial effects were introduced in a crude fashion. Our results on small nitroxide molecules² were found to be consistent

with molecular jumps of moderate angle (the root-mean-square jump angle ~ 1 radian) but the simplified model of free diffusion utilized gave equally good agreement. The present study was undertaken to determine whether a more complete analysis of inertial effects which result from the coupling of the molecular orientational degrees of freedom to the angular momentum could alter the results previously obtained.

The basis of our theoretical analysis of the slow tumbling ESR spectra has been the stochastic Liouville meth-

od³ as utilized by Freed, Bruno, and Polnaszek.⁴ In the past work, it has only been employed in combined spin and orientational space, the random behavior of the latter being described by a Markoff process.⁵ However, the stochastic-Liouville method is quite general, and for the problem of inertial effects one may introduce the combined orientational-angular momentum degrees of freedom in terms of which the Markoff process is defined. This generalization clearly renders the problem considerably more complex, but it has still been possible to obtain some useful results and insights.

Our analysis builds on some of the extensive recent work on inertial effects in rotational diffusion. In particular, we have found the work of Fixman and Rider⁶ lends itself quite naturally to adaptation to our stochastic-Liouville approach for slow tumbling esr spectra. Also, some of the earlier discussion by Sack on this subject has been useful.^{7a,b} Hubbard has also very recently discussed this subject.^{7c}

II. General Approach

We start with the stochastic-Liouville equation of motion for the spin-density matrix⁴

$$\frac{\partial}{\partial t} \rho(\Psi, t) = [-i\mathcal{H}(\Omega)^x - \Gamma_\Psi] \rho(\Psi, t) \quad (1)$$

and

$$\Gamma_\Psi P_0(\Psi) = 0 \quad (1a)$$

Here $\mathcal{H}(\Omega)^x$ is the superoperator of the orientation-dependent spin Hamiltonian and Γ_Ψ is a Markoffian operator for the collection of variables Ψ , which include the orientational angles Ω . In particular, for the consideration of inertial effects, Ψ includes the angular momentum (or velocity) variables as well. $P_0(\Psi)$ in eq 1a is the unique equilibrium distribution over all the variables in Ψ . We shall consider specifically (1) motion about a fixed axis, i.e., one-dimensional free rotational diffusion and (2) three-dimensional free rotational diffusion of a spherical top.

The unsaturated absorption of the λ_j th transition is obtained from $\text{Im } \bar{Z}_{\lambda_j}$ where⁴

$$\bar{Z}(\omega)_{\lambda_j} = \int d\Psi Z(\Psi, \omega)_{\lambda_j} P_0(\Psi) \quad (2)$$

and

$$\rho(\Psi, t)_{\lambda_j} = e^{i\omega t} Z(\Psi, \omega)_{\lambda_j} \quad (3)$$

That is $Z(\Psi, \omega)_{\lambda_j}$ is the steady-state solution of $\rho(\Psi, t)$ for the λ_j th transition and is time independent in the frame rotating with impressed frequency ω . Also, $Z(\omega)_{\lambda_j}$ is the equilibrium average over all variables comprising Ψ .

Substituting of eq 3 into 1 leads for the case of no saturation to^{4,5}

$$\{[\omega - \mathcal{H}_0^x + \mathcal{H}_1(\Omega)^x - i\Gamma_\Psi] Z(\Psi, \omega)\}_{\lambda_j} = \frac{1}{2} \omega_1 [S_-^x \rho_0]_{\lambda_j} \quad (4)$$

where \mathcal{H}_0 is the zero-order orientation-independent and $\mathcal{H}_1(\Omega)$ the perturbing orientation-dependent parts of $\mathcal{H}(\Omega)$, $\omega_1 = \gamma_e B_1$ with B_1 the magnitude of the rf field, S_- is the electron spin lowering operator, and ρ_0 the equilibrium density matrix. The averaging of eq 4 to obtain an expression for $Z(\omega)$ must follow the prescription of first postmultiplying eq 4 by $P_0(\Psi)$ and then integrating over all Ψ .^{3,5} One generally expands $Z(\Psi, \omega)_{\lambda_j}$ in a complete orthonormal set of eigenfunctions (when available) of Γ_Ψ to solve eq 4.⁴ However, when $P_0(\Psi) \neq \text{constant}$ it is usu-

ally more convenient to define⁸

$$\bar{Z}(\Psi, \omega) = P_0^{-1/2}(\Psi) Z(\Psi, \omega) \quad (5)$$

and then expand the $\bar{Z}(\Psi, \omega)$, and this is illustrated below.

(A) *One-Dimensional Free Rotational Diffusion.* By one-dimensional rotation, we mean rotation about a fixed axis. This model has been discussed in detail by Sack^{7a,b} and others.⁹ It is a simple generalization of the one-dimensional Fokker-Planck equation to cover rotational motion.¹⁰

Thus we may write

$$\Gamma_{\gamma, \dot{\gamma}} = \dot{\gamma} \frac{\partial}{\partial \gamma} - \beta \left(\frac{\partial}{\partial \dot{\gamma}} \dot{\gamma} + \beta R \frac{\partial^2}{\partial \dot{\gamma}^2} \right) \quad (6)$$

where γ is the angle of rotation about the fixed axis and $\dot{\gamma}$ its angular velocity. Also β is the damping coefficient and $R \equiv kT/I\beta$ is the diffusion coefficient for reorientation. This two dimensional Markovian operator will have the equilibrium probability distribution

$$P_0(\gamma, \dot{\gamma}) = P_0(\gamma) P_0(\dot{\gamma}) = (1/2\pi) ([2\pi\beta R]^{-1/2} \exp[-\dot{\gamma}^2/2\beta R]) \quad (7)$$

corresponding to a uniform distribution in orientation and a Boltzmann distribution in angular velocity. Because the latter is nonuniform, $\Gamma_{\gamma, \dot{\gamma}}$ given by eq 6 is a nonsymmetric operator. We may symmetrize by the transformation

$$\tilde{\Gamma} = P_0^{-1/2}(\gamma, \dot{\gamma}) \Gamma P_0^{1/2}(\gamma, \dot{\gamma}) = \dot{\gamma} \frac{\partial}{\partial \gamma} - \beta \left(\beta R \frac{\partial^2}{\partial \dot{\gamma}^2} - \frac{\dot{\gamma}^2}{4\beta R} + \frac{1}{2} \right) \quad (8)$$

One then immediately notes that the second term on the right-hand side of eq 8 is (within the constant term of $-1/2$) just the operator for the one-dimensional quantum-mechanical harmonic oscillator. Thus it has harmonic oscillator eigenfunctions as its eigenfunctions with the eigenvalues $n\beta$ ($n = 0, 1, 2, \dots$). Thus one first transforms eq 1 to be

$$\frac{\partial}{\partial t} \tilde{\rho}(\gamma, \dot{\gamma}, t) = [-i\mathcal{H}^x - \tilde{\Gamma}] \tilde{\rho}(\gamma, \dot{\gamma}, t) \quad (9)$$

where (cf. eq 5)

$$\tilde{\rho}(\gamma, \dot{\gamma}, t) = P_0^{-1/2}(\gamma, \dot{\gamma}) \rho(\gamma, \dot{\gamma}, t) \quad (9a)$$

Then the matrix elements of $\tilde{Z}(\gamma, \dot{\gamma}, \omega)$ for the relevant transitions may be expanded in complete sets of eigenfunctions for γ and $\dot{\gamma}$ as

$$\tilde{Z}(\gamma, \dot{\gamma}, \omega)_{\lambda_j} = \sum_{r,n} [C_{m,n}(\omega)]_{\lambda_j} f_r(\gamma) h_n(\dot{\gamma}) \quad (10)$$

with

$$f_r(\gamma) = \frac{1}{\sqrt{2\pi}} e^{ir\gamma} \quad (10a)$$

$$h_n(\dot{\gamma}) = [(2\pi\beta R)^{1/2} 2^n n!]^{-1/2} \exp\left(\frac{-\dot{\gamma}^2}{4\beta R}\right) H_n\left(\frac{\dot{\gamma}}{\sqrt{2\beta R}}\right) \quad (10b)$$

and

$$P_0^{1/2}(\gamma, \dot{\gamma}) = f_0(\gamma) h_0(\dot{\gamma}) \quad (10c)$$

where $H_n(x)$ are the Hermite polynomials. Thus

$$\tilde{\Gamma} f_r(\gamma) h_n(\dot{\gamma}) = E_{r,n} f_r(\gamma) h_n(\dot{\gamma}) = (n\beta + ir\dot{\gamma}) f_r(\gamma) h_n(\dot{\gamma}) \quad (11)$$

and the "matrix elements" of $\tilde{\Gamma}$ may be obtained from the known properties of the Hermite functions $h_n(\dot{\gamma})$. Then in

a manner analagous to eq 16-21 of I we have for the λ_j th transition (from eq 4 and 10)

$$(\Delta\omega_\lambda - in\beta)[C_{r,n}]_{\lambda_j} + \sum_{r'} \int_0^{2\pi} d\gamma f_{r'}^* [\mathcal{H}_1^x C_{r',n}]_{\lambda_j} f_{r'} + r\{\sqrt{\beta R(n+1)}[C_{r,n+1}]_{\lambda_j} + \sqrt{\beta Rn}[C_{r,n-1}]_{\lambda_j}\} = q\omega_\lambda \delta_{r,0} \delta_{n,0} d\lambda_j \quad (12)$$

[Note $\Delta\omega_\lambda = \omega - \omega_\lambda$, $d_{\lambda_j} = \frac{1}{2}\omega_1(S_-)_{\lambda_j}$, $q = \hbar/NkT$, with N the number of spin eigenstates.] We have, in obtaining eq 12, utilized the fact that \mathcal{H}_1^x does not depend explicitly on angular velocity, but it does depend on orientation. The absorption for the λ_j th transition is given by

$$\begin{aligned} \text{Im } \bar{Z}(\omega)_\lambda &= \text{Im} \int_0^{2\pi} d\gamma \int_{-\infty}^{\infty} d\tilde{\gamma} Z(\gamma, \tilde{\gamma}, \omega)_\lambda P_0(\gamma, \tilde{\gamma}) \\ &= \text{Im} \int_0^{2\pi} d\gamma \int_{-\infty}^{\infty} d\tilde{\gamma} \tilde{Z}(\gamma, \tilde{\gamma}, \omega)_\lambda f_0(\gamma) h_0(\tilde{\gamma}) \\ &= \text{Im} [C_{0,0}]_{\lambda_j} \end{aligned} \quad (13)$$

It is possible to replace the Brownian diffusion case by a "strong-collision-in-angular-velocity-space" model which has been referred to as an extended diffusion or J-diffusion model.¹¹ This possibility, as well as related ones, are discussed by Sack.^{7a,b} For our purposes, it is easy to show from Sack's expressions (cf. eq 2.11 of 7a) that for the case where each collision results in $\tilde{\gamma}$ being restored to its equilibrium distribution given by $P_0(\tilde{\gamma})$ (but with γ unchanged by the collision), one merely may replace

$$n\beta \longrightarrow \beta(1 - \delta_{n,0}) \quad (14)$$

in eq 12. (Such simple changes with model have an analogy in the methods of treating orientational-jump models.)^{2a}

Equations 12 and 13 may then be solved in the usual manner for different values of R and β by truncating the eigenfunction expansion in n and r after a sufficient number of terms are taken. We are, however, primarily interested in the three-dimensional case which may be handled analogously, although it is considerably more complex. This one-dimensional model is, however, useful in illustrating how the general format of the theory may be applied. Also we shall use it later to attempt a simplified treatment of the three-dimensional case.

(B) *Three-Dimensional Free Rotational Diffusion.* Here we make considerable use of the treatment of Fixman and Rider.⁶ They treat the cases of both Brownian (or Langevin) diffusion and extended diffusion from a stochastic Liouville-type approach. In particular one has for a spherical-top in these cases

$$-\Gamma = i\nu S + \mathcal{L} \quad (15)$$

where \mathcal{L} is the relaxation or diffusion operator for the angular velocity \mathbf{v} , which for a Brownian model is^{6,7b}

$$\mathcal{L} = \beta[\nabla_{\mathbf{v}} \cdot \mathbf{v} + R\beta \nabla_{\mathbf{v}}^2] \quad (16)$$

The inertial or streaming term νS (where $\nu = |\mathbf{v}|$), describes the dynamical coupling of angular momentum ($\mathbf{L} = I\mathbf{v}$) and orientation.^{6,7b} One has

$$S = \mathbf{l} \cdot \mathbf{j}_u$$

where

$$\mathbf{l} = \mathbf{v}/\nu \text{ and } \mathbf{j}_u \equiv -i\mathbf{u} \times \nabla_u \quad (17)$$

where \mathbf{u} is a unit orientational vector, the components of which give the projections of the laboratory unit z axis vector (\mathbf{k}) in a molecular coordinate frame.⁶ (This repre-

sentation is adequate for an axially symmetric $\mathcal{H}_1(\Omega)$, and we are only considering spherical top motion.) Thus S depends on the orientation of \mathbf{u} : θ_u, φ_u as well as the orientation of \mathbf{l} in the molecular coordinate frame or θ_v, φ_v . The products of spherical harmonics $Y_{nm}(\theta_u, \varphi_u)$ and $Y_{j'p'}(\theta_v, \varphi_v)$ form a basis set in which to evaluate S . Fixman and Rider find for their purposes that the coupled linear combinations which are eigenfunctions of the "angular momentum-type" operators $\mathbf{J} = \mathbf{j}_u + \mathbf{j}_v$ and $M = m + m'$ (the components of \mathbf{j}_u and \mathbf{j}_v on the molecular z axis) are more desirable for evaluating S simply. However, in the slow tumbling problem, where the perturbation $\mathcal{H}_1(\Omega)$ enters in a more complex fashion, it appears a little more convenient to choose the natural basis set for $\mathcal{H}_1(\Omega)$ ($\propto Y_{no}(\theta_u, \varphi_u)$) in the simple axially symmetric secular g tensor case, see below), which is the simple product representation.¹²

Now eq 16 leads to the equilibrium distribution in ν

$$P_0(\nu) = \left(\frac{I}{2\pi kT}\right)^{3/2} \exp(-I\nu^2/2kT) \quad (18)$$

and one may symmetrize \mathcal{L} (and Γ) by the analogous transformation to that used in eq 8. The eigenfunctions of $\tilde{\mathcal{L}}$ (the symmetrized form) are

$$kjp) = Y_{jp}(\theta_v, \varphi_v) R_{kj}(\nu) \quad (19)$$

where

$$R_{kj}(\nu) = \left[\frac{2\pi^{1/2} k!}{(j+1/2+k)!}\right]^{1/2} P_o(\nu)^{1/2} \nu^j L_k^{j+1/2}(\nu^2) \quad (19a)$$

and $L_k^{j+1/2}$ is the associated Laguerre polynomial. The eigenvalues of \mathcal{L} are for Brownian (or Langevin) diffusion⁶

$$\tau_{jk}^{-1} \equiv \langle kjp | \tilde{\mathcal{L}} | k'j'p' \rangle = +\delta_{kk'} \delta_{jj'} \delta_{pp'} (j+2k)\beta \quad (20)$$

In the case of extended diffusion (i.e., each collision thermalizes \mathbf{L}) one obtains^{6,7a,b}

$$\tau_{jk}^{-1} \equiv \langle kjp | \tilde{\mathcal{L}} | k'j'p' \rangle = +\delta_{kk'} \delta_{jj'} \delta_{pp'} \beta(1 - \delta_{j,0} \delta_{k,c}) \quad (21)$$

The "matrix elements" of νS are found to be

$$\begin{aligned} \langle Lm; kjp | \nu S | L'm'; k'j'p' \rangle &= \langle kjp | \nu | k'j'p' \rangle \times \\ &\langle Lm; jp | S | L'm'; j'p' \rangle = \\ &\delta_{L,L'} \delta_{m,m'} \delta_{j,j'} \delta_{p,p'} [L(L+1) - m(m-1)]^{1/2} - \\ &\delta_{k',k-1} (k+1)^{1/2} + \delta_{j',j+1} S_{j+1}(L,m,m',p,p') [\delta_{k,k'} (j+3/2 + \\ &k)^{1/2} - \delta_{k',k-1} (k)^{1/2}] \sqrt{\beta R/2} \end{aligned} \quad (22)$$

where

$$\begin{aligned} S_{j\pm 1}(L,m,m',p,p') &= [(2|j\pm 1|+1)(2j+1)3]^{1/2} \times \\ &\begin{pmatrix} j\pm 1 & 1 & j \\ 0 & 0 & 0 \end{pmatrix} \times \{m\delta_{m,m'} \begin{pmatrix} j\pm 1 & 1 & j \\ -p & 0 & p \end{pmatrix} \delta_{p,p'} (-)^j + \\ &\frac{1}{\sqrt{2}} \delta_{m',m-1} \delta_{p',p+1} [L(L+1) - m(m-1)]^{1/2} \times \\ &\begin{pmatrix} |j\pm 1 & 1 & j \\ -(p+1) & 1 & p \end{pmatrix} (-)^p - \frac{1}{\sqrt{2}} \delta_{m',m+1} \delta_{p',p-1} \times \\ &[L(L+1) - m(m+1)]^{1/2} \begin{pmatrix} |j\pm 1 & 1 & j \\ -(p-1) & -1 & p \end{pmatrix} (-)^p\} \end{aligned} \quad (23)$$

For an (axially symmetric) secular perturbation, one only needs terms for which $M = m + p = 0$ and $M' = m' + p' = 0$. In view of the complexity of the problem, we only consider here this simplest of esr cases, i.e., a single line

broadened by an axially symmetric g tensor. (A detailed discussion of the expressions for the case of an axially symmetric nitroxide is given by Bruno.¹³) We may then write⁴

$$\mathfrak{H}_1(\Omega) = \left(\frac{4\pi}{5}\right)^{1/2} Y_{2,0}(\theta_u, 0) \mathfrak{H}_S \quad (24)$$

$$\mathfrak{H} \equiv 2/3\hbar^{-1}\beta_o B_o (g_{\parallel} - g_{\perp}) \quad (24a)$$

where B_o is the magnitude of the dc magnetic field, and g_{\parallel} and g_{\perp} are the parallel and perpendicular components of the g tensor. The matrix elements of $\mathfrak{H}_1(\Omega)$ are simply

$$\langle Lm; kjp | \mathfrak{H}_1(\Omega) | L'm'; k'j'p' \rangle = (-)^m \mathfrak{H} (2L'+1)^{1/2} (2L+1)^{1/2} \begin{pmatrix} L & 2 & L' \\ 0 & 0 & 0 \end{pmatrix} \begin{pmatrix} L & 2 & L' \\ -m & 0 & m \end{pmatrix} \times \delta_{m,m'} \delta_{k,k'} \delta_{j,j'} \delta_{p,p'} \quad (25)$$

We may then expand the spin-density "matrix elements" as

$$\tilde{Z}(\theta_u, \varphi_u, \theta_v, \varphi_v, L, \omega)_{\lambda} = \sum_{L,m,k,j} [C_{L,m,k,j}(\omega)]_{\lambda} \times Y_{L,m}(\theta_u, \varphi_u) Y_{j,m}(\theta_v, \varphi_v) R_{k,j}(v) \quad (26)$$

and in an analogous manner to eq 13 one obtains

$$\text{Im } \bar{Z}(\omega) = \text{Im } [C_{o,o,o,o}(\omega)]_{\lambda} \quad (27)$$

for the single (λ th) transition with matrix elements equivalent to eq 12

$$[(\omega - \omega_0) - i\tau_{jk}^{-1}] C_{L,m,k,j} + \sum_{L'} \langle L,m; kj-m | \mathfrak{H}_1(\Omega) | L',m; kj-m \rangle C_{L',m,k,j} - \sum_{k',j',m'} \langle L,m; kj-m | vS | L',m'; k'j'-m' \rangle C_{L',m',k',j'} = q\omega_{\lambda} d_{\lambda} \delta_{L,o} \delta_{m,n} \delta_{k,n} \delta_{j,o} \quad (28)$$

The solution may be simplified by noting that only the following linear combinations are needed

$$\bar{C}_{L,m,k,j} = \frac{1}{\sqrt{2}} (C_{L,m,k,j} \pm C_{L,-m,k,j}) \quad m \neq 0 \quad (29)$$

where the + sign is for even j and the - sign for odd j .

(C) *An Approximate Approach.* As may be seen, the coupled equations defining even the simplest esr problem are themselves very complex. It is thus not very practical to attempt to solve a free diffusion model for more complex slow-tumbling esr cases such as a nitroxide. We therefore have examined a highly simplified description of inertial effects. Essentially what we have done is to employ the one dimensional model in modified form. That is, we replace eq 15-17 simply by

$$\Gamma = i|j_u|^2/2 - \beta \left(\frac{\partial}{\partial v} v + \beta R \frac{\partial^2}{\partial v^2} \right) \quad (30)$$

where $|j_u|^2/2$ is defined by

$$|j_u|^2/2 Y_{L,m} \equiv [L(L+1)]^{1/2} Y_{L,m} \quad (30a)$$

In this fashion the angular velocity diffusion of the spherical top is treated simply in terms of its magnitude, while the effects of the orientation of v on the description of the orientational motion of the molecule are neglected. We show below that this assumption results in a description

of inertial effects on molecular reorientation which is equivalent to an earlier approximate treatment by Steele.¹⁴ In Steele's analysis the approximation amounted to defining a rotational-diffusion tensor as

$$R_{i,j}(t) = \int_0^t \langle v_i(0)v_j(t) \rangle dt$$

This assumption neglects the noncommutativity of the angular momentum operators.

A comparison of eq 30 with 6 immediately shows that the treatment given in section A for one-dimensional free-rotational diffusion applies. One need only make the replacements in eq 12 of $f_r(\gamma) \rightarrow Y_{Lm}(\theta_u, \varphi_u)$, $r^2 \rightarrow L(L+1)$, and $\int_0^{2\pi} d\gamma \rightarrow \int_0^{2\pi} d\theta_u \int_0^{2\pi} d\varphi_u$. In particular, we have for the axially symmetric g tensor mechanism

$$[(\omega - \omega_0) - i(T_2^{-1} + n\beta)] C_{L,n} - \mathfrak{H} \sum_{L'} (2L'+1)^{1/2} (2L+1)^{1/2} \begin{pmatrix} L & 2 & L' \\ 0 & 0 & 0 \end{pmatrix} C_{L',n} + \sqrt{\beta R} \sqrt{L(L+1)} \left[\sqrt{(n+1)} C_{L,n+1} + \sqrt{n} C_{L,n-1} \right] = q\omega_{\lambda} d_{\lambda} \delta_{L,o} \delta_{n,o} \quad (31)$$

and again

$$Z''(\omega) = \text{Im } C_{o,o} \quad (32)$$

For the case $R/\beta \ll 1$, one expects that eq 31 should be equivalent to the spectrum for simple Brownian reorientation. One may readily show this to be so by considering the third term on the left-hand side of eq 31 as a perturbation compared to diagonal elements $n\beta$. Then, to second order in this third term, we obtain for the coefficients $C_{L,o}$

$$[(\omega - \omega_0) - i(T_2^{-1} + RL[L+1])] C_{L,o} - \mathfrak{H} \sum_{L'} (2L'+1)^{1/2} (2L+1)^{1/2} \times \begin{pmatrix} L & 2 & L' \\ 0 & 0 & 0 \end{pmatrix} C_{L',o} = q\omega_{\lambda} d_{\lambda} \delta_{L,o} \quad (33)$$

which is identical with the equation obtained in I for simple rotational diffusion.

Suppose, on the other hand, $R/\beta \geq 1$. Then coefficients $C_{L,n}$ for $n > 0$ become significantly coupled into the $C_{L,o}$ coefficients that ordinarily determine the spectrum. Suppose one may initially neglect the term in \mathfrak{H} in eq 31, i.e., $\mathfrak{H} \ll \beta, R$. Then, for this case we need consider the coupling of $C_{L,n}$ to the other $C_{L,n'}$. Let us first consider the simplified coupled set of equations

$$[(\omega - \omega_0) - in\beta] a_{L,n} + (\sqrt{n+1} a_{L,n+1} + \sqrt{n} a_{L,n-1}) \gamma_L = \delta_{n,o} \quad (34)$$

where $\gamma_L = [R\beta L(L+1)]^{1/2}$. Equation 34 may be solved for $a_{L,o}$, and it generates a continued fraction, the solution of which is known.³ It yields

$$a_{L,o}(\omega) = i \int_0^{\infty} \exp\{-L(L+1)\frac{R}{\beta}(e^{-\beta t} - 1 + \beta t) - i(\omega - \omega_0)t\} dt \equiv i j_L(\omega - \omega_0) \quad (35)$$

which is the Fourier-Laplace transform of a type of correlation function well known in Brownian motion theory and obtained by Steele in his approximate treatment of inertial effects in rotational diffusion (for a spherical rotor).¹⁴ If we now introduce the effects of \mathfrak{H} to lowest

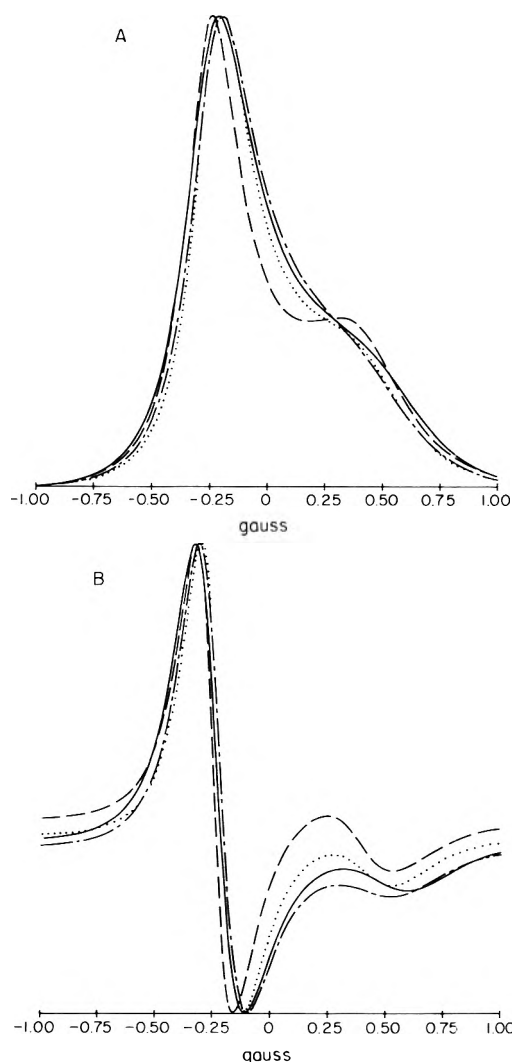


Figure 1. Comparison of line shapes for axially symmetric g tensor for different free rotational diffusion models: A, absorption line shapes; B, first derivative line shapes. The different rotational diffusion models are, simple Brownian; ———, motion described in full three-dimensional angular momentum space for Brownian particle with $\beta = 4R$ and $R = 0.13|\mathfrak{F}|$; - - - -, motion described in one-dimensional angular momentum space for Brownian particle with $\beta = 4R$ and $R = 0.13|\mathfrak{F}|$; - - - -, simple free diffusion with $\beta/R = (R\tau)^{-1} = 4$ and $R = 0.105|\mathfrak{F}|$. All have $\tau_R = 1.72 \times 10^{-7}$ sec, $g_{\parallel} = 2.00235$, $g_{\perp} = 2.00310$, $B_0 = 3300$ G, $(2/3^{1/2})T_2^{-1}/|\gamma_e| = 0.02$ G.

order, so that $C_{0,0} \approx 1$, we then obtain from eq 31

$$\left[\left(\omega - \omega_0 - \frac{2}{7} \mathfrak{F} \right) - i(5)^{-1} \mathfrak{F}^2 j_2 \left(\omega - \omega_0 - \frac{2}{7} \mathfrak{F} \right) \right] C_{0,0} \cong 1 \quad (36)$$

And since $R/\beta \gg \mathfrak{F}$, one may let $j_2(\omega - \omega_0 - (2/7)\mathfrak{F}) \approx j_2(0)$ for values of ω for which the resonance signal is not negligible.

The approximation suggested by Egelstaff in another connection¹⁵ and which served as the basis of our earlier simplified model of free diffusion^{2a} is to estimate the half-width for the (approximate) form of the $j_L(\omega)$ given by eq 35 and then use it to replace the inverse eigenvalues $[RL(L+1)]^{-1}$ appropriate for the rotational diffusion operator. (For $R/\beta \ll 1$, the result is of course just $[RL(L+1)]^{-1}$ cf. eq 33.) This is equivalent to approximating the $j_L(\omega)$ of eq 35 to a Lorentzian. In actual fact, it is highly

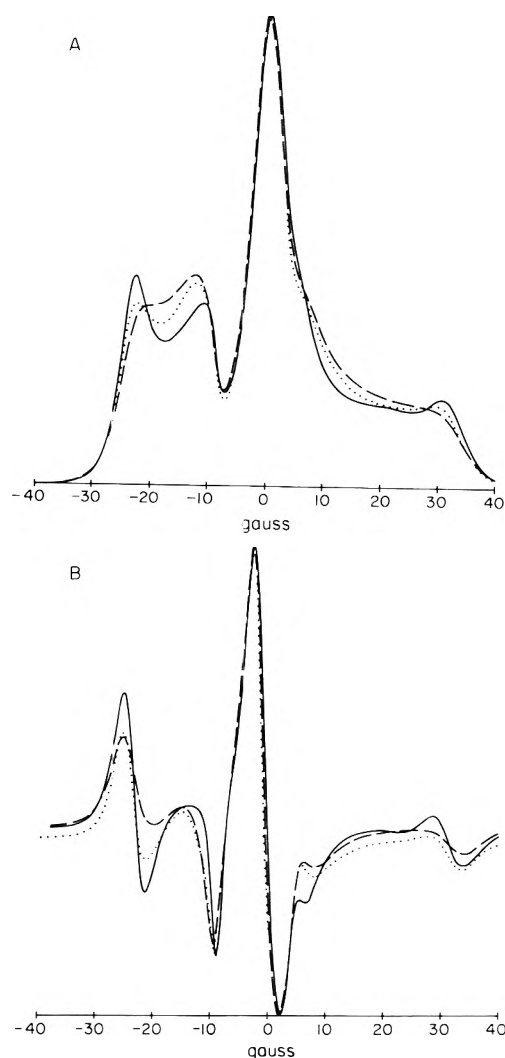


Figure 2. Comparison of line shapes for axial nitroxide for different free rotational diffusion models: A, absorption line shapes; B, first derivative line shapes. The different rotational diffusion models are, simple Brownian diffusion with $R = 0.0856|\mathfrak{F}|$ ($\tau_R = 2.10 \times 10^{-8}$ sec); ———, motion described in one-dimensional angular momentum space with $\beta = 4R$ and $R = 0.164|\mathfrak{F}|$ ($\tau_R = 2.16 \times 10^{-8}$ sec); - - - -, simple free diffusion with $\beta/R = (R\tau)^{-1} = 4$ and $R = 0.182|\mathfrak{F}|$ ($\tau_R = 1.58 \times 10^{-8}$ sec). All have $g_{\parallel} = 2.00270$, $g_{\perp} = 2.00750$, $A_{\parallel} = 32$ G, $A_{\perp} = 6$ G, $B_0 = 3300$ G, and $(2/3^{1/2})T_2^{-1}/|\gamma_e| = 0.3$ G.

non-Lorentzian for $L(L+1)R/\beta \geq 1$, becoming a Gaussian for $L(L+1)R/\beta \gg 1$. Also, the deviations from Lorentzian character of $j_L(\omega)$ are greater for greater values of ω , i.e., the short-time effects are more important.⁹ Thus as the tumbling slows down and $\tau > R/\beta$, then, e.g., $j_2(\omega - \omega_0 - (2/7)\mathfrak{F})$ is no longer well approximated by a Lorentzian over the region of ω for which there is a nonnegligible ESR signal.

There is still another and more serious way in which an Egelstaff-type approximation breaks down for $\mathfrak{F} \geq R/\beta$. In eq 31 $C_{0,0}$ is coupled to the $C_{L,0}$ ($L > 0$) by \mathfrak{K}_1 and these $C_{L,0}$ then couple to the $C_{L,n}$ ($n > 0$) (by the inertial terms) which then bring in the effects of the angular velocity diffusion. As \mathfrak{F} becomes larger, the coupling of the $C_{L,n}$ to the $C_{L,n}$ ($n \geq 0$) becomes important, leading, for example, to indirect coupling of the $C_{0,0}$ to the $C_{0,n}$ ($n > 0$) indicating that the mixing of effects of angular velocity diffusion into the spectrum is becoming more complex than even that predicted only by the frequency dependent

$j_L(\omega)$ given by eq 35.¹⁵ This represents the kind of complication which sets in when several time scales (*i.e.*, spin-relaxation, orientational relaxation, and angular velocity diffusion) all become comparable.

While we have discussed the complicating effects of inertial motion on slow tumbling spectra in terms of the approximate model, similar problems apply to the more complex situations for the more rigorous descriptions of inertial effects. However, as we shall find, they appear to have a *canceling* effect.

III. Results

(A) *Single-Line Axially Symmetric g Tensor.* One finds that for $\beta \gg R$ the proper Brownian rotational diffusion results are obtained for all inertial models of section II in both the fast and slow motional region. However, for $\beta \leq R$ they exhibit significant differences. This is illustrated in Figure 1 for $\beta = 4R$ for line shapes calculated from eq 27–28 and 31–32. Also included for comparison are the line shapes for Brownian rotational diffusion and for the simple free diffusion model. All models were calculated to have the same rotational correlation time τ_R , such that, if the spectrum were in the fast motional region, all models would give the same Lorentzian width.^{2a} While all the inertial-effect models yield spectra which deviate somewhat from that for Brownian rotational diffusion, one is struck by the fact that the approximate one-dimensional angular momentum model of eq 31 yields results qualitatively different from any other case. It shows the inertial effects for this model lead to a sharpening of the features of the Brownian rotational diffusion spectrum, while the line shapes from the complete model of eq 28 as well as the simple free diffusion case show the inertial effects to cause a smoothing out of the features. The results for the latter two cases are quite similar. We have also found that line shapes calculated for extended diffusion (eq 21 for eq 28 and eq 14 for eq 31) give results which deviate only very slightly from the line shapes for the Langevin diffusion model (eq 20 for eq 28 and eq 31).

(B) *Axial Nitroxide.* The detailed equations for all the inertial models considered above are given by Bruno.¹³ We show in Figure 2 a comparison of the line shapes calculated for $\beta = 4R$ for all models except the complete three-dimensional angular momentum case,¹³ since this case is extremely complex. The value of R was slightly adjusted in each of the models so that the distance between the outer first derivative extrema would be the same. As was seen for the axially symmetric g tensor, the inertial

effects from the approximate one-dimensional momentum produce line shapes with sharper features than the Brownian rotational diffusion. This is again in direct contrast to the simple free rotational diffusion model line shape (as well as any of the comparable appearing line shapes for the moderate jump models discussed in ref 2a).

It is anticipated, from the results for the g tensor case and the similar structure of the equations in that case and that for the axial nitroxide,¹³ that the complete three-dimensional angular-momentum treatment will yield line shapes similar to those for the simple free-diffusion results. In that case it would still be difficult to distinguish an inertial model from that of moderate jump models on the basis of line shape alone, and other considerations would be required.^{2b}

References and Notes

- (1) Supported in part by the National Science Foundation (Grant No. GP-13780) and the Materials Science Center, Cornell University.
- (2) (a) S. A. Goldman, G. V. Bruno, C. F. Polnaszek, and J. H. Freed, *J. Chem. Phys.*, **56**, 716 (1972); (b) J. Hwang, R. P. Mason, and J. H. Freed, to be submitted for publication.
- (3) R. Kubo, *Advan. Chem. Phys.*, **15**, 101 (1969); *J. Phys. Soc. Jap., Suppl.*, **26**, 1 (1969).
- (4) J. H. Freed, G. V. Bruno, and C. F. Polnaszek, *J. Phys. Chem.*, **75**, 3385 (1971). Hereafter referred to as I.
- (5) A recent review is given by J. H. Freed, *Ann. Rev. Phys. Chem.*, **23**, 265 (1972).
- (6) M. Fixman and K. Rider, *J. Chem. Phys.*, **51**, 2425 (1969).
- (7) (a) R. A. Sack, *Proc. Phys. Soc. (London)*, **70**, 402 (1957); (b) **70**, 414 (1957); (c) P. S. Hubbard, *Phys. Rev. A*, **6**, 2421 (1972); **8**, 1429 (1973), has very recently also treated the solutions of the Langevin equation for a spherical top. His mathematical analysis proceeds somewhat differently from that of Fixman-Rider, although the Langevin model considered is the same. All these authors considered, of course, only the correlation functions appropriate for the motional narrowing problem in magnetic resonance. Hubbard's mathematical treatment, designed to give a perturbation expansion in the parameter R/β does not appear to be as convenient for adaptation to the slow tumbling problem as we have found the Fixman-Rider approach. Hubbard does find that the early Steele model (ref 14) gives unsatisfactory corrections to the correlation functions for nonnegligible R/β , and this, in our quite different slow tumbling context, is also found to be the case as discussed below.
- (8) C. F. Polnaszek, G. V. Bruno, and J. H. Freed, *J. Chem. Phys.*, **58**, 3185 (1973).
- (9) J. H. Freed, "ESR Relaxation in Liquids," L. T. Muus and P. W. Atkins, Ed., Plenum, New York, N. Y., 1972, Chapter VIII.
- (10) J. H. Freed, *J. Chem. Phys.*, **56**, 1407 (1972).
- (11) R. G. Gordon, *J. Chem. Phys.*, **44**, 1830 (1966).
- (12) In the coupled representation the effect of $\mathcal{K}_L(\Omega)$ in the slow tumbling problem is to destroy the invariance of $J = L$ which exists in motional narrowing problems.
- (13) G. V. Bruno, Ph.D. Thesis, Cornell University, Ithaca, N. Y., 1973.
- (14) W. A. Steele, *J. Chem. Phys.*, **38**, 2404, 2411 (1963).
- (15) This latter effect can be traced to the fact that $\mathcal{K}_L(\Omega)$ is *not* an explicit function of angular velocity. If the term in $\mathcal{K}_L(\Omega)$ of eq 31 were simply multiplied by $\delta_{n,0}$, one may show that the resulting expressions are equivalent to eq 33 with $RL(L+1) \rightarrow [j_L(\omega - \omega_0 - \dot{\phi})]^{-1}$.

Infrared Attenuated Total Reflection Spectra of Adsorbed Layers at the Interface between a Germanium Electrode and an Aqueous Solution of Sodium Laurate

Tatsuo Higashiyama

College of Liberal Arts, Okayama University, Tsushima, Okayama 700, Japan

and Tohru Takenaka*

Institute for Chemical Research, Kyoto University, Uji, Kyoto-Fu 611, Japan (Received September 24, 1973)

Polarized infrared attenuated total reflection (ATR) measurements have been made on thin layers adsorbed on a germanium ATR plate electrode from an aqueous solution of sodium laurate. A platinum plate was immersed in the solution as an auxiliary electrode and was electrically connected to the germanium plate. When necessary, electric potentials lower than 0.5 V were applied between the two plates. It is found that when the concentration of the aqueous solution is less than *ca.* 10 mM, the adsorbed layers consist of an assembly of crystallites of lauric acid. The crystallites are monoclinic and uniaxially oriented so that their crystallographic *c* axes make an angle of 39° with the *z* axis normal to the germanium surface. Reference to the crystal structure of lauric acid indicates that the axes of the hydrocarbon chains of the lauric acid molecules also give rise to uniaxial orientation and make an angle of 35° with the *z* axis. When the concentration of the aqueous solution approaches or exceeds the critical micelle concentration, laurate ion micelles are adsorbed, in which the hydrocarbon chains are flexible and the carboxylate groups are oriented so that their bisectors are almost normal to the germanium surface. The electric potential applied between the germanium and platinum plates influences the adsorption phenomena. Effects of pH and temperature are also considered. A possible mechanism for the acid adsorption is proposed.

Introduction

Many studies have been made on infrared transmission spectra of adsorbed molecules on solid surface.^{1,2} This method is very sensitive, and the shape and position of absorption bands are affected not only by the structure and motion of adsorbed molecules but also by their surroundings. However, little information has been obtained about the orientation of adsorbed molecules, because fine powders with large surface area have been used as adsorbents and the infrared dichroism of absorption bands due to the adsorbed molecules cannot be observed.

Harrick³ and Fahrenfort,⁴ on the other hand, have proposed the technique of attenuated total reflection (ATR) for obtaining infrared spectra of organic compounds which cannot be readily studied by transmission measurements. Since the infrared radiation totally reflected within optically transparent crystals of high refractive index interacts with materials closely attached to the surface of the crystals, the ATR method is useful in studies of the structure of thin surface layers, such as adsorbed layers and built-up films. Furthermore, application of polarized infrared radiation to the ATR method gives information about molecular orientation in surface layers. In fact, using the polarized infrared ATR method, Takenaka and coworkers⁵⁻⁷ have studied molecular structure and orientation in built-up films transferred from monolayers spread on water to germanium ATR plates. Haller and Rice⁸ have demonstrated the usefulness of this method in studies of alcohol adsorption on surfaces of known structure of single-crystal α -aluminum oxide. Low and coworkers⁹ have studied adsorption of stearic acid from carbon tetrachloride solution onto surfaces of germanium and α -aluminum oxide plates. Furthermore, Harrick¹⁰ has discussed an ATR theory for

thin films on transparent substrates, and Hansen¹¹⁻¹³ has derived general approximate equations for the change in reflectance of a stratified medium due to the presence of very thin films. These theoretical works are significant in analysis of the polarized infrared ATR studies of adsorbed layers.

In the present work, the method was extended to studies of molecular structure and orientation in thin layers adsorbed at the interface between a germanium ATR plate electrode and an aqueous solution of sodium laurate. A platinum plate was immersed in the aqueous solution as an auxiliary electrode and was electrically connected to the germanium plate. When necessary, electric potentials lower than 0.5 V were applied between the germanium and platinum plates, the former being positive. In these studies, the conducting germanium plate served as the ATR plate and the adsorbent, and further as the electrode. The electric potential applied across the interface influenced the adsorption phenomena. The effects of concentration, pH, and temperature were also considered.

Experimental Section

A sample of sodium laurate was synthesized and purified as previously reported.¹⁴ Pure water was prepared by redistillation in Pyrex of distilled water which had passed through an ion-exchange resin column.

Polarized infrared ATR spectra of adsorbed layers on the germanium plate were recorded on a Perkin-Elmer Model 521 grating spectrophotometer equipped with a Perkin-Elmer multiple ATR attachment and a wire grid polarizer. The ATR attachment has been designed so as to provide an internal angle of incidence of 45°. The details of an adsorption cell which fits into the ATR attachment

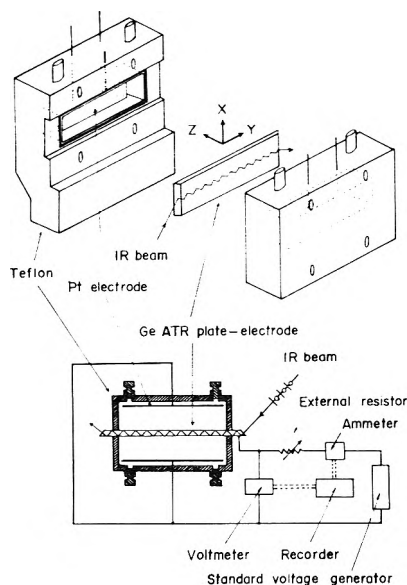


Figure 1. Schematic drawing of adsorption cell for ATR measurements and electric circuit.

are shown in Figure 1, together with the electric connection. The cell was essentially the same as that designed by Mark and Pons,¹⁶ who have made infrared ATR studies of chemical species at electrode surfaces during electrolysis. It was composed of two solution holders¹⁷ made of Teflon, and also served as a holder for the germanium trapezoidal ATR plate, 50 mm long, 18 mm high, and 2 mm thick. The plate was made of monocrystalline pure germanium which had a specific resistance of $40 \Omega \text{ cm}$. The effective adsorption area of the germanium plate which was in contact with the sample solution was $39 \text{ mm} \times 12 \text{ mm}$ on each face. These dimensions and an internal angle of incidence of 45° gave 20 reflections of the radiation at the germanium-solution interfaces. Infrared radiation passing through both the upper and lower surfaces of the germanium plate *outside* of the effective adsorption area was eliminated by covering them with pieces of aluminum foil.

A platinum plate, 36 mm long and 9 mm high, was inserted in each solution compartment as an auxiliary electrode at a distance of *ca.* 10 mm from the germanium plate and was electrically connected to the germanium plate. When necessary, electric potentials lower than 0.5 V (dc) were applied between the germanium and platinum plates by use of a standard voltage generator. In such cases, the conducting germanium plate served not only as the ATR plate and the adsorbent but also as the electrode. The current and the potential difference between the two plate electrodes were measured, and sometimes recorded.

After each experiment, the germanium plate was repolished on a plane ground pitch plate covered with a silk cloth. A Linde polishing material dispersed in a detergent solution was used. The plate was then thoroughly rinsed with water followed by ultrasonic cleaning in ethyl alcohol and in chloroform.

X-Ray diffraction patterns of the adsorbed layers were obtained by means of a Rigaku Denki X-ray diffractometer.

All adsorption studies were carried out in a room of constant temperature ($25 \pm 0.2^\circ$) and constant humidity ($45 \pm 2\%$).

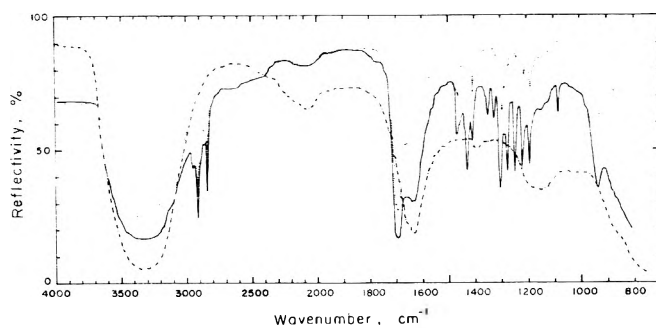


Figure 2. Infrared ATR spectra of water (chain line) and lauric acid adsorbed from a 2 mM aqueous solution of sodium laurate. Solid and dotted lines refer to the orientation of the electric vectors parallel (R) and perpendicular (R_{\perp}) to the plane of incidence, respectively.

Results and Discussion

(A) *Spectra and Structure of Adsorbed Layers.* The adsorption studies were first carried out for a 2 mM aqueous solution of sodium laurate at pH of 7.2. When this solution was introduced into the adsorption cell with the electrodes disconnected, the infrared ATR spectrum was recorded as shown by the chain line in Figure 2. The identical spectrum was obtained even 1 hr after the introduction of the solution. This spectrum is merely that of water with weak peaks (at *ca.* 1400 and 1150 cm^{-1}) due to rubber packings.¹⁸ This indicates that no adsorption of chemical species except water takes place on the germanium surfaces.

It was found in this aqueous solution that an electric potential of *ca.* 0.8 V was generated between the germanium and platinum electrodes, the latter being positive. When the electrodes were connected, all the water peaks at *ca.* 3350, 2100, and 1650 cm^{-1} began to weaken and a number of new peaks began to appear. The peak intensities reached constant values in *ca.* 60 min after the electric connection was made (Figure 3). These facts suggest that the water molecules which were previously adsorbed on the germanium surfaces were replaced with other species, and that an equilibrium was achieved in *ca.* 60 min. The current was *ca.* 0.1 mA at first and decreased with time attaining the constant value of *ca.* 0.06 mA in *ca.* 60 min, showing a good correspondence to the changes in the peak intensities. Figure 2 also shows the polarized infrared ATR spectra of the adsorbed layer recorded after equilibrium is achieved. The solid line refers to an orientation of the electric vector parallel to the plane of incidence (R) and the dotted line refers to the electric vector perpendicular to that (R_{\perp}). Apparently the new peaks cannot be ascribed to sodium laurate¹⁴ but are characteristic of lauric acid.^{19,20} Assignments of the major peaks have been well established; the 2920- and 2850-cm^{-1} peaks are attributable to the antisymmetric and symmetric CH_2 stretching vibrations, respectively, the broad peak at 1700 cm^{-1} to the $\text{C}=\text{O}$ stretching vibration, the 1465-cm^{-1} peak to the CH_2 scissoring vibration, the 1410-cm^{-1} peak to the same vibration of the α -methylene group, the 1430- and 1300-cm^{-1} peaks to the coupled COH in-plane deformation and C-O stretching vibrations, and the 930-cm^{-1} peak to the OH out-of-plane deformation vibration. The fact that the adsorption of lauric acid takes place at the interface between the germanium plate and the aqueous solution of sodium laurate suggests that a reaction of sodium laurate to give lauric acid occurs at the

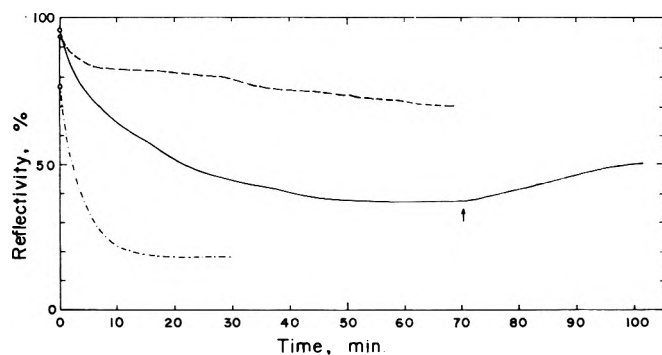


Figure 3. Change in reflectivity for the 2920-cm^{-1} peak during the course of adsorption: solid line, $R = 0\ \Omega$ and $E = 0\ \text{V}$; broken line $R = 5\ \text{k}\Omega$ and $E = 0\ \text{V}$; chain line, $R = 0\ \Omega$ and $E = 0.5\ \text{V}$.

interface. The appearance of regularly spaced peaks (the progression bands) of medium intensity between 1350 and $1180\ \text{cm}^{-1}$ (assigned mainly to the CH_2 wagging vibration¹⁹⁻²²) indicates that the hydrocarbon chains of the adsorbed molecules are in the planar trans-zigzag configuration,^{23,24} and that the adsorbed layer is in the crystalline state.^{19,20} The number and the position of the progression band are indicative of the presence of ten CH_2 groups in each hydrocarbon chain of the adsorbed molecules.²¹

In Figure 2, extremely high parallel polarization is found for the progression bands as well as for the 1430-cm^{-1} peak, while apparent but low parallel polarization is seen for the remaining major peaks. This indicates that lauric acid assumes a certain orientation in the adsorbed layer with respect to the z axis normal to the germanium surface (see Figure 1). Detailed discussions of the molecular orientation will be given in the latter parts of this paper.

Figure 3 represents the change in the amount adsorbed with time as indicated by the change in reflectivity for the 2920-cm^{-1} peak. The solid line shows the reflectivity change recorded without external resistance (Figure 1).²⁵ The reflectivity decreases with time and attains an equilibrium value in ca. 60 min, as mentioned above.²⁶ If the electric circuit is disconnected at this stage (the arrow in Figure 3), the reflectivity gradually increases, indicating the desorption of the adsorbed molecules. When an external resistance of $5\ \text{k}\Omega$, for example, is inserted in the circuit, the decrease of the reflectivity becomes very slow as shown by the broken line in Figure 3. When, on the other hand, an electric potential of $0.5\ \text{V}$ is applied between the positive germanium and negative platinum electrodes without the external resistance, the reflectivity decreases very rapidly and reaches a small constant value in ca. 20 min (the chain line in Figure 3). In spite of the large differences in rates and amounts of adsorption, the polarized ATR spectra of the adsorbed layers were qualitatively the same in the three cases. Application of higher voltages, of over $3\ \text{V}$, yielded a rapid decrease of the reflectivity followed by a gradual increase. In the latter stage, a generation of small bubbles of oxygen was observed around the germanium electrode in the aqueous solution. It is therefore conceivable that the electrolysis of water becomes appreciable at such higher voltages, resulting in the desorption of the molecules from the germanium surfaces.

In Figure 4, the polarized ATR spectrum (R_{\parallel}) of the adsorbed layer on the germanium plate in the aqueous solution (the dotted line) is compared with that for the same sample recorded after the germanium plate was re-

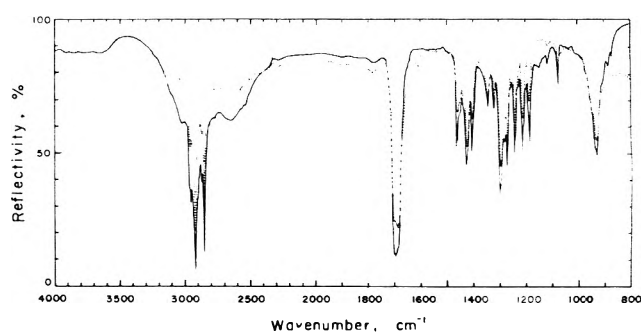


Figure 4. Comparison of ATR spectra (R) of the adsorbed layer recorded in the aqueous solution (dotted line) and in air (solid line). For ready comparison, the water peaks in the dotted line were cancelled by use of compensation in the reference beam.

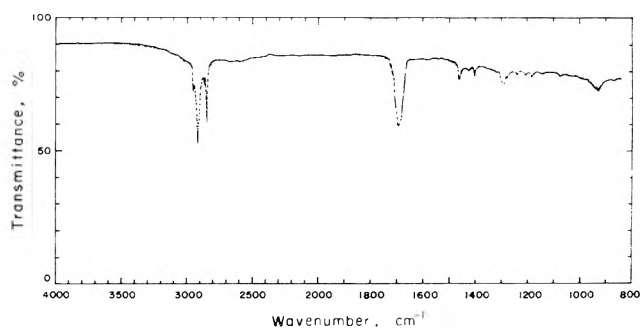


Figure 5. Polarized infrared transmission spectra of lauric acid adsorbed from a $2\ \text{mM}$ aqueous solution of sodium laurate recorded in air. Solid and dotted lines refer to the orientation of the electric vectors parallel to the x and y axes of the germanium plate, respectively.

moved from the aqueous solution and air dried at room temperature (the solid line). For ready comparison, the water peaks in the dotted line were cancelled by use of compensation in the reference beam. Although there is a close resemblance between the two, the peaks are apparently stronger in the solid line than in the dotted line. This is also true for the P_{\perp} spectra. It is obvious from these facts that the molecular orientation in the adsorbed layer may be identical in both states. Calculations of the mean square electric field at the germanium-solution interface and that at the germanium-air interface by use of equations of Hansen²⁷ (eq 5-7 in the next section) lead to the conclusion that peaks of the adsorbed layer are stronger in the aqueous solution than in air for parallel and perpendicular polarization.¹¹⁻¹³ Apparently, the reverse is the case of Figure 4. On the other hand, Fujiyama²⁸ has theoretically pointed out that if there is a transparent thin layer between an ATR plate and absorbing film, the peak intensity of the film is decreased to some extent depending upon the thickness of the transparent layer. Therefore, one possible interpretation of the intensity difference observed in Figure 4 is that there is a thin layer of bound water between the germanium plate and the adsorbed layer in the aqueous solution. Details of the water layer have not been obtained as yet.

Polarized transmission spectra of the adsorbed layer, the ATR spectra of which were given in Figure 2, were recorded in air and reproduced in Figure 5. The solid and dotted lines refer to the orientation of the electric vectors parallel to the x and y axes (Figure 1) of the germanium plate, respectively. The two spectra are identical irrespective of the direction of the electric vectors. From this fact

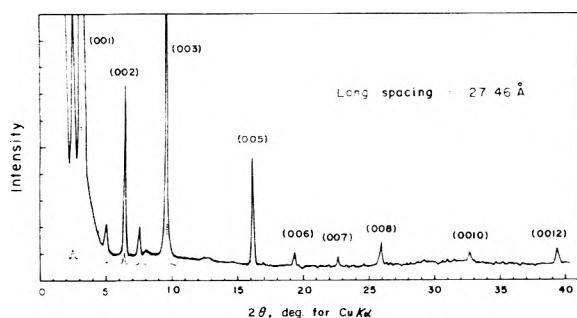


Figure 6. X-Ray diffraction pattern of lauric acid adsorbed from a 2 mM aqueous solution of sodium laurate.

and the above-mentioned results of the polarized ATR spectra in Figure 2, it may be concluded that the adsorbed molecules are at random in the xy plane but assume a certain orientation along the z axis. In other words, the molecules may give rise to a uniaxial orientation with respect to the z axis.

Figure 6 shows the X-ray diffraction patterns of the adsorbed layer. An analysis of the main peaks yields a long spacing of 27.46 Å. This value is in good agreement with one of the unit-cell parameters $c \sin \beta = 27.42$ Å of the lauric acid crystals (C form) given by Vand, Morley, and Lomer,²⁹ who have reported from X-ray analysis that the crystal is monoclinic with $a = 9.524$, $b = 4.965$, $c = 35.39$ Å, and $\beta = 129^\circ 13'$. This agreement and the results of uniaxial orientation of the lauric acid molecules in the adsorbed layer reveal that it consists of an assembly of C-form crystallites,³⁰ which are oriented so that their crystallographic ab planes are parallel to the germanium surface (the xy plane) and the c axes give rise to uniaxial orientation with respect to the z axis with an angle of $39^\circ 13'$ between the c and z axes. Therefore, reference to the crystal structure of lauric acid²⁹ indicates that the axes of the hydrocarbon chains of the lauric acid molecules make uniaxial orientation around the z axis with an angle of 35° between the chain axis and the z axis. This will be confirmed by means of ATR spectroscopy in the next section.

(B) *Quantitative ATR Studies of Molecular Orientation.* It is well known in reflection measurements of a stratified medium that the reflectivities R_{\parallel} and R_{\perp} for polarized radiations with the electric vectors parallel and perpendicular to the plane of incidence are generally expressed by complicated equations including the angle of incidence θ_1 and the complex refractive index \hat{n} which is shown by

$$\hat{n} = n + ik \quad (1)$$

Here n is the real part of the refractive index, and k is a constant called the extinction coefficient and appears in Lambert's absorption coefficient α which is given by

$$\alpha = 4\pi k/\lambda \quad (2)$$

where λ is the wavelength of radiation *in vacuo*.

Recently, Hansen¹¹⁻¹³ has derived general approximate equations for reflectivity changes caused by the presence of very thin films (much thinner than a quarter wavelength) such as adsorbed layers. Here we consider a three-phase plane-bounded system shown in Figure 7. Phase 1 is the semiinfinite incident phase which is germanium in the present case, phase 2 the anisotropic adsorbed layer of thickness h_2 , and phase 3 the semiinfinite final phase which is aqueous solution or air. The plane of incidence is the yz plane, the y and z axes being parallel and perpen-

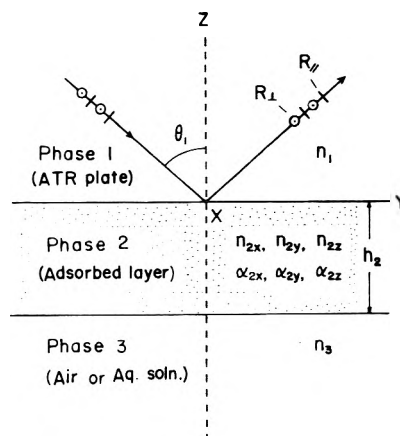


Figure 7. Geometry for attenuated total reflection from a three-phase plane-bounded system with anisotropic second phase and transparent initial and final phases.

dicular to the interfacial plane, respectively. The x axis is perpendicular to the plane of incidence.

In the present case of internal reflection, the change in reflection adsorbance, $\Delta A \equiv \log (R_0/R)$, caused by the thin film is given by the following equations for perpendicular and parallel polarization

$$\Delta A_{\perp} = \frac{n_{2x}\alpha_{2x}h_2N}{\ln 10n_1 \cos \theta_1} \langle E^2 \rangle_x^0 \quad (3)$$

and

$$\Delta A_{\parallel} = \frac{h_2N}{\ln 10n_1 \cos \theta_1} \left\{ n_{2y}\alpha_{2y} \langle E^2 \rangle_y^0 + \frac{n_z^4}{(n_{2z}^2 + k_{2z}^2)^2} n_{2z}\alpha_{2z} \langle E^2 \rangle_z^0 \right\} \quad (4)$$

Here R_0 is the reflectivity when the film does not absorb. The numerical subscripts refer to the phase, n_{2x} , n_{2y} , and n_{2z} are components of the refractive index of the film along the x , y , and z axes, respectively, α_{2x} , α_{2y} , and α_{2z} are those of the absorption coefficient, and N is the number of reflections. The subscript s refers to a standard reference film which has similar refractive index and thickness to the adsorbed layer and $\alpha = 0$. Furthermore, $\langle E^2 \rangle_x^0$, $\langle E^2 \rangle_y^0$, and $\langle E^2 \rangle_z^0$ are three components of the mean square electric field at the interface in the no-film case, where phase 1 is directly attached to phase 3. In the ATR region where θ_1 is greater than the critical angle, they are given by²⁷

$$\langle E^2 \rangle_x^0 = \frac{2\xi_1^2}{n_1^2 - n_3^2} \quad (5)$$

$$\langle E^2 \rangle_y^0 = -\frac{2\xi_3^2}{n_3^2} \frac{\xi_1^2}{n_3^2 \cos^2 \theta_1 - n_1^2 \cos^2 \theta_3} \quad (6)$$

and

$$\langle E^2 \rangle_z^0 = \frac{2n_1^2 \sin^2 \theta_1}{n_3^2} \frac{\xi_1^2}{n_3^2 \cos^2 \theta_1 - n_1^2 \cos^2 \theta_3} \quad (7)$$

if those in the incident radiation are taken as unity. For any phase j , $\xi_j = \hat{n}_j \cos \theta_j = (\hat{n}_j^2 - n_1^2 \sin^2 \theta_1)^{1/2}$, where θ_3 is the angle of refraction in phase 3, and ξ_3^2 is negative in this case.

By using proper values, $n_1 = 4.00$ for germanium, $n_3 = 1.00$ for air, $\theta_1 = 45^\circ$, and $N = 20$, and making the convenient assumption that $n_{2x} = n_{2y} = n_{2z} = n_3 = 1.44$,³² from eq 3-7 we have

$$\Delta A_{\perp} = 4.72\alpha_{2x}h_2 \quad (8)$$

and

$$\Delta A_{\parallel} = 4.40\alpha_{2y}h_2 + 5.03\alpha_{2z}h_2 \quad (9)$$

In this calculation, k_{2z}^2 of the denominator in the second term of eq 4 is neglected, because it is much less than unity.

If, on the other hand, it is possible to make transmission measurements of the sample film, we can obtain the dichroic ratio D_{xy} as the ratio between the absorbances A_x and A_y for normal incident radiations polarized along the x and y axes, and we have

$$D_{xy} = A_x/A_y = \alpha_{2x}/\alpha_{2y} \quad (10)$$

Therefore, measurements of R_{\parallel} and R_{\perp} in eq 8 and 9 and D_{xy} in eq 10 will yield the values of $\alpha_{2x}h_2$, $\alpha_{2y}h_2$, and $\alpha_{2z}h_2$, and make possible discussions of molecular orientation.

As was seen in Figure 5, the adsorbed layer of lauric acid gives rise to identical transmission spectra irrespective of the direction of the electric vectors of polarized radiations. This means from eq 10 that $D_{xy} = 1$ and $\alpha_{2x} = \alpha_{2y}$ for all the peaks measured. Therefore, if the values of R_{\parallel} and R_{\perp} are obtained from the polarized ATR spectra of the adsorbed layer, we can calculate the values of $\alpha_{2x}h_2 (= \alpha_{2y}h_2)$ and $\alpha_{2z}h_2$ from eq 8 and 9.

In this study, the antisymmetric and symmetric CH_2 stretching vibration peaks at 2920 and 2850 cm^{-1} are used for evaluations of $\alpha_{2x}h_2$ and $\alpha_{2z}h_2$, because these vibrations are known to be pure modes which do not mix with other modes. Both their transition moments M_{2920} and M_{2850} lie in the plane of the methylene group, the latter pointing in the direction of the bisector of the HCH angle and the former being normal to it. Therefore, M_{2920} , M_{2850} , and the axis of the hydrocarbon chain are mutually perpendicular. Thus, from the values of R_{\parallel} and R_{\perp} for the 2920- and 2850- cm^{-1} peaks obtained from the air-dried layer of Figure 2 we have the values of $\alpha_{2x}h_2$ and $\alpha_{2z}h_2$ as shown in Table I.

In the case of uniaxial orientation of the crystallites mentioned above, the orientations of the three mutually perpendicular axes are shown in Figure 8. According to Fraser,³⁴ the angle ϵ between the z axis and M_{2920} and the angle θ between the z axis and M_{2850} are expressed by

$$(\alpha_{2z}/\alpha_{2x})_{2920} = 2 \cot^2 \epsilon \quad (11)$$

and

$$(\alpha_{2z}/\alpha_{2x})_{2850} = 2 \cot^2 \theta \quad (12)$$

Furthermore, if ϕ is the angle between the z axis and the axis of the hydrocarbon chain, we have

$$\cos^2 \epsilon + \cos^2 \theta + \cos^2 \phi = 1 \quad (13)$$

The results of this calculation for the adsorbed molecules are given in Table I. Taking into account the rough approximation used in the calculation as well as the experimental errors introduced in the present study, the value $\phi = 32^\circ$ thus obtained is in satisfactory agreement with the above-mentioned value of 35° obtained from X-ray analysis of the lauric acid crystal.²⁹ This indicates the appropriateness of the above-mentioned hypothesis of uniaxial orientation of the crystallites.

A high parallel polarization of the progression bands (mainly due to the CH_2 wagging vibration¹⁹⁻²²) in Figure 2 can be understood easily on the basis of this result, be-

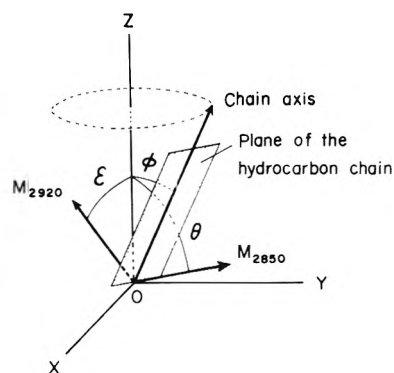


Figure 8. Uniaxial orientation of transition moments M_{2920} and M_{2850} and of the axis of the hydrocarbon chain around the z axis.

TABLE I: Orientation of Lauric Acid Adsorbed from a 2 mM Aqueous Solution of Sodium Laurate

| Wave number, cm^{-1} | $\alpha_{2x}h_2$ (= $\alpha_{2y}h_2$) | $\alpha_{2z}h_2$ | α_{2z}/α_{2x} | Angles |
|-------------------------------|---|------------------|---------------------------|---|
| 2920 | 0.117 | 0.0477 | 0.408 | $\epsilon = 66^\circ$ $\theta = 70^\circ$ $\phi = 32^\circ$ |
| 2850 | 0.0847 | 0.0215 | 0.254 | |

cause their transition moments lie toward the axis of the hydrocarbon chain.

(C) *Effect of Various Factors.* The adsorption phenomena in the present study were found to be influenced by various factors such as concentration, pH, and temperature of the aqueous solution as well as the electric potential applied between the two electrodes. The effect of the electric potential on the adsorption rate and amount of lauric acid was shown in Figure 3.

When the pH of a 2 mM aqueous solution of sodium laurate was raised to 9.9, for example, by the addition of sodium hydroxide, no adsorption occurred even 1 hr after the two electrodes were connected. Adsorption was observed, however, when an electric potential higher than ca. 0.2 V was applied between the two electrodes, the germanium electrode being positive.

It was also found that the pH of the aqueous solution of sodium laurate increased with concentration, and the amount of lauric acid adsorbed on the germanium plate decreased with an increase in concentration. When, however, the concentration of the aqueous solution was greater than ca. 10 mM (pH \sim 8.1), the adsorbed layer gave rise to ATR spectra different from those of lauric acid. Figure 9 shows the polarized ATR spectra of the surface layer adsorbed from a 30 mM solution (pH 9.0) with the electrodes connected. Since the peaks of the adsorbed layer were weak in the aqueous solution,³⁵ the spectra were recorded after the plate was removed from the solution and slightly dried by use of a water aspirator. Though the peak intensities were increased about threefold in the reflectivity scale by these operations, the spectra were quite similar to those obtained in the aqueous solution. This may also be interpreted as indicating the presence of bound water between the germanium surface and the adsorbed layer as mentioned in the case of acid adsorption.

Apparently, the spectra in Figure 9 are similar to the transmission spectra of the concentrated aqueous solution of sodium laurate.¹⁴ This suggests that the chemical species adsorbed under these conditions are laurate ions probably forming micelles. Since the critical micelle con-

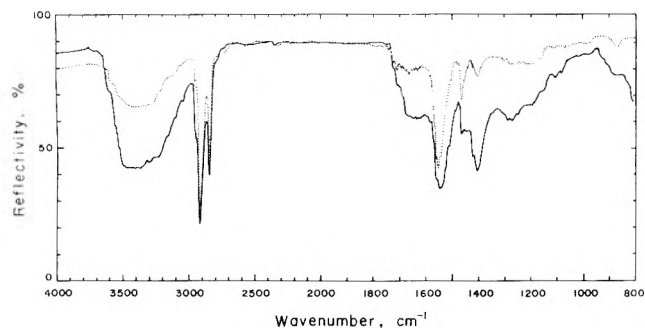


Figure 9. Polarized infrared ATR spectra of laurate ion adsorbed from a 30 mM aqueous solution of sodium laurate recorded in the dry state. Solid and dotted lines refer to the orientation of the electric vectors parallel ($R_{||}$) and perpendicular (R_{\perp}) to the plane of incidence, respectively.

centration (cmc) of the aqueous solution of sodium laurate is roughly 20 mM at room temperatures, we can conclude that the adsorption of the laurate ion micelles would take place at concentrations approaching or greater than the cmc.

Disappearance of the sharp progression bands between 1350 and 1180 cm^{-1} means that the hydrocarbon chains of laurate ions are flexible and twisting in the adsorbed micelles. In other words, the methylene groups in the hydrocarbon chains are spinning about the C-C bonds in the adsorbed layers.

While a parallel dichroism is observed for the peaks at 2920 (the antisymmetric CH_2 stretching vibration), 2850 (the symmetric CH_2 stretching vibration), 1550 (the antisymmetric COO^- stretching vibration), and 1460 cm^{-1} (the CH_2 scissoring vibration), an extremely high parallel dichroism can be seen for the 1410- cm^{-1} peak attributed mainly to the symmetric COO^- stretching vibration. Since the transition moment of this vibration lies in the COO^- plane pointing in the direction of the bisector of the OCO angle, carboxylate groups are probably oriented in the adsorbed layer so that their bisectors are almost normal to the plane of the interface. It is interesting that the broad peaks of water centered at ca. 3350 and 1650 cm^{-1} give rise to very high dichroism along the plane of incidence. This is indicative of a pronounced orientation of the water molecules, which may be bound to the OH groups of the germanium surface through hydrogen bonding.

When a lower electric potential was applied between the two electrodes, both the rate and amount of micelle adsorption increased to some extent. When, however, a higher electric potential was applied, the adsorbed layers were found to be changed from laurate ion micelles to lauric acid crystallites, the boundary value of the electric potential being dependent upon pH and concentration. It was ca. 2 V for a 20 mM aqueous solution (pH 8.7).

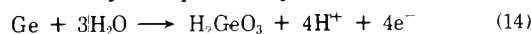
The effect of temperature on the adsorption phenomena was not so pronounced; the amount of the adsorbed species decreased with increasing temperature.

(D) *Mechanism of Acid Adsorption.* It is well known that laurate ion is hydrolyzed in aqueous solutions of sodium laurate and, in the course of time, lauric acid is liberated from the solutions especially at low concentrations. Therefore, the adsorption of lauric acid may result from this process. It was found, however, in the present study that the adsorption of lauric acid did not occur from a saturated aqueous solution of lauric acid including excess

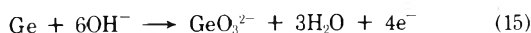
fine crystallites even when proper external electric potential was applied between the germanium and platinum electrodes. When, on the other hand, sodium hydroxide was added to this solution to bring its pH value to ~ 7 , the adsorption of lauric acid did occur. It is, therefore, likely that free acid is not adsorbed on the germanium plate, but the acid adsorption proceeds through the laurate ion.

If this is true, a reaction of laurate ion to give lauric acid should take place. If the required proton is directly supplied from the solvent water, the solution around the germanium electrode should become alkaline. However, pH measurements and colorimetric analyses with phenolphthalein indicated that the solution around the germanium electrode was not so highly alkaline, while the solution around the platinum electrode became highly alkaline, and the pH of the bulk solution increased as the adsorption proceeded. These facts suggest that the proton should be supplied from other sources.

It was also found in the present study that germanium dissolved into the solution during the course of adsorption. According to Beck and Gerischer,³⁶ the dissolution in acidic solution may be expressed by



and that in highly alkaline solution by

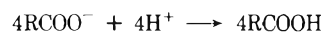


It is apparent from eq 14 and 15 that the dissolution of germanium into acidic solution may be a source of protons, whereas the dissolution into highly alkaline solution may not be a source.

Thus, one possible mechanism for acid adsorption on germanium from aqueous solutions of sodium laurate can be expressed as follows: at the germanium electrode



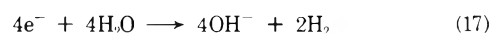
and



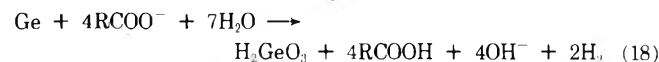
or, as a whole



and at the platinum electrode



Here, RCOO^- and RCOOH represent laurate ion and lauric acid, respectively. The overall reaction is therefore



Equation 18 means that the process of acid adsorption consists essentially of dissolution of germanium and hydrolysis of laurate ion followed by adsorption. Therefore, the process may be regarded as a kind of electrodeposition. This mechanism and the hypothesis that eq 15 is the predominant reaction in a highly alkaline solution may satisfactorily explain the above-mentioned fact that acid adsorption is suppressed by increasing the pH. Equation 18 may also explain the fact that acid adsorption is accelerated by application of an external electric potential between the germanium and platinum electrodes.

The two-electrode approach used in the present study may not allow ones to arrive at any real feel for the electrochemical potential of the germanium electrode surface. At this stage, however, the simple qualitative observation of potential dependency of the adsorption may be sufficient.

References and Notes

- (1) L. H. Little, "Infrared Spectra of Adsorbed Species," Academic Press, London, 1966.
- (2) M. L. Hair, "Infrared Spectroscopy in Surface Chemistry," Marcel Dekker, New York, N. Y., 1967.
- (3) N. J. Harrick, *J. Phys. Chem.*, **64**, 1110 (1960).
- (4) J. Fahrenfort, *Spectrochim. Acta*, **17**, 698 (1961).
- (5) T. Takenaka, K. Nogami, H. Gotoh, and R. Gotoh, *J. Colloid Interface Sci.*, **35**, 395 (1971).
- (6) T. Takenaka, K. Nogami, and H. Gotoh, *J. Colloid Interface Sci.*, **40**, 409 (1972).
- (7) T. Takenaka and K. Nogami, *Bull. Chem. Soc. Jap.*, **45**, 2367 (1972).
- (8) G. L. Haller and R. W. Rice, *J. Phys. Chem.*, **74**, 4386 (1970).
- (9) R. T. Yang, M. J. D. Low, G. L. Haller, and J. Fenn, *J. Colloid Interface Sci.*, **44**, 249 (1973).
- (10) N. J. Harrick, "Internal Reflection Spectroscopy," Interscience, New York, N. Y., 1967.
- (11) W. N. Hansen, in "Optical Studies of Adsorbed Layers at Interfaces," Symposia of the Faraday Society, No. 4, 1970.
- (12) W. N. Hansen in "Progress in Nuclear Energy," Series IX, Analytical Chemistry, Vol. 11, H. A. Elion and D. C. Stewart, Ed., Pergamon Press, Oxford, 1972.
- (13) W. N. Hansen in "Advances in Electrochemistry and Electrochemical Engineering," P. Delahay and C. W. Tobias, Ed., Vol. 9, Interscience, New York, N. Y., 1973.
- (14) R. Gotoh and T. Takenaka, *J. Chem. Soc. Jap. (Pure Chem. Sec.)*, **84**, 392 (1963).
- (15) This is the average value. The semiangle of the radiation cone incident upon the ATR plate is ca. 3° . The error due to this beam convergence was estimated to be relatively small and was ignored in this study.
- (16) H. B. Mark, Jr., and B. S. Pons, *Anal. Chem.*, **38**, 119 (1966).
- (17) The capacity of each solution holder is 5.9 ml.
- (18) These peaks can be cancelled by placing a similar but empty cell in the reference beam of the spectrophotometer.
- (19) R. G. Sinclair, A. F. McKay, and R. N. Jones, *J. Amer. Chem. Soc.*, **74**, 2570, 2575 (1952).
- (20) P. J. Corish and D. Chapman, *J. Chem. Soc.*, 1746 (1957).
- (21) R. A. Maiklejohn, *Anal. Chem.*, **29**, 329 (1957).
- (22) H. Susi, *J. Amer. Chem. Soc.*, **81**, 1535 (1959); *J. Amer. Oil Chem. Soc.*, **37**, 431 (1960).
- (23) R. G. Snyder, *J. Mol. Spectrosc.*, **4**, 411 (1960); **7**, 116 (1961).
- (24) M. Tasumi, T. Shimanouchi, and T. Miyazawa, *J. Mol. Spectrosc.*, **9**, 261 (1962).
- (25) The total internal resistance of the ammeter and standard voltage generator was ca. 100 Ω .
- (26) A comparison between the peak intensities of the adsorbed layer and those of built-up films of lauric acid⁵ whose numbers of layers have been known suggests that the number of adsorbed layers is roughly 20 in an equilibrium state.
- (27) W. N. Hansen, *J. Opt. Soc. Amer.*, **58**, 380 (1968).
- (28) T. Fujiyama in "Spectrochemistry '68-B," Y. Morino, T. Shimanouchi, S. Fujiwara, and M. Oki, Ed., Nankodo, Tokyo, 1968.
- (29) V. Vand, W. Morley, and T. R. Lomer, *Acta Crystallogr.*, **4**, 324 (1951).
- (30) This is also supported by the fact that the peak due to the OH out-of-plane deformation vibration of the adsorbed layer appears at 930 cm^{-1} (Figure 2).³¹
- (31) R. F. Holland and J. R. Nielsen, *Acta Crystallogr.*, **16**, 902 (1963).
- (32) The value at 25° obtained by extrapolating a linear relation³³ between the refractive index of liquid lauric acid and temperature.
- (33) Nippon Yukagaku Kyokai, "Yushi Kagaku Binran," Maruzen, Tokyo, 1958, Chapter 3.
- (34) R. D. B. Fraser, *J. Chem. Phys.*, **21**, 1511 (1953); **28**, 1113 (1958); **29**, 1428 (1958).
- (35) When the electric circuit was disconnected, the peaks further diminished until they became either very weak or unobservable.
- (36) F. Beck and H. Gerischer, *Ber. Bunsenges. Phys. Chem.*, **63**, 500 (1959). Although they have taken into account the contribution of positive holes to eq. 14, it is neglected in the present discussion.

Skeletonized Films and Measurement of Their Optical Constants

M. S. Tomar¹

Department of Physics, University of Roorkee, Roorkee, India (Received April 30, 1973)

Optical properties of molecular films of organic long-chain compounds deposited by the Blodgett-Langmuir technique have already been studied. Optical properties of skeletonized built-up Langmuir films have not been reported thus far. In the present work, ellipsometric studies of these "skeletonized" films are presented. The optical constants reported here are seen to be lower than the unskeletonized molecular films.

Introduction

Ellipsometry is an increasingly important technique for the optical study of solid surfaces or thin films adsorbed on a solid substrate. In most of the work on this subject, the adsorbed layer is considered to be isotropic. The optical properties of the birefringent films have been reported by many authors.^{2,3} Schopper⁴ gave the theoretical formulation of anisotropic films, whose optic axis lies normal to the film surface. We have recently⁵ used his formulations for the first time for experimental investigations. The ellipsometry of anisotropic films have been treated by Engelsen⁶ and recently by Tomar and Srivastava.⁷ The latter gave a theory of ellipsometry which is applicable to absorbing or nonabsorbing anisotropic (uniaxial or biaxial) films adsorbed on a absorbing substrate. With the help of an ellipsometer, we studied the optical constants of Blodgett-Langmuir films of various long-chain organic

compounds. In the present work, an attempt has been made to study ellipsometrically the optical constants of "skeletonized" molecular films of barium stearate, palmitate, margarate, and behenate.

Experimental Section

(1) *Deposition of Molecular Films (Barium Stearate).* Barium stearate films containing the desired number of layers were "built up" on properly selected optically smooth glass slides by the well-known technique of Blodgett and Langmuir (BL).^{8,9} For depositing the film, a monolayer of stearic acid dissolved in benzene (concentration commonly 3×10^{-4} by weight) was spread on the surface of doubly distilled or deionized water (specific resistance 6×10^5 ohm cm) containing 0.3×10^{-4} M BaCl₂, the pH of the solution having been held at about 6.5 by addition of a small amount (4.0×10^{-4} M) of potassium bicarbonate.

The monolayer was transferred from the water surface to the slide by a repeated dipping and withdrawal process, the spread stearic acid film being kept under suitable two-dimensional pressure with oleic acid as "piston oil" (surface pressure 29.0 dyn/cm). Under these conditions, a layer is transferred every time the slide is dipped or withdrawn and in the built-up film the molecules in adjacent layers in the crystal lattices are oppositely oriented. In the above delicate technique, greatest care was taken to minimize vibrations and dust contamination which cause the spread monolayer to break up resulting in cracks and voids in deposited film. The temperature of the ambient medium was maintained at 20–22°, as required. The films of barium palmitate, margarate, and behenate were deposited by a similar process, taking palmitic, margaric, and behenic acid, respectively, instead of stearic acid (used for barium stearate).

(2) "Skeletonization" Process. The films built up by the BL technique are monomolecular layers and composed of a mixture of stearic acid and neutral stearate. We can remove this stearic acid content by dipping the film into a benzene solution. For this, the films are soaked for 8–10 sec in pure benzene solution (BDH, 99.99% pure) and then withdrawn. Benzene dissolves the stearic acid and leaves the barium stearate as a skeleton with air filling the spaces previously occupied by stearic acid (or palmitic, margaric, and behenic acid). The proportion of each component (barium stearate and stearic acid) in the unsoaked film is determined by the barium concentration and the pH of the water solution used in building the film. The process of removing acid content from the film is known as a "skeletonization process." The films thus obtained are homogeneous and reproducible, provided a solution of the same pH is used. Also, great care is taken when soaking the film in benzene for a fixed time. The skeletonized films are birefringent as reported by Blodgett-Langmuir.⁹ The skeletonized films of barium palmitate, margarate, and behenate are also obtained by the same method.

These films are transparent and show no color on the microscope slide used. After the films are skeletonized, vivid colors are seen. This may be due to the decrease in refractive index of the film. The best quality skeletonized films are obtained when the films contained less than 100 layers. Films of varied refractive indices can be obtained by varying the pH of the solution.⁹ In the present work, the films studied were prepared only at pH ≈ 6.5. In case the films are discontinuous, and the patches and cracks can be easily examined by the ordinary reflected light.

(3) *Ellipsometric Observations.* The required number of monolayer are deposited on clean stainless steel slides and studied with an ellipsometer. In our set up, the quarter wave plate (compensator) is used on the analyzer arm just after the sample. Polarizer and analyzer are mounted on the collimating and analyzing arms of the ellipsometer, respectively. Null detection in output is obtained by a photomultiplier detection system.

The ellipticity ϵ and azimuth θ of the reflected light are easily measured and, consequently, we obtained the phase change Δ and amplitude ratio ($r_p/r_s = \tan \psi$) by the following relations¹⁰

$$\cos 2\psi = \cos 2\epsilon \cos 2\theta$$

$$\tan \Delta = \tan 2\epsilon / \sin 2\theta$$

Thus the ellipsometric parameters involved with the theoretical results are obtained experimentally.

Measurement Technique

The polarizer is set at 45° to the plane of incidence. Initially, quarter wave plate and sample are absent and the analyzer is crossed with the polarizer in the direct light ($\lambda = 5893 \text{ \AA}$) so that no light leaves the analyzer. When a sample is introduced, the azimuth major axis of the reflected ellipse may be found by rotating the analyzer from a position A_1 to a position A_2 , which gives minimum intensity. Then $\theta = A_2 - A_1$. If the quarter wave plate is introduced in this azimuth, a linear vibration results and the analyzer is rotated to position A_3 so as to produce extinction. Then $A_3 - A_2 = \epsilon$. Thus ϵ and θ are experimentally measured. Finally, Δ and ψ are obtained using the above equations. In the ellipsometry of anisotropic films,⁷ Δ and ψ are related to film parameters by the relations

$$R_p/R_s = \tan \psi e^{i\Delta} = \frac{(\gamma_p + \gamma_{2p} e^{-2i\beta_p})(1 + \gamma_{1s}\gamma_{2s} e^{-2i\beta_s})}{(1 + \gamma_{1p}\gamma_{2p} e^{-2i\beta_p})(\gamma_{1s} + \gamma_{2s} e^{-2i\beta_s})} \quad (1)$$

where r_1 and r_2 are the Fresnel reflection coefficients at air-film and film-substrate interfaces, respectively, and β is the phase thickness. Subscript p and s denote the vibration parallel and perpendicular to the plane of incidence, respectively, and Z is the direction of the optic axes of the uniaxial film. The anisotropic Fresnel's reflection coefficients are

$$r_{1s} = \frac{n_1 \cos \phi_1 - a_s}{n_1 \cos \phi_1 + a_s} \quad r_{1p} = \frac{n_x^2 \cos \phi_1 - n_1 a_p}{n_x^2 \cos \phi_1 + n_1 a_p}$$

$$r_{2s} = \frac{a_s - n_2 \cos \phi_2}{a_s + n_2 \cos \phi_2} \quad r_{2p} = \frac{\bar{n}_z a_p - n_z^2 \cos \phi_2}{\bar{n}_z a_p + n_z^2 \cos \phi_2}$$

where $a_s = (n_x^2 - n_1 \sin^2 \phi_1)^{1/2}$, $a_p = (n_x/n_z)(n_z^2 - n_1 \sin^2 \phi_1)^{1/2}$, $\bar{n}_z \equiv n_2 - ik_2$ and $\beta_s = (2\pi d/\lambda)a_s$, $\beta_p = (2\pi d/\lambda)a_p$, where ϕ_2 is the complex angle of refraction in the substrate media, and is evaluated by the standard method.¹¹ Substituting the above expressions in eq 1, we obtain a complex equation in Δ and ψ . Separating real and imaginary part from eq 1, we get two equations in Δ and ψ , which may be represented as

$$\Delta = f_n(n_x, n_z, d)$$

$$\psi = f_n(n_x, n_z, d) \quad (2)$$

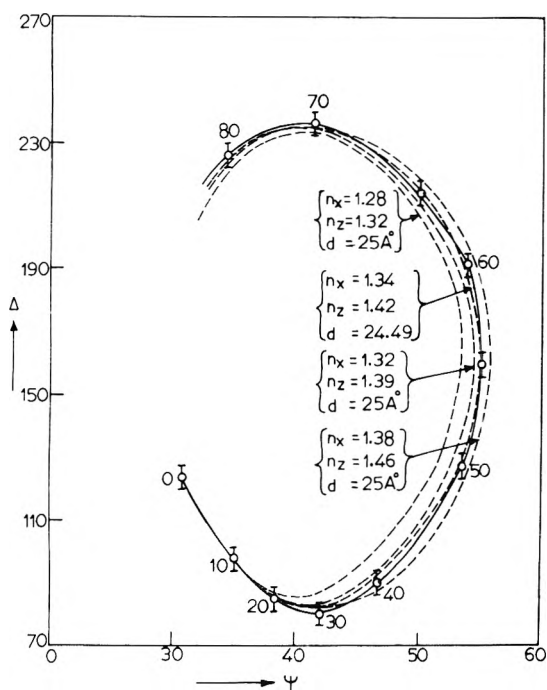
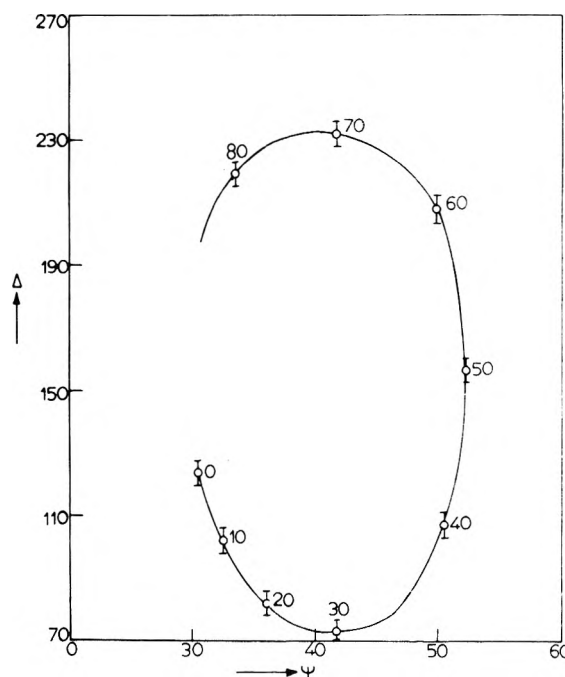
Here n_x and n_z are the two refractive indices of the (uniaxial) film and ($d = nd_1$) is the thickness of the film. n is the number of monolayers in the film and d_1 the monolayer thickness. Thus knowing Δ and ψ , one can calculate the optical constants and thickness. Δ and ψ are measured at k different thicknesses d and a set of $2k$ data is obtained. If the optical constants of the film with uniaxial symmetry are unknown there are $k + 4$ adjustable parameters or $k + 2$ if the film is considered to be isotropic. Hence minimum of four measurements are needed in order to determine all parameters. If we assume that the optical parameters over whole range of thicknesses of the film are constant, the calculation of the optical constants is a least-squares refinement of the crucial parameters

$$F = \sum_i^R (\Delta_{\text{expt}}^i - \Delta_{\text{theory}})^2 + (\psi_{\text{expt}}^i - \psi_{\text{theory}})^2$$

From preliminary calculations, where we assumed that $n_x = n_z$. The layer thickness d_i for the i th measurement is then obtained by calculating Δ and ψ at various thicknesses and refractive indices. By successive iteration a set

TABLE I: Measured Refractive Indices and Thickness per Layer for the Skeletonized Built-up Films

| | No. of layers | n_x | n_z | d_1 |
|---------------------------------|---------------|-----------------|-----------------|----------------|
| Barium palmitate | 10-20 | 1.23 ± 0.01 | 1.39 ± 0.02 | 22.7 ± 0.2 |
| | 30-40 | 1.23 ± 0.03 | 1.40 ± 0.01 | 22.7 ± 0.4 |
| | 40-50 | 1.24 ± 0.01 | 1.37 ± 0.01 | 22.8 ± 1.0 |
| | 50-60 | 1.22 ± 0.02 | 1.38 ± 0.02 | 22.6 ± 0.6 |
| | Av | 1.23 | 1.38 | 22.7 |
| Unskeltonized ^a film | | 1.43 | 1.59 | 23.4 |
| Barium margarate | 10-20 | 1.29 ± 0.01 | 1.45 ± 0.01 | 23.9 ± 0.4 |
| | 30-40 | 1.28 ± 0.02 | 1.43 ± 0.01 | 23.4 ± 0.8 |
| | 50-60 | 1.26 ± 0.02 | 1.45 ± 0.02 | 23.3 ± 0.2 |
| | 70-80 | 1.29 ± 0.03 | 1.43 ± 0.03 | 22.8 ± 0.4 |
| | Av | 1.28 | 1.44 | 23.3 |
| Unskeltonized film | | 1.40 | 1.54 | 24.5 |
| Barium behenate | 10-20 | 1.38 ± 0.03 | 1.51 ± 0.02 | 29.1 ± 0.6 |
| | 40-50 | 1.36 ± 0.02 | 1.48 ± 0.01 | 30.0 ± 0.4 |
| | 50-60 | 1.36 ± 0.02 | 1.50 ± 0.04 | 29.0 ± 0.2 |
| | 70-80 | 1.38 ± 0.04 | 1.49 ± 0.03 | 28.9 ± 0.6 |
| | Av | 1.37 | 1.49 | 29.2 |
| Unskeltonized film | | 1.48 | 1.66 | 30.8 |

^a Reference 7.

Figure 1. Δ - ψ curve for skeletonized barium stearate films with various layer thicknesses: (---) theoretical curve; (—) experimental curve.

Figure 2. Experimental Δ - ψ curve for skeletonized barium palmitate films of various layer thicknesses.

 of parameters n_i , d_i may be found that make

$$F_i = (\Delta_{\text{expt}}^i - \Delta_{\text{theory}}^i)^2 + (\psi_{\text{expt}}^i - \psi_{\text{theory}}^i)^2$$

arbitrarily small. The least-squares calculations are now started using the initial d_i values obtained by assuming the film media to be isotropic and the refractive index to be same average value of the n_i 's just obtained. The isotropic values of n and d_i thus obtained serves as initial value for the anisotropic least-squares refinement, *i.e.*, $n_x = n_z = n(\text{isotropic})$. Engelsen's⁶ ALGOL computer program was changed to Fortran IV and is used in the IBM 360 computer.

Ellipsometric parameters Δ and ψ are measured for these (*i.e.*, barium stearate, palmitate, margarate, and behenate) skeletonized films. Measurements were made in two zones. The optical constant of the stainless steel slide

was obtained by the usual method.¹² The values thus obtained⁷ were found to be $n_2 = 2.47$ and $k_2 = 3.46$. The angle of incidence was 70° and sodium light is used as a source.

Results and Discussions

The experimental Δ - ψ curve for skeletonized barium stearate films for various monolayers is given in Figure 1. To show the error analysis, the theoretical Δ - ψ curves obtained using various sets of indices and monolayer thickness are also given in Figure 1. The theoretical curve that best fits with the experimental Δ - ψ is also given in the figure. The value of optical constant and thickness per monolayer which fits best is seen to be $n_x = 1.34$, $n_z = 1.42$, and $d_1 = 24.49 \text{ \AA}$. The values thus obtained are seen to be in good agreement with earlier results. Barium stearate was examined previously by Blodgett and Langmuir⁹

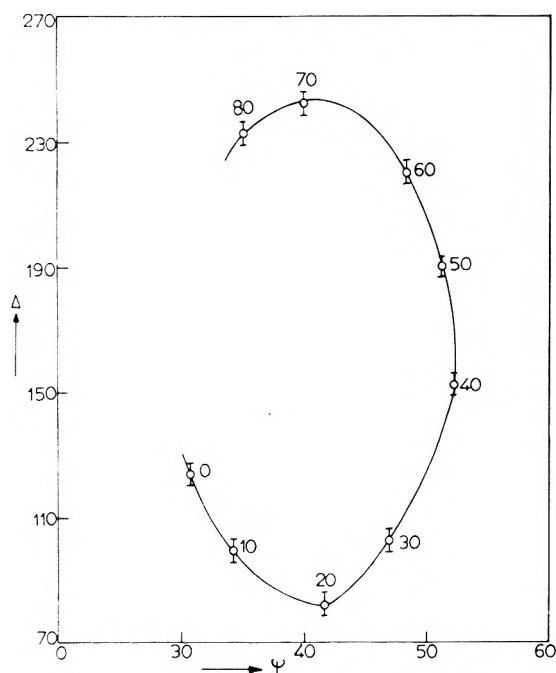


Figure 3. Experimental Δ - ψ curve for skeletonized barium margarate films of various layer thicknesses.

(i.e., $n_x = 1.32$, $n_z = 1.39$, and $d_1 = 24.78 \text{ \AA}$) using visual interferometry. Therefore, it may be clearly seen that ellipsometric results can give a better picture of experimental data, which otherwise also shows good agreement with the Blodgett-Langmuir values. The anisotropy ($n_z - n_x$) for these films is seen to be slightly higher when compared⁷ to the unskeltonized films of barium stearate. Figures 2-4 show the Δ - ψ curve for skeletonized barium pamitate, margarate, and behenate films with varying number of layers in the film. To the author's knowledge, the optical constants of these skeletonized films have not been reported thus far using the ellipsometric technique. The optical constants and thickness of these films are obtained using the mathematical method adopted above. Δ and ψ are the simultaneously measurable quantities. To determine experimental error for a single measurement, we keep ψ fixed for single set since ψ is insensitive¹³ while Δ is sensitive to the surface. Hence by keeping ψ fixed we have shown the error in a single measurement of Δ and the standard deviation from the mean value of Δ for a single measurement is indicated in Figures 1-4.

The optical constants of these skeletonized films are seen to be lower than the unskeltonized films.⁷ The comparison can be seen from the table. This decrease in refractive indices depends on the quantity of material re-

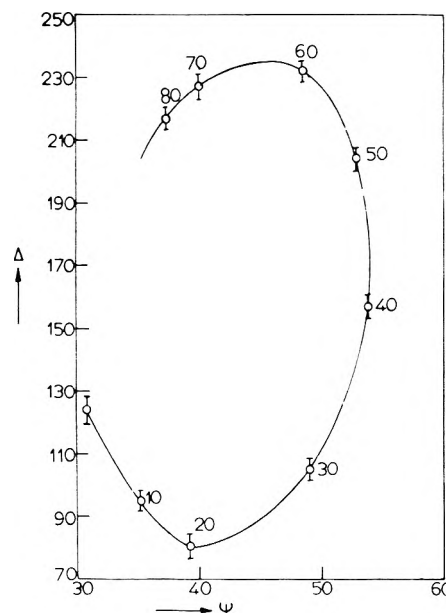


Figure 4. Experimental Δ - ψ curve for skeletonized barium behenate films of various layer thicknesses.

moved and the pH values of the solution. In the present work, solutions were maintained at $\text{pH} \approx 6.5$ and the films were dipped in pure benzene solution for about 10 sec. At $\text{pH} \approx 6.5$, approximately 36% free acid is dissolved.⁹ Blodgett and Langmuir have given data for some of the skeletonized barium stearate films prepared in different pH solutions.

Acknowledgment. My sincere thanks are due to Dr. D. den Engelsen, Philips Research Laboratory, Eindhoven, The Netherlands, for providing the listed program for the calculations.

References and Notes

- (1) Address correspondence to the Department of Physics, Indian Institute of Technology, Delhi, Hauz Khas, New Delhi-110029, India.
- (2) (a) A. Wunsche, *Ann. Phys.*, **25**, 201 (1970); (b) L. P. Mosteller and F. Wooten, *J. Opt. Soc. Amer.*, **58**, 511 (1968).
- (3) G. A. Bootsma and F. Meyer, *Surface Sci.*, **14**, 52 (1969).
- (4) H. Schopper, *Z. Phys.*, **132**, 146 (1952).
- (5) M. S. Tomar and V. K. Srivastava, *J. Appl. Phys.*, in press.
- (6) D. den Engelsen, *J. Opt. Soc. Amer.*, **61**, 1460 (1971).
- (7) M. S. Tomar and V. K. Srivastava, *Thin Solid Films*, **15**, 207 (1973).
- (8) K. B. Blodgett, *J. Amer. Chem. Soc.*, **57**, 1007 (1935).
- (9) K. B. Blodgett and I. Langmuir, *Phys. Rev.*, **51**, 964 (1937).
- (10) H. G. Jerrard, *Surface Sci.*, **16**, 137 (1969).
- (11) O. S. Heavens in "Physics of Thin Films," Vol. 2, G. Hass and R. E. Thum, Ed., Academic Press, London, 1966, p 206.
- (12) A. Rothen and M. Hanson, *Rev. Sci. Instrum.*, **19**, 839 (1948).
- (13) F. L. McCrackin, E. Passaglia, R. R. Stromberg, and H. L. Steinberg, *J. Res. Nat. Bur. Stand., Sect. A*, **67**, 363 (1963).

From the borders of organic chemistry ... To the borders of theoretical physics:

Inorganic Chemistry brings you a broad range of authoritative information presenting both experimental and theoretical studies in all phases of inorganic chemistry.

Each month, this rapidly growing journal brings you the data you need on synthesis and properties of new compounds, quantitative studies regarding structure, and thermodynamics of inorganic reactions.

When you've seen the 50 or more papers offered in each issue, you'll also want to look through the Notes and Correspondence sections for their concise exchange of scientific views and ideas.

To order INORGANIC CHEMISTRY today, just complete and return the form below.



... another ACS service



Inorganic Chemistry

Inorganic Chemistry
American Chemical Society
1155 Sixteenth Street, N.W.
Washington, D.C. 20036

Yes, I would like to receive INORGANIC CHEMISTRY at the one-year rate checked below:

| ACS Member Personal-Use | U.S. | Canada | Latin America | Other Nations |
|-------------------------|----------------------------------|----------------------------------|----------------------------------|----------------------------------|
| One-Year Rate | <input type="checkbox"/> \$16.00 | <input type="checkbox"/> \$22.00 | <input type="checkbox"/> \$22.00 | <input type="checkbox"/> \$23.00 |
| Nonmember | <input type="checkbox"/> \$54.00 | <input type="checkbox"/> \$58.00 | <input type="checkbox"/> \$58.00 | <input type="checkbox"/> \$59.00 |

Bill me Bill company Payment enclosed

Name _____

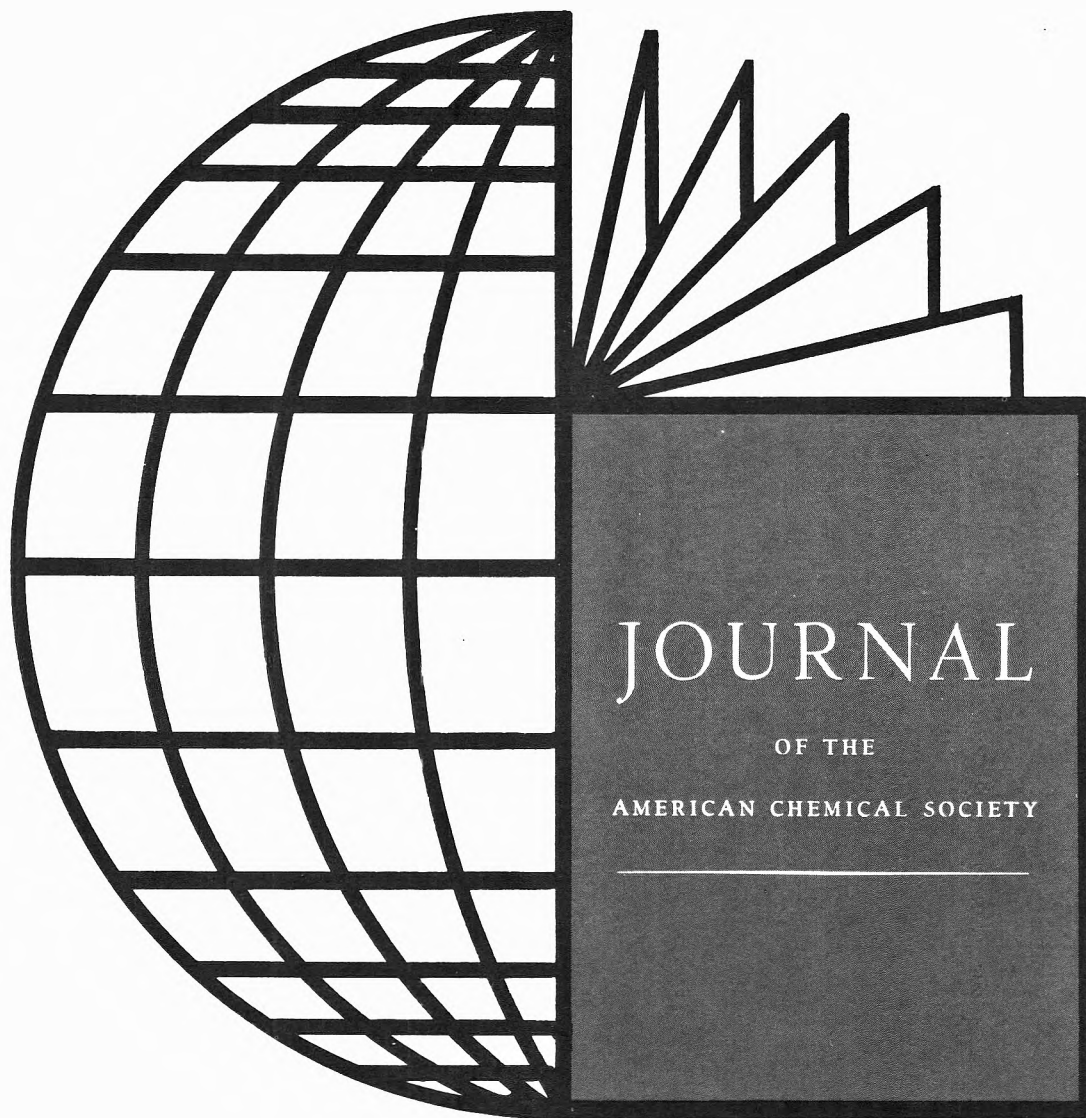
Street _____

Home
Business

City _____

State _____

Zip _____



Most cited chemical journal in the entire world

... and one of publishing's best subscription values! That's right! You pay less per page for JACS—the most widely cited journal in chemistry—than for any other major scientific journal in the world.

But don't subscribe to this internationally respected journal because it's inexpensive. Subscribe because you will receive biweekly original research articles that cover ALL chemical research areas ... together with many concise, up-to-the-minute Communications. Regardless of your major field of interest in chemistry, you'll find an abundance of authoritative and definitive data in each issue that cuts across ALL chemical research areas and is valuable and relevant to *your* work as well.

Order your own personal subscription to the number one chemical journal now. Complete and return the form.



... another ACS service

Journal of the American Chemical Society
American Chemical Society
 1155 Sixteenth Street, N.W.
 Washington, D.C. 20036

1974

Yes, I would like to receive the JOURNAL OF THE AMERICAN CHEMICAL SOCIETY AT the one-year rate checked below:

| | U.S. | Canada** | Latin America** | Other Nations** |
|----------------------------------|---------------------------------------|---|----------------------------------|----------------------------------|
| ACS Member One-Year Rate* | <input type="checkbox"/> \$22.00 | <input type="checkbox"/> \$27.00 | <input type="checkbox"/> \$27.00 | <input type="checkbox"/> \$28.00 |
| Nonmember | <input type="checkbox"/> \$66.00 | <input type="checkbox"/> \$71.00 | <input type="checkbox"/> \$71.00 | <input type="checkbox"/> \$72.00 |
| Bill me <input type="checkbox"/> | Bill company <input type="checkbox"/> | Payment enclosed <input type="checkbox"/> | | |

Air freight rates available on request.

Name _____
 Street _____ Home
 Business
 City _____ State _____ Zip _____

*NOTE: Subscriptions at ACS member rates are for personal use only. **Payment must be made in U.S. currency, by international money order, UNESCO coupons, U.S. bank draft, or order through your book dealer.